IntechOpen

Light-Emitting Diode

An Outlook On the Empirical Features and Its Recent Technological Advancements

Edited by Jagannathan Thirumalai

LIGHT-EMITTING DIODE - AN OUTLOOK ON THE EMPIRICAL FEATURES AND ITS RECENT TECHNOLOGICAL ADVANCEMENTS

Edited by **Jagannathan Thirumalai**

Light-Emitting Diode - An Outlook On the Empirical Features and Its Recent Technological Advancements
http://dx.doi.org/10.5772/intechopen.70968
Edited by Jagannathan Thirumalai

Contributors

Alfonso Gago-Calderón, Rami D. Orejón-Sanchez, Manuel J. Hermoso-Orzáez, Baiquan Liu, Dongxiang Luo, Peng Xiao, Zhiyuan He, Qunxing Liu, Guijie Li, Yuanbin She, Hideki Hirayama, Luiz Pereira, Manish Kumar, Miguel Ribeiro, Natalio Milardovich, Leandro Prevosto, Jagannathan Thirumalai

Notice

First published in London, United Kingdom, 2018 by IntechOpen
eBook (PDF) Published by IntechOpen, 2019
IntechOpen is the global imprint of INTECHOPEN LIMITED, registered in England and Wales, registration number: 11086078, The Shard, 25th floor, 32 London Bridge Street
London, SE19SG – United Kingdom
Printed in Croatia

British Library Cataloguing-in-Publication Data
A catalogue record for this book is available from the British Library

Additional hard and PDF copies can be obtained from orders@intechopen.com

Light-Emitting Diode - An Outlook On the Empirical Features and Its Recent Technological Advancements
Edited by Jagannathan Thirumalai

p. cm.

Print ISBN 978-1-78923-750-4

Online ISBN 978-1-78923-751-1

eBook (PDF) ISBN 978-1-83881-496-0

Meet the editor

Dr. J. Thirumalai received his PhD from Alagappa University, Karaikudi, in 2010. He was also awarded the Postdoctoral Fellowship from Pohang University of Science and Technology, Republic of Korea, in 2013. He worked as an assistant professor in physics at the B.S. Abdur Rahman University, Chennai, India (2011–2016). Currently, he is working as Assistant Professor of Physics, SASTRA Deemed University, Kumbakonam (Tamil Nadu), India. His research interests focus on luminescence, self-assembled nanomaterials, and thin film optoelectronic devices. He has published more than 50 SCOPUS/ISI indexed papers and 10 book chapters, edited six books, and is a member of several national and international societies such as RSC, OSA, etc. He has edited two books for InTechOpen. He served as a principal investigator for a funded project towards the application of luminescence-based thin film optoelectronic devices, funded by the Science and Engineering Research Board, India.

Contents

Preface

The manufacture of light emitting diodes (LEDs) has opened many opportunities in science and technology by providing work for novel smart display gadgets. The triumph of emerging micro- and nanosized LEDs has become lengthened with advanced hi-tech improvements in technologies. Ultimately, the LED can be broken down into three major categories: (i) traditional inorganic LEDs, (ii) organic LEDs (small molecule OLEDs, polymer LEDs, passive matrix OLEDs, and active matrix OLEDs), and (iii) high brightness LEDs. With the increased demand for OLED-based touchscreens, electronics manufacturers are increasingly turning to UV LEDs because of their many benefits in bonding applications for OLED flat panel manufacturing. The benefits to manufacturers include high productivity, environmental safety and friendliness, and a reliable solution to how these products are cured. LEDs are low cost, fascinating, and important to humankind. Capitalizing on the latest applications of LEDs has proffered innovative technological advancements, which have been rapidly implemented for groundbreaking research, especially in the subnanoscale, which involves physical and chemical properties of the lighting process.

For more than a decade, semiconductor technology has been elevated to greater heights. The result is in the form of nifty semiconductor electronic devices. Furthermore, commercially available LEDs and OLEDs deliver enhanced illumination with low power consumption and have longer lifetimes too. Undoubtedly, these innovations have survived the impact of the different sizes, shapes, and even the circuit design to which an LED can be affixed. Also, the production of LEDs encompasses the following: flexible thin film LEDs and OLEDs, color capability, low power consumption, brighter images, wide viewing angles, fast response times, low cost, extended lifespan, UV sensitivity, restriction of hazardous substances manufacturing compatibility (lead free), etc., in comparison with their traditional counterparts. There are a number of concrete motives for switching to LED bulbs, due to their durability, chemical stability, extended lifetime, cost-effectiveness, etc. In addition, LEDs are not oversensitive to temperature or humidity, making them ideal for active indoor and outdoor lighting. Unlike *compact fluorescent* lamps (CFLs), which contain a minor quantity of mercury, LEDs are not manufactured with any precarious material making them safe both around the home (even if broken) and when they are disposed of.

Globally, there is a faster growth into an additional defensible way of living environment, the LEDs and OLEDs captivating over the illumination space by replacing with CFL bulbs. For some reasons, LEDs still do not dominate the commercial market, which is still controlled by the first generation of LED light bulbs that have narrow light beams. and that the flea market prices were at first besides costs more. However, all these issues are being overcome with the help of recent advancements in LED technology. Clusters of LED precut chips are being assembled during the fabrication of second-generation LED lights. These are known as surface-

mounted diodes. The modern generation of LED lighting uses chip on board technology, as well as new filament technology that contributes to the outcome of incandescence. The present day sees the latest fabrication techniques on LEDs and OLEDs providing scientific developments at the frontline of optical sciences with good international prospects. As a result, the aforesaid technological advancements in LEDs and OLEDs may perhaps be desired for these applications. The capability to imitate modern LED devices from microscale to nanoscale is of pivotal importance to the advancement in micro- and nanotechnologies. This book forms the basis for a better fundamental understanding of the capabilities and limitations of LEDs, and also may suggest better, cheaper, or alternative lighting technologies.

The broad spectrum of this book provides exhaustive coverage of selected advanced topics in LEDs and OLEDs by highly experienced authors. Also, research scientists from dissimilar areas are very often prolifically employed in the field of LEDs and OLEDs all over the global network. This book describes the advanced knowledge of frontline subjects in LED and OLED materials and their applications. The chapters of the book have been contributed by eminent scholars active in recent research and development in materials science, and are ideal for researchers and students to gain an understanding of the basic ideas that are imperative to the pertinent areas of research. It is our expectation that you, the readers, will find this book of immense help in your research.

The book consists of seven chapters dealing with LEDs and their phototoxic-cum-bactericidal effect of blue LED irradiation, the history of LEDs and OLEDs with necessary examples, DC network indoor and outdoor LED lighting, white organic LEDs with thermally activated delayed fluorescence emitters, tetradentate cyclometalated platinum (II) complex-based efficient organic LEDs, the impact of the use of large LED lighting loads in low-voltage networks, highly efficient OLEDs using thermally activated delayed fluorescent materials, and AlGaN deep ultraviolet LEDs.

I would like to thank all the contributors of the chapters for their tremendous efforts in creating outstanding work. Last but not least, I would like to express my sincere gratitude to Ms. Danijela Sakic, publishing process manager, for effective communication and assistance during the preparation of this book.

Jagannathan Thirumalai
SASTRA Deemed University
Tanjavur, India

Chapter 1

Introductory Chapter: The Impression of Light-Emitting Diodes in Space-Age Advancements and Its Effect of Blue LED Irradiation

Jagannathan Thirumalai

Additional information is available at the end of the chapter

http://dx.doi.org/10.5772/intechopen.79375

1. A succinct evidence of light-emitting diode

Amid the supreme contemporary machineries in lamps and lighting devices, Light-emitting diodes (LEDs) have an enormous amount of novel applications day by day, and flattering ever more prevalent and manageable to the societal benign. Basically, the LED is connected to direct current which emits light in the visible region of spectrum. While experimenting with silicon carbide (crystal detectors) and a cat's whisker, the first discovery of electroluminescence phenomenon using light emitting diode was noticed back at the beginning of the twentieth century (1907), by a British radio engineer H J Round and the assistant to Guglielmo Marconi [1, 2]. In 1927, the phenomenon of electroluminescence in the diodes used in radio sets was studied by a Russian radio researcher Oleg Vladimirovich Losev. Also a credit toward his research, he has published a paper named Luminous carborundum [silicon carbide] detector and detection with crystals [3]. At room (298 K), low (77 K) temperature and even in other semiconductor alloys, the infrared emission was observed by employing the simple diode structures with indium phosphide (InP), silicon-germanium (SiGe), gallium arsenide (GaAs), and gallium antimonide (GaSb) alloys by Rubin Braunstein in 1955 [4]. Years later in the fall 1961, the first infrared LED was invented and patented by Robert Biard and Gary Pittman [5–7]. In 1962, the first visible red LED was invented by Nick Holonyack, using gallium arsenide phosphide (GaAsP) as a substrate for the diode [8]. By employing gallium arsenide phosphide in the diode, the first yellow LED was invented by M George Craford in 1972 [9]. In 1968, the Monsanto Company was the leading group of institution has made a mass-production of visible red LEDs as indicators using gallium arsenide phosphide (GaAsP). Nevertheless, it was not in anticipation of the 1970s that LEDs befitted popular as

soon as Fairchild Optoelectronics instigated manufacturing the low-cost LED devices [10]. In 1976, Thomas P. Pearsall invented a new semiconductor LED materials to be used in fiber optics and telecommunication systems with tremendously bright and high efficiency [11]. In 1979, first blue LED using gallium nitride (GaN) was designed by Shuji Nakamura of Nichia Corporation. By dint of creative techniques, the Fairchild Optoelectronics have made LED into profitable manufactured goods with diversity of usages based on packaging and a planar process of chip production. [5–8].

Among the utmost topical technological advancements in lamps lighting devices, LEDs have enormous amount of application niches. Day by day, LEDs are flattering more attractive and more accessible to the common people. For the past few decades semiconductor technology has progressed to greater statures. The result is in the form of smart gadgets and the LEDs which give enhanced illumination with low power ingesting and better life span too.

The LED can be lingering further into three major categories are: (1) traditional inorganic LEDs, (2) organic LEDs (small molecule OLED, polymer LED, passive matrix OLED, active matrix OLED), (3) high brightness LEDs. Further, **Table 1** provides the detailed information about the historical developments in LED and OLED [1–55].

Traditional Inorganic LEDs: By employing various inorganic materials, the traditional type LEDs are made and therefore called as inorganic LEDs. A number of extensively used LEDs have been fabricated using semiconductor materials like aluminum-gallium arsenide (AlGaAs) and indium-gallium nitride (InGaN). Furthermore, with different doping concentrations in inorganic semiconductor material, the traditional inorganic LEDs are used nowadays. These are obtainable in souk with various sizes, shapes and colors like single color LED, surface mounted LED, flashing LED and multicolor LED.

Organic LEDs: Using organic materials, the organic LEDs have been fabricated, which are fictitious from carbon-based polymers and semiconductors. Organic light-emitting diode (OLED) is a thin film of organic compound which consists of a PN junction made by an emissive electroluminescent layer. Further, the emissive layer emits light in Ref. to an electric current and this layer of organic material is positioned among two electrodes. In general, it is realized that as a minimum one of the electrodes must be a transparent one. The organic LEDs are factory-made in the form of thin films; hence, these are given that a small portion for diffusion through which the light engenders, and these can be used for larger surface area. Furthermore, the OLEDs are available in the form of small molecule OLED, polymer LED, passive matrix OLED, and active matrix OLED.

High brightness LEDs: This type of high brightness (HB) comprises both inorganic and organic LEDs, and these are broadly employed for lighting applications. In essence, this type of LEDs is nearly similar as organic LEDs; however, these HBLEDs could produce a very high brightness of light output with respect to the OLEDs. For engendering high brightness, these LEDs require a high current and high-power debauchery; as a result, these LEDs were kept on the heat sink for eradicating the liberation of unnecessary heat.

All these three types have found enormous progresses in their light output in recent years. However, the normal quantum yield is exceeding 100 lm/W for the inorganic

Light-emitting diode (inorganic LED)			**Organic light-emitting diode (OLED)**		
Year	Historical development	Ref.	Year	Historical development	Ref.
1907	The first discovery of electroluminescence phenomenon using light emitting diode were noticed back at the beginning of the twentieth century, was discovered by a British radio engineer *H J Round* and assistant to *Guglielmo Marconi* while investigating with silicon carbide (crystal detectors) and a cat's whisker	[1, 2]	1950 to 1955	André Bernanose and coconspirators at Université de Nancy, France, consummate the first innovations of electroluminescence in organic materials. By applying the high alternating voltages in air to materials for instance acridine orange (*N,N,N′,N′*-Tetramethylacridine-3,6-diamine), whichever set down on or melted on the thin film layer of cellophane or cellulose. The mechanism put forward of any kind of excited electrons or direct excitation of the dye molecules.	[30–33]
1927	A Russian radio researcher *Oleg Vladimirovich Losev* was experimenting the phenomena of electroluminescence (dealing with the emission spectrum of light radiation in regard to the current–voltage physiognomies of SiC cat's whisker diodes) in the diodes especially employed in radio sets. He has inquisitively published an article called Luminous carborundum [silicon carbide] detector and detection with zincite & iron glance crystals.	[3, 4]	1960	From New York University, Martin Pope and few of his accomplices fabricated the ohmic dark-injecting electrode contacts to organic crystals. These acquaintances are the root of injection of charges in all contemporary OLED gadgets.	[34, 35]
1935	The French physicist Georges Destriau discovers light emission (electroluminescence) in zinc sulfide. Further the effect can be called as "Lossew Light".	[5–8]	1963	Pope's group as well first perceived direct current (DC) electroluminescence under vacuum on a single pure crystal of anthracene and on anthracene crystals doped with tetracene based on a lesser area silver electrode at 400 V under the process of field-accelerated electron excitation of molecular fluorescence.	[36]
1939	Zoltan Bay together with Gyorgy Szigeti received a U.S. patent on "Electroluminescent light sources" which were made of a lighting device using SiC, with an possibility on boron carbide (BC), that emitted white, yellowish white, or greenish white contingent on impurities present; these light sources were the ancestors of light-emitting diodes (LEDs).	[5–8]	1965	Pope's group described the nonoccurring of an external electric field, the recombination of a thermalized electron and hole electroluminescence mechanism can be instigated on anthracene crystals, and as a result the conducting level of anthracene dwell in the higher energy than the energy level of exciton.	[37]
1951	After the discovery of transistor, Shockley and his collaborators Howard Briggs and James Haynes applied for manifest on infrared LED by employing Germanium and Silicon.	[5–8]	1965	For the first time, W. Helfrich and W. G. Schneider developed the double-injection recombination electroluminescence in an anthracene single crystal by the usage of hole and electrons injection electrodes.	[38]

Light-emitting diode (inorganic LED)			Organic light-emitting diode (OLED)		
1952	Kurt Lehovec and his research team have applied for a patent aimed at SiC diodes that emit light. The research team has grown n-type SiC doped with arsenic and then literally acquaints using boron with a beam of electron to produce p-SiC for the junction.	[5–8]	1965	Dow Chemical patented a method of preparing electroluminescent cells using the mechanism of electronic excitation at the contacts between the graphite particles and the anthracene molecules.	[39]
1955	Rubin Braunstein observed infrared emission generated by simple diode structures using gallium antimonide (GaSb), GaAs, indium phosphide (InP), and silicon-germanium (SiGe) alloys at room (298 K) and at low (77 K) temperature and even in other semiconductor alloys as well.	[9]	1975	Roger Partridge patented the first observation of electroluminescence from polymer films and his device contained of a thick film of poly(N-vinylcarbazole) equal to 2.2 micrometers located among two charge injecting electrodes and further the work got consequently published in 1983.	[40–44]
1958	Rubin Braunstein and Egnor Loebner, working at Radio Corporation of America (RCA) patented a green LED made from lead antimonide (PbSb) dot amalgamate to p-type Germanium (Ge).	[10]	1987	Ching W. Tang and Steven Van Slyke at Eastman Kodak develop the first practical OLED device. This device utilized a two-layer structure with distinct electron and hole transporting layers such that the light emission through recombination process can happen in the intermediate of the organic layer; this would yield in the enhancement in efficiency and a decline in operating voltage.	[45]
1961	James Robert Biard and Gary Pittman invented the infrared radiation from GaAs when electric current is applied and patented a first infrared LED.	[11–13]	1990	J. H. Burroughes *et al.* reported a research on high efficiency green light-emitting polymer-based device by employing poly(p-phenylene vinylene) with a film thickness of 100 nm.	[46]
1962	Nick Holonyack (regarded as Father of LED) invented the first practical visible spectrum of red LED with high efficiency by using gallium arsenide phosphide (GaAsP) as a substrate for the diode.	[14]	1994	Universal Display Corporation (UDC) is a developer and manufacturer of organic light emitting diodes (OLED) technologies (profitable for phosphorescent-based OLEDs and also respective supple, stacked and transparent OLEDs) and materials in regard to the supplier of services to the display and lighting industries.	[47]
1968	MONSANTO Company becomes the first organization to churn out visible red LEDs based on gallium arsenide phosphide (GaAsP).	[5–8]	1998	As an additional advantage the printable and flexible displays were developed using Polymer LEDs.	[48]
1970	FAIRCHILD Optoelectronics (Part of Monsanto Electronic Materials Group) produce commercially successful LEDs.	[5–8]	2004	The potential advantages of OLEDs include thin, cost effective displays along with high contrast, color gamut, low driving voltage, and widespread observing angle.	[49]

Light-emitting diode (inorganic LED)			Organic light-emitting diode (OLED)		
1971	By employing gallium nitride the first blue LED was developed by Jacques Pankove.	[15]	2008	The organic materials could be considered as small organic molecules in a crystalline phase, or polymers. OLEDs could be widely employed to create display imaging for portable electronic devices like mobile phones, MP3 players, and digital cameras, while conceivable for imminent uses comprise televisions and lighting applications.	[50]
1972	M George Craford invented the first yellow LED using gallium arsenide phosphide (GaAsP) in the diode with an enhanced illumination of red and LEDs with red-orange emission by factors of ten.	[16]	2013	Zhenan Bao et al., have evaluated an innovative approach to develop a large-area organic semiconductor thin film with highly oriented single crystalline domains.	[51]
1974	Stevenson published a patent, reveals a category of gallium nitride (GaN) LED that illuminates light in the visible (violet) region of the spectrum. By employing organic and inorganic phosphors GaN LED may convert lower frequencies (lower energy) with good conversion efficiency. Further he suggests, by employing dissimilar phosphors, all the primary colors may be prepared from this similar basic device."	[17]	2015	Consequent researches have been technologically advanced on polymer-based multilayer device, plastic electronics, production of novel OLED-based devices were grown rapidly and so on.	[52]
1976	Thomas P. Pearsall invented a new semiconductor material having exceptionally bright LED and high efficiency in lieu of usage in fiber optics and telecommunications.	[5–8]	2016	OLED Display Forecasts 2016–2026: The up-to-date development in plastic and flexible display technology analysis. With reference to a deep profundity of the technological analysis and the remaining logjams, IDTechEx has predicted all types of OLED display flea market toward its future prospects.	[53]
1987	Using AlGaAs (aluminum gallium arsenide) diodes, the Hewlett Packard has produced the first application, encompasses lighting and usage of light bulbs in vehicles brake light, traffic lights and so on.	[5–8]	2017	OLED technology delivers three decades of display innovation with high brightness.	[54]
1989	Cree Inc. declared the first commercially accessible blue LED based on indirect band gap silicon carbide (SiC) semiconductor.	[5–8]	2018	Owing to its intrinsic benefits and upcoming prospect OLED has been applied to widespread applications. Nowadays, OLED is widely employed in smart mobile phones, notebooks, smart watches, TV, visual reality (VR) devices, smart wearable devices, on-board displays, etc.	[55]

Light-emitting diode (inorganic LED)			Organic light-emitting diode (OLED)
1991	Masayuki Senoh, scholar at NICHIA is successful in fabricating p-type gallium nitride (GaN).	[5–8]	
1991	A multi-LED-chip methodology in which the light emitted from three LED chips emitting the three primary colors (red, green, and blue) is mixed to generate white light.	[18]	
1994	Using p-n junction gallium nitride (GaN), the first high illumination blue LED was fabricated by Shuji Nakamura of Nichia Corporation.	[5–8]	
1995	Using indium tin oxide (InSnO), a transparent contact LED was made by Alberto Barbieri.	[5–8]	
1999	PHILIPS LUMILEDS launched power LEDs accomplished of incessant usage by the side of one watt.	[5–8]	
2002	LUMILEDS made 5 WATT LEDs having a luminous efficacy of 18–22 lumens per watt.	[5–8]	
2006	The first LEDs about 100 lumens per watt are manufactured.	[5–8]	
2008	BILKENT University reports the luminous efficacy about 300 lumens per watt from the visible light and warm light by means of nanocrystals.	[5–8]	
2009	CAMBRIDGE University bangs a method for making silicon-based gallium nitride LEDs.	[5–8]	
2010	LEDs of a definite color with a gargantuan luminous efficacy of 250 lumens per watt are heretofore being technologically advanced under laboratory circumstances.	[5–8]	
2010	Solid-state lighting (SSL) is a developing field that potentials enactment features and efficiencies are to use and to harvest enormous extents in terms of energy-economics perspective.	[19, 20]	

Light-emitting diode (inorganic LED)			Organic light-emitting diode (OLED)
From 2010 onward	High luminous efficiency and, consequentially, low power consumption (67 lm/W, Philips, 2010; 94 lm/W, Philips, 2010; commercial LED light bulbs with source efficacies >100 lm/W, by multiple manufacturers, 2015).	[21]	
2011	Elgala et al., discussed about the optical wireless (OW) as a capable balancing technology for RF technology has grew newfangled impetus powered by noteworthy utilizations in solid state lighting technology.	[22]	
2014	The Cree Company declared a laboratory-result efficacy of 303 lm/W for a white LED lamp (excluding power supply) with a related color temperature of 5150 K at an injection current of 350 mA. The OSRAM Company proclaimed a lamp efficacy of 215 lm/W and a system efficacy (including power supply) of 205 lm/W for a white LED lamp system along with a color temperature of 3000 K.	[23, 24]	
2014	Zhang et al. showed that the phosphor-in-glass-based white LED shows not only have remarkable features like heat- and humidity resistance, in addition to that it possess high luminous efficacy of 124 lm/W with a correlated color temperature of 6674 K and a color rendering index of 70.	[25]	
2015	The commercial, Light Fidelity (Li-Fi) is designated as a Visible Light Communications (VLC) system running wireless communications itinerant at very extreme haste. The process is by a rapid adoption of indoor and outdoor solid-state lighting will serve as a powerful platform for a new means of delivering data (swaggering speeds of up to 224 gigabits per second approx.) visible light communication (VLC) or Li-Fi.	[26]	

Light-emitting diode (inorganic LED)			Organic light-emitting diode (OLED)
2016	LED Technology Breakthroughs: There were many exciting and surprising technology breakthroughs, based on statistics compiled by LED inside there were at least 10 major technology advancements this year.	[27]	
2017	K. P. Acharya et al., have demonstrated on the high efficiency colloidal quantum dot-polymer hybrid light emitting diodes (QLEDs) that show external quantum efficiencies >12% for all the three primary colors (21% from green) from a positive aging effect (the efficiency of the QLED gets augmented with time).	[28, 29]	
	In the market, nowadays world's top LED-based device manufacturing companies like CREE, NICHIA, Toyoda Gosei, OSRAM, Lumileds (Philips), Seoul Semiconductor, LG Innotek, Edison Opto., EPISTAR, Seoul Semiconductor, San'an Optoelectronics, Sony, Samsung and so on, making high brightness LEDs, LED chips, HD-TVs with excellent lumens output, durability and lifetime, etc.		

Table 1. Historical developments in LED and OLED.

white-phosphor-based LEDs. Also, it could be found that general lighting applications using OLEDs with a rating 50 lm/W [53–55].

2. Recent space-age advancements of LED and its phototoxic-cum-bactericidal effect of blue LED irradiation

In the past few years, incredible developments have been made in LED technologies. In the ambience of lighting industry, LED technology forms one of the energetic forces besides new lighting notions and applications. The accelerated change produce in product design yields the respective powerful light sources. One of the more fundamental advancements, which has promise in the LED arena, is from the nanotechnology referred to as "quantum dots." Being make a breakthrough in efficiency, the respective ultra-small crystals would possess unique

properties that could be tuned to emit light covering the visibility spectrum. This is highly important because when these particles are in a confined state, they would have the potential to provide diverse options for color for a while producing an improved white. The uniformity, quality, and tonal color of an LED source desperately add to its allure in usage in commercial production applications. Color stability in fact is one of the more accelerating developments seen recently. Using inorganic packaging associated with flip-chip mounting, the features of the phosphor layer are matched to each chip's individual characteristics. As a result, firms could now suggest white LEDs that have a highly precise prefixed color temperature without the discarding necessary to account for natural changes in color. Another significant advancement in LED technologies has to be done with the material which is in the usage in their production and the resulting efficacy of that production. With one emerging technology, LED lighting could be made with a mixture of organic and inorganic materials. The cumulative effect of this technology is somewhat than typical four or five layers of material would be necessary in producing the product; this new material necessitates just one layer. This vividly lowers the cost of production and produces the manufacturing process relatively easier. This is yielding lower cost for LED light sources while performance continues to enhance. This emerges the new technology to more and more potential applications all over the time [56].

A recent study of the bactericidal and phototoxic effect of blue LED irradiation revealed that LED irradiation persuades apoptosis by triggering a mitochondria-mediated pathway and reducing the preliminary growth rate of melanoma cells [57]. Oh et al. observed that irradiation with blue LEDs abridged cell feasibility and thus persuaded apoptotic cell death with the mouse A20 and human RAMOS B-cell lymphoma cells [58]. As a potential risk of high energy LED lamps, lighting at night may disturb the body's biological clock, the circadian rhythm. According to the Harvard Health Letter "Blue light has a dark side," the blue wavelengths seem to be the most harmful at night and comprise a large portion in the emission of CFLs and LED lamps [59, 60].

3. Conclusion

The promulgation of LED lighting has led to prompt progressions in LED lighting technologies over the past few eons across the globe with state-of-the-art scientific advancements; however, evidences besides authenticates that it has been and will spread out to be vitally important in the direction of revolutionary investigation against innovative applications for the societal cause. Among the most important notable advancement in sundry fields of LED and OLED has the roadmap for flexible OLEDs points to the emergence of foldable, rollable displays and the espousal of OLED in smart mobile phones will reach more than 70% by 2020 [54], and this will probably too occur in tablets, laptops, and televisions with subsequently more rapid OLED market share growth. However, the difference of opinion on the bactericidal and phototoxic effect of blue LED irradiation, associated to such parts that need remain to be enhanced for these groundbreaking global improvements on harmful free lighting for the global cause. Thus, studies on peerless LED/OLED hi-tech environs might give way to the future harbingers of green energy in the upcoming scenario.

Acknowledgements

All authors contributed toward data analysis, drafting and revising the chapter and agree to be accountable for all aspects of the work.

The authors apologize for inadvertent omission of any pertinent references.

Conflict of interest

The authors declare that there is no conflict of interests regarding the publication of this chapter.

Author details

Jagannathan Thirumalai

Address all correspondence to: thirumalaijg@gmail.com; thirumalaijg@hotmail.com

Department of Physics, School of Electrical and Electronics Engineering, Srinivasa Ramanujan Centre, SASTRA University, Kumbakonam, Tamil Nadu, India

References

[1] Round HJ. A note on carborundum. Electrical World. 1907;**19**:309

[2] Margolin J. The Road to the Transistor; 1993. http://jmargolin.com/history/trans.htm

[3] Losev OV. Luminous carborundum (silicon carbide) detector and detection with crystals. Russian Journal Telegrafiya I Telefoniya Bez Provodov (Wireless Telegraphy and Telephony). 1927;**44**:485-494

[4] Lossev OV. CII. Luminous carborundum detector and detection effect and oscillations with crystals. The London, Edinburgh, and Dublin Philosophical Magazine and Journal of Science: Series 7. 1928;**6**(39):1024-1044. DOI: 10.1080/14786441108564683

[5] http://en.wikipedia.org/wiki/Light-emitting_diode

[6] http://www.led-evolution.com/Technology/benefits-of-LED.html

[7] http://www.passion-ledlighting.com

[8] https://www.iitk.ac.in/solarlighting/files/brief_history_of_LEDs.pdf

[9] Braunstein R. Radiative transitions in semiconductors. Physical Review. 1955;**99**(6):1892-1893. DOI: 10.1103/PhysRev.99.1892

[10] Braunstein R, Loebner EE. Semiconductor device for generating modulated radiation. RCA Corp, assignee, U. S. Patent 3102201. Issued: Aug. 27th, 1963

[11] Biard JR, Bonin EL, Carr WN, Pittman GE. GaAs infrared source. International Electron Devices Meeting, Washington, D.C. Oct. 1962. Vol. 8, pp. 96

[12] Biard JR, Pittman GE. Semiconductor radiant diode. U.S. Patent 3293513. Issued: Dec. 20th, 1966

[13] Carr WN, Pittman GE. One-watt GaAs p-n junction infrared source. Applied Physics Letters. 1963;**3**(10):173-175. DOI: 10.1063/1.1753837

[14] Nick H, Bevacqua SF. Coherent (visible) light emission from Ga(As1−x Px) junctions. Applied Physics Letters. 1962;**1**(4):82. DOI: 10.1063/1.1753706

[15] Pankove JI, Miller EA, Berkeyheiser JE. Journal of Luminescence. 1973;**6**:54

[16] George Craford M. IEEE Spectrum. February 1995;**32**(2):52-55 ISSN 0018-9235

[17] Stevenson DA, Rhines WC, Maruska HP. U. S. Patent. 1974;**3**(819):974

[18] Stinson JW. U. S. Patent. 1991;**4**(992):704

[19] Tsao JY, Saunders HD, Creighton JR, Coltrin ME, Simmons JA. Solid-state lighting: An energy-economics perspective. Journal of Physics D: Applied Physics. 2010;**43**(35):354001. DOI: 10.1088/0022-3727/43/35/354001

[20] Tsao JY, Coltrin ME, Crawford MH, Simmons JA. Proceedings of the IEEE. 2010;**98**(7): 1162-1179

[21] Cho J, Park JH, Kim JK, Fred Schubert E. White light-emitting diodes: History, progress, and future. Laser & Photonics Reviews. 2017;**1** of **17**:1600147. DOI: 10.1002/lpor.201600147

[22] Elgala H, Mesleh R, Haas H. IEEE Communications Magazine. 2011;**49**:56-62. DOI: 10.1109/MCOM.2011.6011734

[23] Cree Company. http://www.cree.com/News-and-Events/Cree-News/Press-Releases/2014/March/300LPW-LEDbarrier

[24] Osram Company. http://www.osram.com/osram_com/press/press-releases/_trade_press/2014/osram-constructsthe-worlds-most-efficient-led-lamp/index.jsp

[25] Zhang R, Lin H, Yu Y, Chen D, Xu J, Wang Y. A new-generation color converter for high-power white LED: Transparent Ce^{3+}:YAG phosphor-in-glass. Laser Photon. Rev. 2014;**8**(**1**):158-164. DOI: 10.1002/lpor.201300140

[26] Luciom Company. http://w-o-lifi.blogspot.kr/2015/05/some-products-from-luciom-company.html

[27] LED Technology Breakthroughs. https://www.ledinside.com/news/2016/12/led_technology_breakthroughs_in_2016

[28] Acharya KP, Titov A, Hyvonen J, Wang C, Tokarz J, Holloway PH. High efficiency quantum dot light emitting diodes from positive aging. Nanoscale. 2017;**9**:14451-14457. DOI: 10.1039/c7nr05472f

[29] LED world. LED World Mag; 2017. http://ledworldmag.com/magazines

[30] Bernanose A, Comte M, Vouaux P. A new method of light emission by certain organic compounds. Journal de Chimie Physique. 1953;**50**:64. DOI:10.1051/jcp/1953500064

[31] Bernanose A, Vouaux P. Organic electroluminescence type of emission. Journal de Chimie Physique. 1953;**50**:261. DOI: 10.1051/jcp/1953500261

[32] Bernanose A. The mechanism of organic electroluminescence. Journal de Chimie Physique. 1955;**52**:396. DOI: 10.1051/jcp/1955520396

[33] Bernanose A, Vouaux P. Relation between organic electroluminescence and concentration of active product. Journal de Chimie Physique. 1955;**52**:509

[34] Kallmann H, Pope M. Positive hole injection into organic crystals. The Journal of Chemical Physics. 1960;**32**:300. DOI: 10.1063/1.1700925

[35] Kallmann H, Pope M. Bulk conductivity in organic crystals. Nature. 1960;**186**(4718):31-33. DOI: 10.1038/186031a0

[36] Pope M, Kallmann HP, Magnante P. Electroluminescence in organic crystals. The Journal of Chemical Physics. 1963;**38**(8):2042. DOI: 10.1063/1.1733929

[37] Sano M, Pope M, Kallmann H. Electroluminescence and band gap in Anthracene. The Journal of Chemical Physics. 1965;**43**(8):2920. DOI: 10.1063/1.1697243

[38] Helfrich W, Schneider W. Recombination radiation in Anthracene crystals. Physical Review Letters. 1965;**14**(7):229-231. DOI: 10.1103/PhysRevLett.14.229

[39] Gurnee E, Fernandez, R. Organic Electroluminescent Phosphors. U.S. Patent 3,172,862, Issue date: March 9, 1965

[40] Partridge RH. Radiation sources. U.S. Patent 3,995,299. Issue date: November 30, 1976

[41] Partridge R. Electroluminescence from polyvinylcarbazole films: 1. Carbazole cations. Polymer. 1983;**24**(6):733-738. DOI: 10.1016/0032-3861(83)90012-5

[42] Partridge R. Electroluminescence from polyvinylcarbazole films: 2. Polyvinylcarbazole films containing antimony pentachloride. Polymer. 1983;**24**(6):739-747. DOI: 10.1016/0032-3861(83)90013-7

[43] Partridge R. Electroluminescence from polyvinylcarbazole films: 3. Electroluminescent devices. Polymer. 1983;**24**(6):748-754. DOI: 10.1016/0032-3861(83)90014-9

[44] Partridge R. Electroluminescence from polyvinylcarbazole films: 4. Electroluminescence using higher work function cathodes. Polymer. 1983;**24**(6):755-762. DOI: 10.1016/0032-3861(83)90015-0

[45] Tang CW, Vanslyke SA. Organic electroluminescent diodes. Applied Physics Letters. 1987;**51**(12):913. DOI: 10.1063/1.98799

[46] Burroughes JH, Bradley DDC, Brown AR, Marks RN, MacKay K, Friend RH, Burns PL, Holmes AB. Light-emitting diodes based on conjugated polymers. Nature. 1990; **347**(6293):539-541. DOI: 10.1038/347539a0

[47] https://en.wikipedia.org/wiki/Universal_Display_Corporation (1994)

[48] Hebner TR, Wu CC, Marcy D, Lu MH, Sturm JC. Ink-jet printing of doped polymers for organic light emitting devices. Applied Physics Letters. 1998;**72**(5):519. DOI: 10.1063/1.120807

[49] Bardsley JN. International OLED technology roadmap. IEEE Journal of Selected Topics in Quantum Electronics. 2004;**10**:3-4. DOI: 10.1109/JSTQE.2004.824077

[50] Kho M-J, Javed T, Mark R, Maier E, David C. Final Report: OLED Solid State Lighting. Kodak European Research. Cambridge Science Park, Cambridge, UK; March 4, 2008

[51] Bao Z, Diao Y, Giri G, Xu J, Kim DH, Becerril HA, Stoltenberg RM, Lee TH, Xue G, Mannsfeld SCB, Bao Z. Solution coating of large-area organic semiconductor thin films with aligned single-crystalline domains. Nature Materials. 2013;**12**(7):665-671. DOI: 10.1038/nmat3650

[52] National Research Council. The Flexible Electronics Opportunity. The National Academies Press; 2015. pp. 105-106 ISBN 978-0-309-30591-4

[53] OLED Display Forecasts 2016-2026: The Rise of Plastic and Flexible Displays Technology analysis and detailed forecasts by market segment and display type By Dr Guillaume Chansin, Dr Khasha Ghaffarzadeh and Dr Harry Zervos; 2016. https://www.idtechex.com/research/reports/oled-display-forecasts-2016-2026-the-rise-of-plastic-and-flexible-displays-000477.asp

[54] http://www.ledsmagazine.com/articles/2017/03/oled-technology-delivers-three-decades-of-display-innovation.html

[55] Applications of OLED; 2018. http://www.visionox.com/en/oleddetail.html

[56] http://www.gtvinc.com/advancements-led-technologies/

[57] Oh P-S, Na KS, Hwang H, Jeong H-S, Lim S, Sohn M-H, Jeong H-J. Effect of blue light emitting diodes on melanoma cells: Involvement of apoptotic signaling. Journal of Photochemistry and Photobiology. B. 2014;**142**:197. DOI: 10.1016/j.jphotobiol. 2014.12.006

[58] Oh P, Hwang H, Jeong H, Kwon J, Kim H, Kim M, Lim S, Sohn M, Jeong H. Blue light emitting diode induces apoptosis in lymphoid cells by stimulating autophagy. The International Journal of Biochemistry & Cell Biology. 2016;**70**(1):13-22. DOI: 10.1016/j.biocel.2015.11.004

[59] Health & Science. https://www.washingtonpost.com/national/health-science/some-cities-are-taking-another-lookat-led-lighting-after-ama-warning/2016/09/21/98779568-7c3d-11e6-bd86-b7bbd53d2b5d_story.html

[60] Harvard Health Lett. http://www.health.harvard.edu/staying-healthy/blue-light-has-a-dark-side. Updated: December 30, 2017. Published: May, 2012

Chapter 2

DC Network Indoor and Outdoor LED Lighting

Alfonso Gago-Calderón,
Rami D. Orejón-Sánchez and
Manolo J. Hermoso-Orzáez

Additional information is available at the end of the chapter

http://dx.doi.org/10.5772/intechopen.74974

Abstract

LED lighting products have become a significant revolution in this technological sector. These components are, by nature, digital emitters created with semiconductor crystals that are powered with very low voltage and direct current (DC). Under these conditions, they have become one of the most relevant actors in the present tendency that is recovering the DC as the channel to transport and distribute energy and is reinforcing the photovoltaic (PV) panels as a relevant sustainable energy source that allows to improve the efficiencies of all types of lighting installations with the local self-generated energy. An analysis of the working principles of this component and the mechanism implemented for their control as lighting equipment to be powered with both conventional alternate current (AC) and DC is presented. A specific differentiation is done upon indoor and outdoor applications where new standards and regulations, specific technical procedures, and singular experimental project descriptions are detailed. The results expose the advantages and difficulties of implementation of this new DC paradigm, the main conclusion obtained up to this moment, and trends of future evolution.

Keywords: direct current grid, smartgrid, photovoltaic energy, LED lighting, LED drivers

1. Introduction

The manufacturing industry is pushing a technological evolution toward the general adoption of the increasingly extended digital systems. This process has been observed in cameras, televisions, automotive controlling, telephones, and, lately, in lighting products with the introduction of LEDs as effective light sources.

In this last sector, this new nature implies bigger energy efficiencies (which make a major contribution to sustainability as, approximately, 20% of the total energy consumed in the world is used for indoor and outdoor illumination [1]) and robustness and easiness of control (allowing brightness regulation, status supervision, or even the generation of a proprietary data transmission network [2]). However, minimizing energy usage within this new trend goes far beyond the light source and the saving that can be achieved through occupancy sensing and dimming. It also brings a new way or energy use: the opportunity for better efficiency also extends to their power grid.

As LEDs work naturally on direct current (DC), drivers are a basic requirement for any lighting equipment powered with the common alternate current (AC) power network of public lighting and buildings. The movement toward a new DC grid allows to enhance the characteristics of LED luminaires: better global efficiencies (minimizing power conversions) and reliability (AC/DC systems have a natural lifetime expectation significantly lower than the LEDs, and they are the most common point of failure in AC luminaires), simplifies household equipment (eliminating many small power supplies), and may obtain better security conditions as very low voltage distribution (VLDC <75 V_{DC} European Council Directive 73/23/EEC) may be possible in many cases. Moreover, advance lighting controls are being developed that are fully integrated inside these DC systems at no higher cost [3].

Until recently, DC LED lights were designed exclusively to be used with battery-based off-grid power sources. However, DC grids have been investigated more intensely in the last decade since many renewable energy sources as well as electronic and control technologies are being developed.

Modern energy consumption grids are thought to be powered in DC either by renewable energy—mainly photovoltaic (PV) panels—centralized AC/DC conversion units, energy storage systems—bank of batteries, electric cars (V2G), and so on—or a combination of all of them.

In this chapter, we analyze the evolution and present developments of new DC energy consumption grids and how LED control technologies are evolving to adapt themselves to these new powering models. Lately, we expose, analyze, and discuss several significant initiatives and projects developed for both indoor and outdoor related to DC LED lighting.

1.1. DC grids

The world runs on AC since electrical power transmission was introduced in the last quarter of the nineteenth century, and AC and DC competed to become the standard power distribution system in the process known as the "War of the Currents."

The light bulb, incorporating a high-resistance carbon filament, was industrially developed in the last quarter of the eighteenth century. Thomas Alva Edison was developing an industry to manufacture these bulbs but also to provide a complete infrastructure of power plants, transportation grids, and end-use devices such as fuses and switches. Edison opted for DC to share the same grid that was used to power electric engines, which ran this way at the time.

However, George Westinghouse (Westinghouse Electric Corporation) focused on the limited range of the low-voltage DC. At a time when power electronics were too limited, he found in

1883 the first technically usable transformer which made possible to step up and down easily the AC voltage to carry power over long distances from a power plant.

As DC electricity was not converted efficiently into high voltages until the 1960s, a DC power network implied the installation of small/medium power plants in every block of a city (which reduces the efficiency of the system), and, besides, Nikola Tesla presented in 1888 the first AC engine, eliminating the other greatest argument for building up DC grids.

More than 120 years later, AC still constitutes the basis of our power infrastructure. However, two converging factors have renewed the interest in DC power consumption grids in this last decade:

- There are better alternatives for decentralized power generation, PV panels being its most significant technology. They produce DC power and so do chemical batteries, which are the most practical storage technology for PV systems [4].
- Most of our electrical appliances operate internally on DC power. AC electricity is transformed into DC with specific nonefficient internal converters.

Within the next 15 years, more than half of the total household loads are expected to run directly on DC, and LED lights are one of the main actors of this trend [5].

1.2. LED technology

LEDs are an "old" technology that, in recent years, is undergoing numerous advances and transformations toward new applications that are leading the latest revolution in the lighting industry [6].

The first fully electronic-type light source consists of a semiconductor diode base on the junction of two segments of a crystal. When a differential voltage is applied on both extremes of the diode—direct way polarization—it generates photons with an electromagnetic radiation of a specific frequency related by the Planck constant. This allows efficient monochromatic light generation if the frequency emitted is within the range of the human eye vision (~400–700 nm). The research on dopants and crystal structures has led to more efficient and higher-power LEDs. However, white-light sources have been possible through a long path of development generated aside this type of semiconductor.

At the end of the 1990s, the blue LED became a reality developed by Isamu Akasaki and Hiroshi Amano (Nagoya University) and Shuji Nakamura (Nichia Corp). They were awarded with the Nobel Prize in physics in 2014 for this work. They were looking for a precise tool to improve optic data storage systems but they also achieved the basic principle of the latest breakthrough in LED technology: a very efficient and stable white-light emission using phosphorus, not as a dopant, but as a coating for the silicon crystal of blue LEDs and, consequently, to be able to use these devices as sources in general lighting applications as substitutes of fluorescent bulbs and discharge lamps (see **Figure 1**).

Mass-produced LEDs are reaching rapidly comparable results to prototypes being developed in research laboratories, and the electronic drivers that operate LED lamps are also constantly improving on efficiency and robustness. Present projections are contingent on technology developments that achieve the goal of 200 lm/W luminaire efficacy by 2025 [7].

Figure 1. High power 3000 K white XTE LED by CREE. Blue emitter with phosphorus cover.

2. Working behavior of a high-power LED

The light output of a high-power (HP) LED depends basically on two factors: the electric inputs—forward voltage ("Vf") and current ("If") values—and its crystal junction temperature ("Tj"). This last value inevitably increases as electrons and holes combine.

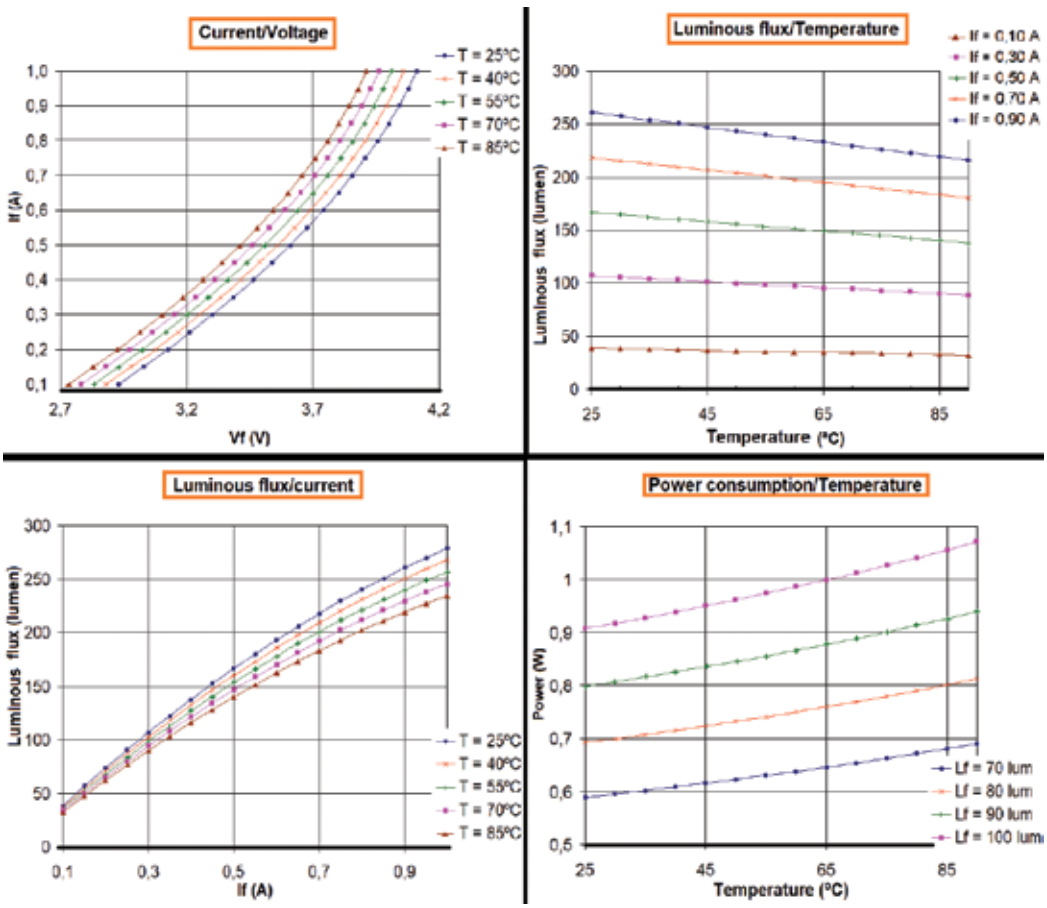

Figure 2. Working parameters of a high-power XT-E white LED by CREE.

Given a constant "Tj," the illuminance of HP LED varies linearly with its "If" at small values and tends to saturate at higher values. Otherwise, if a constant current (CC) drive is forced, the light emitted moves down as "Tj" increases. This is caused by the variation relationship between "Vf" and "Tj," which is approximately proportional [8]. For the XT-E LED by CREE, the typical relationship is −2.5 mV/°C. This effect makes itself visible in the displacement of its working curves. These "Vf"-"If"-"Tj"-"Luminous flux" relationship curves of the mentioned LED are shown in **Figure 2**.

Consequently, if a CC is applied on the LED, the increase in the junction temperature causes only a slight decrease in its "Vf" drop and, at the same time, in the illumination obtained, creating a natural mechanism of negative feedback that maintains the stability of the system.

However, if we use a constant "Vf" with LEDs, its power consumption increases along with its "Tj," produced by a significant increment in the forward current, creating a positive feedback that will finally conduct to a catastrophic burn failure. This phenomenon is generally known as thermal runaway and is the reason why the standard method of driving LEDs is the use for DC current sources.

3. DC LED drivers

Because of this electrical behavior of HP LEDs, in case of DC supply, we need to have a current control device in series with the LEDs to guarantee stable working conditions. Creating a regulated current source can go from a very simple concept, using a passive polarization resistor, to a more complex solution using active current regulator circuits. Here, we summarize the general trends found in the study and the market to achieve this objective, accounting nonsteady (batteries) and steady (switching converter outputs) DC sources.

3.1. Passive control methods: polarization resistors

The simplest driver is a current-limiting resistor placed along with the powered LEDs. The reduction in the polarization voltage of LEDs due to temperature increment is compensated with the larger drop in the resistor (negative feedback effect). If the supply voltage is very well defined and stable, close to "Vf," this is the simplest, most reliable, and long-lasting LED driver. However, it is not significantly efficient as all the required current is driven through these impedances generating a significant amount of heat, and a substantial resistance value is required to keep current within an adequate range. If the voltage source is not stable, the brightness of the LED would vary remarkably because a small voltage variation would already lead to large changes of the output power. This system is only able to correct the variations of the behavior of the LED due to the changes of its "Tj."

3.2. Active control methods

3.2.1. Linear power drivers

Active current control uses bipolar or MOSFET transistors as regulation devices or feedback elements to regulate the current driven through the LEDs. In contrast to the polarization resistors,

this solution is the next step in a complexity qualification as it uses again a resistor but now as a current sensor load that is able to modify the gate signal of the control transistor. The resistor can be of a much lower value as it will not work as a limitation but as a sensor.

The obtained efficiency is also good in case there is a constant forward DC voltage source on the range of the nominal polarization voltage of the LED because the control neglects the entire voltage drop in the semiconductor. If the voltage variation is within ±10% of the nominal LED polarization, voltage efficiency can still be above 84% on the worst case [9].

This solution can be improved using linear voltage regulators (LVRs) set as CC control elements (e.g., LM317 or NTE956) instead of transistors [10]. They use an internal voltage reference that offers a more accurate solution, but they have a minimum dropout voltage—as high as a few volts—which introduces significant energy loses (see **Figure 3**).

In general, these types of solutions, as well as the first option, have as main advantages that both include no EMIF generation as there is no current commutations (thus, no filtering is required). However, they allow a limited supply voltage range; the LED load voltage has to be lower than the supply voltage, and there are significant energy losses due to heat dissipation.

3.2.2. CC switch-mode converter drivers

This is the most implemented type of solution for commercial DC LED lighting drivers. Although there are many different variations, three standardized models are widely recognized to configure CC generators for HP LEDs. Each of them is prepared for a different relationship between the supply and the LED voltage that has to be maintained independently of the variations that can suffer the supply or the load due to "Tj" changes:

- Buck converters: very efficient step-down topology with many implementations: synchronous switching, average current, peak current, or hysteric control.
- Boost converters: step-up topology very common in battery-powered equipment. The two basic implementations are inductive boosts or charge pumps.
- Boost-buck converters (single-winding fly-back converters): they drive power loads with both step-up and step-down requirements. This model is characteristic from stand-alone systems powered with batteries where input voltage can suffer large variations. They are more flexible but less efficient than the two previous options.

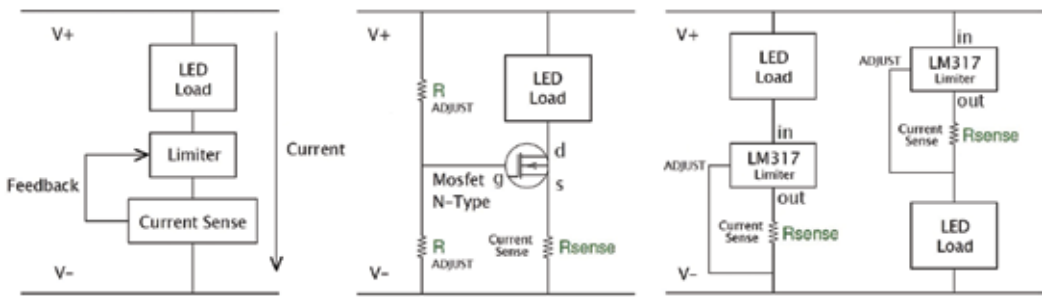

Figure 3. Linear power LED driver configurations: (A) MOSFET and (B) linear voltage regulator.

http://dx.doi.org/10.5772/intechopen.74974

A large number of ICs from many manufacturers are available in the market to implement these types of drivers. Efficiencies over 95% can be achieved with adequate designs as observed in **Figure 4**. However, these CC drivers present the following main drawbacks:

a. They do not control the temperature of LEDs. This defines their lifetime expectation.

b. They include components that are not as reliable as LEDs (inductors, electrolytic capacitors, etc.) which become the weakest points of these types of lamps.

c. They generate an electric conversion that provides a current-regulated output. In all cases, this reduces efficiency, performance, and, as mentioned, reliability.

3.2.3. LED matrix temperature-feedback drivers

Another driver option is to use MOSFET transistors as commutators to create a pulse-width modulation (PWM) signal that controls the energy introduced into the LED matrix. Under this concept, DC lamps can be driven with an electronic circuit that applies regulated current PWM cycles according to the LED matrix temperature or the voltage level of the source.

The control principle assures that the temperature of the LED is kept below high values to guarantee the expected lifetime in all working conditions using only a reliable hardware architecture of very few components: one low-power microcontroller, one temperature sensor, and a power MOSFET (N-type) that acts as the control actuator in the LED matrix, plugging or unplugging this with a PWM commutation (see **Figure 5**).

This control architecture can execute, if required, a smooth reduction on the active period of the LED driving signal (from a normal status of 100% active) to reduce the power consumption. This

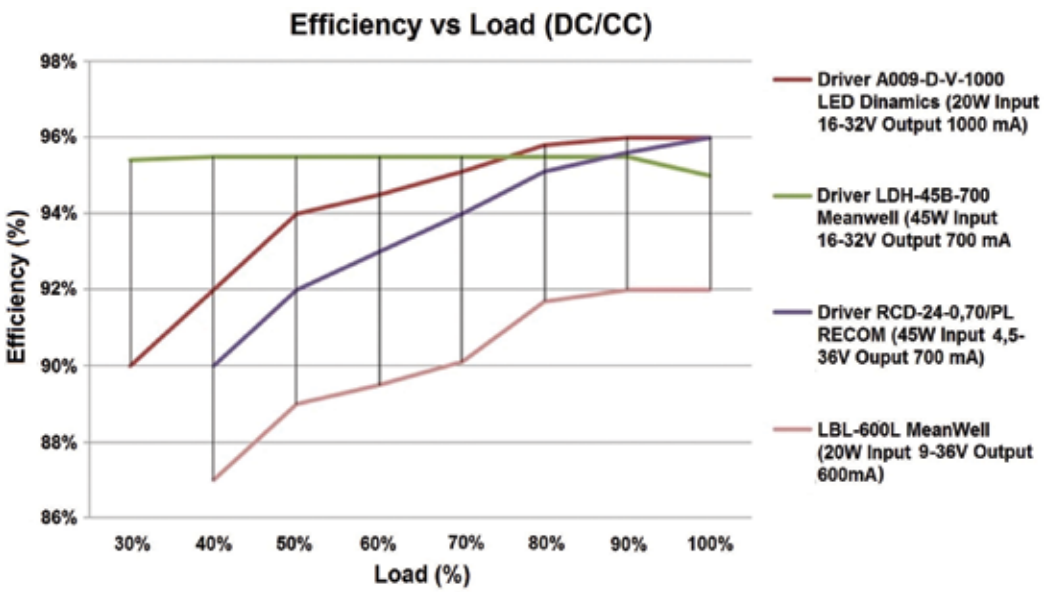

Figure 4. Efficiency versus load curve of commercial DC/CC switch-mode converter drivers.

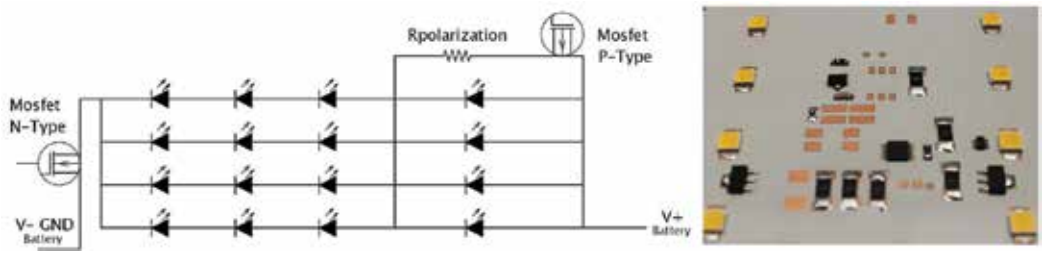

Figure 5. LED lamp with temperature and input voltage-feedback driver implementation.

implies reducing the light emitted but also the heat generated inside the LEDs. This situation can be reached by either abnormal working operation conditions or unusually high working temperatures. This control is a negative feedback compensation mechanism of current increments due to high "Tj" while powering with constant voltage DC values. The commutation frequency must be high enough to avoid significant flickering and low enough to produce no excessive EMIF. Values between 0.5 and 1.0 KHz are suitable.

A common DC driver adapts the grid values to the specific impedance of an LED matrix, but it is possible to flip this concept and evolve this driver to be able to modify the impedance of its LED lamp to adapt it to the variable voltage of a nonsteady power source.

The LED matrix may include also a P-channel MOSFET in series with a small impedance resistor (R) placed in parallel with the first LEDs connected on each branch of our matrix. This scheme is designed to adapt the lamp to the wide range of voltage supply of batteries. For example, the circuit in **Figure 5** is prepared for the voltage supplied by a 12 V_{DC} lead acid battery that can vary between 11 and 15 V_{DC}. The exponential V-I relationship of a white LED makes its brightness decrease dramatically when the voltage gets below 12.3 V_{DC} (3.1 V_{DC} per diode), generating unsatisfactory luminance. If the control detects an input voltage below this threshold, it activates the second PWM signal that takes out the first LED of each branch of the lamp for discrete moments. In this way, the impedance of the matrix is reduced keeping the rest of the LEDs with adequate "Vf" polarization and brightness.

This sample LED luminaire design varies its consumption from 13 (at 12.6V_{DC}) to 7.5 W (at 11 V_{DC}). This behavior can be considered good for PV stand-alone systems as the lamp consumption is reduced at low voltage (low energy in the battery) which contributes to a safe management of the system while maintaining a good level of illumination. The energy efficiency of the proposed control scheme is, on average, 15% higher than the one obtained with a CC switch converter control powering the same LED lamp [11].

3.3. Control method selection

Designers may consider that if the voltage of the LED lamp is just below that of the DC source, both linear current regulators and temperature feedback controllers are simple, high-efficient, cost-effective, and very reliable solutions. If the design is well adjusted to the input voltage, efficiencies can be extremely high; otherwise, significant loses appear. In those cases,

switching current regulators are needed: boost or boost-buck solutions if the voltage of the LED lamp is over the DC source voltage and buck implementations if the voltage of the matrix of emitters is significantly below (80% or less) the DC source voltage.

3.4. Advantages of DC versus AC drivers

DC LED lighting allows eliminating components that are necessary in AC/DC conversion. To compare the component effort required in solutions with AC and DC current supplies, **Figure 6** shows a block diagram of a typical lamp driver AC operated. Once it reaches the last stage of the chain (DC/DC box), all the abovementioned for LED matrix powering are applicable [9].

These blocks are as follows:

- Filter: It suppresses high-frequency contents of the input source. Most of the international regulations (e.g., IEC 61000-3 or IEEE STD 519-2014) order that the maximum total harmonic distortion (THD) of the voltage and current signals generated must be under certain limits. It is also a necessary part of an active power factor corrector (PFC). It may still be required in DC drivers if switched conversions are used to avoid the generation of fluctuations in the energy source.
- Rectifier: It is typically implemented with a bridge of diodes. It might also be useful in DC operation to allow an arbitrary connection of the positive and negative lines. However, this problem may be solved with a mechanical system that avoids a wrong connection.
- PFC circuit: It increases the ratio between the useful (W) and the total power (VA) consumed by the driver. Many drivers use switch converters (typically a boost-type circuit) but this requires an input filter to limit high-frequency THD generation. The next review of the IEC 61000-3-2 intends to raise the requirement of integrating a PCF circuit in any lamp driver from 25 to 5 W.

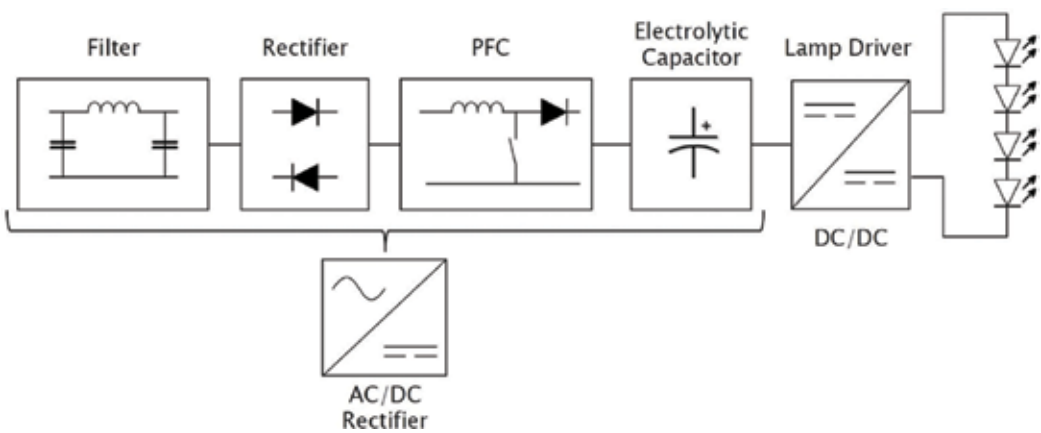

Figure 6. Typical topology of an AC lamp driver.

- Electrolytic capacitor: It levels the pulsating rectified voltage signal. In DC, they can suppress voltage dips of the energy source but most lighting applications may consider acceptable to pass them and allow short flickers on the LEDs.

The LED driver can be housed in an external case or in the device itself (which is much cheaper and significantly simplifies the luminaire configuration). Eliminating the AC/DC components

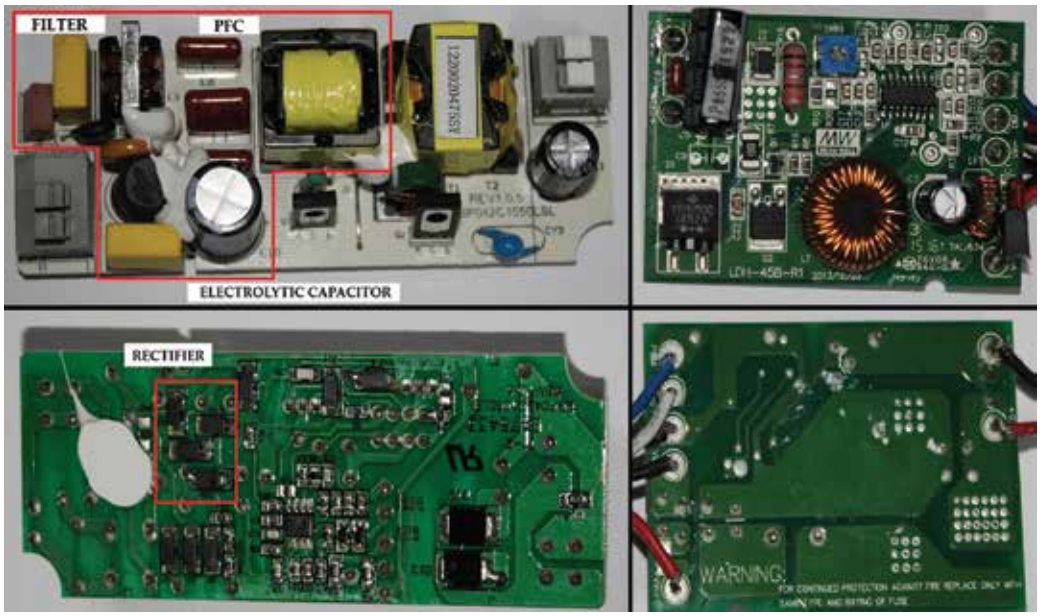

Figure 7. Typical topology of a common AC lamp driver compared to a DC counterpart.

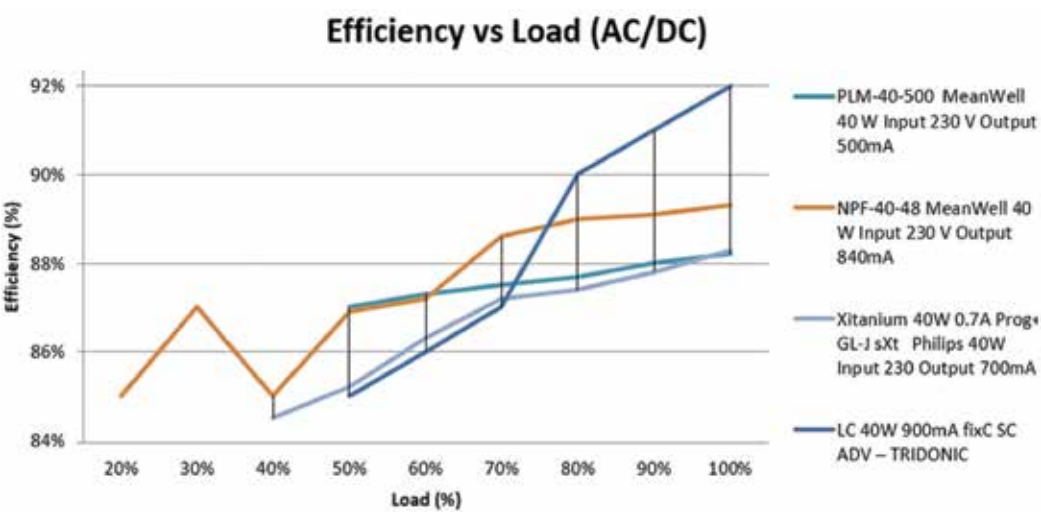

Figure 8. Efficiency versus load curve of commercial AC/CC switch-mode converter drivers.

means less space requirements, cost reduction, and simpler installation. Between 40 and 50% of the printed circuit board (PCB) in an AC/DC, LED driver is occupied by the AC components.

Figure 7 shows a photograph of two LED drivers. On the left, we present a 42-W AC unit by Eagle Rise with PF corrected over 0.95, an efficiency between 0.89 and 0.92 (60–100% loads) and no dimming possibilities. All parts that are necessary for AC conversion are highlighted. On the right, we have a $24V_{DC}$ (18–$32V_{DC}$ range) input LDH-45B-700 DC dimmable LED driver by Mean Well with efficiencies between 0.95 and 0.96 (30–100% loads). It has no input diode bridge so that polarity has to be checked before powering the equipment.

Figure 8 presents, similar to **Figure 4**, the efficiency of four commercial AC/CC drivers versus their load. These curves present larger slopes and an average decrement of efficiency of 5–6% compared to their DC/CC counterparts.

4. Indoor and outdoor DC-lighting experience

Nowadays, the US is the country that is adapting more DC-lighting installation in a context where, according to the 2016 calculation of its Energy Information Administration (EIA), this country used 15% of all its consumed energy for lighting purposes [12]. This is a significant reduction from the 22% calculated in 2009 due to the massive installation of LED equipment and efficiency initiatives as the AC to DC residential and commercial indoor grid translations. On account of this, these two sectors figure as very significant with 7% of the total electricity consumed (approx. 279 billion kWh) [13].

If all general purpose lighting equipment in the world were converted to LED light sources (agreeing an average 40% saving at each point), their energy consumption could be decreased by around 1000 TW h/year, reducing 200 million tons of greenhouse gas emission [7]. Any additional development that allows higher efficiencies, as the elimination of the AC losses, has also significant relevance due to the large amount of energy involved.

4.1. Indoor direct current indoor led lighting: trends and applications

On average, 80% of the energy used in modern buildings power DC loads. Low-power devices (≤50 W), like most indoor LED lamps, are responsible for 35–50% of this use, and all of them work with small power-wasting converters. LEDs and DC power distribution in buildings can notably enhance the efficiency of this significant amount of energy.

As it is considerably difficult to eliminate all the AC loads and the general distribution grid, the basic consensus is to replace all the many AC/DC converters placed on each luminaire with a common centralized frontend to provide high-efficiency conversion and protection and then conduct the electric power in DC to the LED fixtures.

4.1.1. Development of systems

LED matrixes may work from just 3.3 V_{DC}. Over this voltage, many possible solutions can be implemented using different serial/parallel LED configurations. It is important to select the

most appropriate solution to achieve the highest energy efficiency and the safest operation conditions. The main problem is that these two concepts are here antagonists. A significant number of DC distribution systems have emerged over the years, and, at present, it seems yet far to achieve a unique standard. Special focus has been put over several specific supply voltage levels along with the type of cable and connections to be used. The most developed proposals are presented in **Table 1**. The most significant aspects that are important to consider choosing one of these systems for a specific installation are described in the subsequent text.

4.1.1.1. Solar energy

These renewable sources are not yet the perfect solutions but match significantly well with LED lighting. In fact, DC LED lighting was first developed to be powered off-grid exclusively with solar energy as LED-lighting technology is efficient enough as to reduce its required

Range	Characteristics	V_{DC}	Details	Standards
VLDC	ADVANTAGES	12	Most used in cars, trucks, motor homes, caravans, and boats	UL 1838 & UTSFfSHS (Universal Technical Standard for Solar Home Systems) [14]
<75 V_{DC} Council Directive 73/23/EEC	• Safe from electric shock and fire hazard			
	• Many commercially available devices	24	Intermediate solution	UL 2108
	• No grounding needed		Low voltage conversions inside the DC lamps	Emerge Alliance (US) www.emergealliance.org
	• No protection against direct contact is required			
<60 V_{DC}	• Simple adaptation of PV generators and batteries	48	Allows working with higher power devices	IEC 60364–7-715:2011 EDISON project (EU) http://www.project-edison.eu/ [13]
NFPA 70 National Electrical Code	DISADVANTAGES	60	Ethernet cabling combines power and control.	PoE (Power over Ethernet) Lighting systems [15, 16]
	• - Relatively high cable losses (depends on the length)		Maximum allowed: 100 W at 60 V	
DC <1500 V_{DC}	ADVANTAGES	380	Similar DC voltage than 230 V_{AC} (needs equal insulation properties). Generates only about one-third of the losses in converters and cables [17]	IEC SG 4 Group "LVDC distribution systems up to 1500V_{DC}"
Low Voltage Directive (LVD) 2006/95/EC	• - Minimum cable losses			TBINK-LVDC working group at DKE/VDE
	DISADVANTAGES			
	• - Complex security systems are required			
	• - Arcing appears when a load is unplugged			
	Internal arcing chambers. Voltage broken protection			
	Standard IEC 60947–2 -3			

Table 1. Common voltage levels for DC indoor lighting: characteristics and standards.

consumption within PV power generation capability, especially when combined with control systems that are able to regulate energy consumption to avoid deep discharges.

According to the nature of LEDs, PV panels, and batteries, it is easy to use LVDC with this type of integrations as they allow a more flexible PV panel configuration and reduce voltage conversions.

4.1.1.2. Cable losses

Cable losses are determined by their length, diameter, and the conducting material. A copper wire with a 10-mm^2 cross section, distributing 100 W at 12 V_{DC} over a 10-m distance, generates an energy loss of 3%. If this length increases to 50 m, energy loss becomes 16% and for 100 m raises to 32% (which erases all the efficiency advantages of DC lighting). Cable losses also limit the use of high power luminaires. In a $12V_{DC}$ 10-mm^2 copper wire, 1-kW LED projector has 16% energy losses in a 1-m cable and 47% in 3 m. Working with higher voltages, even still within VLDC, reduces these losses by a square factor of the voltage variation. Moving from 12 to $48V_{DC}$ improves cable transmission efficiency by a factor of 16.

The spatial layout is very important to limit this distribution problem. Large buildings will require several energy AC/DC converters placed in different powering sectors. Another way to reduce cable losses is to set up several independent power supply units (PV panels and batteries) in these sectors. Although this strategy implies the use of extra solar charge controllers, this might be the most efficient way to illuminate large buildings.

4.1.1.3. Protections

Protection systems are among the main challenges in the design and operation of DC lighting. DC power distribution, as well as AC, becomes more dangerous as its voltage level increases but, in all cases, fast-speed fault protection, including coordination and interruption, is the essential requirement to be protected against failures as short circuits.

The primary protection in DC lighting grids is the circuit disconnection by overcurrent detection devices: circuit breaker or fuses. They have to be specifically designed as in DC there is no zero crossing in the waveform and they have to break the full fault current. However, they are becoming more common as more DC installations are generated. On the other hand, as total power is reduced and the most extended standards work in VLDC, grid-lighting protection is usually incorporated inside the driver modules with solid-state circuit breakers, and there is no need of adding it externally.

4.1.2. Research installation experiences

Several significant experimental research installations involving DC lighting with published results are presented in **Table 2** [18].

4.2. DC outdoor led lighting: trends and applications

Worldwide, outdoor public lighting means, on average, a reduced amount of the total energy usage (3% of the total energy consumed) compared with that used for indoor installations

Project	V_{DC}	Details	Results and conclusions
Philips Research Eindhoven (NL) [19]	380	2 kWpk photovoltaic (PV) 54 LED downlights (37 W) 3 power grids of 100 m length (3 × 2.5 mm^2)	DC energy demand 2.24% lower than the AC equivalence
Fort Bragg, North Carolina (US) [20]	24	Bosch DC microgrid: 15 kW PV array. 44 DC lights. Direct power from 100 kW lithium-ion battery system	VEEI: 1.80 W_{AC}/m^2/100Lux of AC fluorescents Vs 0.87 W_{DC}/m_2/100Lux of the 380 VDC LEDs
Fraunhofer Institute in Erlangen (GR) [21]	380 & 24	DC office building with lighting and a 24 V DC grid for electronic loads. Batteries back-up storage	The DC system demonstrated electricity savings ranging from 2.7 to 5.5% over an equivalent AC system
Xiamen University, Xiamen (PRC) [22]	380 & 24	150 kWp solar panels. 20 kW LED lighting:14 W tube lights as T5 fluorescent tubes retrofits	DC microgrid with bidirectional inverter and battery storage. Static payback period 5.5 years ($0.887/W)

Table 2. DC indoor-lighting experimental research installations.

(17%) [1]. However, this is still a major market where efficiency improvements can make significant advances in sustainability.

Planning a similar approach than those presented in indoor lighting, one of the first studies generated to compare DC versus AC grids in outdoor LED lighting was realized in 2013. The results of a 220 V_{DC} centralized street-lighting system over conventional 230 V_{AC} power system showed that the efficiency can be improved by 13 (full loads) and 17% (dimmed loads) [23].

However, and independently of this trend that is still under a very early stage of development, the first and most consolidated architecture used to develop DC LED streetlight is the autonomous solar-powered equipment. Modern PV DC luminaires have become the most extended element by virtue of its simplicity, function, and robustness of its components: battery, LED luminaire, and PV panels. This technical evolution and the growth of emerging countries with underdeveloped electrification infrastructures have boosted the market of lighting installations powered only by locally produced energy from the sun [24].

Park et al. [25] remark that the development and installation costs of a micro-distributed ESS-based smart LED streetlight system have been reduced by 33% in just a few years. Moreover, Loomba and Asgotraa [26] claim that DC solar microgrids are 25–30% more efficient than their AC counterparts. The global energy efficiency benefits may vary a lot depending on the location. According to information from the World Bank, the average electric transmission losses are only 4% in Germany and the Netherlands but raise slightly, 6%, in the USA and China and much more, between 15 and 20%, in Turkey and India.

Solar low-power equipment is widespread and participates already in many in-use installations. As an example, we have participated in a public-lighting renewal project developed with 1365 autonomous 50 W LED lighting poles in the city of Cuimba (Angola), as illustrated in **Figure 9**. The equipment used is designed to store enough energy to work three nights with no solar energy input. Development installation costs were reduced in more than 35% compared to renew and bury the AC grid existing already.

Figure 9. Solar autonomous public streetlight installation in Cuimba, Angola, 2017.

However, there are still uncertainties about the technical capability of this type of equipment in order to match their performance to their AC grid equivalents in lighting installations with large regulatory requirements: high-density traffic roads. We present a technical evaluation of the capability of present equipment to achieve these requirements in different global locations based on energy generation capability of solar panels, efficiency of DC LED luminaires, and capacity and long-term reliability of batteries.

4.2.1. Dimensioning of an autonomous led-lighting installation

The DIALux software has been used to size the requirements of the luminaires to fulfill the requirements of the ME2 and ME3 roads with geometric aspects as presented in **Table 3**. We simulate these specifications with different high-class DC LED street luminaires by three manufacturers (Philips, Solitec, and Schreder Socelec), and the results are compared with the normative classification assigned. The power and luminance requirements for each manufacturer

Road parameters	**Road Type A**	**Road Type B**
Road classification	ME3a	ME2
Number of lanes	2	4
Road width	7 m	14 m
Interdistance	30 m	35 m
Height of light point	9 m	12 m
Placement setup	Unilateral	Bilateral face to face
Luminaires manufacturer/model	**Luminous flux/power**	**Luminous flux/power**
Solitec/Navia G	8805 lm/80 W	12,101 lm/110 W
Philips/UniStreet	7654 lm/76 W	11,050 lm/110 W
Schreder/Ampera	9905 lm/87 W	11,972 lm/105 W

Table 3. Geometric data and luminaires selection for the ME2 and ME3 roads under study.

to achieve the objectives established are also presented in **Table 3**. All three results are very similar, and for the rest of the study, we use the average power in each road case. Dimming during the night is included as energy efficiency regulations advice for this possibility. This leads to a total energy consumption of 75% of the nominal value calculated previously. Moreover, the battery storage system has to accumulate at least double of the energy to bright as programmed for one night.

There are two power distribution possibilities: autonomous poles with PV panels and storage systems integrated with each luminaire (simplest installation) or an independent renewable generation system that powers a smart micro-grid with several luminaries (more complex and expensive due to wiring canalization). The first option is limited by the amount of PV surface that is mechanically adaptable in a single pole. The availability of each solution depends on the amount of energy that is possible to generate depending on the geographical latitude. This value conditions the functional elements of the facilities, the simplicity and cost of the installation, the protection requirements, and maintenance and operation cost. Several representative locations have been chosen between or close to the Tropics of Cancer and Capricorn as these are the regions that receive the greatest amount of solar radiation. The PV energy generation capability on the main cities of this portion of the world is shown in **Figure 10**. For calculation purposes, the extreme representative possibilities are found in the following:

- Rabat, Morocco (2770 Wh/m^2 per day). Latitude 34°00′47″N. Its radiations present considerable differences along the year, and it has long nights in winter.
- Brasilia, Brazil (4523 Wh/m^2 per day). Latitude 15°46′46″S. On the other hand, it receives very constant solar radiations, and the night duration is similar all year long.

The equations used to define the power generation capability by PV panels in these two locations are presented in **Table 4**. **Table 5** shows the components required to light both classes of roads under study on the worst scenario (design day in winter in the city of Rabat), and **Figure 11** explains that while in Brasilia, it is possible to install fully integrated autonomous

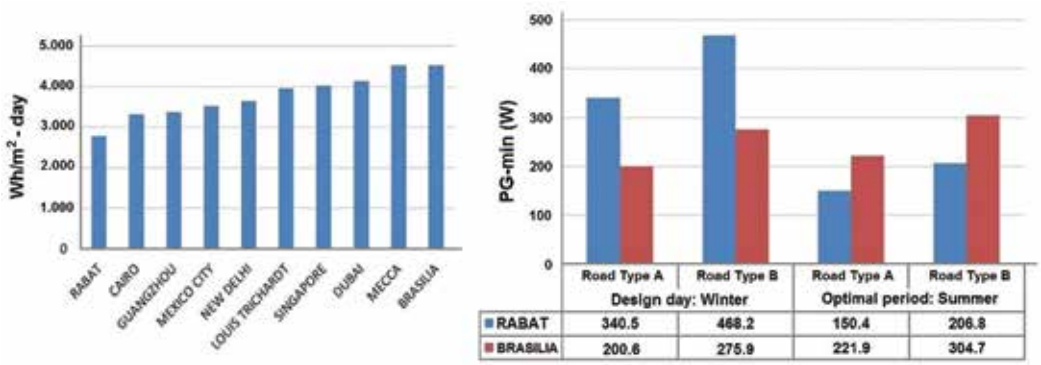

Figure 10. Solar energy input and design requirements of the streetlighting equipment for capital cities close to the tropics.

Minimum power required by the photovoltaic generator	
$P_{G-min} = \frac{W_d \cdot G_{CEM}}{G_{(\alpha,\beta)} \cdot K_T}$	• Wd: Energy consumption [Wh/day] • G_CEM: Standard radiation, 1000 W/m² • $G(\alpha,\beta)$: Incident radiation in the panel [Wh/m²-day] • K_T: Battery and regulator efficiency [%]
Energy accumulation system	
$C_N = \frac{Q_d \cdot A}{PD_{MAX} \cdot \eta_{Con}}$	• Q_d: Nominal daily capacity [Ah/day] • A: Days of autonomy • PD_{MAX}: Maximum discharge depth of the battery • η_con: Battery and regulator performance • U_n: Rated voltage of the photovoltaic generator [V]
Regulation system	
$U_{OC(Tmin)} = U_{OC} + \beta \cdot (T_{min} - 25)$ $I_R = 1,25 \cdot I_{G,sc}$	• $U_{OC\ (TMIN)}$: Rated voltage of the photovoltaic generator [V] • T_{min}: Historical minimum temperature (°C) • U_{OC}: Open circuit voltage [V] • $I_{G,SC}$: Short-circuit current of the generator [A]

Table 4. Equations for the dimensioning of LED luminaires powered by photovoltaic panels.

PV luminaire poles to fulfill ME2 and ME3 requirements in Rabat, this is not possible with ME2 roads as, at least, 2.52 m² of 30 kg PV panels are required, which makes it impossible to integrate them on top of a single lighting pole due to mechanical limitations.

Type of road		**A (ME3)**	**B (ME2)**
Photovoltaic generator	PG-min design	340.5 W	468.2 W
	Equipment	SunPower SPR-X21–345	2 x HIT-235
	Surface	1.60 m²	2.52 m²
	Weight	18.6 kg	30.0 kg
Energy accumulation and regulation system	Cn	$C_{10,14}$ = 95.88 Ah	$C_{10,13}$ = 263.60 Ah
	Equipment	Move MPA 110–12	Move MPA 245-6XL
	Weight	33.3 kg	39.0 kg
	Number	4	4
	Voltage	12 V	6 V
Energy regulatory system	Equipment	Steca Tarom 4545–48	Steca Solarix 2020-x2
	Weight	0.8 kg	0.5 kg
	Uoc	≤100 V	≤60 V
	I	45 A	20 A

Table 5. Component requirements for a solar LED luminaire at worst case: city of Rabat.

Rabat	Cn [Ah]	t_A [Ah]	$U_{OC(Tmin)}$ [V]	I_R [A]
ROAD TYPE A	95,88	10,14	72,39	8,00
ROAD TYPE B	263,60	10,13	51,80	14,60

Brasilia	Cn [Ah]	t_A [Ah]	$U_{OC(Tmin)}$ [V]	I_R [A]
ROAD TYPE A	148,40	15,09	51,80	7,30
ROAD TYPE B	145,60	19,00	73,46	7,50

Figure 11. Basic configurations and available integrations for ME3 (Type A) and ME2 (Type B) road regulation accomplishment in the cities of Rabat and Brasilia.

Nowadays and according to these results, this technology has still a further step to evolve before autonomous pole luminaries can be used on high-density traffic roads worldwide with autonomy assurance. However, many demonstration projects are already being constructed. For example, autonomous PV luminaires have been installed in the A^{-62} motorway (ME3 road), in Salamanca, Spain. In this case, promoters also appraise the quick installation process (only 3 days) that avoids large dangerous installation process along traffic conditions.

5. Conclusions

Many Scientifics and technicians consider that the conversion of the lighting sector toward a full DC environment is its natural evolution trend as LED technology has become the basic engine of almost any new equipment developed for both indoor and outdoor applications.

Better energy efficiencies and larger lifetime expectations are the basic economic forces that are conducting this process that, nevertheless, is still facing considerable challenges in this primitive stage of development.

The unavailability of DC infrastructures and the lack of training/educations are the main drawbacks that are being overcome as universities and private research centers have considered this a priority research line. However, some other concerns are still far to be solved such as the consolidations of worldwide regulations and standards that ensure acceptable energy savings and total human safety. The first parameter varies significantly in each experimental installations ranging from 3 to 30% [18]. This will also lead to establish common safety

procedures and voltage levels for LED-lighting DC grids that will allow mass production of devices that may work anywhere as well as their AC equivalents.

Considering the relationship between LEDs and PV energy generation, the direct interconnection possibility and the advance in efficiency of the new light emitters have renewed the interest in autonomous applications, both stand-alone and with a backup energy grid. Thus, the number of solar-powered LED equipment installed is increasing exponentially. However, a further step in the evolution of these two technologies is still expected to improve the integration capability and the autonomy in high-latitude locations.

Acknowledgements

We would like to acknowledge Alfonso C. Gago-Bohórquez for the deep critical reading, Tiara L. Orejón-Sánchez for her useful recommendations, and the Solitec Foundation (Spain) for its support in contributing with technical resources.

Author details

Alfonso Gago-Calderón[1]*, Rami D. Orejón-Sánchez[1] and Manolo J. Hermoso-Orzáez[2]

*Address all correspondence to: agago@uma.es

1 Department of Graphic Expression, Design and Projects, Universidad de Málaga, Spain

2 Department of Graphic Expression, Design and Projects, Universidad de Jaen, Spain

References

[1] Montoya F-G, Peña-García A, Juaidi A, Manzano-Agugliaro F. Indoor lighting techniques: An overview of evolution and new trends for energy saving. Energy and Buildings. 2017;**140**:50-60. DOI: 10.1016/j.enbuild.2017.01.028

[2] Held G. Introduction to Light Emitting Diode Technology and Applications. Boca Raton, FL (USA): CRC Press; 2016. 161p. ISBN: 9781420076622

[3] Jhunjhunwala A, Vasudevan K, Kaur P, Ramamurthi B, Bitra S, Uppal K. Energy efficiency in lighting: AC vs DC LED lights. In: International Conference on Sustainable Green Buildings and Communities (SGBC); December 2016. IEEE. pp. 1-4

[4] Ciriminna R, Meneguzzo F, Albanese L, Pagliaro M. Solar street lighting: A key technology en route to sustainability. Wiley Interdisciplinary Reviews: Energy and Environment. 2017;**6**(2). DOI: 10.1002/wene.218

[5] Willems S, Aerts W. Study and Simulation of a DC Micro Grid with focus on Efficiency, Use of Materials and Economic Constraints. Leuven, Belgium: University of Leuven; 2014

[6] Pimputkar S, Speck J-S, DenBaars S-P, Nakamura S. Prospects for LED Lighting. Nature Photonics. 2009;**3**(4):180-182. DOI: 10.1038/nphoton.2009.32

[7] National Academies of Sciences. Assessment of Solid-State Lighting, Phase Two. Washington, DC (USA): The National Academies Press; 2017. 100 p. ISBN 978-0-309-45257-1. DOI: 10.17226/24619

[8] Biber C. LED light emission as a function of thermal conditions. In Twenty-Fourth Annual IEEE Semiconductor Thermal Measurement and Management Symposium, 2008. Semi-Therm 2008; IEEE; 16-20 March 2008; San Jose, CA, USA. pp. 180-184. DOI: 10.1109/STHERM.2008.4509387

[9] Waffenschmidt E. Direct current (DC) supply grids for LED lighting. LED Professional. 2015;**48**. Available from: http://www.100pro-erneuerbare.com/netze/publikationen/2014-10-Waffenschmidt-DC_Grid_for_LED-LpS2014/Waffenschmidt-DC_Grid_for_LED-LpS2014.pdf

[10] Winder S. Power Supplies for LED Driving. 2nd ed. Newnes; 2016. p. 320. ISBN: 9780081010242

[11] Gago-Calderón A, Fernández-Ramos J, Narvarte L. Temperature-controlled light-emitting diode lamp for photovoltaic rural applications. Progress in Photovoltaics: Research and Applications. 2013;**21**(2):232-239. DOI: 10.1002/pip.1170

[12] International Energy Agency [IEA]. Market-based Instruments for Energy Efficiency Policy Choice and Design. Paris (France): OECD/IEA; 2017. Available from: https://www.iea.org/publications/insights/insightpublications/MarketBased_Instruments_for_Energy_Efficiency.pdf [Accessed: 2018-01-14]

[13] Thielemans S, Di Zenobio D, Touhafi A, Lataire P, Steenhaut K. DC grids for smart LED-based lighting: The EDISON solution. Energies. 2017;**10**(10):1454. DOI: 10.3390/en10101454

[14] Calderón A-G, Fernández L-N, Moreno L-M-C, Barba J-S. LED bulbs technical specification and testing procedure for solar home systems. Renewable and Sustainable Energy Reviews. 2015;**41**:506-520. DOI: 10.1016/j.rser.2014.08.057

[15] Rosenheck T. POE for Organizations with a Repetitive Building Type. Building Performance Evaluation. Cham (Switzerland): Springer; 2018. pp. 183-192. DOI: 10.1007/978-3-319-56862-1_14

[16] Tuenge J, Poplawski M. PoE Lighting System Energy Reporting Study Part 1. Solid-State Lighting Program Building Technologies Office, Office of Energy Efficiency and Renewable Energy, U.S. Department of Energy; 2017. PNNL-26284. Available from: https://energy.gov/sites/prod/files/2017/03/f34/ssl-poe-part1_feb2017.pdf [Accessed: 2018-01-14]

[17] Wuthipong S. MW Scale Stand-Alone PV Hybrid Mini Grid System. Presentation at World Alternative Energy Forum; Chiang Mai, Thailand, 1;.-14. Dec. 2012. Available from: http://www.adicet.cmru.ac.th/waef2012/ [Accessed: 2018-01-14]

[18] Vossos V, Johnson K, Kloss M, Khattar M, Gerber D, Brown R. Review of DC Power Distribution in Buildings: A Technology and Market Assessment. Lawrence Berkeley National Laboratory; 2017. Available from: https://cloudfront.escholarship.org/dist/prd/content/qt2dd536p1/qt2dd536p1.pdf [Accessed: 2018-01-14]

[19] Boeke U, Wendt M. DC power grids for buildings. IEEE 1st International Conference on DC Microgrids; 7-10 June 2015; Atlanta, USA. pp. 180-184. DOI: 10.1109/ICDCM.2015.7152040

[20] Fregosi D, Ravula S, Brhlik D, Saussele J, Frank S, Bonnema E, Wilson E. A comparative study of DC and AC microgrids in commercial buildings across different climates and operating profiles. IEEE 1st International Conference on DC Microgrids; 7-10 June 2015; Atlanta, USA. pp. 159-164. DOI: 10.1109/ICDCM.2015.7152031

[21] Weiss R, Ott L, Boeke U. Energy efficient low-voltage DC-grids for commercial buildings. IEEE 1st International Conference on DC Microgrids; 7-10 June 2015; Atlanta, USA. pp. 154-158. DOI: 10.1109/ICDCM.2015.7152030

[22] Zhang F, Meng C, Yang Y, Sun C, Ji C, Chen Y, Yang G. Advantages and challenges of DC microgrid for commercial building a case study from Xiamen university DC microgrid. IEEE 1st International Conference on DC Microgrids; 7-10 June 2015; Atlanta, USA. pp. 355-358. DOI: 10.1109/ICDCM.2015.7152068

[23] Panguloori R, Mishra P, Kumar. Power distribution architectures to improve system efficiency of centralized medium scale PV street lighting system. Solar Energy. 2013;**97**:405-413. DOI: 10.1016/j.solener.2013.08.034

[24] Khalil A, Rajab Z, Amhammed M, Asheibi A. The benefits of the transition from fossil fuel to solar energy in Libya: A street lighting system case study. Applied Solar Energy. 2017;**53**(2):138-151. DOI: 10.3103/S0003701X17020086

[25] Park S, Kang B, Choi M, Jeon S, Park S. A micro-distributed ESS-based smart LED streetlight system for intelligent demand management of the micro-grid. Sustainable Cities and Society. 2017. In Press. DOI: 10.1016/j.scs.2017.10.023

[26] Loomba P, Asgotraa S. DC solar microgrids—A successful technology for rural sustainable development. 2016 IEEE PES Power Africa Conference; 28 June-3 July 2016; Livingstone, Zambia. DOI: 10.1109/PowerAfrica.2016.7556601

Chapter 3

White Organic Light-Emitting Diodes with Thermally Activated Delayed Fluorescence Emitters

Dongxiang Luo, Zhiyuan He, Peng Xiao,
Qunxing Liu and Baiquan Liu

Additional information is available at the end of the chapter

http://dx.doi.org/10.5772/intechopen.75564

Abstract

Recently, thermally activated delayed fluorescence (TADF) organic light-emitting diodes (OLEDs) have attracted both academic and industrial interest due to their extraordinary characteristics, such as high efficiency, low driving voltage, bright luminance, lower power consumption, and potentially long lifetime. In this chapter, various approaches to realize white OLEDs (WOLEDs) with TADF emitters have been introduced. The recent development of WOLEDs based on all TADF emitters, WOLEDs based on TADF and conventional fluorescence emitters, and WOLEDs based on TADF and phosphorescence emitters is highlighted. Particularly, the device structures, design strategies, working mechanisms, and electroluminescent processes of the representative high-performance WOLEDs with TADF emitters are reviewed. Moreover, challenges and opportunities for further enhancement of the performance of WOLEDs with TADF emitters are presented.

Keywords: white, organic light-emitting diodes, thermally activated delayed fluorescence, lighting, display

1. Introduction

In 1987, Tang and his coworker reported the first organic light-emitting diodes (OLED) [1]. Since then, OLEDs have been the object of intense research because of the superior properties, including bright luminance, excellent efficiency, fast response, good stability as well as the flexible characteristic [2–5]. Currently, there are a large number of available commercial applications in our life, such as televisions, lamps as well as cell phones. In addition, after the invention of OLED, other kinds of LEDs (e.g., polymer LED, quantum-dot LED, nanoplatelet

LED, and perovskite LED) were also reported [6–10]. By dint of the strategies used in OLEDs, the performance of these LEDs can be greatly enhanced. Besides, with the increasing understanding of the insight of OLEDs, the concepts utilized in OLEDs can also be applied to other optoelectrical devices, which is beneficial to the development of related fields [11–13].

To satisfy the requirements of energy-saving lighting and high-quality displays, white OLED (WOLED) has been considered to be one of the most promising candidates. Since the pioneer WOLEDs made by Kido and his coworkers, the WOLED technology is greatly improved [14, 15]. During the last 24 years, the power efficiency (PE) was enhanced from less than 1 lm/W to more than 100 lm/W [16–18], indicating that WOLEDs are promising for the lighting and displays filed. In terms of lighting application, WOLEDs require a standard fluorescent tube efficiency (40–70 lm/W) and ≥10,000 h of lifetime at the luminance of ≥1000 cd/m^2 [19–21]. Besides, the color rendering index (CRI) above 80 is required for the indoor lighting, and the Commission International de L'Eclairage (CIE) chromaticity coordinates of WOLEDs should be located near white light equal-energy point (0.33, 0.33) [22–25]. Moreover, for the high-quality lighting, other characterization parameters (e.g., correlated color temperature (CCT), color stability, and driving voltage) of WOLEDs are also required to be taken into account [26–30].

In 2012, Adachi et al. made a breakthrough on the thermally activated delayed fluorescence (TADF) material, which has been considered as the third-generation OLED emitter [31–33]. Different from the conventional fluorescent emitters in which only the singlet excitons (25%) can emit light since the radiative decay of triplet excitons (75%) is spin forbidden, TADF emitters could harness both singlet and triplet excitons since triplet excitons can be harvested as delayed fluorescence through their upconversion from a lowest triplet state to a lowest singlet state by inducing an efficient reverse intersystem crossing (RISC) [34–38]. Therefore, similar to phosphorescence emitters, a maximum internal quantum efficiency (IQE) of 100% can be realized [39–42]. Due to the outstanding properties (e.g., free noble metal, high efficiency, low driving voltage, bright luminance, lower power consumption, and potentially long lifetime), TADF emitters have been actively investigated to develop WOLEDs [43–45]. Although efficient TADF emitters were only demonstrated 6 years ago and WOLEDs with TADF emitters were just reported 4 years ago, the performance of WOLEDs with TADF emitters has been improved step by step [46]. For example, WOLEDs with TADF emitters can exhibit nearly 20% external quantum efficiency (EQE) [47], which is comparable to state-of-the-art phosphorescence WOLEDs and fluorescence/phosphorescence hybrid WOLEDs [29, 30, 48–54]. Thus, WOLEDs with all TADF emitters have great potential to the lighting and display field.

Herein, we first introduced the basic concepts of TADF emitters, which are beneficial to comprehend WOLEDs with TADF emitters. Then, we summarize the main approaches to realize WOLEDs with TADF emitters in recent years. More specifically, we highlight the recent development of WOLEDs based on all TADF emitters, WOLEDs based on TADF and conventional fluorescence emitters, and WOLEDs based on TADF and phosphorescence emitters. Particularly, the device structures, design strategies, working mechanisms, and electroluminescent processes of the representative high-performance WOLEDs with TADF emitters are

reviewed. Finally, challenges and opportunities for further enhancement of the performance of WOLEDs with TADF emitters are presented.

2. Fundamental concepts of TADF emitters

Due to the effect of spin statistics, when holes injected from the anode meet electrons injected from the cathode, singlet and triplet excitons will be formed with a ratio of 1:3 [55]. In the case of the first-generation OLED emitters (i.e., conventional fluorescence emitters), only the singlet excitons (25%) can emit light since the radiative decay of triplet excitons (75%) is spin forbidden, as shown in **Figure 1**. Therefore, the EQE of fluorescence WOLEDs is usually below 5%, considering that the outcoupling factor is ~20%. For the second-generation OLED emitters (i.e., phosphorescence emitters), they can not only harvest triplet excitons via the triplet-triplet energy transfer but also harvest singlet excitons via the singlet-triplet intersystem crossing process (ISC) due to the heavy-atom effect [56]. Thus, the EQE of phosphorescence WOLEDs can be as high as 20%.

In terms of the third-generation OLED emitters (i.e., TADF emitters), a small energy gap ($\triangle E_{ST}$) between singlet (S_1) and triplet (T_1) excited states is required and can be attained by carefully designing organic molecules [31]. Generally, the S_1 level was considerably higher in energy than the T_1 level by 0.5–1.0 eV, because of the electron exchange energy between these

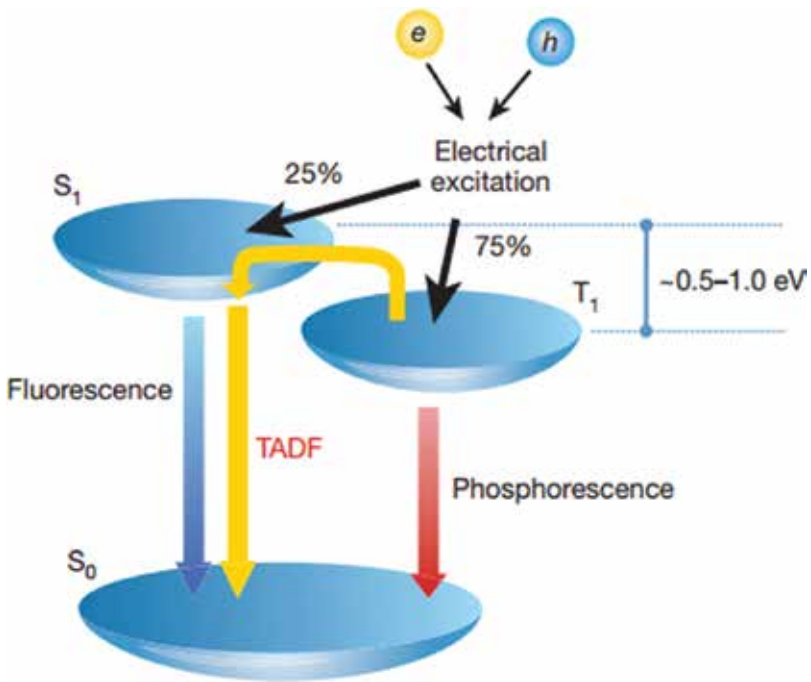

Figure 1. An energy diagram of a conventional organic molecule. H is hole and e is electron. Reproduced from Ref. [31].

levels. However, to enhance thermal upconversion (i.e., $T_1 \rightarrow S_1$ RISC), the molecular design of TADF materials requires small $\triangle E_{ST}$, typically less than 0.2 eV, to overcome competitive non-radiative decay pathways, leading to highly luminescent TADF materials [57]. In addition, to enhance the photoluminescence efficiency of TADF materials, the geometrical change in molecular conformation between its ground state (S_0) and S_1 states should be restrained to suppress non-radiative decay. As a result, the maximum theoretical IQE of TADF emitters can be 100%.

3. Approaches to realize WOLEDs with TADF emitters

3.1. Basic aspects of WOLEDs with TADF emitters

Similar to phosphorescence emitters, the use of TADF emitters is very promising to achieve WOLEDs. This is because TADF emitters can (1) harness triplet excitons, (2) exhibit excellent efficiency, and (3) show usually broad emission spectra with rather large full width at half maximum of about 100 nm, which is wider than that of conventional fluorescent materials because of their charge-transfer nature [31–47].

To attain the high performance, the device structures, design strategies, working mechanisms, and electroluminescent processes of the WOLEDs with TADF emitters should be well manipulated. For example, unlike conventional fluorescence emitters, the T_1 of TADF emitters is necessary to be considered when designing a WOLED architecture, since hosts or nearby layers with low T_1 would quench the triplet excitons, which leads to the low efficiency. Besides, the location of TADF emitters is needed to be investigated, since the energy transfer would occur between the contacted different emitters (e.g., energy can transfer from high-energy TADF emitters to low-energy emitters). To date, various approaches have been reported to develop WOLEDs with TADF emitters, such as the exploitation of all TADF emitters, the combination of TADF and conventional fluorescence emitters, and the mixture of TADF and phosphorescence emitters.

3.2. WOLEDs with all TADF emitters

The most directed approach to develop WOLEDs with TADF emitters is the exploitation of all TADF emitters. That is to say, all blue, green, and red emitters are TADF materials. By selecting high-T_1 hosts and charge transport materials, high-performance WOLEDs can be attained. More specifically, the conventional fluorescent host should possess high T_1, which should be particularly higher than the blue TADF materials. Otherwise, the triplet excitons of emitters would be quenched by the host, resulting in low performance. Moreover, high-T_1 charge transport materials should be selected, which is used to confine the triplet excitons in the EML, leading to the excitons being well consumed.

Adachi and his coworkers for the first time adopted such an approach to develop highly efficient WOLEDs with all TADF emitters [46]. **Figure 2** depicts the device structure: ITO/1,4,5,8,9,11-hexaazatriphenylene hexacarbonitrile (HAT-CN, 10 nm)/9,9′,9″-triphenyl-9H,9′H,9″H-3,3′:6′,3″-tercarbazole (Tris-PCz, 35 nm)/10 wt% 1,2,3,4-tetrakis(carbazol-9-yl)-5,6-dicyanobenzene

http://dx.doi.org/10.5772/intechopen.75564

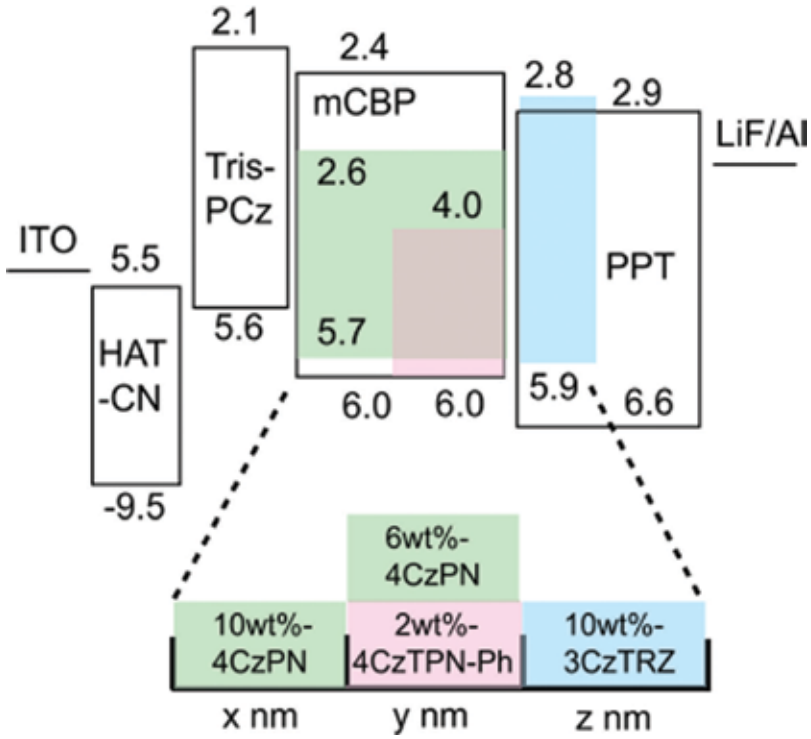

Figure 2. The WOLED structures and energy level diagram. Reproduced from Ref. [46].

(4CzPN): 3,3-Di(9H-carbazol-9-yl)biphenyl (mCBP, green EML) (x nm)/6 wt% 4CzPN: 2 wt% 41,4-dicyano-2,3,5,6-tetrakis (3,6-diphenylcarbazol-9-yl)benzene (CzTPN-Ph): mCBP (red EML) (y nm)/10 wt% 9-(3-(9H-carbazol-9-yl)-9-(4-(4,6-diphenyl-1,3,5-triazin-2-yl)phenyl)-9H-carbazol-6-yl)-9H-carbazole (3CzTRZ): 2,8-bis(diphenylphosphoryl) dibenzo-[b,d] thiophene (PPT, blue EML) (z nm)/PPT (50 nm)/LiF/Al. In this device, the T1 level of mCBP host is 2.9 eV, which is much higher than that of blue, green, and red TADF emitters, ensuring the high efficiency. Besides, PPT has a high T_1 of 3.1 eV, suggesting a good confinement of the triplet excitons. By optimizing the charge generation zone via the adjustment of different EML thickness (the total thickness is set to be x + y + z = 15 nm), the WOLED achieved a maximum EQE of over 17%, a peak PE of 34.1 lm/W with CIE coordinates of (0.30, 0.38).

3.3. WOLEDs with TADF and conventional fluorescence emitters

Considering that triplets could be harnessed by TADF emitters, it is promising to realize the unity IQE by combining traditional fluorescent materials with TADF emitters [61]. For such an approach, the TADF molecules would act as the triplet harvester, which is used to harness the triplets for the conventional other-color fluorescence materials. As a result, highly efficient white light can be produced [42–44].

In 2016, Li et al. reported high-efficiency and high CRI WOLEDs with the chromaticity-adjustable yellow TADF emitter 2-(4-phenoxazinephenyl)thianthrene-9,9′,10,10′-tetraoxide

(PXZDSO2) [47]. By combining the conventional deep-blue fluorescence emitter NI-1-PhTPA and PXZDSO2, the two-color WOLED showed a maximum EQE of 15.8% (device W3). Then, since the chromaticity of the EML containing PXZDSO2 could be tuned to yellowish green, they introduced a deep-red fluorescence emitter DBP (dibenzo{[f,f′]-4, 4′,7,7′-tetraphenyl}diindeno[1,2,3-cd:1′,2′,3′-lm]perylene) subtly to fabricate three-color WOLED, achieving the most efficient ever EQE of 19.2% with a CRI of 68 (device W4) and the highest ever CRI of 95 with an EQE of 15.6% (device W6). The configurations are ITO/HATCN/TAPC/EMLs/TmPyPB/LiF/Al, in which device W3 has the EML of CBP: 8 wt% NI-1-PhTPA (10 nm)/CBP (3 nm)/CBP: 6 wt% PXZDSO2 (15 nm)/CBP (3 nm)/CBP: 8 wt% NI-1-PhTPA (10 nm), device W4 has the EML of CBP: 7 wt% NI-1-PhTPA (10 nm)/CBP (3 nm)/CBP: 3 wt% PXZDSO2 (5 nm)/CBP: 5 wt% PXZDSO2: 0.3 wt% DBP (5 nm)/CBP:3 wt% PXZDSO2 (5 nm)/CBP (3 nm)/CBP: 7 wt% NI-1-PhTPA (10 nm), device W6 has the EML of CBP: 10 wt% NI-1-PhTPA (10 nm)/CBP (3 nm)/CBP: 5 wt%PXZDSO2: 0.35 wt% DBP (15 nm)/CBP (3 nm)/CBP: 10 wt% NI-1-PhTPA (10 nm). The device working mechanisms can be described as follows. For device W3, (1) since NI-1-PhTPA is a deep-blue fluorescence emitter and CBP: 6 wt% PXZDSO2 emits a yellow light with broad spectrum, high-performance two-color WOLEDs were realized; (2) given the almost equal T_1 level of NI-1-PhTPA and PXZDSO2, the efficiency roll-off occurs if they are directly in contact due to the triplet exciton quenching by NI-1-PhTPA; (3) the efficiency roll-off can be further induced as the formed triplet excitons of NI-1-PhTPA cannot be utilized by PXZDSO2; (4) to stabilize the recombination zone which occurs in whole EMLs since NI-1-PhTPA/CBP are bipolar and avoid triplet exciton quenching by NI-1-PhTPA, two 3-nm CBPs were inserted between the blue and yellow EMLs, restraining the inevitable Förster

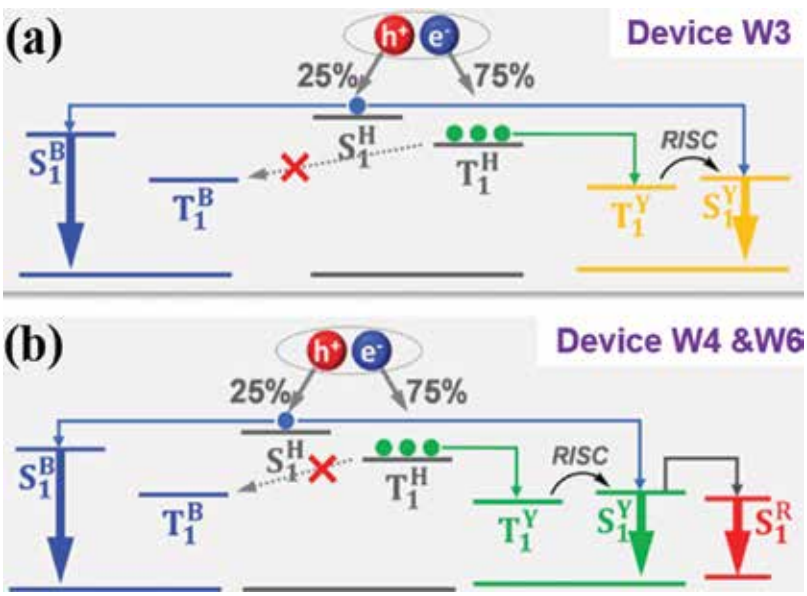

Figure 3. Function mechanisms of the use of singlets/triplets. (a) Device W3 and (b) devices W4 and W6. H, B, Y, and R represent CBP, NI-1-PhTPA, PXZDSO2, and DBP, respectively. Reproduced from Ref. [47].

energy transfer from NI-1-PhTPA to PXZDSO2; (5) to reduce the triplet exciton energy loss via nonradiative transition process, blue-fluorescence emitter was dispersed in CBP for blue emission, leading to most excitons being generated at CBP; and (6) triplet energy transferred from CBP gives most of triplet excitons of PXZDSO2 since triplet excitons typically have long diffusion lengths (≈100 nm), as shown in **Figure 3a**. Hence, an EQE of 15.8% was achieved for device W3. For device W4, (1) a deep-red fluorescence emitter DBP was conceived to be used; (2) PXZDSO2 was an assistant host for DBP to realize a red-light emission due to an efficient energy transfer from the S1 of PXZDSO2; (3) the doping concentration of PXZDSO2 was decreased to reduce intermolecular aggregation and thus blue-shifted emission (20 nm), achieving green emission, complementary to emissions of NI-1-PhTPA and DBP; (4) a red EML of CBP: 5 wt% PXZDSO2: 0.3 wt% DBP was inserted between two green EMLs of CBP: 3 wt% PXZDSO2 to receive singlet exciton energy transferred from the PXZDSO2 molecules in both sides to give both green and red emissions; (5) the two doped blue EMLs and CBP interlayers located at both sides of the green EMLs to give a blue emission and to confine the PXZDSO2 triplet excitons, respectively, as shown in **Figure 3b**. Thus, an EQE of 19.2% was achieved for device W4. Furthermore, an EML consisting of improved DBP doping concentration was utilized instead of the green and red EMLs for candle-style warm WOLEDs (device W6), achieving a high CRI of 95.

3.4. WOLEDs with TADF and phosphorescence emitters

Since both TADF and phosphorescence emitters can harvest singlet and triplet excitons, the mixture of TADF and phosphorescence emitters is a significant approach to construct WOLEDs. By virtue of their respective advantages, high efficiency and long lifetime can be realized simultaneously [44, 58]. In particular, there is tremendous interest in mixing blue TADF emitters with green/red or complementary color phosphorescence emitters. This is because blue TADF materials (1) are naturally advantageous to achieve high triplet energies due to their reduced singlet-triplet splits, (2) can possess high efficiency, and (3) can harvest the triplets [59–61]. For this kind of WOLED (i.e., mixing blue TADF and other-color phosphorescence emitters), it is generally called hybrid WOLEDs [21].

In 2014, Zhang and coworkers demonstrated hybrid WOLEDs via the use of blue TADF emitter, obtaining the peak efficiency as high as 47.6 lm/W [59]. The device structure is ITO/HATCN (5 nm)/NPB (40 nm)/TCTA (10 nm)/mCP: 4,5-bis(carbazol-9-yl)-1,2-dicyanobenzene (2CzPN, 11 nm, blue EML)/TAZ: 4 wt% (acetylacetonato)bis[2-(thieno[3,2-c]pyridin-4-yl)phenyl]iridium(III) (PO-01, 4 nm, orange EML)/TAZ (40 nm)/LiF (0.5 nm)/Al (150 nm), as shown in **Figure 4**. The factors for the high performance are as follows: (1) mCP is chosen to be the host for 2CzPN due to the wide energy gap and high T_1 of 3.0 eV, since the host of the TADF material plays an important role in determining the efficiency; (2) 2CzPN is placed nearest to the main recombination zone, ensuring that excitons can diffuse throughout the emissive region to produce a desired color-balanced output; (3) triplets formed on 2CzPN can be harvested by either energy transfer to the low-lying triplet states of the phosphor PO-01 (2.2 eV) or thermal upconversion to the emissive singlet states, eliminating the energy loss; and (4) the recombination zone is fixed as the voltage increases by 2CzPN due to its charge-trapping ability, achieving a stable white emission.

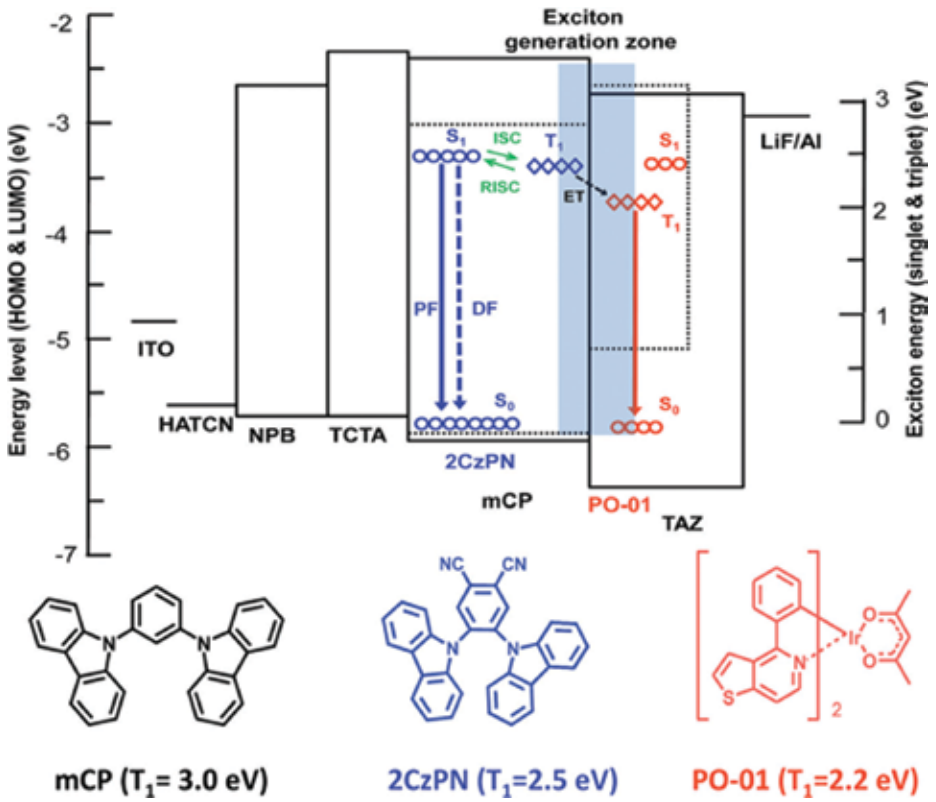

Figure 4 Schematic diagrams of the working mechanisms. The gray-filled rectangle represents the main exciton generation zone. PF is the prompt fluorescence while DF is the delayed fluorescence. RISC indicates the reverse ISC and ET denotes the energy transfer. Reproduced from Ref. [59] with permission from the Royal Society of Chemistry.

Although high-performance hybrid WOLEDs based on TADF materials have been demonstrated, there are still some problems, even for these state-of-the-art devices [59–61]. For example, (1) the driving voltages are somewhat high (e.g., 3.2 V at 1 cd m^{-2} [61]); (2) the luminances are very low (e.g., only ~10,000 cd m^{-2} [61]); (3) the efficiency at high luminance is not high (e.g., <6 lm W^{-1} at 10,000 cd m^{-2} [61]); (4) the CRI is not high enough; and (5) negligible attention has been paid to the lifetime of TADF-based hybrid WOLED.

To solve the issues, Luo et al. recently reported high-performance two-color and three-color hybrid WOLEDs [62]. The two-color WOLED exhibits (1) low voltage (i.e., 2.9 V at 1 cd m^{-2}); (2) high luminance (103,756 cd m^{-2}); (3) maximum EQE and PE of 23.5% and 70.92 lm W^{-1}, respectively; and (4) 21.59 lm W^{-1} at 10,000 cd m^{-2}. The three-color WOLED exhibits (1) low voltage and high luminance (51,514 cd m^{-2}); (2) superior CRI of 94; and (3) EQE and PE of 17.3% and 46.09 lm W^{-1}, respectively. The configuration of the two-color WOLEDs is ITO/HAT-CN (100 nm)/TAPC (20 nm)/mCP: 9,9′,9″,9‴-((6-phenyl-1,3,5-triazine-2,4-diyl) bis(benzene-5,3,1-triyl))tetrakis(9*H*-carbazole) (DDCzTrz, 10 nm, 20%)/interlayers (3 nm)/ bis[2-(2-hydroxyphenyl)-pyridine] beryllium ($Bepp_2$): bis(2-phenyl-4,5-dimethylpyridinato) [2-(biphenyl-3-yl)pyridinato] iridium(III) ($Ir(dmppy)_2(dpp)$, 15 nm, 1:2%)/$Bepp_2$ (35 nm)/

LiF (1 nm)/Al (160 nm), where interlayers are none, mCP and 2,6-bis(3-(carbazol-9-yl)phenyl)pyridine (26DCzPPy) for devices W11, W12, and W13, respectively. The configuration of the two-color WOLED is ITO/HAT-CN (100 nm)/TAPC (20 nm)/mCP: DDCzTrz (10 nm, 20%)/26DCzPPy (interlayer, 3 nm)/$Bepp_2$: $Ir(dmppy)_2(dpp)$: $Ir(piq)_3$ (15 nm, 1: 2%: 1.3%)/$Bepp_2$ (35 nm)/LiF (1 nm)/Al (160 nm). Unlike previous TADF-based hybrid WOLEDs, the bipolar interlayer is demonstrated to enhance the performance. Particularly, it is demonstrated that the use of interlayer can enhance the lifetime (2.3 times). The working mechanism of the two-color WOLED can be described as follows, which is beneficial to comprehend the reason why the bipolar interlayer can enhance the performance. For W11, since mCP and $Bepp_2$ are p-type and n-type materials, respectively, holes and electrons are easily accumulated at the mCP/$Bepp_2$ interface, forming singlet and triplet excitons, as shown in **Figure 5a**. The triplets on blue EML can (1) convert into singlets via the RISC procedure and then generate the blue emission, and (2) transfer to the low energy of yellow phosphor $Ir(dmppy)_2(dpp)$ via the Dexter process and then generate part of yellow emission (the other part of yellow emission is originated from excitons on the yellow EML). However, the main exciton generation

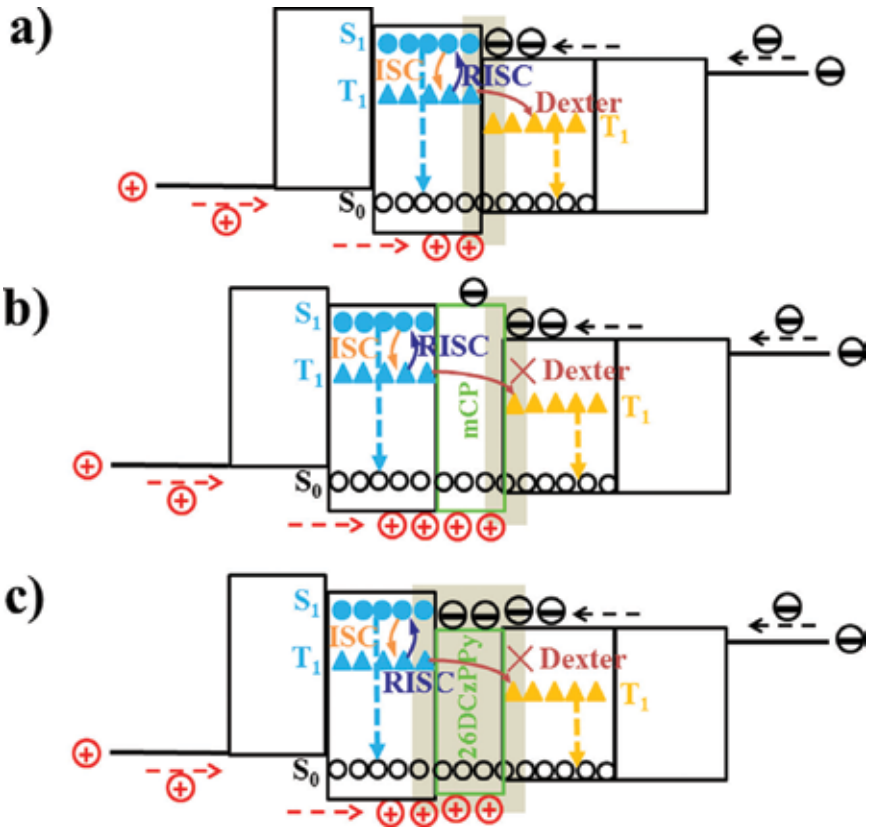

Figure 5 A schematic illustration of the working mechanism of (a) W11, (b) W12, and (c) W13. The gray-filled rectangles are the main exciton generation zones. The Dexter energy transfer can occur in W11, while it is prohibited in both W12 and W13. Reproduced from Ref. [62].

zone of W11 is narrow, unfavorable to the performance. Similarly, the main exciton generation zone of W12 is located at the mCP interlayer/$Bepp_2$ interface, as shown in **Figure 5b**. As a result, excitons are more easily harvested by $Ir(dmppy)_2(dpp)$ instead of DDCzTrz since $Ir(dmppy)_2(dpp)$ is close to the main exciton generation zone. However, a part of electrons can pass through the thin interlayer via the tunneling process and then meet holes, which can generate excitons to guarantee the blue emission. For W13, by way of the bipolar interlayer and the suitable energy levels of 26DCzPPy, both holes and electrons can be easily passed through 26DCzPPy, as shown in **Figure 5c**. As a result, excitons can be formed at both the mCP/26DCzPPy and 26DCzPPy/$Bepp_2$ interfaces, leading to a broad exciton generation zone, which ensure the high performance of W23. Besides, since the Dexter energy transfer from DDCzTrz to $Ir(dmppy)_2(dpp)$ is also prevented due to the 3 nm 26DCzPPy, the yellow emission mainly results from excitons on the yellow EML.

Another effective approach to develop WOLEDs with TADF and phosphorescence emitters is the mixture of green TADF and other-color phosphorescence emitters. In this case, the TADF emitters are adopted as the emitters for WOLEDs because they may be compatible with phosphorescence emitters and not quench triplet excitons of the phosphorescence emitters, otherwise triplet excitons will be wasted.

Kim et al. reported this approach by combining a green TADF with red/blue phosphorescence materials to organize high-efficiency hybrid-type WOLEDs [45]. In their WOLED, energy transfer between a blue phosphorescent material and a green TADF emitter was efficient and could be managed by controlling the doping concentration of emitters. A maximum EQE of 20.2% was achieved by optimizing the device structure of the hybrid-type WOLEDs. The device structure is ITO (50 nm)/poly(3,4-ethylenedioxythiophene): poly(styrenesulfonate) (PEDOT:PSS, 60 nm)/TAPC (20 nm)/mCP (10 nm)/mCP: iridium(III) bis[(4,6-difluorophenyl)-pyridinato-N,C^2]picolinate (FIrpic): (4 s,6 s)-2,4,5,6-tetra(9H-carbazol-9-yl)isophthalonitrile (4CzIPN) (12.5 nm)/TPBI: $Ir(pq)_2acac$ (12.5 nm, 3%)/diphenylphosphine oxide-4-(triphenylsilyl)phenyl (TSPO1, 35 nm)/LiF (1 nm)/Al (200 nm), where 4CzIPN is the green TADF emitter, and FIrpic and $Ir(pq)_2acac$ are blue and red phosphorescence emitter, respectively, as shown in **Figure 6**. To explore the possibility of this type of WOLEDs, hybrid OLEDs with blue-emitting FIrpic and green-emitting 4CzIPN were first fabricated. By optimizing the concentration of FIrpic and 4CzIPN, a maximum EQE of the hybrid OLEDs was 19.2% at 5% FIrpic and 0.5% 4CzIPN. Given that the EQE of mCP: FIrpic OLED is <20%, such superior EQE of hybrid OLED suggests that 4CzIPN would not quench FIrpic triplet emission. In fact, T_1 of FIrpic can be transferred to 4CzIPN and then make a contribution to the 4CzIPN TADF emission. For this hybrid OLED, there are three main energy transfer processes, that is, energy transfer processes from mCP to FIrpic, mCP to 4CzIPN, and FIrpic to 4CzIPN dominate the blue and green emissions of the hybrid OLEDs. After the successful exploration of hybrid OLED, Kim et al. combined this system and red phosphorescence emitting layers, attaining high-efficiency WOLEDs. The factors for the high-performance of WOLEDs can be summarized as follows: (1) the hybrid OLEDs doped with FIrpic and 4CzIPN showed a high quantum efficiency, which ensure the high efficiency of blue-green-emitting layer. In this emitting layer, energy transfer from FIrpic to 4CzIPN is

http://dx.doi.org/10.5772/intechopen.75564

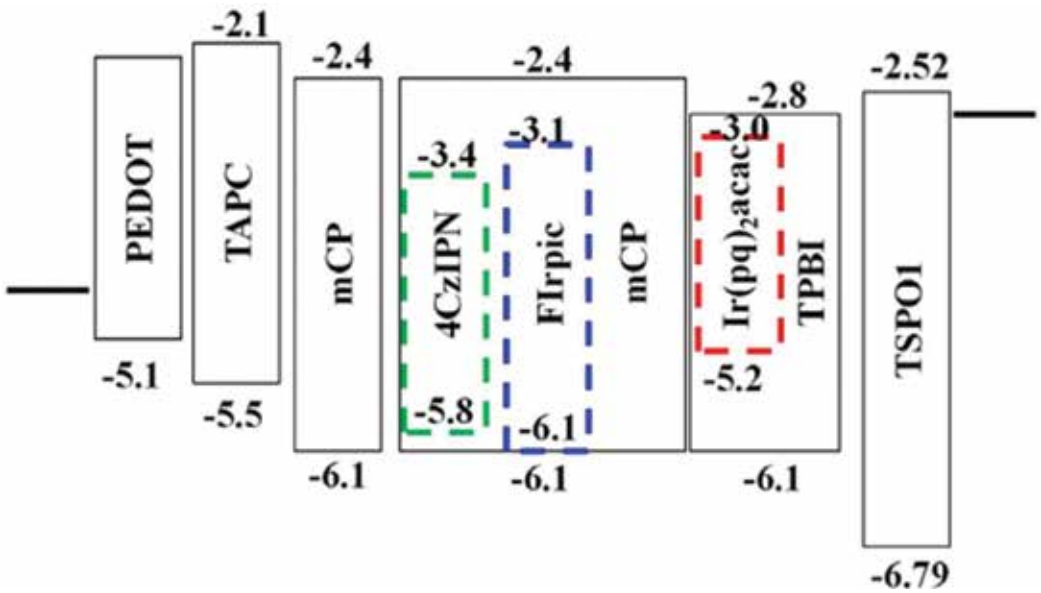

Figure 6. The energy level diagram and device architecture of the WOLED. Reproduced from Ref. [45].

efficient, leading to no non-radiative triplet exciton quenching of FIrpic by 4CzIPN. (2) The energy transfer from mCP to dopant materials in the FIrpic and 4CzIPN co-doped emitting layer is very efficient. (3) FIrpic activates the delayed emission of 4CzIPN through an efficient energy transfer, which resulted in the high quantum efficiency of the hybrid-emitting layer. (4) The balanced charge density in the emitting layer contributed to the high quantum efficiency. The TPBI: $Ir(pq)_2acac$-emitting layer efficiently injects electrons due to electron transport properties of TPBI, which improved charge balance in the emitting layer in combination with hole transport-type mCP: FIrpic: 4CzIPN-emitting layer.

4. Summary and outlook

As a novel kind of OLED emitter, TADF materials show many unique characteristics, which have been demonstrated to develop high-performance WOLEDs. Thanks to the hard endeavors of researchers, the performance of WOLEDs is now comparable to state-of-the-art phosphorescence WOLEDs and fluorescence/phosphorescence hybrid WOLEDs. In this chapter, the focus is the development of WOLEDs by manipulating TADF emitters. Specifically, we highlight the recent development of WOLEDs based on all TADF emitters, WOLEDs based on TADF and conventional fluorescence emitters, and WOLEDs based on TADF and phosphorescence emitters. Particularly, the device structures, design strategies, working mechanisms, and electroluminescent processes of the representative high-performance WOLEDs with TADF emitters are reviewed.

Although the performance of WOLEDs with TADF emitters has been enhanced over the past few years, there are still many challenges before they can be large-scale commercialized production, such as the efficiency, lifetime, and cost. However, it is deserved to point out that these issues are also hindrances for other kinds of WOLEDs. For example, there is still much room for the efficiency of WOLEDs to the theoretical limit of 248 lm/W (standard light source (D65) from 400 to 700 nm wavelength) [63]. Therefore, the photoluminescence quantum efficiency of the emissive materials (TADF or other-type emitters), the charge balance, and outcoupling efficiency of the devices should be further enhanced.

Besides, despite the efficiency of WOLEDs with TADF emitters that can be high enough, there are some other parameters that are needed to be enhanced. Particularly, the stability and efficiency roll-off of WOLEDs with TADF emitters still lags behind other kinds of WOLEDs. For example, fluorescence WOLEDs can show an extremely long lifetime of 150,000 h at an initial luminance of 1000 cd/m^2 [64], while hybrid WOLEDs based on conventional blue fluorescence emitters can possess a long lifetime of >30,000 h at 1000 cd/m^2 [65]. However, it is still difficult for WOLEDs with TADF emitters to achieve long lifetime, which may be attributed to the instability of TADF emitters. For example, Wang et al. recently reported the first WOLED with TADF emitters realizing long lifetime (2025 h at 1000 cd/m^2) [66]. However, it is noted that the lifetime still cannot meet the requirement of large-scale commercialized productions. Hence, to solve this issue, stable TADF emitters are urgently explored [57]. In addition, fluorescence WOLEDs, hybrid WOLEDs based on conventional blue fluorescence emitters or even phosphorescence WOLEDs with extreme color stability ($\triangle$CIE = (0.00, 0.00)) in the whole luminance/driving voltage have been reported [28, 67–70]. However, the color stability of WOLEDs with TADF emitters is usually unstable, indicating that more efforts are required to manage this difficulty. Furthermore, the efficiency roll-off in WOLEDs with TADF emitters is not ideal, particularly for the PE roll-off [71]. As a consequence, only low efficiency can be attained at high luminances, which is not beneficial to the practical applications. To loosen this bottleneck, the charge balance, energy barriers between nearby layers, and materials selection should be well manipulated [72–76]. With the endeavor of academic and industrial researchers to enhance the materials design and device engineering, we believe that WOLEDs with TADF emitters can play a significant role in the marketplace in the near future, which is beneficial to our human society.

Acknowledgements

The authors are grateful to the National Natural Science Foundation of China (Grant No. 61704034), the Key Platforms and Research Projects of Department of Education of Guangdong Province (Grant Nos. 2016KTSCX034 and 2016KTSCX031), the Guangdong Natural Science Foundation (Grant No. 2016A030310360), and the financial support from Scientific Research Starting Foundation of Foshan University (Gg040926) and Foshan Science and Technology innovation special funds (2017EZ100111).

Conflict of interest

The authors declare no competing financial interest.

Author details

Dongxiang Luo[1], Zhiyuan He[2], Peng Xiao[3], Qunxing Liu[2] and Baiquan Liu[4,5]*

*Address all correspondence to: bqliu1012@gmail.com

1 School of Materials and Energy, Guangdong University of Technology, Guangzhou, China

2 China Electronic Produce Reliability and Environmental Testing Research Institute, Guangzhou, China

3 School of Physics and Optoelectronic Engineering, Foshan University, Foshan, China

4 Institute of Polymer Optoelectronic Materials and Devices, State Key Laboratory of Luminescent Materials and Devices, South China University of Technology, Guangzhou, China

5 LUMINOUS! Center of Excellence for Semiconductor Lighting and Displays, School of Electrical and Electronic Engineering, Nanyang Technological University, Singapore

References

[1] Tang CW, VanSlyke VA. Organic electroluminescent diodes. Applied Physics Letters. 1987;**51**:913-915

[2] Helander MG, Wang ZB, Qiu J, Greiner MT, Puzzo DP, Liu ZW, Lu ZH. Chlorinated indium tin oxide electrodes with high work function for organic device compatibility. Science. 2011;**332**:944-947

[3] Sasabe H, Kido J. Development of high performance OLEDs for general lighting. Journal of Materials Chemistry C. 2013;**1**:1699-1707

[4] Yang X, Zhou G, Wong WY. Functionalization of phosphorescent emitters and their host materials by main-group elements for phosphorescent organic light-emitting devices. Chemical Society Reviews. 2015;**44**:8484-8575

[5] Liu B, Gao D, Wang J, Wang X, Wang L, Zou J, Ning H, Peng J. Progress of white organic light-emitting diodes. Acta Physico-Chimica Sinica. 2015;**31**:1823-1852

[6] Burroughes JH, Bradley DDC, Brown AR, Marks RN, Mackay K, Friend RH, Burns PL, Homes AB. Light-emitting diodes based on conjugated polymers. Nature. 1990;**348**:352-352

[7] Sun QJ, Wang YA, Li LS, Wang D, Zhu T, Xu J, Yang C, Li Y. Bright, multicoloured light-emitting diodes based on quantum dots. Natute Photonics. 2007;**1**:717-722

[8] Dai XL, Zhang ZX, Jin YZ, Niu Y, Cao HJ, Liang XY, Chen LW, Wang JP, Peng XG. Solution-processed, high performance light-emitting diodes based on quantum dots. Nature. 2014;**515**:96-100

[9] Chen Z, Nadal B, Mahler B, Aubin H, Dubertret B. Quasi-2D colloidal semiconductor nanoplatelets for narrow electroluminescence. Advanced Functional Materials. 2014;**24**:295-302

[10] Li J, Xu L, Wang T, Song J, Chen J, Xue J, Dong Y, Cai B, Shan Q, Han B, Zeng H. 50-fold EQE improvement up to 6.27% of solution-processed all-inorganic perovskite $CsPbBr_3$ QLEDs via surface ligand density control. Advanced Materials. 2017;**29**:1603885

[11] Xiao Z, Liu F, Geng X, Zhang J, Ding L. A carbon-oxygen-bridged ladder-type building block for efficient donor and acceptor materials used in organic solar cells. Science Bulletin. 2017;**62**:1331-1336

[12] Xiao Z, Jia X, Ding L. Ternary organic solar cells offer 14% power conversion efficiency. Science Bulletin. 2017;**62**:1562-1564

[13] Xiao Z, Jia X, Li D, Wang S, Ding L. 26 mA cm^{-2} Jsc from organic solar cells with a low-bandgap nonfullerene acceptor. Science Bulletin. 2017;**62**:1494-1496

[14] Kido J, Hongawa K, Okuyama K, Nagai K. White light-emitting organic electroluminescent devices using the poly (N-vinylcarbazole) emitter layer doped with three fluorescent dyes. Applied Physics Letters. 1994;**64**:815-817

[15] Kido J, Kimura M, Nagai K. Multilayer white light-emitting organic electroluminescent device. Science. 1995;**267**:1332-1334

[16] Ou QD, Zhou L, Li YQ, Chen S, Chen JD, Li C, Wang QK, Lee ST, Tang JX. Light-emitting diodes: Extremely efficient white organic light-emitting diodes for general lighting. Advanced Functional Materials. 2015;**24**:7249-7256

[17] Liu B, Wang L, Xu M, Tao H, Gao D, Zou J, Lan L, Ning H, Peng J, Cao Y. Extremely stable-color flexible white organic light-emitting diodes with efficiency exceeding 100 lm W^{-1}. Journal of Materials Chemistry C. 2014;**2**:9836-9841

[18] Wu SF, Li SH, Wang YK, Huang CC, Sun Q, Liang JJ, Liao LS, Fung MK. White organic LED with a luminous efficacy exceeding 100 lm w^{-1} without light out-coupling enhancement techniques. Advanced Functional Materials. 2017;**27**:1701314

[19] Yang X, Zhou G, Wong WY. Recent design tactics for high performance white polymer light-emitting diodes. Journal of Materials Chemistry C. 2014;**2**:1760-1778

[20] Jou JH, Kumar S, Agrawal A, Li TH, Sahoo S. Approaches for fabricating high efficiency organic light emitting diodes. Journal of Materials Chemistry C. 2015;**3**:2974-3002

[21] Liu B, Li X, Tao H, Zou J, Xu M, Wang L, Peng J, Cao Y. Manipulation of exciton distribution for high-performance fluorescent/phosphorescent hybrid white organic light-emitting diodes. Journal of Materials Chemistry C. 2017;**5**:7668-7683

[22] Wang Q, Ma D. Management of charges and excitons for high-performance white organic light-emitting diodes. Chemical Society Reviews. 2010;**39**:2387-2398

[23] Gather MC, Kohenen A, Meerholz K. White organic light-emitting diodes. Advanced Materials. 2011;**23**:233-248

[24] Chang YL, Lu ZH. White organic light-emitting diodes for solid-state lighting. Journal of Display Technology. 2013;**9**:459-468

[25] Kamtekar KT, Monkman AP, Bryce MR. Recent advances in white organic light-emitting materials and devices (WOLEDs). Advanced Materials. 2010;**22**:572-582

[26] Jou JH, Hsieh CY, Tseng JR, Peng SH, Jou YC, Hong JH, Shen SM, Tang MC, Chen PC, Lin CH. Candle light-style organic light-emitting diodes. Advanced Functional Materials. 2013;**23**:2750-2757

[27] Jou JH, Wu MH, Shen SM, Wang HC, Chen SZ, Chen SH, Lin CR, Hsieh YL. Sunlight-style color-temperature tunable organic light-emitting diode. Applied Physics Letters. 2009;**95**:013307

[28] Liu BQ, Wang L, Gao DY, Xu M, Zhu XH, Zou JH, Lan LF, Ning HL, Peng JB, Cao Y. Harnessing charge and exciton distribution towards extremely high performance: The critical role of guests in single-emitting-layer white OLEDs. Materials Horizons. 2015;**2**:536-544

[29] Su SJ, Gonmori E, Sasabe H, Kido J. Highly efficient organic blue- and white-light-emitting devices having a carrier- and exciton-confining structure for reduced efficiency roll-off. Advanced Materials. 2008;**20**:4189-4194

[30] Reineke S, Lindner F, Schwartz G, Seidler N, Walzer K, Lüssem B, Leo K. White organic light-emitting diodes with fluorescent tube efficiency. Nature. 2009;**459**:234-238

[31] Uoyama H, Goushi K, Shizu K, Nomura H, Adachi C. Highly efficient organic light-emitting diodes from delayed fluorescence. Nature. 2012;**492**:234-238

[32] Zhang Q, Tsang D, Kuwabara H, Hatae Y, Li B, Takahashi T, Lee SY, Yasuda T, Adachi C. Nearly 100% internal quantum efficiency in undoped electroluminescent devices employing pure organic emitters. Advanced Materials. 2015;**27**:2096-2100

[33] Nishimoto T, Yasuda T, Lee SY, Kondo R, Adachi C. A six-carbazole-decorated cyclophosphazene as a host with high triplet energy to realize efficient delayed-fluorescence OLEDs. Materials Horizons. 2014;**1**:264-269

[34] Zhang QS, Li B, Huang SP, Nomura H, Tanaka1 H, Adachi C. Efficient blue organic light-emitting diodes employing thermally activated delayed fluorescence. Nature Photonics. 2014;**8**:326-332

[35] Wang H, Meng LQ, Shen XX, Wei XF, Zheng XL, Lv XP, Yi YP, Wang Y, Wang PF. Light-emitting diodes: Highly efficient orange and red phosphorescent organic light-emitting diodes with low roll-off of efficiency using a novel thermally activated delayed fluorescence material as host. Advanced Materials. 2015;**27**:4041-4047

[36] Kim BS, Lee JY. Engineering of mixed host for high external quantum efficiency above 25% in green thermally activated delayed fluorescence device. Advanced Functional Materials. 2015;**24**:3970-3977

[37] Rajamalli P, Senthilkumar N, Gandeepan P, Huang PY, Huang MJ, Yang CY, Chiu MJ, Chu LK, Lin HW, Cheng CH. A new molecular design based on thermally activated delayed fluorescence for highly efficient organic light emitting diodes. Journal of the American Chemical Society. 2015;**138**:628-634

[38] Kim GH, Lampande R, Im JB, Lee JM, Lee JY, Kwon JH. Controlling the exciton lifetime of blue thermally activated delayed fluorescence emitters using a heteroatom-containing pyridoindole donor moiety. Materials Horizons. 2017;**4**:619-624

[39] Yang ZY, Mao Z, Xie ZL, Zhang Y, Liu SW, Zhao J, Xu JR, Chi ZG, Aldred MP. Recent advances in organic thermally activated delayed fluorescence materials. Chemical Society Reviews. 2017;**46**:915-1016

[40] Tao Y, Yuan K, Chen T, Xu P, Li H, Chen R, Zheng C, Zhang L, Huang W. Thermally activated delayed fluorescence materials towards the breakthrough of organoelectronics. Advanced Materials. 2014;**26**:7931-7958

[41] Masui K, Nakanotani H, Adachi C. Analysis of exciton annihilation in high-efficiency sky-blue organic light-emitting diodes with thermally activated delayed fluorescence. Organic Electronics. 2013;**14**:2721-2726

[42] Zhang D, Duan L, Li C, Li Y, Li H, Zhang D, Qiu Y. High-efficiency fluorescent organic light-emitting devices using sensitizing hosts with a small singlet-triplet exchange energy. Advanced Materials. 2014;**26**:5050-5055

[43] Zhao B, Zhang TY, Li WL, Su ZS, Chu B, Yan XW, Jin FM, Gao Y, Wu H. Organic electronics highly efficient and color stable single-emitting-layer fluorescent WOLEDs with delayed fluorescent host. Organic Electronics. 2015;**23**:208-212

[44] Zhang L, Li XL, Luo D, Xiao P, Xiao W, Song Y, Ang Q, Liu B. Strategies to achieve high-performance white organic light-emitting diodes. Materials. 2017;**10**:1378

[45] Kim BS, Yook KS, Lee JY. Above 20% external quantum efficiency in novel hybrid white organic light-emitting diodes having green thermally activated delayed fluorescent emitter. Scientific Reports. 2014;**4**:6019

[46] Nishide JI, Nakanotani H, Hiraga Y, Adachi C. High-efficiency white organic light-emitting diodes using thermally activated delayed fluorescence. Applied Physics Letters. 2014;**104**:233304

[47] Li XL, Xie GZ, Liu M, Chen DC, Cai XY, Peng JB, Cao Y, Su SJ. High-efficiency WOLEDs with high color-rendering index based on a chromaticity-adjustable yellow thermally activated delayed fluorescence emitter. Advanced Materials. 2016;**28**:4614-4619

[48] Sun YR, Giebink NC, Kanno H, Ma BW, Thompson ME, Forrest SR. Management of singlet and triplet excitons for efficient white organic light-emitting devices. Nature. 2006;**440**:908-912

[49] Schwartz G, Reineke S, Rosenow TC, Walzer K, Leo K. Triplet harvesting in hybrid white organic light-emitting diodes. Advanced Functional Materials. 2009;**19**:1319-1333

[50] Liu BQ, Nie H, Zhou XB, Hu SB, Luo DX, Gao DY, Zou JH, Xu M, Wang L, Zhao ZJ, Qin AJ, Peng JB, Ning HL, Cao Y, Tang BZ. Manipulation of charge and exciton distribution based on blue aggregation-induced emission fluorophors: A novel concept to achieve high-performance hybrid white organic light-emitting diodes. Advanced Functional Materials. 2016;**26**:776-783

[51] Sun N, Wang Q, Zhao YB, Chen YH, Yang DZ, Zhao FC, Chen JS, Ma DG. High-performance hybrid white organic light-emitting devices without interlayer between fluorescent and phosphorescent emissive regions. Advanced Materials. 2014;**26**:1617-1621

[52] Schwartz G, Pfeiffer M, Reineke S, Walzer K, Leo K. Harvesting triplet excitons from fluorescent blue emitters in white organic light-emitting diodes. Advanced Materials. 2007;**19**:3672-3676

[53] Ye J, Zheng CJ, Ou XM, Zhang XH, Fung MK, Lee CS. Management of singlet and triplet excitons in a single emission layer: A simple approach for a high-efficiency fluorescence/phosphorescence hybrid white organic light-emitting device. Advanced Materials. 2012;**24**:3410-3414

[54] Liu BQ, Wang L, Gao DY, Zou JH, Ning HL, Peng JB, Cao Y. Extremely high-efficiency and ultrasimplified hybrid white organic light-emitting diodes exploiting double multifunctional blue emitting layers. Light: Science & Applications. 2016;**5**:e16137

[55] Baldo MA, O'Brien DF, Thompson ME, Forrest SR. Excitonic singlet-triplet ratio in a semiconducting organic thin film. Physical Review B. 1999;**60**:14422-14428

[56] Baldo MA, O'brien DF, You Y, Shoustikov A, Sibley S, Thompson ME, Forrest SR. Highly efficient phosphorescent emission from organic electroluminescent devices. Nature. 1998;**395**:151-154

[57] Zhang DD, Cai MH, Zhang YG, Zhang DQ, Duan L. Sterically shielded blue thermally activated delayed fluorescence emitters with improved efficiency and stability. Materials Horizons. 2016;**3**:145-151

[58] Higuchi T, Nakanotani H, Adachi C. High-efficiency white organic light-emitting diodes based on a blue thermally activated delayed fluorescent emitter combined with green and red fluorescent emitters. Advanced Materials. 2015;**27**:2019-2023

[59] Zhang DD, Duan L, Li YL, Zhang DQ, Qiu Y. Highly efficient and color-stable hybrid warm white organic light-emitting diodes using a blue material with thermally activated delayed fluorescence. Journal of Materials Chemistry C. 2014;**2**:8191-8197

[60] Zhang DD, Duan L, Zhang YG, Cai MH, Zhang DQ, Qiu Y. Highly efficient hybrid warm white organic light-emitting diodes using a blue thermally activated delayed fluorescence emitter: Exploiting the external heavy-atom effect. Light: Science & Applications. 2015;**4**:e232

[61] Wu ZB, Luo JJ, Sun N, Zhu LP, Sun HD, Yu L, Yang DZ, Qiao XF, Chen JS, Yang CL, Ma DG. High performance hybrid white organic light-emitting diodes with superior efficiency/color rendering index/color stability and low efficiency roll-off based on a blue thermally activated delayed fluorescent emitter. Advanced Functional Materials. 2016;**26**:3306-3313

[62] Luo DX, Yang YB, Huang L, Liu BQ, Zhao Y. High-performance hybrid white organic light-emitting diodes exploiting blue thermally activated delayed fluorescent dyes. Dyes and Pigments. 2017;**147**:83-89

[63] Yoshihiro O. Color rendering and luminous efficacy of white LED spectra. Proceedings of SPIE. 2004;**5530**:88-98

[64] Duan L, Zhang DQ, Wu KW, Huang XQ, Wang LD, Qiu Y. Controlling the recombination zone of white organic light-emitting diodes with extremely long lifetimes. Advanced Functional Materials. 2011;**21**:3540-3545

[65] Liu BQ, Wang L, Xu M, Tao H, Zou JH, Gao DY, Lan LF, Ning HL, Peng JB, Cao Y. Efficient hybrid white organic light-emitting diodes with extremely long lifetime: The effect of n-type interlayer. Scientific Reports. 2014;**4**:7198

[66] Wang Z, Li X, Ma Z, Cai X, Cai C, Su S. Exciton-adjustable interlayers for high efficiency, low efficiency roll-off, and lifetime improved warm white organic light-emitting diodes (WOLEDs) based on a delayed fluorescence assistant host. Advanced Functional Materials. 2018;**28**:1706922

[67] Chen J, Zhao F, Ma D. Hybrid white OLEDs with fluorophors and phosphors. Materials Today. 2014;**17**:175-183

[68] Chen S, Qu Q, Kong M, Zhao X, Yu Z, Jia P, Huang W. On the origin of the shift in color in white organic light-emitting diodes. Journal of Materials Chemistry C. 2013;**1**:3508-3524

[69] Zhao F, Zhang Z, Liu Y, Dai Y, Chen J, Ma D. A hybrid white organic light-emitting diode with stable color and reduced efficiency roll-off by using a bipolar charge carrier switch. Organic Electronics. 2012;**13**:1049-1055

[70] Zhao F, Chen Y, Wang Q, Ma D. Studies of fluorescence/phosphorescence hybrid white organic light-emitting diodes. Scientia Sinica Chimica. 2013;**43**:398

[71] Guo JJ, Li XL, Nie H, Luo WW, Gan SF, Hu SM, Hu RR, Qin AJ, Zhao ZJ, Su SJ, Tang BZ. Achieving high-performance nondoped OLEDs with extremely small efficiency roll-off by combining aggregation-induced emission and thermally activated delayed fluorescence. Advanced Functional Materials. 2017;**27**:1606458

[72] Sun N, Wang Q, Zhao Y, Yang D, Zhao F, Chen J, Ma D. A hybrid white organic light-emitting diode with above 20% external quantum efficiency and extremely low efficiency roll-off. Journal of Materials Chemistry C. 2014;**2**:7494-7504

[73] Sun N, Zhao Y, Zhao F, Chen Y, Yang D, Chen J, Ma D. A white organic light-emitting diode with ultra-high color rendering index, high efficiency, and extremely low efficiency roll-off. Applied Physics Letters. 2014;**105**:013303

[74] Yu L, Wu Z, Xie G, Zeng W, Ma D, Yang C. Molecular design to regulate the photophysical properties of multifunctional TADF emitters towards high-performance TADF-based OLEDs with EQEs up to 22.4% and small efficiency roll-offs. Chemical Science. 2018;**9**:1385-1391. DOI: 10.1039/C7SC04669C

[75] Zhang D, Cao X, Wu Q, Zhang M, Sun N, Zhang X, Tao Y. Purely organic materials for extremely simple all-TADF white OLEDs: A new carbazole/oxadiazole hybrid material as a dual-role non-doped light blue emitter and highly efficient orange host. In: Journal of Materials Chemistry C. 2018. DOI: 10.1039/C7TC04969B

[76] Yu L, Wu Z, Xie G, Zhong C, Zhu Z, Ma D, Yang C. An efficient exciton harvest route for high-performance oleds based on aggregation-induced delayed fluorescence. Chemical Communications (Cambridge, England). 2018;**54**:1379-1382. DOI: 10.1039/c7cc09925h

Chapter 4

The Impact of the Use of Large Non-Linear Lighting Loads in Low-Voltage Networks

Natalio Milardovich, Leandro Prevosto,
Miguel A. Lara and Diego Milardovich

Additional information is available at the end of the chapter

http://dx.doi.org/10.5772/intechopen.76752

Abstract

The principal numerical and experimental results obtained by the authors on the harmonic power losses in low-voltage networks in the lighting area have been summarized in this review. Light-emitting diodes (LEDs) and compact fluorescent lamp (CFL) loads were considered. Four-core cables and four single-core cable arrangements were examined. The cables were modeled by using electromagnetic finite element analysis software. It was found that the cross section of the neutral conductor plays an important role in the derating of the cable ampacity due to the presence of a high level of triplen harmonics in the distorted current. In order to reduce the third-order harmonic currents in the neutral conductor, an experimental investigation of diversity factors for LED in combination with CFL and LED lamps was also performed. Attention was paid to the reduction of the third-order harmonic current, which is mainly responsible for the strong increase in power losses in the neutral conductor of low-voltage installations. The convenience of having LED lamps designed to operate as two-phase loads is suggested for certain applications.

Keywords: LED, CFL, non-linear lighting loads, harmonic currents, energy losses, low-voltage networks

1. Introduction

Today, non-linear devices constitute a bigger part of the electrical load in industrial and commercial power systems. Non-linear devices generate harmonics in line currents, resulting in a large number of problems for electrical equipment, such as capacitors, circuit breakers, electronic equipment, metering, conductors and telephones [1–3]. The presence of harmonic currents in electric systems has increased in recent times due to several factors (increased use

of solid-state energy conversion devices, industrial variable speed drive systems and cutting and welding equipment). Significant sources of harmonic currents in power systems also include electric devices such as compact fluorescent lamps (CFLs), power transformers operating near saturation and computer system installations [4–6].

Nowadays, with the technological advancement in semiconductors, light-emitting diode (LED) lamps are becoming a promising lighting technology due to its superior energy efficiency, longer lifetime and a better visual performance compared to most of the conventional light sources [7–9]. Due to these unique features, CFLs are now being replaced by LED, seeking a reduction in lighting costs and a lower impact on environment. In general lighting applications, a compact ac/dc (alternating current/direct current) converter should be used to supply dc current to LEDs, which introduces non-linearity to the system [10–12]. As non-linear loads, LEDs might produce highly distorted currents. Although the input power of a single LED is quite low, an incoming widespread use of them in lighting could create significant additional harmonic losses in the existing low-voltage lines [13]. Since several national standards allow for the neutral conductor reducing sizing with respect to the phase conductors, many of these existing low-voltage installations have the cross section of the neutral conductor approximately equal to half of the phase conductors.

A large number of works were conducted on LEDs as an energy-efficient lamp, but most of them have been devoted to the internal driver circuit design [10–12, 14–17]. Several other works have concentrated on the light distribution and visual performance of LED lamps [18–20]. A few contributions focused on harmonic emissions of LED lamps [12, 21–24].

When significant harmonic currents are present in low-voltage supply systems, additional Joule losses occur in the phase or line conductors as well as the neutral conductor. Significant harmonic currents may be present in secondary circuits of three-phase wye-connected transformers and single-phase transformers. Zero sequence harmonic currents flow in the phase conductors and are added in the neutral conductor, thus resulting in even higher harmonic current flow in the neutral conductor [25, 26]. Thus, the harmonic current flow in the neutral must be considered in the design of the supply system. The presence of harmonic currents in the supply conductors affects the ampacity of the supply system because of the additional ohmic losses [13, 26–28]. The determination of ohmic losses is complicated by the fact that the resistance of the cables is frequency dependent. Specifically, the resistance is increased with frequency because of the skin effect and proximity effect in the conductors and proximity effect from metallic conduit (if present) [26, 29]. The effects of harmonic currents in the neutral conductors can be evaluated with the same methods as for the phase or line conductors. However, the harmonic current magnitudes may be different in the neutral conductors due to non-cancelation of zero sequence harmonic currents and the cancelation of the positive and negative sequence harmonic currents. Thus, the neutral conductor becomes an additional heat-generating conductor and must be considered in the ampacity calculation for three-phase wye-connected and single-phase circuits [26–28]. Besides the knowledge of the increased losses due to harmonic currents, it is significant also for the economic evaluation of measures that attenuate harmonic currents. Such measures can be, for instance, passive or active harmonic filters [30, 31] or controlling the current unbalance in three-phase distribution systems by node reconfiguration [32].

A research on the diversity factor for combinations of LED lamps with powers in the range 3 to 8 W was presented in [33]. It was found that the diversity factor becomes smaller if a large number of lamps are combined. However, such a reduction was more significant for high-order harmonic currents. In particular, a diversity factor close to one for the third-order harmonic was found for the combinations studied. In [34] an investigation was presented on the diversity factor for combinations of LED and FCL lamps. The measurements showed a considerable reduction of the diversity factor for higher harmonic currents, but, on the other hand, the low-order harmonics did not show a significant decrease.

The principal numerical and experimental results obtained by the authors on the harmonic power losses in low-voltage networks feeding large LED and CFL loads have been summarized in this review. Attention was paid to the reduction of low-order harmonic currents, especially the third one, which is mainly responsible for the strong increase in power losses in the neutral conductor of low-voltage installations [13]. The convenience of having LED lamps designed to operate as two-phase loads is suggested for certain applications of significant power demand.

2. Harmonic losses in low-voltage networks

2.1. Harmonic emission of LED and CFL

Figure 1 shows the current in one phase and in the neutral conductor of a four-core cable that feeds a balanced load of three identical LEDs (one per phase). Specifically, **Figure 1** was obtained by testing the Philips 8 W LED. It can be seen that the LED current is highly distorted with respect to a sinusoidal waveform and that the fundamental frequency of the current in the neutral conductor is 150 Hz (i.e. the frequency of the third harmonic). Because the third-order harmonic currents (and their multiples) are zero sequence, they are added to the neutral

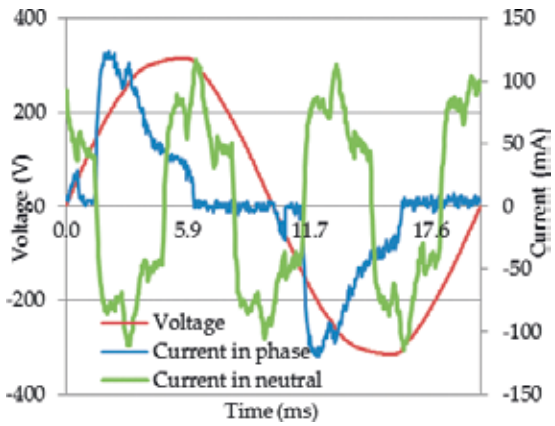

Figure 1. Voltage and current waveforms in one phase and current in the neutral conductor [35].

conductor. All experiments were done with an almost sinusoidal voltage waveform. The total harmonic distortion (THD) of the phase voltage waveform was relatively low (< 3%).

A frequency domain analysis of the current harmonics ($I_{pu}(h)$) produced by several commercially available LEDs is presented in **Figure 2**. In this figure, $I_{pu}(h)$ was expressed in per unit of the fundamental current harmonic ($h = 1$ corresponding to a harmonic frequency of $f = 50$ Hz, with h being the order of the harmonic).

The experimental data can be approximately described by the power law:

$$\frac{I(h)}{I(1)} = h^m, \tag{1}$$

where $m = -1.2 \pm 0.2$. Eq. (1) (which is indicated by a solid line in **Figure 2**) defines the harmonic signature of the examined LED lamps. It is observed in **Figure 2** that the amplitude of the harmonic currents decreases almost inversely with the order of the harmonic, thus indicating that the third-order one is usually the most significant one. Note that the data corresponded to LEDs from 3 to 120 W. FCLs also tend to present considerable amplitudes in their third-order harmonics [34]. **Figure 3** shows the amplitude of the third harmonic current (expressed in per unit of the fundamental harmonic) of several commercially available LEDs and CFLs, with powers varying between 3 and 23 W. The red line (representing a constant value of 86%) indicates one of the criteria established by IEC 61000–3-2 [36] for the harmonic emission limits for lamps having an active input power < 25 W (i.e. that the third harmonic current should not exceed 86% of the fundamental one).

As it can be seen in **Figure 3**, the lamps tested meet the quoted emission limit imposed by IEC, except for one of them (LED 9 W Sica), which is slightly above it.

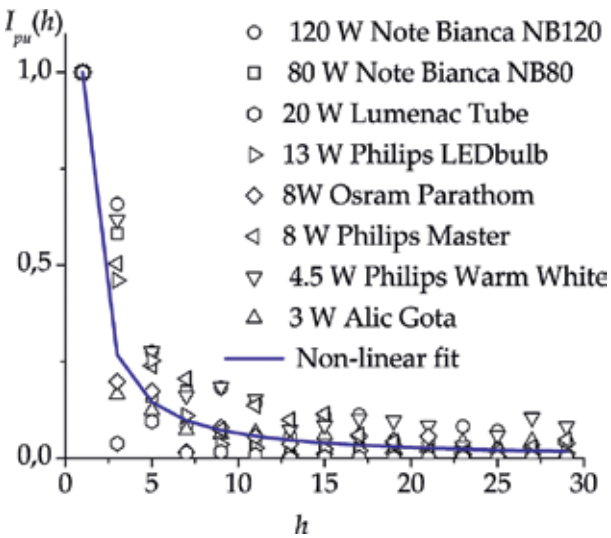

Figure 2. Frequency domain analysis of the current harmonics on several commercially available LEDs. The blue line represents the power law given by Eq. (1) [13].

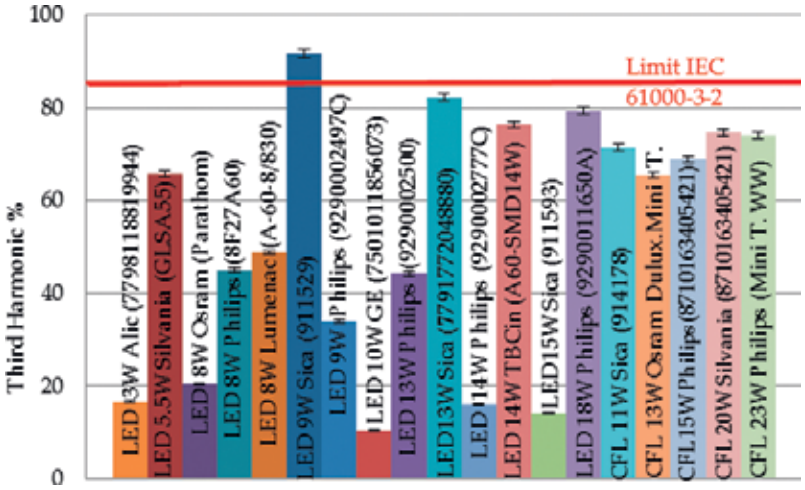

Figure 3. Third-order harmonic current amplitude for the investigated lamps [35].

A power quality analyzer (Fluke 435-II) was used in the measurements presented here.

2.2. Numerical simulation of the harmonic losses in low-voltage networks

Two different types of cables were examined. The first type was an arrangement of four single-core cables in contact with each other, as they are specified by IEC 60502–1 [37]. The schematic of the used cable arrangement is shown in **Figure 4**, while its geometric dimensions are summarized in **Table 1**.

As the conductors in all cables were assumed solid in the modeling, the conductor dimensions showed in **Table 1** are slightly smaller than the actual dimensions. This assumption leads to results that are on the conservative side. Cases where the conductors were copper and the cross section of the neutral conductor was approximately equal to half of phase conductors were modeled.

The second type corresponded to four-core cables as they were specified by CENELEC Standard HD603 [38]. In this case, a large cross-sectional sector-shaped cable, namely, $3 \times 240 + 120$ mm^2, was examined.

In a conductor where the conductivity is sufficiently high, the displacement current density can be neglected, and the conduction current density is given by the product of the electric field and the electrical conductivity (ohm's law). With these simplifications, the Maxwell's equations are

$$\nabla \times \left(\frac{\overline{B}}{\mu} \right) = \sigma \overline{E}, \tag{2}$$

$$\nabla \times \overline{E} = -\frac{\partial \overline{B}}{\partial t}, \tag{3}$$

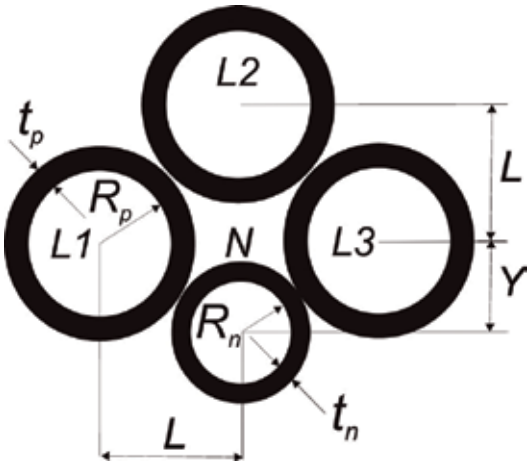

Figure 4. Layout of the examined single-core arrangement (taken from [13]).

	Nominal cable cross section [mm^2]			
Dimensions [mm]	3 × 35 + 16	3 × 70 + 35	3 × 120 + 70	3 × 240 + 120
Phase conductor radius [R_p]	3.3	4.7	6.2	8.8
Neutral conductor radius [R_n]	2.3	3.3	4.7	6.2
Thickness of phase conductor insulation [t_p]	2.6	2.8	3.1	4.0
Thickness of neutral conductor insulation [t_n]	2.4	2.6	2.8	3.1
Distance [L]	8.4	10.6	13.1	18.0
Distance [Y]	6.5	8.2	10.5	12.7

Table 1. Dimensions of the modeled cable arrangement.

where $\overline{B}$ is the magnetic field, μ is the magnetic permeability, σ is the conductor electrical conductivity and $\overline{E}$ is the electric field. Introducing the magnetic vector potential $\overline{A}$ ($\overline{B} \equiv \nabla \times \overline{A}$) in Eq. (3), $\overline{E}$ can be expressed as

$$\overline{E} = -\nabla V - \frac{\partial \overline{A}}{\partial t}, \tag{4}$$

(where V is the electrostatic potential), and Eq. (2) becomes

$$\nabla \times \left[\frac{\nabla \times \overline{A}}{\mu}\right] = -\sigma \nabla V - \sigma \frac{\partial \overline{A}}{\partial t}. \tag{5}$$

The electromagnetic software [39] solved the diffusion equation (Eq. (5)) to obtain the spatial distribution of the total current density ($\overline{J}$) over each conductor's surface (S), having as input the measurable current in the conductor:

$$\begin{aligned} I &= \int \bar{J} \cdot d\bar{S} = \int \left(\bar{J}_0 + \bar{J}_{eddy}\right) \cdot d\bar{S} \\ &= \frac{V}{R_{dc}} - \sigma \int \frac{\partial \bar{A}}{\partial t} \cdot d\bar{S}, \end{aligned} \tag{6}$$

where I is the total current and R_{dc} is the dc conductor resistance ($\bar{J}_0$ is the spatial average current density generated by potential electric fields, while $\bar{J}_{eddy}$ is the (eddy) current density induced by rotational fields). Eq. (6) assumed a uniform electrical conductivity over the conductor surface. This is justified because simple estimates showed that the temperature variations over the conductor's surface

$$\Delta T \approx \frac{\Lambda^2}{\kappa} \sigma E^2, \tag{7}$$

(where κ is the conductor thermal conductivity and $\Lambda = R/2.4$ and R is the conductor radius) due to the non-uniform distribution of the Joule heat caused by the skin and proximity effects are very small because of the large value of the thermal conductivity.

At each harmonic frequency, the software calculates the losses per unit length in each conductor using the integral:

$$P(h) = \frac{1}{\sigma} \int J(h)^2 \, dS, \tag{8}$$

where $P(h)$ is the harmonic losses per unit conductor length and $J(h)$ is the current density corresponding to the harmonic of order h.

The cables were modeled in two dimensions assuming that at each harmonic frequency, balanced, three-phase and sinusoidal currents flow through them. The three-phase conductors were assumed carrying the following currents:

$$I_{L1} = I_p \cos\left(2\pi h f t + \phi_h\right), \tag{9}$$

$$I_{L2} = I_p \cos\left(2\pi h f t - h \frac{2}{3}\pi + \phi_h\right), \tag{10}$$

$$I_{L3} = I_p \cos\left(2\pi h f t + h \frac{2}{3}\pi + \phi_h\right), \tag{11}$$

where I_p is the current peak value, φ_h is the angle phase of the harmonic order h and $L1$, $L2$ and $L3$ are the three phases.

For non-triplen harmonic ($h \neq 3N$, with $N = 1, 2, 3, \ldots$), the neutral conductor only carries the eddy currents calculated by the software. Notice that in this case, $h = 3N + 1$ represents the direct sequence harmonics, while $h = 3N - 1$ represents inverse sequence harmonics. For triplen harmonics the current in the neutral conductor was assumed as

$$I_N = 3I_p \cos(2\pi hft + \pi). \quad (12)$$

In order to obtain an accurate distribution of the current density over the conductor sections, it was checked that the size of the local numerical mesh was less than half the characteristic skin penetration length for each harmonic order.

The study domain for the cases of sector-shaped and four single-core cables, showing the non-uniform numerical grid (with up to about 4000 mesh cells), is presented in **Figure 5**. At the boundary of the domain (at a radius up to ten times the cable size), it was assumed that $\overline{A} = 0$ because the magnetic field vanishes at a large distance (as compared to the cable size) from the cable.

The simulation results were obtained for $\mu = 4\ \pi \times 10^{-7}$ H/m (non-magnetic material was considered). The copper electrical conductivity at 293 K was taken as $\sigma = 5.8 \times 10^7\ \Omega^{-1}\ m^{-1}$ according to IEC 60028 [40]. The σ value was correspondingly corrected for other cable operating temperatures.

Figure 6 illustrates the spatial distribution of the root-mean-square (rms) value of the total current density over the conductors of cables of large sections submitted to harmonic currents of different frequencies. **Figure 6(a)** corresponds to a $3 \times 240 + 120$ mm^2 sector-shaped cable submitted to a 15 A (peak value) fifth-order harmonic current, while **Figure 6(b)** corresponds to an arrangement of four single-core cables ($3 \times 70 + 35$ mm^2) submitted to a 30 A (peak value) third-order harmonic current. The magnetic field lines produced by the current are also shown in **Figure 6**. A noticeable reduction in the effective area of current circulation due to the skin and proximity effects is observed in **Figure 6(a)**, thus causing a considerable increase of the ac conductor resistance (*R*ac) as compared to the dc resistance, (*R*dc), which in turn results in high heat losses. In **Figure 6(b)** the neutral conductor is assumed to carry the algebraic sum of the phase currents.

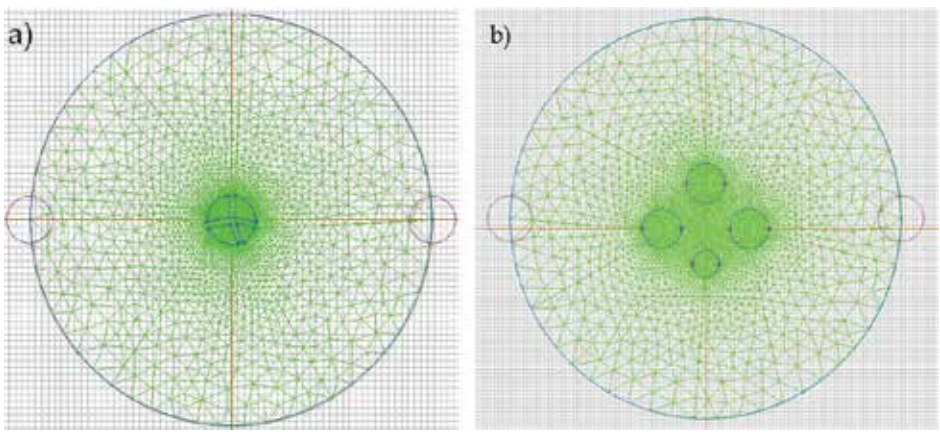

Figure 5. Non-uniform numerical grid generated by the software for the case of a four-core sector-shaped cable (a) and four single-core cables (b).

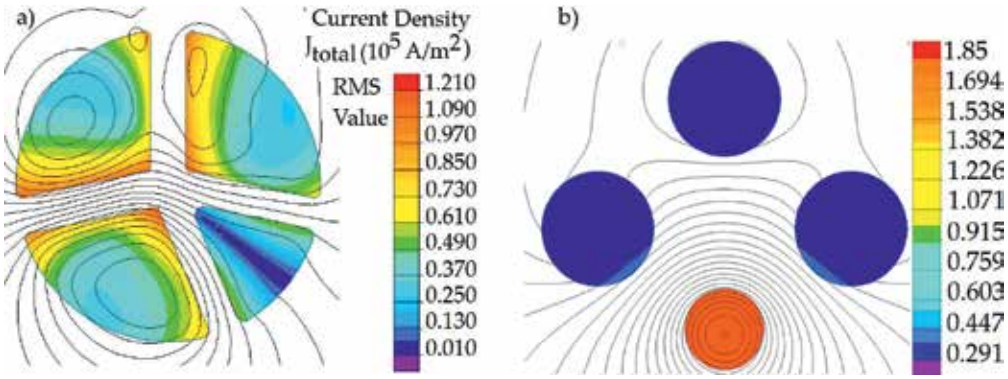

Figure 6. Spatial distribution of the rms current density for the fifth-order (h = 5) harmonic in a sector-shaped cable of $3 \times 240 + 120$ mm^2 (a) and for the third-order (h = 3) harmonic in four single-core cables of $3 \times 70 + 35$ mm^2 (b).

To calculate the R_{ac} conductor resistance, an ac steady-state harmonic analysis was employed. Only the odd harmonics, up to the 29th, were considered. A higher value of this upper limit did not have appreciable impact to the obtained results. Due to the geometry of the cables, the losses in the phase conductors are not identical. In fact, the losses in phase conductors $L1$ and $L3$ (**Figure 4**) are the same, but those in $L2$ are different. The losses per unit length in the three-phase conductors, when a symmetrical current of rms value $I_{rms}(h)$ and of frequency $f\,h$ flows through them, can be defined as $P_{L1}(h)$, $P_{L2}(h)$ and $P_{L3}(h)$, for L1, L2 and $L3$, respectively. The uneven heat generation inside the cable is a fact that also needs to be considered when calculating the derating of cable ampacity. According to [41], not only the average cable temperature but also the temperature at any point along the insulation of the cable should not exceed the maximum permissible one. Therefore, for derating of the cable ampacity, the maximum conductor losses should be considered and not their average. For non-triplen harmonic ($h \neq 3\ N$), the neutral conductor only carries the eddy currents calculated by the software, so the maximum cable losses can be represented by an effective conductor resistance per unit length $R_{eff}(h)$ for the harmonic order h, which was defined as

$$3P_{L\max}(h) \;+\; P_N(h) \;\equiv\; 3{I_{rms}}^2(h)\,R_{eff}(h)\ , \tag{13}$$

where

$$P_{L\,\max}(h) \;\equiv\; \max\{P_{L1}(h), P_{L2}(h), P_{L3}(h)\}. \tag{14}$$

When triplen harmonics are present, the neutral conductor picks up the current. An effective resistance that reflects the maximum losses of the phase conductors ($\tilde{R}_{eff}(h)$) and another resistance ($R_{ac\,N}(h)$) that reflects the losses of the neutral conductor were defined as

$$3P_{L\max}(h) \;\equiv\; 3{I_{rms}}^2(h)\,\tilde{R}_{eff}(h)\ , \tag{15}$$

$$P_N(h) \;\equiv\; {I_{rms\,N}}^2(h)\,R_{ac\,N}(h)\ , \tag{16}$$

where

$$I_{rms\,N}(h) \equiv 3\ I_{rms}(h), \tag{17}$$

is the neutral conductor current for the harmonic current of order h. The resistances $R_{eff}(h)$ and $\tilde{R}_{eff}(h)$ will be referred, from now on, as $R_{ac}(h)$. The ratio $R_{ac}(h)/R_{dc}$ for the phase and neutral conductors of the cables described in **Table 1** and for a $3 \times 240 + 120$ mm^2 four-core cable are shown in **Figures 7(a)** and **(b)**, respectively. As expected, the ratio $R_{ac}(h)/R_{dc}$ for the phase conductors increases with both frequency and conductor cross section due to skin and proximity effects. The curve is not smooth but presents spikes at triplen harmonics.

This is mainly due to the increased losses in conductors $L1$ and $L3$ when zero sequence currents flow in the phase conductors and thereby in the neutral conductors. The ratio $R_{ac}(h)/R_{dc}$ for the neutral conductor is shown only for triplen harmonics, because only when triplen harmonics are present the neutral conductor picks up the current (other than eddy currents). It is evident from **Figures 7(a)** and **(b)** that the ratio of the neutral conductor is much smaller than that of the respective phase conductors. This occurs because the zero sequence currents decrease the proximity effect significantly on the neutral conductor when its position, relative to the phase conductors, is as shown in **Figure 4**.

The simulation results corresponded to a conductor operating temperature of 343 K, which is the maximum conductor temperature for PVC-insulated cables according to IEC 60502–1 [12]. It was checked that large variations in this temperature value (in the range 283 to 343 K) only render slightly variations (less than 10%) in the conductor resistance ratio. The results of the employed electromagnetic model were validated by comparison to (a) the numerical model developed in [27] and (b) the formulae given in the standard IEC 60287–1-1 [42] for thee single-core cable arrangements. The differences in the calculated ratios $R_{ac}(h)/R_{dc}$ were in both cases less than 3% in the whole considered frequency range.

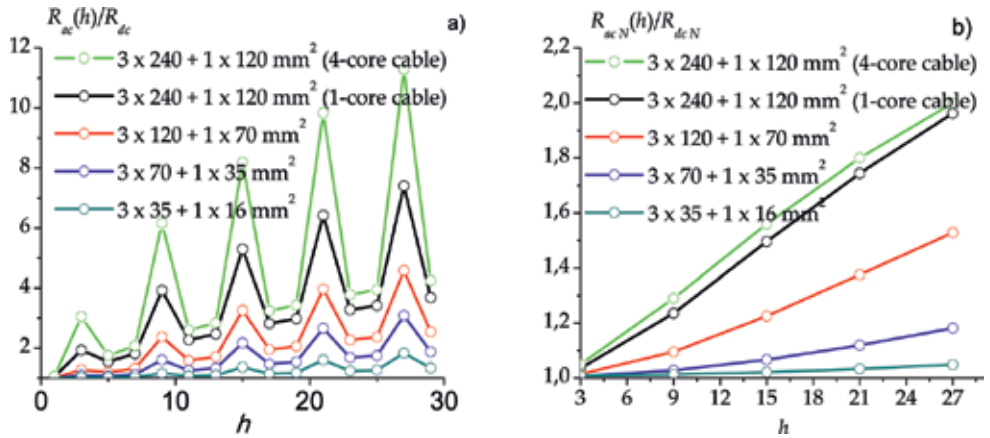

Figure 7. Variation with the harmonic order of the ratio $R_{ac}(h)/R_{dc}$ for various examined cables, (a) for the phase conductors and (b) for the neutral conductor.

The cable losses can be approximately calculated by the following formula:

$$P_{loss} = 3\sum_{h=1}^{29} {I_{rms}}^2(h)\, R_{ac}(h) + \sum_{h=3N}^{27} (3 I_{rms}(h))^2 R_{ac\,N}(h), \tag{18}$$

where the first term on the right-hand side represents the losses in the phase conductors and the second term is the losses in the neutral conductor. This second term is present only when triplen harmonics are considered (i.e. $h = 3, 9, 15, 21, 29$). The values of $R_{ac}(h)$ and $R_{ac\,N}(h)$ were shown in **Figures 7(a)** and **(b)**, respectively. It is important to compare the above calculated cable losses (Eq. (18)) with the losses produced in an identical cable but carrying an undistorted electric current of a rms value of $I_{rms}(1)$. To do this, the cable losses ratio defined as

$$\xi \equiv \frac{P_{loss}}{3\,{I_{rms}}^2(1)\, R_{ac}(1)}, \tag{19}$$

were calculated by using the harmonic signature given by Eq. (1) for the cables described in **Table 1** and for a $3 \times 240 + 120$ mm^2 four-core cable as was specified by CENELEC Standard HD603 [38]. The results obtained for the upper bound of m ($= -1.0$) are shown in **Table 2**. The assumption on the m value leads to results that are on the conservative side.

As it is observed in **Table 2**, for a four-core cable with a cross section of 3 x 240 + 120 mm^2, the power losses reach 2.5 times the value corresponding to an undistorted current of the same rms value of the first harmonic of the LED current. Even for cables with relatively small cross sections, such as $3 \times 35 + 16$ mm^2, this ratio reaches about 2.1. Furthermore, if the skin and proximity effects are neglected in the cable losses given by Eq. (18) (the conductor radius is small as compared to the characteristic skin penetration length and the distances of the nearby conductors are large as compared to the conductor radius) and thus ξ is not dependent on the cable cross section, the loss ratio still reaches 2.0 for $m = -1.0$. The increase in the losses is mainly due to the harmonic content of the distorted current.

As shown **Table 2**, large LED-like loads generate huge harmonic losses resulting in additional conductor heating. This heating will result in a higher-temperature rise of the cable which can exceed its rated temperature, thus requiring the derating of the cable ampacity.

Cable type	**Nominal cable cross section [mm^2]**	ξ
Arrangement of four single-core cables	$3 \times 35 + 16$	2.1
	$3 \times 70 + 35$	2.1
	$3 \times 120 + 70$	2.0
	$3 \times 240 + 120$	2.3
Four-core cable	$3 \times 240 + 120$	2.5

Table 2. Calculated cable loss ratio ξ of various examined PVC-insulated low-voltage cables feeding LED-type loads.

3. Reduction of the harmonic losses in low-voltage networks

In order to reduce the third-order harmonic currents by properly combining lamps that have an important phase difference in their corresponding harmonic currents (rather than combining lamps in a random way), the phase angle ($\varphi 3$) of the third-order harmonic currents was first measured (with respect to the fundamental harmonic voltage angle of the phase 1) for the CFL and LED lamps. The results are given in **Table 3**.

Data in **Table 3** correspond to time-averaged values over an interval of 5 minutes with a sampling rate of 1 S/s. The data were taken applying nominal voltage to the lamps once they acquired their stable working temperature. A power quality analyzer (Fluke 435-II) was used in the measurements. The experimental uncertainty (mainly due to statistical fluctuations) was within $\pm 5^{\circ}$. In order to match the measuring range of the instrument used to the relatively small currents of the lamp combinations, the currents were measured by using low-inductance (around 0.1 mH) coils. It was verified during the measurements that the inductance introduced in the circuit by the coils does not appreciably affect the results. The uncertainty ($\pm$ 2%) in the current measurement due to the position sensitivity of the used flexible current probe was accounted for. The information provided by the instrument was processed through the PowerLog 4.3.1 software.

During the measurements, the phase angles of the third-order harmonic currents were remarkably stable as shown in **Figure 8**. The corresponding experimental uncertainty (mainly due to statistical fluctuations) was within $\pm 5^{\circ}$.

In order to achieve a considerable attenuation effect of the third-order harmonic currents for a given combination of lamps, they should not only fulfil with the condition that its third-order harmonic be strongly out of phase (as is the case of LED Alic 3 W and LED Philips 8 W), but also the amplitudes of each harmonic current should be similar, i.e. the ratio between the amplitudes of the third-order harmonic current of each lamp should be approximately united. **Table 4** shows the results of the ratio between the amplitudes of the third-order harmonic

Lamp type	φ_3 (degrees)	Lamp type	φ_3 (degrees)
LED Alic 3 W	95	LED Philips 14 W	−33
LED Sylvania 5.5 W	−112	LED TBC in 14 W	−126
LED Osram 8 W	−126	LED Sica 15 W	−130
LED Philips 8 W	−77	LED Philips 18 W	−125
LED Lumenac 8 W	−9	CFL Sica 11 W	−114
LED Sica 9 W	−153	CFL Osram 13 W	−111
LED Philips 9 W	−9	CFL Philips 15 W	−111
LED GE 10 W	−49	CFL Sylvania 20 W	−119
LED Philips 13 W	2	CFL Philips 23 W	−108
LED Sica 13 W	−129		

Table 3. Angle of the third-order harmonic current of the lamps used [35].

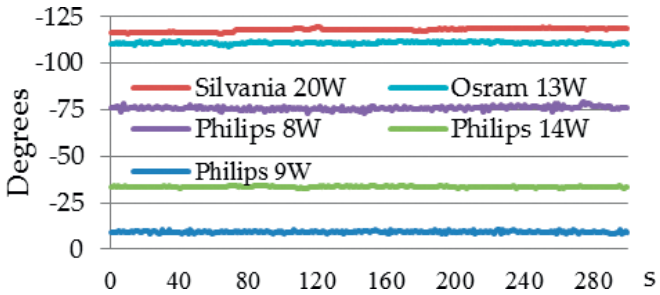

Figure 8. Stability of the phase angle of the third-order harmonic current for several lamps used [35].

currents for several selected combination types LED-LED and LED-CFL of the lamps used in this work. The corresponding experimental uncertainty (mainly due to statistical fluctuations) was within ±7%.

To find the level of attenuation of the third-order harmonic currents as a consequence of the combinations of lamps, it is useful to define the diversity factor for the harmonic current, as the ratio between the vector sum (as measured) and the arithmetical sum (as calculated) of the third-order harmonic currents:

$$DF_3 \equiv \frac{|\text{vector sum of current harmonic}|}{\text{arithmetic sum of current harmonic}}. \tag{20}$$

Note that a value of $DF_3 \approx 1$ indicates an inadequate combination of lamps, which generates a minimum attenuation of the third-order harmonic currents, whereas $DF_3 << 1$ implies an optimum combination, with a maximum attenuation of this harmonic current. **Figure 9** shows the dependence of measured DF_3 for selected lamp combinations on the difference between the corresponding phase angles of the third-order harmonic currents. The solid curves represent the diversity factor calculated for limit values of the ratio between the amplitudes of the third-order harmonic current of each lamp of the combination (values calculated for a ratio = 1 are indicated with a blue line while for a ratio = 7 with a red line). Note that these values are close to the minimum and maximum ratios obtained in the different combinations proposed, as it was indicated in **Table 4**.

It is seen in **Figure 9** that a number of combinations of LED and CFL lamps lead to a considerably decrease in the content of the third-order harmonic current. As expected, the maximum attenuation of the third harmonic amplitude is achieved with harmonic ratios close to 1 and for harmonic phase angle differences close to 180°. These results are different from those reported by other studies [33, 34] where lower-order harmonics did not exhibit a very large reduction in amplitude. However, it should be noted that in [33, 34] random combinations of lamps were used.

Note that the results presented in **Figure 9** were obtained combining two lamps; however, the same results could be obtained between two arbitrary sets of lamps, provided that each set is formed by the same number of elements. Currently, CFLs are being replaced by LEDs gradually, and in several lighting installations, the two technologies coexist. From the point of view of the reduction of the third harmonic, the combinations of lamps of different technologies are

usually convenient. For the lamps evaluated, the change of technology (CFL to LED) not only improves the level of illumination and reduces the content of third harmonic but also decreases the active power demanded by the installation, reducing also the environmental impact.

In order to better show the contribution of the proposed solution, the measured spectrum of the harmonic currents (expressed in per unit of the fundamental harmonic current), both in

Lamp combination	Ratio between the amplitudes (rms) of the third-order harmonic current of each lamp of the combination
CFL Philips 23 W-LED Philips 18 W	1.1
CFL Philips 15 W-LED Philips 13 W	1.8
LED Lumenac 8 W-LED Sica 9 W	1.9
LED Philips 13 W-LED Sica 13 W	1.9
LED Osram 8 W-LED Lumenac 8 W	2.3
CFL Sica 11 W-LED Philips 9 W	2.6
LED Sica 9 W-LED Philips 9 W	2.8
CFL Sica 11 W-LED Osram 8 W	4.6
CFL Philips 15 W-LED Philips 14 W	4.7
LED Philips 14 W-LED TBC in 14 W 114 W	4.7
CFL Sica 11 W-LED GE 10 W	6.7
CFL Sylvania 20 W-LED Philips 14 W	6.8

Table 4. Tested combinations of lamps [35].

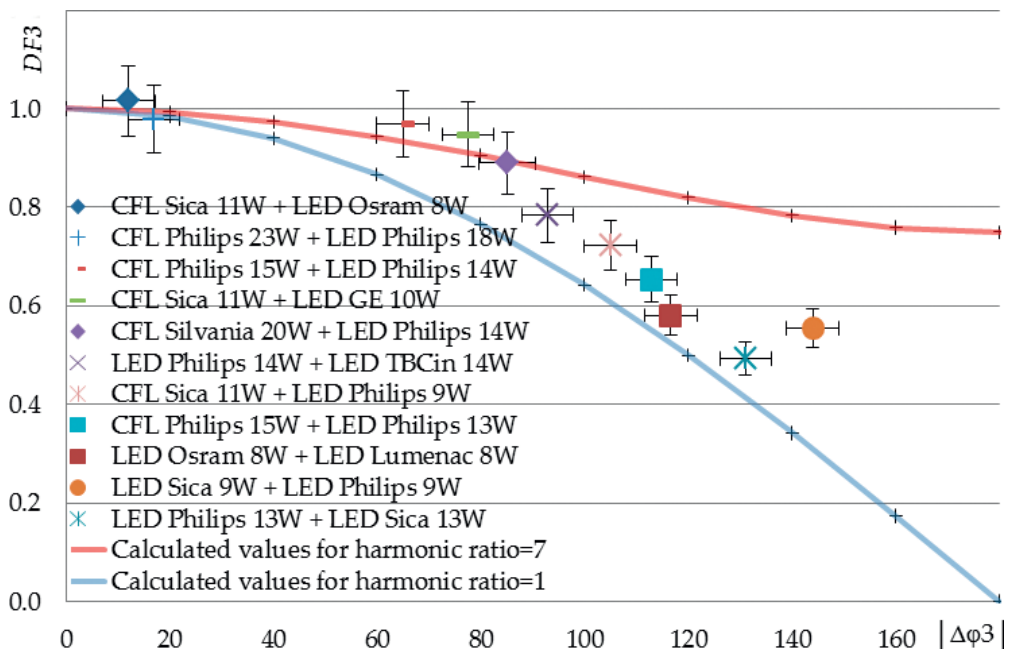

Figure 9. Attenuation of the third harmonic by combination of lamps [35].

one phase and in the neutral conductor of a four-core cable, feeding balanced single-phase loads formed by selected LED-LED combination is shown in **Figures 10(a)** and **(b)**, respectively. The corresponding spectrums for the individual lamps are also shown. Harmonic currents up to the order h = 19 were measured. In addition, the rms value of the total current in both conductors is presented in **Figures 10(a)** and **(b)**.

It is seen in **Figure 10** that the selected LED combination leads to a significant decrease in the third-order harmonic content of the line current. Notice also that the RMS value of the total current of the combination is considerable lower than the corresponding value of the individual lamp having the higher harmonic content of the combination (LED Sica 9 W), being similar to that of the LED Lumenac 8 W.

As it can be seen in **Figure 10**, the RMS value of the total current of the combination is strongly reduced with respect to that of the LED Sica 9 W, mostly due to a decrease in the content of the third-order harmonic current, although some reduction is also observed for the high-order harmonics. It is important to note that the current of the LED Sica 9 W has a strong component of the third-order harmonic (exceeding the emission limit imposed by IEC as quoted in Section 1) and also of high-order harmonics (h = 9 and 15). As the overall harmonic power losses in the neutral conductor depend on the RMS value of the total current, a marked reduction in the harmonic losses with respect to that of the LED Sica 9 W (and even with respect to the LED Lumenac 8 W) is expected for the tested lamp combination.

Notice also the negligible small value of the first-order harmonic current in the neutral conductor due to the balanced loading of the cable. The small residuals observed are due in part to small asymmetries attributable to the constructive differences between the lamps tested.

The cable harmonic power losses can be approximately calculated by Eq. (18). To quantify the reduction in the harmonic power losses due to the lamp combination, it is useful to compare

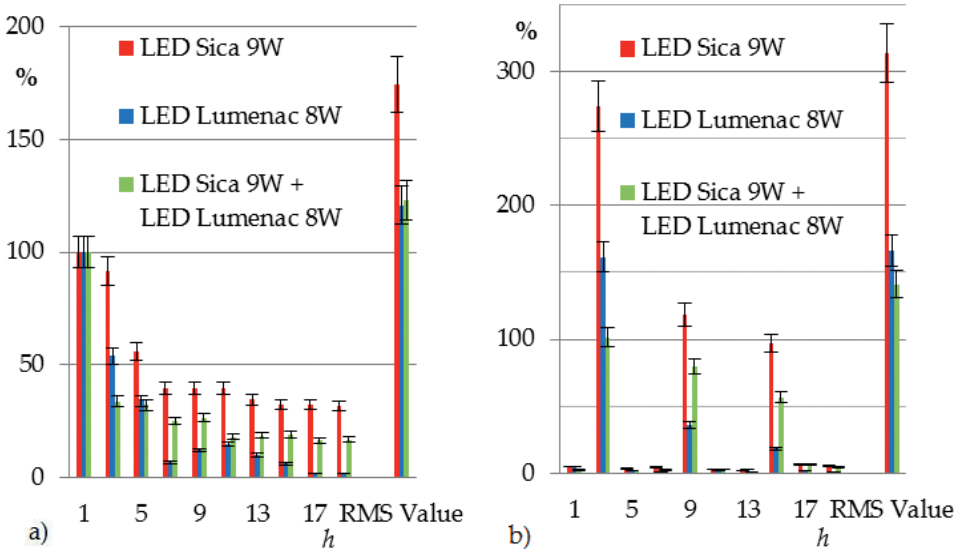

Figure 10. Harmonic current content in one phase (a) and in the neutral conductor (b) of a four-core cable for a selected LED-LED combination.

the above calculated cable losses with the losses produced in an identical cable but carrying an undistorted electric current of the same RMS value as the first harmonic current of the distorted current. To do this, the cable loss ratio defined as

$$\xi \equiv \frac{P_{loss}}{3 {I_{RMS}}^2(1) R_{ac}(1) + {I_{RMS\,N}}^2(1) R_{ac\,N}(1)}, \tag{21}$$

(the first-order harmonic current in the neutral conductor is due to small asymmetries in the single-phase loads) was calculated on the basis of the measured data by neglecting the influence of the harmonic frequency on the resistance of the conductors (i.e. the conductor radius is small compared to the characteristic skin penetration length, and the distances of the nearby conductors are large compared to the conductor radius [29]). For a neutral conductor having a cross section equal to half of the phase conductor section [38], it results in a value of 9.6, 3.3 and 2.8 for the individual lamps LED Sica 9 W and LED Lumenac 8 W and for the combination, respectively, thus showing that the tested lamp combination leads to a significant decrease in the power harmonic losses. A similar result can be obtained for other lamp combination provided that the diversity factor for the third-order harmonic current of the arrangement is small enough.

Note that in lighting loads of substantial power demand such as those considered in this work, it would be convenient from the point of view of the reduction of the power losses to connect the LED lamps between lines (rather than between a line and the neutral conductor). In such case, the third-order harmonic currents (and their multiples) cannot flow through the network since the return path through the neutral conductor does not exist. This suggests the convenience of having LED lamps including ac/dc converters designed to operate as two-phase loads. As quoted before, a large number of the existing low-voltage installations present a neutral conductor with a reduced section (about half of the phase conductor) [38]. These installations when feeding LED loads could present more than twice the losses corresponding to a current without distortion of the same rms as the value of the first harmonic current of the lamps [13]; thus, a marked reduction (over ~ 50%) in the overall harmonic power losses can be expected if the LED lamps (having ac/dc converters designed to operate as two-phase loads) are connected between lines instead as single-phase loads.

4. Conclusions

Calculation of harmonic disturbances in low-voltage network installations having the neutral cross section approximately equal to half of the phase conductors when used for feeding large LED lighting loads was reported. The cables were modeled by using electromagnetic finite element analysis software. Four-core cables and four single-core cable arrangements (three phases and neutral conductor) of small, medium and large conductor cross sections were examined. This study has shown that:

1. The cross section of the neutral conductor plays an important role in the harmonic losses and thus in the derating of the cable ampacity, due to the presence of a high level of triplen harmonics in the distorted current.

2. An incoming widespread use of LED lamps in lighting could create significant additional harmonic losses in the supplying low-voltage lines, and thus more severely harmonic emission limits should be defined for LED lamps.

In order to reduce the third-order harmonic currents in the neutral conductor, an experimental investigation of diversity factors for LED in combination with CFL and LED lamps was also performed. An experimental investigation of diversity factors for LED (light emitting diode) in combination with CFL (compact fluorescent lamps) and LED lamps with nominal powers <25 W was presented. In contrast to other works, attention was paid to the reduction of low-order harmonics, especially the third one, which is mainly responsible for the strong increase in power losses in the neutral conductor of the low-voltage installations. The results showed that a number of selected combinations of LED and CFL lamps lead to a considerable decrease in the content of the third-order harmonic current. These results are different from those reported by other studies where lower-order harmonics did not exhibit a very large reduction in amplitude. However, it should be noted that in those studies random combinations of lamps were used. The convenience of having LED lamps designed to operate as two-phase loads is suggested for certain applications of significant power demand.

Acknowledgements

N. M. and L. P. acknowledge financial support by the National Technological University (PID 3568). L. P. and M. A. L. are members of the CONICET. We have reused our own original work published in *Advanced Electromagnetic Journal* to write part of the presented chapter.

Author details

Natalio Milardovich[1]*, Leandro Prevosto[2], Miguel A. Lara[3] and Diego Milardovich[4]

*Address all correspondence to: njmilardovich@gmail.com

1 Electrical Discharge Group, Department of Electromechanical Engineering, Venado Tuerto Regional Faculty, National Technological University, Venado Tuerto (Santa Fe), Argentina

2 Electrical Discharge Group, Department of Electromechanical Engineering, Venado Tuerto Regional Faculty, National Technological University, CONICET, Venado Tuerto (Santa Fe), Argentina

3 Master in Energy for Sustainable Development, Faculty of Exact Science, Eng. and Surveying, Rosario National University, Rosario (Santa Fe), Argentina

4 Faculty of Exact Science, Eng. and Surveying, Rosario National University, Rosario (Santa Fe), Argentina

References

[1] Subjak JS, Mc Quilkin JS. Harmonics-causes, effects, measurements, and analysis: An update. IEEE Transactions on Industry Applications. 1990;**26**:1034-1042

[2] Wagner VE et al. Effects of harmonics on equipment. IEEE Transactions on Power Delivery. 1993;**8**:672-680

[3] Carpinelli G, Caramia P, Di Vito E, Losi A, Verde P. Probabilistic evaluation of the economical damage due to harmonic losses in industrial energy system. IEEE Transactions on Power Delivery. 1996;**11**:1021-1028

[4] Puchalapalli S, Pindoriya NM. Harmonics assessment for modern domestic and commercial loads: A survey. In: Proceedings of the IEEE International Conference on Emerging Trends in Electrical Electronics & Sustainable Energy Systems (ICETEESES); 11-12 March 2016; India. New York: IEEE; 2016. pp. 120-125

[5] Rice DE. Adjustable speed drive and power rectifier harmonics their effect on power systems components. IEEE Transactions on Industry Applications. 1986;**22**:161-177

[6] Dwyer R, Khan AK, Mc Granaghan M, Tang L, Mc Cluskey RK, Sung R, Houy T. Evaluation of harmonic impacts from compact fluorescent lights on distribution systems. IEEE Transactions on Power Systems. 1995;**10**:1772-1779

[7] Azevedo IL, Morgan MG, Morgan F. The transition to solid-state lighting. Proceedings of the IEEE. 2009;**97**:481-510. DOI: 10.1109/JPROC.2009.2013058

[8] Chong-Tan S. General n-level driving approach for improving electrical-to-optical energy-conversion efficiency of fast-response saturable lighting devices. IEEE Transactions on Industrial Electronics. 2010;**57**:1342-1353

[9] van Driel WD, Fan XJ. Solid state lighting reliability. New York: Springer; 2013. p. 613. DOI: 10.1007/978-1-4614-3067-4

[10] Chen W, Ron Hui SI. Elimination of an electrolytic capacitor in AC/DC light-emitting diode (LED) driver with high input power factor and constant output current. IEEE Transactions on Power Electronics. 2012;**27**:1598-1607

[11] Qu X, Wong SC, Tse CK. Resonance assisted buck converter for offline driving of power LED replacement lamps. IEEE Transactions on Power Electronics. 2011;**26**:532-540

[12] Li S, Tan S-C, Lee CK, Waffenschmidt E, Ron Hui SI, Tse CK. A survey, classification, and critical review of light-emitting diode drivers. IEEE Transactions on Power Electronics. 2016;**31**:1503-1516. DOI: 10.1109/TPEL.2015.2417563

[13] Milardovich N, Prevosto L, Lara MA. Calculation of harmonic losses and ampacity in low-voltage power cables when used for feeding large LED lighting loads. Advanced Electromagnetism. 2014;**3**:50-56. DOI: 10.7716/aem.v3i1.258

[14] Gu L, Ruan X, Xu M, Yao K. Means of eliminating electrolytic capacitor in AC/DC power supplies for LED lightings. IEEE Transactions on Power Electronics. 2009;**24**:1399-1408

[15] Ruan X, Wang B, Yao K, Wang S. Optimum injected current harmonics to minimize peak-to-average ratio of LED current for electrolytic capacitor-less AC-DC drivers. IEEE Transactions on Power Electronics. 2011;**26**:1820-1825

[16] Arias M, Lamar DG, Sebastian J, Balocco D, Diallo AA. High-efficiency LED driver without electrolytic capacitor for street lighting. IEEE Transactions on Industry Applications. 2013;**49**:127-137

[17] Lo YK, Wu KH, Pai KJ, Chiu HJ. Design and implementation of RGC LED drivers for LCD backlight modules. IEEE Transactions on Industrial Electronics. 2009;**56**:4862-4871

[18] Muthu S, Schuunnans FJ, Pashley M. Red, green, and blue LEDs for white light illumination. IEEE Journal of Quantum Electronics. 2002;**8**:333-338

[19] Hui SYR, Qin YX. A general photoelectro-thermal theory for light emitting diode (LED) systems. IEEE Transactions on Power Electronics. 2009;**24**:1967-1976

[20] Chen HT, Tan SC, Hui SYR. Color variation reduction of GaN-based white light emitting diodes via peak-wavelength stabilization. IEEE Transactions on Power Electronics. 2014; **29**:3709-3719

[21] Uddin S, Shareef H, Mohamed A, Hannan MA. An analysis of harmonics from LED lamps. In: Proceedings of the Asia-Pacific Symposium on Electromagnetic compatibility (APEMC); 21-24 May 2012; Singapore. New York: IEEE; 2012. pp. 837-840

[22] Uddin S, Shareef H, Mohamed A. Power quality performance of energy-efficient low-wattage LED lamps. Measurement. 2013;**46**:3783-3795

[23] Castro AG, Rönnbergb SK, Bollen MHJ. Light intensity variation (flicker) and harmonic emission related to LED lamps. Electric Power Systems Research. 2017;**146**:107-114

[24] Aman MM, Jasmon GB, Mokhlis H, Bakar AHA. Analysis of the performance of domestic lighting lamps. Energy Policy. 2013;**52**:482-500

[25] Desmet JJM, Sweertvaegher I, Vanalme G, Stockman K, Belmans RJM. Analysis of the neutral conductor current in a three-phase supplied network with nonlinear single-phase loads. IEEE Transactions on Industry Applications. 2003;**39**:587-593

[26] Meliopoulos APS, Martin MA Jr. Calculation of secondary cable losses and Ampacity in the presence of harmonics. IEEE Transactions on Power Delivery. 1992;**7**:451-459

[27] Demoulias C, Labridis DP, Dokopoulos PS, Gouramanis K. Ampacity of low-voltage power cables under nonsinusoidal currents. IEEE Transactions on Power Delivery. 2007; **22**:584-594

[28] Hiranandani A. Calculation of cable ampacities including the effects of harmonics. IEEE Transactions on Industry Applications. 1998;**4**:42-51

[29] Chien CH, Bucknall RWG. Harmonic calculations of proximity effect on impedance characteristics in subsea power transmission cables. IEEE Transactions on Power Delivery. 2009;**24**:2150-2158

[30] Emanuel AE, Yang M. On the harmonic compensation in nonsinusoidal systems. IEEE Transactions on Power Delivery. 1993;**8**:393-399

[31] Lai JS, Key TS. Effectiveness of harmonic mitigation equipment for commercial office buildings. IEEE Transactions on Industry Applications. 1997;**33**:1104-1110

[32] Chitra R, Neelaveni R. A realistic approach for reduction of energy losses in low voltage distribution network. International Journal of Electrical Power & Energy Systems. 2011;**33**: 377-384

[33] Uddin S, Shareef H, Mohamed A, Hannan MA. An analysis of harmonic diversity factors applied to LED lamps. In: Proceedings of the IEEE International Conference on Power System Technology (POWERCON); 30 Oct-2 Nov 2012; New Zealand. New York: IEEE; 2012. pp. 1-5

[34] Cuk V, Cobben JFG, Kling WL, Timens RB. An analysis of diversity factors applied to harmonic emission limits for energy saving lamps. In: Proceedings of the IEEE International Conference on Harmonics and Quality of Power (ICHQP); 26-29 Sept 2010; Italy. New York: IEEE; 2010. pp. 1-6

[35] Milardovich N, Prevosto L, Lara MA, Milardovich D. On the reduction of the third-order harmonic losses in low–voltage power cables used for feeding large LED and CFL lighting loads. Advanced Electromagnetism. 2017;**6**:46-52. DOI: 10.7716/aem.v6i3.542

[36] Limits for harmonic current emissions (equipment input < 16A per phase), IEC 61000-3-2: 2014

[37] Cables for rated voltages of 1 kV, IEC 60502-1: 2004 (E)

[38] Distribution cables of rated voltage 0.6/1 kV, CENELEC Std. HD603 S1:1994/A2: 2003 E

[39] QuickField Lite, which is a commercially available electromagnetic finite-element analysis software manufactured by Tera Analysis Ltd. QuickField Lite [Internet]. 2017. Available from: https://quickfield.com/edu_lic.htm [Accessed: January 12, 2017]

[40] International standard of resistance for copper, IEC 60028 Ed. 2.0 B: 1925

[41] Electrical Installations of Buildings—Part 5: Selection and Election of Electrical Equipment—Section 523: Current-Carrying Capacities in Wiring Systems, CENELEC Std. HD384.5.523, 2001, S2. Iec 60287

[42] Electric cables-Calculation of the current rating, IEC 60287-1-1, CEI/IEC 60287-1-1:2006

Chapter 5

Tetradentate Cyclometalated Platinum(II) Complexes for Efficient and Stable Organic Light-Emitting Diodes

Guijie Li and Yuanbin She

Additional information is available at the end of the chapter

http://dx.doi.org/10.5772/intechopen.76346

Abstract

As one of the most important phosphorescent emitters, tetradentate cyclometalated platinum(II) complexes have attracted much attention in recent years, because of the high luminescent efficiency, emission spectra, and color tuned easily, especially for the development of high-efficient deep-blue and "pure" blue emitters and single-doped white organic light-emitting diodes (OLEDs). Also, some platinum(II)-based OLEDs exhibited superior operational stability, indicating their potentials in full-color display and solid-state lighting applications. In this chapter, we will introduce the recent advances of the tetradentate cyclometalated platinum(II) complexes, including pyrazole, *N*-heterocyclic carbene, imidazole and pyridine-based complexes, molecular design, photophysical properties, and some of their device performances.

Keywords: platinum complex, tetradentate, OLED, blue emitter, phosphorescence, operational lifetime

1. Introduction

In the 1960s, the first organic electroluminescent spectrum was reported from the crystal of anthracene [1]. In 1987, Tang and VanSlyke from Eastman Kodak Company successfully demonstrated an efficient and practical organic light-emitting diode (OLED) employing tris (8-hydroxyquinolinato)aluminum (Alq_3) as a fluorescent emitter [2]. After that, OLEDs began to attract more and more attention in both academic and industrial researches for their potential applications for full-color displays and solid-state lighting industry.

From the spin statistics, it is well known that the singlet and triplet in the electrogenerated excitons are 25 and 75%, respectively [3]. As a result, OLEDs using fluorescent emitters, which

emit from the singlet excited state, can achieve a peak internal quantum efficiency (IQE) only 25%. However, if heavy metal ion is incorporated into the organic ligand, phosphorescent emitters can break the spin-forbidden reactions, and fast intersystem crossing (IC) from singlet to triplet state can occur owing to the strong electron spin-orbit coupling (SOC); thus, heavy metal complexes have the potential to harvest both the electrogenerated singlet and triplet excitons and achieve 100% IQE. In 1998, Forrest and Thompson et al. and Che et al. first reported the electrogenerated phosphorescent platinum(II) [4] and osmium(II) [5] complexes, respectively. Afterward, more heavy metal complexes were found to be used as efficient phosphorescent materials, like iridium(III), ruthenium(II), palladium (II), rhodium (III), gold(III), and so on, and some reviews about these complexes have been published [6–18]. Among them, iridium(III) complexes have been most widely studied. Green and red phosphorescent iridium(III) emitters developed by Universal Display Corporation (UDC) have been successfully commercialized due to their superior efficiency and long operational lifetime. OLED display doped these emitters that have been adopted for several types of high-end personal electronics, such as Samsung Galaxy, LG OLED television, Apple smart watch, and iPhone X. Compared with the liquid crystal display (LCD), OLED display have many outstanding merits, such as low-cost fabrication methods, high color quality, and high-luminance efficiency and also many advantages of low power consumption, wide-viewing angle, wide temperature range, fast response, etc [19, 20]. Thus, OLED has been widely considered as the next generation of full-color display and solid-state lighting technologies.

The development of high efficient and stable phosphorescent emitters is of the most importance for the development of OLEDs and their application. Although thousands of phosphorescent heavy metal complexes have been reported, the emitters can meet the requirement of commercialized displays, which are extremely rare. Now, considerable challenges still remain, for example, the development of efficient green and red emitters with high color quality, especially for the efficient and stable blue and deep-blue phosphorescent emitters. Much of the previous research work and the commercialized phosphorescent emitters mainly focused on the iridium(III) complexes. However, in the past few years, many reports demonstrated that the photophysical properties and device performances of the platinum(II)-based emitters could compare with or even superior to the iridium(III) ones in many aspects [16]. Also, some unique properties were found for some of the platinum(II) complexes, like narrowband emissive spectra, efficient deep-blue emitting, and excimer formation for single-doped white OLEDs [16]. These properties enable the platinum(II) complexes to have potential to be utilized in commercialized displays.

Taking into account the rapid development and unique properties of the platinum(II) complexes, in this chapter, we will mainly highlight their recent progress regarding their molecular design, photophysical properties, and device performances, especially for the tetradentate ones with cyclometalating ligands based on pyrazole, *N*-heterocyclic carbene, imidazole, and pyridine derivatives.

2. Why employ tetradentate ligands?

Because of the relatively long luminescent lifetime and poor quantum efficiency (φ), platinum(II) complexes were historically not considered as ideal emitters. However, through

judicious molecular design, bidentate platinum(II) complex can also emit strongly with lifetime in microsecond region, such as (ppy)Pt(acac) (**Table 1**) (1) [21]. Due to dsp^2 hybrid orbitals that are adopted for the Pt(II) ion, the molecular configuration of the platinum(II) complexes is square planar. Consequently, bidentate platinum(II) complexes are usually very flexible, and the excited state energy can be consumed by many nonradiative decay pathways, like molecular distortion and bond vibration. This can be proven by the emission spectrum of (ppy)Pt(acac) (**Figure 1**), which exhibits a strong vibrational transition $v_{0,1}$ at 518 nm, and, also, the nonradiative decay rate is 4.5 times faster than that of the radiative decay rate in CH_2Cl_2 solution at room temperature (RT).

The rigidity of the molecule would be enhanced if the tridentate ligand was employed, which could suppress the nonradiative decay pathway and favor to increase the φ. Therefore, Pt(dpyd)Cl (**2**) has a weaker vibrational transition $v_{0,1}$ at 523 nm than that of (ppy)Pt(acac), and the φ is increased to 60% [22]. However, the other monodentate ligand was needed to ensure the neutrality of the molecule. Furthermore, the chloride ion is a weak coordination ligand. All these would disfavor the molecular thermal and electrochemical stabilities. Therefore, more rigid and stable ligands are needed for further development of efficient and stable platinum(II)-based phosphorescent emitters.

Judicious tetradentate ligand design could provide rational coordination sites to the platinum(II) ions and maintain the square planar configuration, which are also of benefit to the material synthesis with high metallization yields. Most importantly, tetradentate platinum(II) complexes would have more rigid molecular configuration and improved photophysical and chemical properties. For example, the φ of the phenoxyl-pyridine (popy)-based complex PtOO3 [16, 23] could be up to over 80% in CH_2Cl_2 solution and be achieved to nearly unity in rigid PMMA matrix. If more rigid carbazolyl-pyridine was incorporated and served as ancillary ligand, the φ could be further improved to 100% yield even in CH_2Cl_2 solution for complex PtON3. Furthermore, tetradentate platinum(II) complexes could be easily modified to improve their photophysical and chemical properties through changing ligand's conjugation degree, utilizing different coordination atoms, adopting various linking groups, or forming five- or six-membered chelates. Thanks to the continuous efforts of the scientific community, many efficient and stable platinum(II) complexes had been developed, making them serve as ideal phosphorescent emitters for OLED applications.

Comp.	In CH_2Cl_2 at RT					In PMMA at RT	
	λ_{max}/nm	φ/%[a]	τ/μs	$k_r/10^5\ s^{-1}$	$k_{nr}/10^5\ s^{-1}$	φ/%	τ/μs
1 [21]	484	15	2.6	0.6	3.3	53	6.0
2 [22]	490	60	3.8	1.6	1.1	73	5.7
3 [16, 23]	512	83	2.0	3.2	1.8	97	4.5
4	520	100[b]	4.2[b]	2.4	0.0	—	—

[a]Absolute quantum efficiency.

[b]φ and τ were measured in a solution of 2-MeTHF.

Table 1. Photophysical properties of the bidentate, tridentate, and tetradentate platinum(II) complexes.

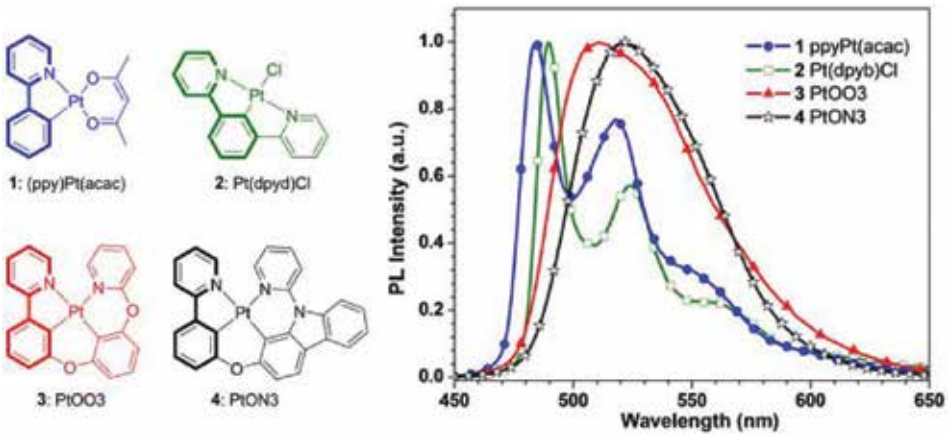

Figure 1. Molecular structures of (ppy)Pt(acac), Pt(dpyd)Cl, PtOO3, PtON3, and their PL spectra in CH_2Cl_2 solution (adapted with permission) [23].

3. Pyrazole-based tetradentate platinum(II) complexes

Because of electron-donating character and relatively weak π-conjugation ability of the nitrogen atom at the 2-position of the pyrazole ring, 1-phenyl-pyrazole (ppy) and its derivatives are widely incorporated into the tetradentate platinum(II) complexes (**Figure 2**). These complexes usually have a high LUMO energy level, making them suitable for developing green to

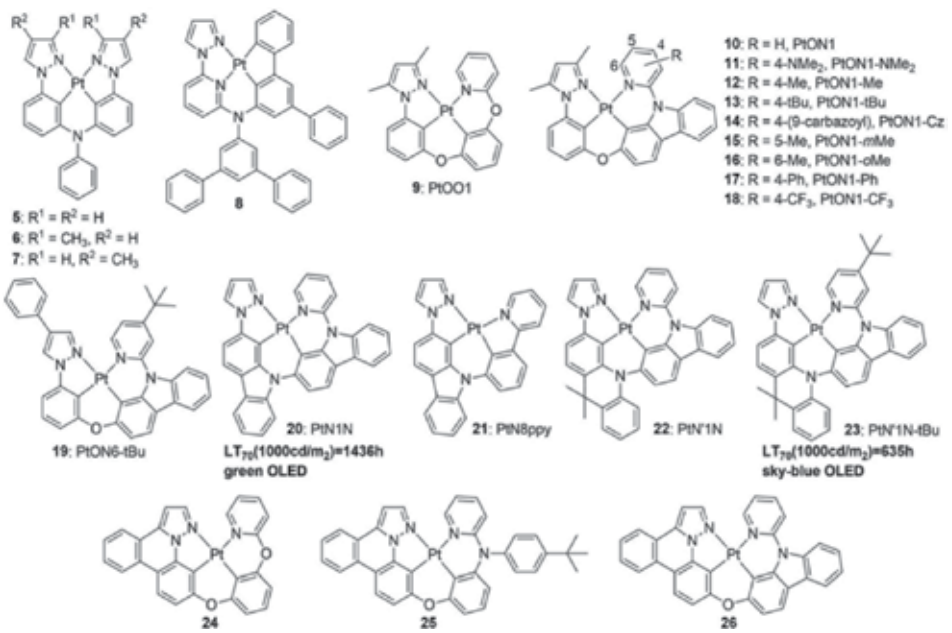

Figure 2. Molecular structures of pyrazole-based tetradentate platinum(II) complexes and operational lifetime of related OLEDs.

blue emitting materials. The photophysical properties and some of the device performances of the pyrazole-based complexes are summarized in **Tables 2** and **3**.

In 2010, Huo et al. reported a series of symmetric tetradentate platinum(II) complexes (**5**–**7**) containing 1-phenyl-pyrazole moieties [24]. All these complexes emit strongly with φ in the range of 37–63%; however, due to the π-conjugation character of the arylamino linking group, their emission energies are relatively low with maximum emission wavelength (λ_{max}) at 474–486 nm in sky-blue and green region. Moreover, excimer emissions were observed for complexes **5** and **7** in solid state peaking at 512 and 516 nm, respectively, because of the strong intermolecular interaction. In 2013, Huo et al. synthesized a 1-(2-pyridinyl)-pyrazole-coordinated complex **8**, which exhibit an even lower emission energy with λ_{max} at 555 nm due to the localization of the first lowest triplet state (T_1) mainly on the biphenyl moiety and the platinum(II) ion [25].

Comp.	In solution at RT					In PMMA at RT		
	Solvent	λ_{max}/nm	FWHM/nm	φ/%	τ/μs	λ_{max}/nm	φ/%	τ/μs
5 [24]	2-MeTHF	484;512	—	56	4.9	—	—	—
6 [24]	2-MeTHF	474	—	37	3.4	—	—	—
7 [24]	2-MeTHF	486;516	—	63	5.7	—	—	—
8 [25]	CH_2Cl_2	555	—	17	4.4	—	—	—
9 [23]	CH_2Cl_2	430;456	—	39	3.0	—	83	7.5
10 [26]	CH_2Cl_2	454;478	85	71	3.3	449	85	4.5
11 [27]	CH_2Cl_2	442	15	80	13.5	440	88	11.3
12 [27]	CH_2Cl_2	444	20	89	10.0	445	84	7.6
13 [27]	CH_2Cl_2	444	20	95	8.9	445	88	8.8
14 [27]	CH_2Cl_2	496	84	53	1.8	480	64	2.0
15 [27]	CH_2Cl_2	450;476	79	82	3.5	445	84	4.3
16 [27]	CH_2Cl_2	450;478	121	45	3.1	449	78	4.8
17 [27]	CH_2Cl_2	546	95	19	0.8	503	88	2.2
18 [27]	CH_2Cl_2	568	104	1.1	0.6	544	29	0.9
19 [27, 28]	CH_2Cl_2	448	19	—	—	447	81	7.4
20 [29]	CH_2Cl_2	491	18	81	12.9	—	90	—
21 [29]	CH_2Cl_2	573	26	40	3.4	—	—	—
22 [30]	CH_2Cl_2	536	111	—	—	476		18.0
23 [30]	CH_2Cl_2	486	46	—	—	476	68	—
24 [31]	CH_2Cl_2	443;471	—	70	—	—	—	—
25 [31]	CH_2Cl_2	449;477	—	24	—	—	—	—
26 [31]	CH_2Cl_2	444;474	—	34	—	—	—	—

Table 2. Photophysical properties of pyrazole-based tetradentate platinum(II) complexes.

Dopant	λ_{max}/nm	FWHM/nm	CIE	η_{EQE}	
				Peak (%)	100 cd/m² (%)
6% PtON1(**10**)[a] [26]	454	46	(0.15, 0.13)	25.2	23.3
2% PtOO1-tBu (**13**)[b] [28]	448	24	(0.151, 0.098)	5.3	2.7
2% PtON6-tBu (**19**)[b] [28]	452	30	(0.147, 0.093)	10.9	6.6
7% PtN1N (**20**)[c] [29]	498	20	(0.15, 0.56)	26.1	25.8
2% PtN8ppy (**21**)[b] [29]	576	28	(0.53, 0.47)	19.3	16.0
6% PtN′1 N-tBu (**23**)[d] [30]	490	34	(0.157, 0.491)	17.8	17.3
30% **24**[e] [31]	540	—	(0.33, 0.57)	16.4	—
20% **25**[e] [31]	456	—	(0.18, 0.30)	7.7	—
20% **26**[e] [31]	541	—	(0.35, 0.55)	15.7	—

[a]Device structure: ITO/HATCN/NPD/TAPC/dopant: 26mCPy/DPPS/LiF/Al.
[b]Device structure: ITO/HATCN/NPD/TAPC/dopant: 26mCPy/DPPS/BmPyPB/LiF/Al.
[c]Device structure: PEDOT:PSS/NPD/TAPC/dopant: 26mCPy/DPPS/BmPyPB/LiF/Al.
[d]Device structure: ITO/HATCN/NPD/TrisPCz/dopant:mCBP)/mCBT/BPyTP/Liq/Al.
[e]Device structure: ITO/HATCN/TAPC/TCTA/dopant: 26mCPy(or CBP)/TmPyPB/Liq/Al.

Table 3. Summary of OLED performances of the pyrazole-based tetradentate platinum(II) complexes.

To develop blue or deep-blue emitters, the arylamino liker should be replaced with less-conjugated ones, like oxygen or functionalized carbon groups. Based on this design, PtOO1 (**9**) was synthesized by employing 1-phenyl-3,5-dimethylpyrazole and phenoxyl-pyridine (popy) like oxygen in Li's group in 2013 [23]. The dominant emission peaks of PtOO1 are at 420 nm at 77 K and 430 nm at room temperature (RT). The φ is relatively low in solution but can be up to 83% with τ of 7.5 μs in PMMA film. However, excimer emission could not be observed; this could be attributed to the boat-like conformation of the two six-membered rings containing the oxygen liker [23] to prevent intermolecular Pt-Pt bond formation.

In 2013, Li's group developed a new type of tetradentate platinum(II) complex PtON1 (**10**) using 3,5-dimethyl-1-phenylpyrazole and thermally and electrochemically stable pyridinyl-carbazole (PyCz) as ligands linked by an oxygen atom [26]. PtON1 exhibits a peak emission at 440 nm with a full width at half maximum (FWHM) of 6 nm at 77 K. However, at RT, the emission spectrum is dramatically broadened, and the FWHM is up to 85 nm with two emission peaks at 454 and 478 nm, respectively, which attributed to dual emission from both the phenyl-pyrazole and PyCz moieties. The φ of PtON1 is much higher than that of PtOO1 in CH_2Cl_2 solution, due to more rigid PyCz moiety. Importantly, PtON1-based blue OLED can achieve a peak external quantum efficiency (EQE) of 25.2% and Commission Internationale de L'Eclairage (CIE) coordinates of (0.15, 0.13) but still short of the "pure" blue CIE coordinates of (0.14, 0.08) designated by the National Television System Committee (NTSC) of the USA in 1931.

To afford deep or "pure" blue emitters, the $CIE_y \leq 0.1$ is needed. To achieve this goal, narrowband emission is required to eliminate the color contamination from the green region. Through a systemic research work, it was found that the emission from the PyCz ligand could be suppressed

by introducing electron-donating group, like -Me, -tBu, and -NMe_2, to the 4-position of the pyridine ring to increase the energy level of the metal-to-ligand charge-transfer (MLCT) states of the PyCz moiety. Therefore, a series of deep-blue emitters, PtON1-NMe_2, PtON1-Me, and PtON1-tBu (**11–13**), were developed peaking at 442–444 nm with FWHM of 15–20 nm and φ not less than 80% in CH_2Cl_2 solution at RT (**Figure 3**) [27]. Moreover, it was also found that the emission color could be easily tuned through changing the substitutions or their positions on the pyridine ring, and all the PtON1 series showed intensive emitting except PtON1-CF_3, especially in PMMA films with φ of 29–88% (**Figure 3**) [27]. Furthermore, PtON6-tBu, employing the 4-phenylpyrazole in place of 3,5-dimethylpyrazole in PtON1, was also developed as a deep emitter, which exhibit narrowband emission spectrum peaking at 448 nm in CH_2Cl_2 and FWHM of 20 nm [28]. The emission energy does not decrease significantly owing that the 4-phenyl group and the pyrazole are not coplanar in PtON6-tBu. What is more is that deep-blue OLEDs doped 2% PtON1-tBu or PtON6-tBu could reach peak EQEs of 5.3 or 10.9% with $CIE_y < 0.1$ [28]. The unsatisfied EQEs are attributed to the high T_1 energy of the deep-blue emitters, making them incompatible with known state-of-the-art host materials. Thus, stable host materials with a high T_1 level are still important for the development of deep-blue OLEDs.

In addition to modifying the cyclometalating ligand, the 1-phenyl-pyrazole ligand can be replaced with low-energy ligand, like pyrazolyl-carbazole, and green emitter PtN1N (**20**) was designed and synthesized in Li's group [29]. PtN1N also gives a very narrow emission spectrum peaking at 491 nm in CH_2Cl_2 solution at RT; the FWHM of 18 nm and Huang-Rhys factor (S_M) of 0.3 for the vibrational transition $v_{0,1}$ peak at 525 nm can be achieved. Moreover, one 7% PtN1N-doped device demonstrated a peak EQE of 26.1% and only decreased slightly to 25.8% at a luminance of 100 cd/m^2. Importantly, employing the nitrogen of the carbazole as linking atom can significantly enhance the chemical and device stability. Therefore, using a known stable device structure, 10% PtN1N-doped green OLED could achieved an operational lifetime at 70% initial luminance, LT_{70}, of 1436 h at 1000 cd/m^2 with peak EQE of 14.3%, which was estimated nearly 72,000 h at a practical luminance of 100 cd/m^2. Furthermore, improved

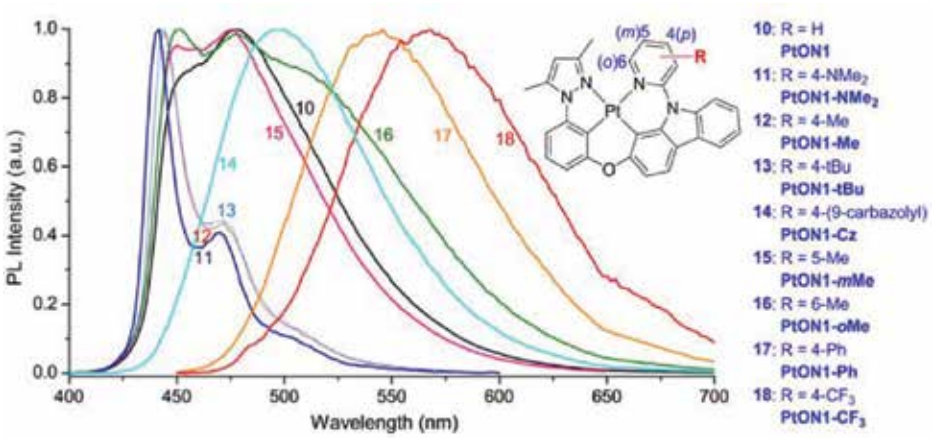

Figure 3. PL spectra comparison of the PtON1 series at RT in CH_2Cl_2 with molecular structures of each emitter inset (adapted with permission) [27].

device by adding an electron-blocking layer (EBL) could achieved peak EQE of 22.1% and still remained 20.3% at 1000 cd/m^2 with operational lifetime LT_{70} of nearly 1200 and 60,000 h at 1000 and 100 cd/m^2, respectively [29]. This device performance is among the highest-efficient green OLEDs reported in literatures. PtN1N also could be employed as an efficient green emitter for the development of white OLED [32]. However, replacing the PyCz for PtN1N with phenylpyridine (ppy) gives an orange emitter PtN8ppy (**21**) because of the localization of the T_1 mainly on the ppy moiety. The peak EQE of a PtN8ppy-based device could also reach close to 20% [29].

The development of efficient and stable blue emitters still maintains a challenge. In order to achieve this goal, chemically and thermally stable ligands must be adopted. Based on the above work, the carbazole in PtN1N was replaced with 9,10-dihydroacridine to break conjugation and increase the T_1 state energy without changing the linking nitrogen atom; therefore, two new tetradentate platinum(II) complexes PtN′1 N (**22**) and PtN′1 N-tBu (**23**) were designed and reported by Li's group recently [30]. Both PtN′1 N and PtN′1 N-tBu show dominant peaks at 476 nm, which blueshifts by 8 nm compared to that of PtN1N in 2-MeTHF at 77 K. Optimized device by employing 10% PtN′1 N-tBu as dopant without EBL could achieve peak EQE of 15.9% and an estimated operational lifetime LT_{70} of 635 h at an initial luminance of 1000 cd/m^2 [30]. This device performance is comparable or superior to the best platinum(II)-[33] and iridium(III) [34]-based blue OLEDs reported in literatures [30]. It was believed that the device performance could be further improved if using state-of-the-art host, electron, and hole-blocking materials.

Recently, Fan and Liao et al. designed and synthesized a series of platinum(II) complexes (**24**–**26**) based on pyrazole[1,5-*f*]phenanthridine-containing ligands [31]. All of them showed high thermal stabilities and strong emission from blue to yellow-green spectral region with φ of 24–70%. The dominate emission peaks of all the three complexes are not much difference, but the emission spectra are more and more broad. Interestingly, the emission from PyCz moiety can be observed clearly for complex **26**, which is much like the PtON1 discussed above [27]. Complex **26** demonstrated the best device performance to achieve peak EQE of 16.4%, but unfortunately the operational lifetime of the device was not reported.

4. *N*-heterocyclic carbene-based tetradentate platinum(II) complexes

Because of the strong δ-donating ability and relatively weak π-accepting property, the *N*-heterocyclic carbene (NHC) unit could shorten the metal-carbene bond length of the NHC-based platinum(II) complexes, shallow the LUMO energy level to widen the HOMO and LUMO gap, and raise the d-d level of the excited state to suppress the thermally activated nonradiative decay. These will be beneficial for the stability of the complexes and the enhancement of quantum efficiency [12, 17]. Therefore, the NHC-based platinum(II) complexes are appropriate to serve as blue and deep-blue phosphorescent OLEDs. However, due to synthetic challenges and shortage of stable host materials with high T_1 state, the reported NHC-based tetradentate platinum(II) complexes are very rare. Especially, their operational lifetime remains unclear. The NHC-based platinum(II) complexes discussed in this chapter are illustrated in **Figure 4**, their photophysical properties are summarized in **Table 4**, and some of their device performances are illustrated in **Table 5**.

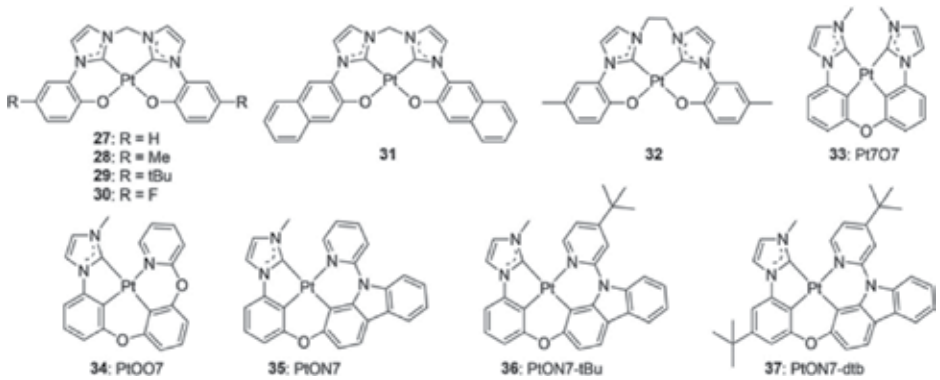

Figure 4. Molecular structures of NHC-based tetradentate platinum(II) complexes.

Comp.	In solution at RT					In PMMA at RT		
	Solvent	λ_{max}/nm	FWHM/nm	φ/%	τ/μs	λ_{max}/nm	φ/%	τ/μs
27 [35]	THF-DMF	457	—	3	0.5	443	29	—
28 [35]	THF-DMF	460	—	7	1.8	448	24	—
29 [35]	THF-DMF	461	—	8	1.8	449	26	—
30 [35]	THF-DMF	443	—	18	3.5	434;451	26	—
31 [36]	THF-DMF	531;562	—	15	47.3	—	—	—
32 [36]	CH_2Cl_2	—	—	—	—	480[a]	—	0.1[a]
Pt7O7 (**33**) [37]	CH_2Cl_2	471	20	71	3.2	—	—	—
PtOO7 (**34**) [26]	CH_2Cl_2	442	66	—	—	442	58	2.5
PtON7 (**35**) [26]	CH_2Cl_2	452	64	78	4.2	452	89	4.1
PtON7-tBu (**36**) [29]	CH_2Cl_2	446	20	83	6.6	—	—	—
PtON7-dtb (**37**) [28]	CH_2Cl_2	446	20	85	5.4	447	91	4.7

[a]Data were collected in solid state.

Table 4. Photophysical properties of NHC-based tetradentate platinum(II) complexes.

Early in 2011, Che's group had developed a series of symmetric bis-NHC-based platinum(II) complexes by employing O^C*C^O ligands (**27–30**, **Figure 4**) [35]. All the four complexes exhibit intense blue phosphorescence ether in solutions (φ, 3–18%) or in PMMA films (φ, 24–29%). Incorporating electron-donating groups into the phenyl rings, like -Me and -tBu, can destabilize the HOMO, resulting in 3–4 nm redshift for the emission spectra of **28** and **29** compared with that of **27**. On the other hand, electron-withdrawing group -F can stabilize the HOMO and make a significant blueshift (**Table 4**). Moreover, blue device doped with **28** exhibited emission peak at about 460 nm with CIE coordinates of (0.16, 0.16), but the EQE was low and was not reported. In 2013, Che's group optimized the blue device doped with 4% complex **29**, which could achieve a high EQE of about 15% with CIE coordinates of (0.19, 0.21)

Dopant	λ_{max}/nm	FWHM/nm	CIE	η_{EQE}	
				Peak (%)	100 cd/m² (%)
3% **28**[a] [35]	~460[b]	~70[b]	(0.16, 0.16)	—	—
4% **29**[c] [36]	460	~70[b]	(0.19, 0.21)	~15	
2% Pt7O7(**33**)[d] [37]	472	20	(0.12, 0.24)	26.3	20.5
14% Pt7O7(**33**)[d] [37]	—	—	(0.37, 0.42)	25.7	21.5
2% PtOO7 (**34**)[e] [26]	446	50	(0.15, 0.10)	7.0	4.1
6% PtON7 (**35**)[f] [26]	458	54	(0.15, 0.14)	23.7	20.4
6% PtON7-tBu (**36**)[g] [29]	450	28	(0.14, 0.09)	17.6	10.7
2% PtON7-dtb (**37**)[g] [28]	451	23	(0.146, 0.088)	17.2	12.4
6% PtON7-dtb (**37**)[g] [28]	452	25	(0.146, 0.091)	19.8	14.7
10% PtON7-dtb (**37**)[g] [28]	452	39	(0.155, 0.130)	19.6	14.9
14% PtON7-dtb (**37**)[g] [28]	454	47	(0.161, 0.169)	19.0	15.5
6% PtON7-dtb (**37**)[h] [28]	451	29	(0.148, 0.079)	24.8	22.7

[a]Device structure: ITO/2-TNATA/NPB/dopant: DP4/TPBi/LiF/Al.
[b]Estimated from the EL spectrum in the reported literature.
[c]Device structure: ITO/TAPC/TCTA/CzSi/dopant: CzSi/TmPyPB/LiF/Al.
[d]Device structure: ITO/HATCN/NPD/TAPC/dopant: mCBP/DPPS/BmPyPB/LiF/Al.
[e]Device structure: PEDOT:PSS/NPD/TAPC/dopant: 26mCPy/PO15/LiF/Al.
[f]Device structure: ITO/HATCN/NPD/TAPC/dopant: 26mCPy/DPPS/LiF/Al.
[g]Device structure: ITO/HATCN/NPD/TAPC/dopant: 26mCPy/DPPS/BmPyPB/LiF/Al.
[h]Device structure: ITO/HATCN/NPD/TAPC/dopant: TAPC:PO15/PO15/BmPyPB/LiF/Al.

Table 5. Summary of blue OLED performances of the NHC-based tetradentate platinum(II) complexes.

(**Table 5**) [36]. What's more is that extended π-conjugation (**31**) or prolonged linking group (**32**) would result in redshift for the emission spectra [36].

In 2014, Li's group reported a symmetric bis-NHC-based platinum(II) complex Pt7O7 (**33**) by employing C^C*C^C ligands (**Figure 4**) [37]. Pt7O7 exhibits a very narrow emission spectrum peaking at 471 nm with FWHM of only 20 nm in diluted CH_2Cl_2 solution at RT. Two percent of Pt7O7-doped blue device demonstrated a peak EQE of 26.3% and still remained 20.5% at 100 cd/m² with broadening the electroluminescent (EL) spectrum (**Table 4**), paving a new way for the development of efficient blue phosphorescent emitters. Importantly, due to the square planar configuration, excimer would form in elevated concentration, and Pt7O7 could serve as single-doped white OLEDs. The device with the best emitting color could be achieved using a concentration of 14% Pt7O7 with a CRI of 70 and CIE coordinates of (0.37, 0.42), which also exhibited a peak EQE of 25.7%. This was the first reported emitter with both efficient monomer and excimer emissions.

In 2013–2015, Li's group successively developed a series of blue and deep-blue OLEDs by employing rigid NHC-based platinum(II) complexes, like PtOO7 (**34**), [26] PtON7 (**35**) [26], PtON7-tBu (**36**) [27, 29], and PtON7-dtb (**37**) [27, 28], which adopted asymmetric tetradentate

ligands containing phenoxyl-pyridine or pyridinyl-carbazole moieties. All of them exhibit distorted molecular geometry that suppresses the excimer and aggregation formation. PtOO7 shows a broad emission peak at 442 nm in CH_2Cl_2 solution and has a φ of 58% and a short τ of 2.5 μs in PMMA film at RT. As expected, PtOO7-based device exhibited a deep-blue emission with a CIE coordinates of (0.15, 0.10); however, the peak EQE was only 7%, due to its high T_1 state level (2.87 eV) and incompatibility with the host material or improper energy-level alignment inside the emissive layer [16].

On the other hand, all the PtON7 series of complexes (**35–37**) have high φ of 78–91% and τ of 4.1–6.6 μs in solution and PMMA film at RT. Additionally, they have a relatively low T_1 state level (2.81–2.82 eV), allowing them to be compatible with the known and efficient host materials. Encouragingly, PtON7-based device demonstrated a blue color with a CIE coordinates of (0.15, 0.14) and peak EQE of 23.7% still remained 20.4% at 100 cd/m^2 [26]. However, due to the broad device emission spectrum (FWHM = 54 nm) and significant green emission contamination, the CIE coordinates of (0.15, 0.14) still fail to reach the standard of the "pure" blue coordinates of (0.14, 0.08) [38].

Further modifications are needed for the development of deep-blue OLEDs. Fortunately, incorporating-tBu group into the 4-position of the pyridine ring can elevate the T_1 energy of the pyridinyl-carbazole moiety and suppress its emission, just like the discussion of PtON1 and PtON1-tBu above [27]. Thus, very narrow emission spectra can be obtained for the PtON7-tBu and PtON7-dtb, which have FWHM of only 20 nm, making them suitable for deep-blue emitters (**Figure 5**) [29]. Importantly, the introduction of the other-tBu group to the phenyl ring can significantly enhance the thermal stability of PtON7-dtb and benefit to the high-quality device fabrication. As expected, PtON7-tBu-based device exhibited a deep-blue color and CIE coordinates of (0.14, 0.09) owing to its narrow emission spectrum and also had a peak EQE of 17.6% [29]. What's more is that PtON7-dtb-based devices demonstrated excellent performances. Increasing the concentration of the PtON7-dtb would broaden the emission spectra; however, no signs of excimer or aggregation formation were observed. Through optimizing the device structure by employing a co-host of hole- and electron-transporting materials, the peak EQE could be further increased to 24.8% and remained 22.7% at practical luminance of 100 cd/m^2 with a highly desirable CIE coordinates of (0.148, 0.079), very close to the "pure" blue coordinates of (0.14, 0.08) [28]. This device performance is the best for the deep-blue

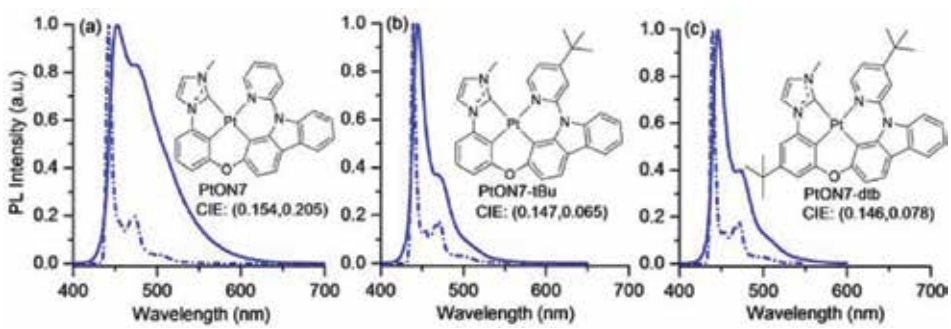

Figure 5. PL spectra of (a) PtON7, (b) PtON7-tBu, and PtON7-dtb at RT in CH_2Cl_2 (solid lines) and 77 K in 2-MeTHF (dash-dotted lines) with molecular structures and CIE coordinates (RT) of each emitter inset (adapted with permission) [27].

phosphorescent OLEDs reported to date [17], and this molecular design by employing asymmetric tetradentate NHC ligands is one of the most successful strategies for the development of deep-blue OLEDs with high color purity. There has also been much progress on the further understanding of the relationship between the molecular modifications and the narrowing of emission band, and research work had been carried out based on the study of the time-dependent density functional theory (TD-DFT), UV, IR, and transient Raman spectra [27, 39, 40].

5. Imidazole-based tetradentate platinum(II) complexes

Compared with the 1-phenyl-pyrazole and phenyl-NHC moieties discussed above, 2-phenyl-imidazole has a greater degree of π-conjugation and a relatively low T_1 state level. Thus, imidazole-based phosphorescent metal complexes often exhibit redshift and serve as sky-blue emitters. Importantly, they are easily compatible with the known stable host and charger-transporting materials, making them suitable for the development of stable blue OLEDs. Imidazole-based iridium(III) blue emitters have been widely studied and demonstrated high quantum efficiency and impressive operational lifetime, although they are still far from meeting the strict requirements of commercialization [17, 34, 41–44]. However, the reported tetradentate imidazole-based platinum(II) complexes are still rare, which are illustrated in **Figure 6**, their photophysical properties are summarized in **Table 6**, and the device performances are illustrated in **Table 7**.

Interestingly, although adopting different ancillary ligands, PtOO2 (**38**) and PtON2 (**39**) nearly have the same T_1 state level, corresponding to their dominant peaks at 462 and 460 nm

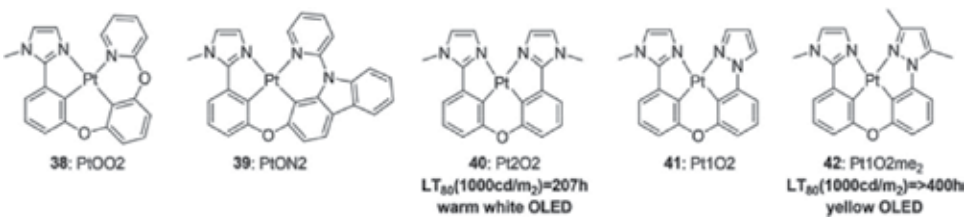

Figure 6. Molecular structures of imidazole-based tetradentate platinum(II) complexes.

Comp.	In CH_2Cl_2 at RT			In PMMA at RT		
	λ_{max}/nm	φ/%	τ/μs	λ_{max}/nm	φ/%	τ/μs
PtOO2 (**38**) [45]	468	64	9.0	—	—	—
PtON2 (**39** [45]	466	61	6.5	—	—	—
Pt2O2 (**40**) [46]	490	—	—	—	84	—
Pt1O2 (**41**) [46]	474	—	—	—	—	—
$Pt1O2me_2$ (**42**) [46]	470	—	—	—	—	—

Table 6. Photophysical properties of imidazole-based tetradentate platinum(II) complexes.

Dopant	CIE	CRI	η_{EQE}		Device LT_{80}
			Peak (%)	1000 cd/m² (%)	1000 cd/m² (h)
8% PtOO2 (**38**)[a] [45]	(0.16, 0.34)	—	23.1	15.7	—
8% PtON2 (**39**)[a] [45]	(0.16, 0.32)	—	22.9	17.5	—
2% Pt2O2 (**40**)[b] [46]	(0.23, 0.57)	—	25.4	18.2	—
16% Pt2O2 (**40**)[b] [46]	(0.48, 0.48)	72	24.6	21.0	—
16% Pt2O2 (**40**)[c] [46]	(0.46, 0.47)	80	12.5	—	207
2% Pt1O2 (**41**)[b] [46]	(0.22, 0.44)	—	24.1	16.9	—
16% Pt1O2 (**41**)[b] [46]	(0.49, 0.48)	57	22.6	19.3	—
2% Pt1O2me_2 (**42**)[b] [46]	(0.23, 0.44)	—	26.5	17.6	—
16% Pt1O2me_2 (**42**)[b] [46]	(0.42, 0.53)	42	24.2	20.6	—
12% Pt1O2me_2 (**42**)[c] [46]	(0.43, 0.50)	—	12.3	—	>400

[a]Device structure I: ITO/PEDOT: PSS/NPD/TAPC/dopant:26mCPy/PO15/BmPyPB/LiF/Al.
[b]Device structure II: ITO/HATCN/NPD/TAPC/dopant: 26mCPy/DPPS/BmPyPB/LiF/Al.
[c]Device structure III: ITO/HATCN/NPD/dopant: CBP/BAlq/Alq/LiF/Al.

Table 7. Device performances of pyrazole-based tetradentate platinum(II) complexes.

in 2-MeTHF at 77 K, respectively [45]. Both of them emit strongly in diluted CH_2Cl_2 solution at RT and exhibit λ_{max} at 468 and 466 nm, respectively (**Table 6**). PtOO2- and PtON2-based devices emitted in the blue-green region and demonstrated high peaking EQEs of 23.1 and 22.9% and still could remain 15.7 and 17.5% at 1000 cd/m² in the device structure I (**Table 7**). Due to the P=O, double bond can be irreversibly reduced by electrons in the device to result in the poor electrochemical stability of the hole-blocking material PO15, and the device lifetime was not run in the literature.

Compared with the nonplanar molecular PtOO2 and PtON2, all planar complexes Pt2O2 (**40**), Pt1O2 (**41**), and Pt1O2me_2 (**42**) show redshift, especially for the symmetric Pt2O2, which peaks at 490 nm in diluted CH_2Cl_2 at RT. Importantly, all the three planar complexes have more rigid configuration, which results in strong intermolecular Pt-Pt interaction to form efficient excimers, enabling them suitably for serving as single-doped white OLEDs for lighting application [46]. All the devices doped with either low or high concentrations exhibited very high peak EQEs from 22.6 to 26.5% using the device structure II and could achieve 16.9–21.0% even at 1000 cd/m² (**Table 7**); this device performance indicated that both the monomer and the excimer were highly efficient in the device settings, which were superior to that of the literature reporting bidentate and tridentate platinum(II) complexes, like FPt, Pt-4, and Pt-16 [46]. What's more is that the triplet-triplet annihilation (TTA) processes at high dopant concentrations, which were often observed in the iridium(III)-based devices, were also not significant for these complexes.

The operational lifetime of the devices is one of important parameters for their potential commercialization. Using the stable device structure III, white OLED doped with 16% Pt2O2 demonstrated an operational lifetime LT_{80} of over 200 h at an initial luminance of 1000 cd/m² with

a color rendering index (CRI) of up to 80 and peak EQE of 12.5% [46]. Due to the strong emission of the excimer, 12% Pt1O2me$_2$-doped device exhibited a yellow emission; however, the operational lifetime LT_{80} could achieve over 400 h at an initial luminance of 1000 cd/m^2, which was twice as long as that of Pt2O2 in the same device setting, and this could be attributed to the lack of high-energy blue emitters in the Pt1O2me$_2$-based device.

6. Pyridine-based tetradentate platinum(II) complexes

2-Phenylpyridine has been widely used as ligand for the iridium(III)- and platinum(II)-based phosphorescent complexes, like Ir(ppy)$_3$, due to its high stability and easy preparation. However, owing to the low T_1 state level, the emitting colors are usually from green to red. So far, various types of pyridine-based tetradentate platinum(II) complexes have been reported; importantly, most of them are highly efficient, and some complexes are so stable that they can achieve the early stage of commercial applications. The pyridine-based tetradentate platinum(II) complexes are illustrated in **Figure 7**, their photophysical properties are summarized in **Table 8**, and some of the device performances based on these complexes are showed in **Table 9**.

In 2010, Huo's group reported three pyridine-based platinum complexes (**43**–**45**) using phenylamine as linking group [24]. Complex **43** exhibits a dominant emission peak at 512 nm in diluted 2-MeTHF solution, and the excimer emission at about 740 nm was observed at elevated concentration, due to the planar molecular configuration. The HOMO level can be stabilized by introducing fluorine atoms into the phenyl rings; thus, complex **44** has a blue-shift of 24 nm with a peaking emission at 488 nm. Because of the electron-donating character of the phenylamine, complex **45** has a shallower HOMO level of −4.56 eV compared to that of complex **43** of −5.27 eV; therefore, significant redshift of 100 nm was observed for complex **45**. All the three complexes show strongly luminescence with φ of 14–75% in solution, and device doped with **43** achieved a peak EQE of 14.7% with coordinates of (0.32, 0.62). Unfortunately, the device stability was not studied in the literature.

In 2012, Fukagawa et al. developed two modified complexes TLEC-025 (**46**) and TLEC-027 (**47**) by incorporating δ-donating groups on the phenylamine to further destabilize the HOMO levels, resulting in redshift to about 620 nm, which were ideal emitters for red OLEDs [47]. TLEC-025-based device demonstrated an operational lifetime LT_{80} of 1290 h with a peak EQE of 18.5% and power efficiency (PE) of 20.7 lm/W at 100 cd/m^2 and still remained 14.4% and 25.2 lm/W at 1000 cd/m^2. Encouragingly, device doped with TLEC-027 achieved further long operational lifetime LT_{80} of 3330 h with similar EQEs and even higher PEs of 25.5 and 30.3 lm/W at 100 and 1000 cd/m^2, respectively. Unfortunately, the molecular structures of the hole-injecting material ND-1501 and electron-transporting material ETM-143 were unknown. Anyway, this was the first time to demonstrate that the platinum(II)-based devices could be as efficient and stable as the iridium(II)-based ones, opening a door for the development of efficient and stable OLEDs by employing platinum(II) complexes.

Pyridine-based tetradentate platinum(II) complex PtOO3 (**48**) with luminescent quantum efficiency of up to 97% in thin film was developed by Li's group in 2013. PtOO3-based device

http://dx.doi.org/10.5772/intechopen.76346

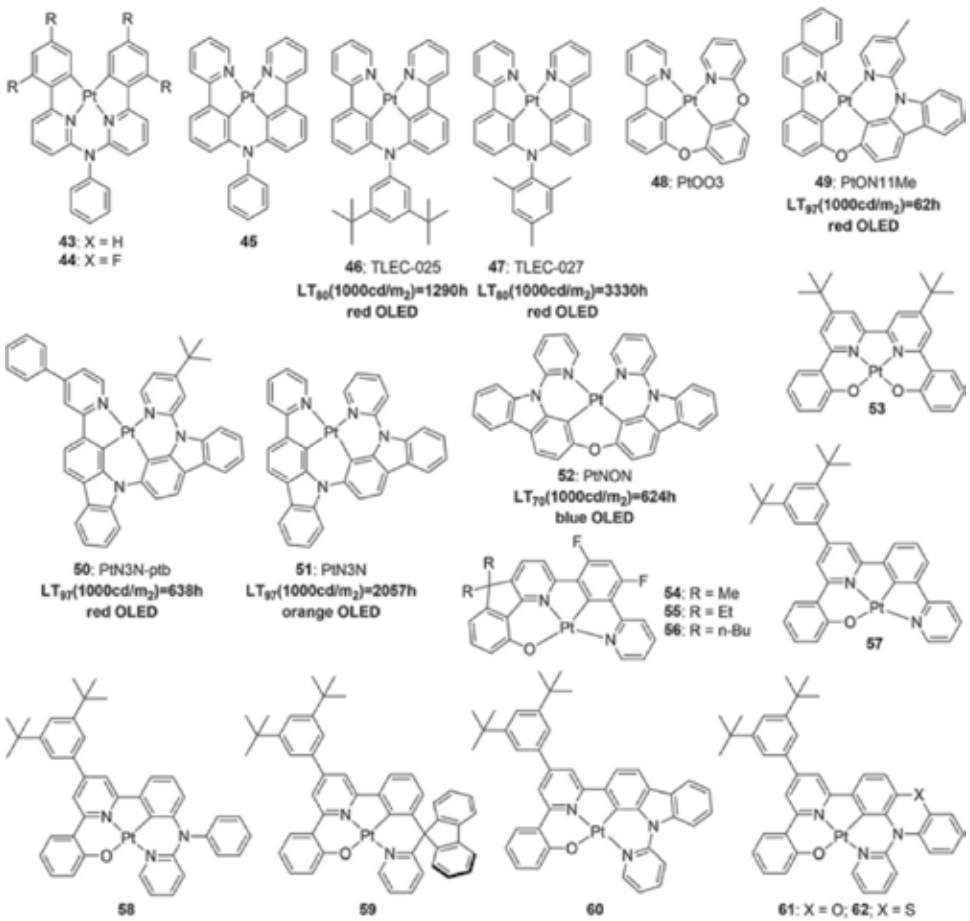

Figure 7. Molecular structures of pyridine-based tetradentate platinum(II) complexes.

performance was compared with that of *fac*-Ir(ppy)$_3$ in the same device structure, and peak EQE of 22.3% could be achieved [23].

A great progress has been made for the development of stable and efficient platinum(II)-based red OLEDs in the past several years. In 2014, Li's group demonstrated a stable red OLEDs with an estimated operational lifetime LT_{97} of 62 h at 1000 cd/m^2 with CIE coordinates of (0.60, 0.36) by employing PtON11Me (**49**) as emitter [48]. One year later, tenfold increase in the operational lifetime was achieved using more stable carbazole-linked emitter, PtN3N-ptb (**50**), and an estimated operational lifetime LT_{97} of 638 h at 1000 cd/m^2 with peak EQE of 10.8%, which used CBP, TrisPCz, and BPyTP as host, electron-blocking, and transporting materials, respectively. Also, the turn on voltage was as low as about 2.0 eV. Moreover, the peak EQE could be increased to 21.5% if using $Bebq_2$ as host material [49]. What's more is that adopting a bilayer emitting material layer (EML) with different dopant concentrations in the same device structure, PtN3N (**51**)-based orange OLED, could achieve a superior operational lifetime LT_{97} of 2057 h at 1000 cd/m^2 and peak EQE of 16.9%. This could be attributed to shift the excision formation zone deep into the EML to suppress the potential fast degradation of

Comp.	In solution at RT				In PMMA at RT		
	Solvent	λ_{max}/nm	φ/%	τ/μs	λ_{max}/nm	φ/%	τ/μs
43 [24]	2-MeTHF	512, 548	74	7.6	514, 551, 595[a]	—	—
44 [24]	2-MeTHF	488, 523	75	11.4	541, 583[a]	—	—
45 [24]	2-MeTHF	613	14	7.6	741, 782[a]	—	—
46 [47]	—	—	—	—	621[b]	58	—
47 [47]	—	—	—	—	620[b,c]	—	—
48 [23]	CH_2Cl_2	512	63	2.0	—	97	4.5
49 [48]	CH_2Cl_2	614	—	3.6	—	40	—
50 [49]	CH_2Cl_2	502	34	—	—	—	—
51 [50]	CH_2Cl_2	582	63	7.3	—	—	—
52 [33]	CH_2Cl_2	508	31	2.6	474	83	3.8
53 [51]	CH_2Cl_2	595	12	1.9	—	—	—
54 [52]	CH_2Cl_2	479, 510, 624	60	5.8	—	—	—
55 [52]	CH_2Cl_2	480, 510, 616	66	5.4	—	—	—
56 [52]	CH_2Cl_2	482, 512, 624	75	17.7	—	—	—
57 [52]	CH_2Cl_2	503	76	4.1	—	—	—
58 [53]	CH_2Cl_2	551	90	4.3	—	74	—
59 [53]	CH_2Cl_2	517	80	5.1	—	91	—
60 [54]	CH_2Cl_2	553, 587	86	6.6	—	—	—
61 [54]	CH_2Cl_2	526	47	5.9	—	—	—
62 [54]	CH_2Cl_2	527	49	8.8	—	—	—

[a]Solid state.

[b]Doped in $Bebq_2$.

[c]Estimated from the emission spectrum.

Table 8. Photophysical properties of pyridine-based tetradentate platinum(II) complexes.

the device [50]. These device performances indicate that the platinum(II)-based complexes are more appealing as phosphorescent emitters in the display applications.

For the development of iridium(III)-based blue emitters containing phenylpyridine moiety, generally, electron-withdrawing groups, like fluorine, are needed to be introduced into the phenyl group to stabilize the HOMO level [21]. However, this would result in electrochemical stability problems to accelerate the device degradation, which was unfavorable to the development of the stable blue OLEDs. In 2016, Li's group developed a new rout for stable and efficient blue OLEDs through breaking the conjugation of the phenylpyridine with a six-membered chelating rings (**52**, PtNON) [33]. Therefore, an operational lifetime LT_{70} of 624 h at 1000 cd/m^2 with peak EQE of 10.7% and CIE coordinates of (0.17, 0.32) was achieved for the PtNON-based blue OLED. This device performance was comparable to the best iridium(III)-based blue OLEDs reported in literatures [34].

Dopant	λ_{max}/nm	CIE	CRI	η_{EQE}		Device LT
				Peak (%)	1000 cd/m² (%)	1000 cd/m² (h)
4% **43**[a] [24]	512	(0.32, 0.62)	—	14.7	—	—
6% **46**[b] [47]	—	(0.662, 0.337)	—	18.5	14.4	LT_{80}: 1920
6% **47**[b] [47]	—	(0.657, 0342)	—	18.2	14.5	LT_{80}: 3330
8% **48**[c] [23]	500	—	—	22.3	17.6	—
6% **49**[d] [48]	—	(0.60, 0.36)	—	4.7	4.6	LT_{97}: 62
10% **50**[e] [49]	—	(0.63, 0.37)	—	10.8	7.8	LT_{97}: 638
2% **50**[f] [49]	—	(0.58, 0.42)	—	21.5	13.5	LT_{97}: 25
10–6% **51**[g] [50]	—	(0.55, 0.45)	—	16.9	15.3	LT_{97}: 2057
6% **52**[h] [33]	—	(0.17, 0.32)	—	10.7	9.1	LT_{70}: 624
10% **54**[i] [52]	—	(0.41, 0.44)	75	11.6	5.5	—
16% **55**[i] [52]	—	(0.41, 0.45)	74	17.0	12.4	—
20% **56**[i] [52]	—	(0.41, 0.45)	76	9.6	8.4	—
4% **57**[i] [52]	—	(0.29, 0.63)	—	9.7	9.5	—
10% **58**[j] [53]	555	(0.44, 0.55)	—	26.0	23.1	—
10% **59**[j] [53]	—	(0.31, 0.64)	—	27.6	25.6	—

[a]Device structure: ITO/CFx/NBP/TCTA/dopant: TPBI:TCTA/TPBI/Alq/LiF/Mg:Ag.
[b]Device structure: ITO/ND-1501/α-NPD/dopant:$Bebq_2$/ETM-143/LiF/Al.
[c]Device structure: ITO/PEDOT:PSS/TAPC/dopant: 26mCPy/PO15/BmPyPB/LiF/Al.
[d]Device structure: ITO/HATCN/NPD/dopant:mCBP:BAlq/BAlq/Alq/LiF/Al.
[e]Device structure: ITO/HATCN/NPD/TrisPCz/dopant: CBP/BAlq/BPyTP/LiF/Al.
[f]Device structure: ITO/HATCN/NPD/TrisPCz/dopant:$Bebq_2$/BAlq/BPyTP/LiF/Al.
[g]Device structure: ITO/HATCN/NPD/TrisPCz/20 wt%**51**: CBP/6 wt%**51**:CBP/BAlq/BPyTP/LiF/Al.
[h]Device structure: ITO/HATCN/NPD/dopant:mCBP/mCBT/BPyTP/LiF/Al.
[i]Device structure: ITO/PEDOT:PSS/dopant:PVK:OXD-7/TmPyPb/TPBi/LiF/Al.
[j]Device structure: ITO/MoO_3/TAPC/dopant:TCTA/TmPyPB/LiF/Al.

Table 9. Device performances of pyridine-based tetradentate platinum(II) complexes.

In fact, a synthetic challenge still remains for the gram-scale preparation of the PtNON and the PtON1 series complexes. Recently, our group developed an efficient approach for the CuCl-catalyzed C-N band cross coupling of carbazoles and 2-bromopyridine derivatives to synthesize 2-bromo-*N*-(hetero)arylcarbazoles. It was found that base t-BuOLi could accelerate the reaction significantly and just a few hours needed to complete the reaction [55]. However, 3–6 days were needed if using K_2CO_3 as base according to the previous reported method [28, 29]. Moreover, a directly hydroxylation of the 2-bromo-*N*-(hetero)arylcarbazoles catalyzed by CuCl was also developed [56]. Both of the approaches are suitable for large-scale synthesis and have been successfully applied in the gram-scale synthesis of PtNON and PdNON, demonstrating its practicability in organic synthesis methodology and materials science [56].

Early in 2013, Che's group had developed a series of symmetric (**53**) [51] and asymmetric (**54–62**) [52–54, 57] phenoxyl-pyridine containing tetradentate platinum(II) complexes. All asymmetric

complexes have high φ of 49–90% and τ of 4.1–17.7 μs in CH_2Cl_2 solutions, and the OLEDs doped these complexes that showed very high brightness, even up to 66,000 cd/m^2 at 10.5 eV. Moreover, the planar rigid molecular configuration enabled the fluorine-containing complexes **54**–**56** to have strong excimer emission at 616–624 nm, making them serve as ideal emitters for single-doped white OLEDs with CRI of up to 76 [52]. However, after introducing sterically bulky 3,5-di-*tert*-butylphenyl group to the pyridine ring, excimer formation was suppressed for the complexes **57**–**62**. Devices doped with complex **58** bridging phenylamine or complex **59** with a spiro linkage demonstrated peak EQEs over 25% and maximal PEs up to 109.4 lm/W using TmPyPB as ETL. The maximal PE of complex **59** could further be improved to 126.0 lm/W if Tm3PyBPZ as ETL, which were the highest among the reported platinum(II)-based OLEDs [53]. In the same year, Che's group developed another series of tetradentate platinum(II) complexes containing carbazole (**60**), phenoxazine (**61**), and phenothiazine (**62**) moieties, which served as yellow phosphorescent emitters combined with blue emitter to make white OLEDs [54].

7. Other types of tetradentate platinum(II) complexes

Besides the four series of tetradentate platinum(II) complexes discussed above, there were also some other new types. In 2015, a series of sky-blue emitters based on 3-(trifluoromethyl)-5-(2-pyridyl)pyrazole or 3-(trifluoromethyl)-5-(2-pyridyl)-1,2,4-triazole containing spiro-arranged tetradentate ligands were developed. The peak EQE of one blue OLED could reach 15.3% and CIE values of (0.190, 0.342) [58]. In 2017, Liao, Fan, and co-workers developed three 1-isopropyl-2-phenyl-benzo[*d*]imidazole-based emitters with decomposition temperature above 400°C, and one device exhibited a peak EQE of 22.3% [59].

Very recently, Fukagawa and co-workers reported great progress in ultrapure green OLEDs based on a NHC emitter PtN7N [60], which was developed by Li's group before 2014 [61]. The optimized OLED showed CIE coordinates of (0.18, 0.74) using a top-emitting OLED with a microcavity structure and also using a boron-based host material [60]. Fukagawa's work demonstrated that the narrowband emitter PtN7N was superior to the iridium(II)-based emitter $Ir(mppy)_3$ for the development of ultrapure green emitter to satisfy the BT.2020 for ultrahigh-definition displays [60], owing to the very small vibrational structures of PtN7N that could be well suppressed by microcavity technology. Similar phenomenon was also observed in the previous report of narrowband green emitter PtN1N vs. PtOO3 [62]. Moreover, Fukagawa's work also demonstrated that the operational stability of PtN7N-based OLEDs could be comparable to that of the $Ir(mppy)_3$-based ones, indicating the promise for the practical application of PtN7N by employing suitable host and charge-transporting materials [60, 63].

8. Conclusion

In summary, after over 10 years of development, the emission spectra of the tetradentate platinum(II)-based OLEDs can cover the whole visible spectrum, they also exhibit high efficiency, and some show high color purity and long operational lifetime, demonstrating their

potential applications for the next-generation full-color display and solid-state lighting. Owing to the square planar and rigid molecular configurations, platinum(II) complexes have many unique and exciting photophysical properties. On the one hand, easy molecular modification enables tunable emission spectra, and the FWHM of the pyrazole- or NHC-carbene-based complexes can achieve no more than 20 nm and can be as narrow as 15 nm. This facilitates them to serve as efficient deep-blue emitters, and device-doped NHC-carbene-based complex successfully realized "pure" blue emitting with CIE coordinates of (0.148, 0.079) and peak EQE of 24.8%. On the other hand, some planar d^8 platinum(II) complexes can form intermolecular Pt-Pt bond to achieve 18e structure in their excited state, making them serve as single-doped white OLEDs with high CRI values. Besides, tetradentate platinum(II)-based green, especially for the red OLEDs, demonstrated superlong operational lifetime and satisfied the requirements of the initial commercialization. What's more is that sky-blue OLEDs also achieved encouraging performances, indicating their bright future for the development of the efficient and stable blue OLEDs.

Despite great progress that has been made for the tetradentate platinum(II) complexes, a challenge remains for the development of the stable deep-blue OLEDs, and more work still be needed. To overcome this challenge, it is important to develop stable host materials with a high enough T_1 state level and highly balanced charge carrier ability. However, through continued efforts of the academia and industry, we believe that these critical issues can be solved and the platinum(II)-based OLEDs will be one candidate for display and lighting applications.

Acknowledgements

The authors thank the National Natural Science Foundation of China (21602198, 21776259, 21476270), the "Qianjiang Talents Plan" (QJD1602017), and AAC Technologies for their financial support. The authors also thank Dr. Tyler Fleetham from the University of Southern California for the measurements of the quantum efficiency and luminescent lifetime of the PtON3.

Abbreviations

Alq_3	tris(8-hydroxyquinolinato)aluminium
BAlq	bis(2-methyl-8-quinolinolato) (biphenyl-4-olato)aluminum
$Bebq_2$	bis(benzo[h]quinolin-10-olato-κN,κO)beryllium(II)
BmPyPB	1,3-bis[3,5-di(pyridin-3-yl)phenyl]benzene
BPyTP	2,7-di(2,2′-bipyridin-5-yl)triphenylene
CBP	4,4′-bis(*N*-carbazolyl) biphenyl
CzSi	9-(4-(*tert*-butyl)phenyl)-3,6-bis(triphenylsilyl)-9*H*-carbazole
DPPS	diphenyl-bis[4-(pyridin-3-yl)phenyl]-silane

HATCN	1,4,5,8,9,12-hexaazatriphenylene-hexacarbonitrile
mCBT	9,9′-(2,8-dibenzothiophenediyl)bis-9*H*-carbazole
26mCPy	2,6-bis(*N*-carbazolyl) pyridine
mppy	3-methyl-2-phenylpyridine
2-MeTHF	2-methyltetrahydrofuran
NPD	*N*,*N*′-diphyenyl-*N*,*N*′-bis(1-naphthyl)-1,1′-biphenyl-4,4″-diamine
OXD-7	1,3-bis[(4-*tert*-butylphenyl)-1,3,4-oxadiazolyl]phenylene
PEDOT:PSS	poly(3,4-ethylenedioxythiophene):poly(styrene sulfonic acid)
PO15	2,8-bis(diphenylphosphoryl)-dibenzothiophene
ppy	2-phenylpyridine
PVK	polyvinylcarbazole
TAPC	di-[4-(*N*,*N*-ditolylamino)-phenyl]cyclohexane
TCTA	4,4′,4″-tris(*N*-carbazolyl)triphenlyamine
2-TNATA	tri(4-(naphthalen-2-yl(phenyl)amino)phenyl)amine
TmPyPB	1,3,5-tri[(3-pyridyl)-phen-3-yl]benzene
Tm3PyBPZ	2,4,6-tris(3-(3-(pyridin-3-yl)phenyl)phenyl)-1,3,5-triazine
TPBi	2,2′,2″-(1,3,5-benzinetriyl)-tris(1-phenyl-1-*H*-benzimidazole)
TrisPCz	9,9′,9″-triphenyl-9*H*,9′*H*,9″*H*-3,3′:6′3″-tercarbazole

Author details

Guijie Li* and Yuanbin She

*Address all correspondence to: guijieli@zjut.edu.cn

College of Chemical Engineering, Zhejiang University of Technology, Hangzhou, China

References

[1] Helfrich W, Schneider WG. Recombination radiation in anthracene crystals. Physical Review Letters. 1965;**14**:229-231. DOI: 10.1103/PhysRevLett.14.229

[2] Tang CW, Vanslyke SA. Organic electroluminescent diodes. Applied Physics Letters. 1987;**51**:913-915. DOI: 10.1063/1.98799

[3] Wohlgenannt M, Tandon K, Mazumdar S, Ramasesha S, Vardeny ZV. Formation cross-sections of singlet and triplet excitons in π-conjugated polymers. Nature. 2001;**409**:494-497. DOI: 10.1038/35054025

[4] Baldo MA, Brien DF, You Y, Shoustikov A, Sibley S, Thompson ME, Forrest SR. Highly efficient phosphorescent emission from organic electroluminescent devices. Nature. 1998;**395**:151-154. DOI: 10.1038/25954

[5] Ma Y, Zhang H, Shen J, Che C. Electroluminescence from triplet metal-ligand charge-transfer excited state of transition metal complexes. Synthetic Metals. 1998;**94**:245-248. DOI: 10.1016/S0379-6779(97)04166-0

[6] You Y, Park SY. Phosphorescent iridium(III) complexes: Toward high phosphorescence quantum efficiency through ligand control. Dalton Transactions. 2009:1267-1282. DOI: 10.1039/B812281D

[7] Chi Y, Chou P-T. Transition-metal phosphors with cyclometalating ligands: Fundamentals and applications. Chemical Society Reviews. 2010;**39**:638-655. DOI: 10.1039/B916237B

[8] Xiao L, Chen Z, Qu B, Luo J, Kong S, Gong Q, Kido J. Recent progresses on materials for electrophosphorescent organic light-emitting devices. Advanced Materials. 2011;**23**:926-952. DOI: 10.1002/adma.201003128

[9] Xiang H, Cheng J, Ma X, Zhou X, Chruma JJ. Near-infrared phosphorescence: Materials and applications. Chemical Society Reviews. 2013;**42**:6128-6185. DOI: 10.1039/C3CS60029G

[10] Fan C, Yang C. Yellow/orange emissive heavy-metal complexes as phosphors in monochromatic and white organic light-emitting devices. Chemical Society Reviews. 2014;**43**:6439-6469. DOI: 10.1039/C4CS00110A

[11] Fleetham T, Li G, Zhu Z-Q, Li J. Development of tetradentate Pt complexes for efficient, stable, and high colour purity blue OLEDs. SID Symposium Digest of Technical Papers. 2015;**46**:411-414. DOI: 10.1002/sdtp.10382

[12] Yang X, Zhou G, Wong W-Y. Functionalization of phosphorescent emitters and their host materials by main-group elements for phosphorescent organic light-emitting devices. Chemical Society Reviews. 2015;**44**:8484-8575. DOI: 10.1039/c5cs00424a

[13] Yang X, Xu X, Zhou G. Recent advances of the emitters for high performance deep-blue organic light-emitting diodes. Journal of Materials Chemistry C. 2015;**3**:913-944. DOI: 10.1039/C4TC02474E

[14] Aliprandi A, Genovese D, Mauro M, Cola LD. Recent advances in phosphorescent Pt(II) complexes featuring metallophilic interaction: Properties and applications. Chemistry Letters. 2015;**44**:1152-1169. DOI: 10.1246/cl.150592

[15] Li K, Tong GSM, Wan Q, Cheng G, Tong W-Y, Ang W-H, Kwong W-L, Che C-M. Highly phosphorescent platinum(II) emitters: Photophysics, materials and biological applications. Chemical Science. 2016;**7**:1653-1673. DOI: 10.1039/C5SC03766B

[16] Fleetham T, Li G, Li J. Phosphorescent Pt(II) and Pd(II) complexes for efficient, high-colour-quality, and stable OLEDs. Advanced Materials. 2017;**29**:1601861. DOI: 10.1002/adma.201601861

[17] Im Y, Byun SY, Kim JH, Lee DR, Oh CS, Yook KS, Lee JY. Recent progress in high-efficiency blue-light-emitting materials for organic light-emitting diodes. Advanced Functional Materials. 2017;**29**:1603007. DOI: 10.1002/adfm.201603007

[18] Ma D, Tsuboi T, Qiu Y, Duan L. Recent progress in ionic iridium(III) complexes for organic electronic devices. Advanced Materials. 2017;**29**:1603253. DOI: 10.1002/adma.201603253

[19] Forrest SR. The path to ubiquitous and low-cost organic electronic applications on plastic. Nature. 2004;**428**:911-918. DOI: 10.1038/nature02498

[20] Kamtekar KT, Monkman AP, Bryce MR. Recent advances in white organic light-emitting materials and devices (WOLEDs). Advanced Materials. 2010;**22**:572-582. DOI: 10.1002/adma.200902148

[21] Brooks J, Babayan Y, Lamansky S, Djurovich PI, Tsyba I, Bau R, Thompson ME. Synthesis and characterization of phosphorescent cyclometalated platinum complexes. Inorganic Chemistry. 2002;**41**:3055-3066. DOI: 10.1021/ic0255508

[22] Williams JAG, Beeby A, Davies ES, Weinstein JA, Wilson C. An alternative route to highly luminescent platinum(II) complexes: Cyclometalation with N^C^N-coordinating dipyridylbenzene ligands. Inorganic Chemistry. 2003;**42**:8609-8611. DOI: 10.1021/ic035083+

[23] Turner E, Bakken N, Li J. Cyclometalated platinum complexes with luminescent quantum yields approaching 100%. Inorganic Chemistry. 2013;**52**:7344-7351. DOI: 10.1021/ic302490c

[24] Vezzu DAK, Deaton JC, Jones JS, Bartolotti L, Harris CF, Marchetti AP, Kondakova M, Pike RD, Huo S. Highly luminescent tetradentate bis-cyclometalated platinum complexes: Design, synthesis, structure, photophysics, and electroluminescence application. Inorganic Chemistry. 2010;**49**:5107-5119. DOI: 10.1021/ic1002226

[25] Huo S, Harris CF, Vezzu DAK, Gagnier JP, Smith ME, Pike RD, Li Y. Novel phosphorescent tetradentate bis-cyclometalated C^C*N^N-coordinated platinum complexes: Structure, photophysics, and a synthetic adventure. Polyhedron. 2013;**52**:1030-1040. DOI: 10.1016/j.poly.2012.06.078

[26] Hang X-C, Fleetham T, Turner E, Brooks J, Li J. Highly efficient blue-emitting cyclometalated platinum(II) complexes by judicious molecular design. Angewandte Chemie International Edition. 2013;**52**:6753-6756. DOI: 10.1002/anie.201302541

[27] Li G, Wolfe A, Brooks J, Zhu Z-Q, Li J. Modifying emission spectral bandwidth of phosphorescent platinum(II) complexes through synthetic control. Inorganic Chemistry. 2017;**56**:8244-8256. DOI: 10.1021/acs.inorgchem.7b00961

[28] Fleetham T, Li G, Wen L, Li J. Efficient "pure" blue OLEDs employing tetradentate Pt complexes with a narrow spectral bandwidth. Advanced Materials. 2014;**26**:7116-7121. DOI: 10.1002/adma.201401759

[29] Li G, Fleetham T, Turner E, Hang X-C, Li J. Highly efficient and stable narrow-band phosphorescent emitters for OLED applications. Advanced Optical Materials. 2015;**3**:390-397. DOI: 10.1002/adom.201400341

[30] Li G, Klimes K, Fleetham T, Zhu Z-Q, Li J. Stable and efficient sky-blue organic light emitting diodes employing a tetradentate platinum complex. Applied Physics Letters. 2017;**110**:113301. DOI: 10.1063/1.4978674

[31] Zhao D, Tang X, Liu X-Y, Fan J, Liao L-S. Highly luminescent platinum(II) complexes based on pyrazolo[1,5-f]phenanthridine-containing ligands. Organic Electronics. 2017; **50**:473-479. DOI: 10.1016/j.orgel.2017.07.002

[32] Norby GE, Park C-D, O'Brien B, Li G, Huang L, Li J. Efficient white OLEDs employing red, green, and blue tetradentate platinum phosphorescent emitters. Organic Electronics. 2016;**37**:163-168. DOI: 10.1016/j.orgel.2016.06.007

[33] Fleetham T, Huang L, Klimes K, Brooks J, Li J. Tetradentate Pt(II) complexes with 6-membered chelate rings: A new route for stable and efficient blue organic light emitting diodes. Chemistry of Materials. 2016;**28**:3276-3282. DOI: 10.1021/acs.chemmater.5b04957

[34] Zhang Y, Lee J, Forrest SR. Tenfold increase in the lifetime of blue phosphorescent organic light-emitting diodes. Nature Communications. 2014;**5**:5008. DOI: 10.1038/ncomms6008

[35] Li K, Guan X, Ma C-W, Lu W, Chen Y, Che C-M. Blue electrophosphorescent organoplatinum(II) complexes with dianionic tetradentate bis(carbene) ligands. Chemical Communications. 2011;**47**:9075-9077. DOI: 10.1039/c1cc12943k

[36] Li K, Cheng G, Ma C, Guan X, Kwok W-M, Chen Y, Lu W, Chen C-M. Light-emitting platinum(II) complexes supported by tetradentate dianionic bis(N-heterocyclic carbene) ligands: Towards robust blue electrophosphors. Chemical Science. 2013;**4**:2630-2644. DOI: 10.1039/C3SC21822H

[37] Li G, Fleetham T, Li J. Efficient and stable white organic light-emitting diodes employing a single emitter. Advanced Materials. 2014;**26**:2931-2936. DOI: 10.1002/adma.201305507

[38] Tsai T-C, Hung W-Y, Chi L-C, Wong K-T, Hsieh C-C, Chou P-T. A new ambipolar blue emitter for NTSC standard blue organic light-emitting device. Organic Electronics. 2009;**10**:158-162. DOI: 10.1016/j.orgel.2008.10.017

[39] Feng T-T, Bai F-Q, Xie L-M, Tang Y, Zhang H-X. Theoretical study and design of highly efficient platinum(II) complexes bearing tetradentate ligands for OLED. RSC Advances. 2016;**6**:11648-11656. DOI: 10.1039/C5RA22754B

[40] Son MR, Cho Y-J, Son H-J, Cho DW, Kang SO. A spectroscopic study on the satellite vibronic band in phosphorescent Pt-complexes with high colour purity. Physical Chemistry Chemical Physics. 2017;**19**:32670-32677. DOI: 10.1039/C7CP06069F

[41] Zhuang J, Li W, Wu W, Song M, Su W, Zhou M, Cui Z. Homoleptic triscyclometalated iridium(III) complexes with phenylimidazole ligands for highly efficient sky-blue OLEDs. New Journal of Chemistry. 2015;**39**:246-253. DOI: 10.1039/C4NJ01316F

[42] Seo J-A, Jeon SK, Gong MS, Lee JY, Noh CH, Kim SH. Long lifetime blue phosphorescent organic light-emitting diodes with an exciton blocking layer. Journal of Materials Chemistry C. 2015;**3**:4640-4645. DOI: 10.1039/C5TC00640F

[43] Yang JW, Lee JY. Correlation of the molecular structure of host materials with lifetime and efficiency of blue phosphorescent organic light-emitting diodes. Physical Chemistry Chemical Physics. 2015;**17**:24468-24474. DOI: 10.1039/C5CP03469H

[44] Zhang L, Zhang Y-X, Hu Y, Shi X-B, Jiang Z-Q, Wang Z-K, Liao L-S. Highly efficient blue phosphorescent organic light-emitting diodes employing a host material with small bandgap. ACS Applied Materials & Interfaces. 2016;**8**:16186-16191. DOI: 10.1021/acsami.6b01304

[45] Ecton J, Fleetham T, Hang X, Li J. Highly efficient blue-green OLEDs from tetradentate cyclometalated platinum complexes. SID EuroDisplay. 2013:152-155. DOI: 10.1002/anie.201302541

[46] Fleetham T, Huang L, Li J. Tetradentate platinum complexes for efficient and stable excimer-based white OLEDs. Advanced Functional Materials. 2014;**24**:6066-6073. DOI: 10.1002/adfm.201401244

[47] Fukagawa H, Shimizu T, Hanashima H, Osada Y, Suzuki M, Fujikake H. Highly efficient and stable red phosphorescent organic light-emitting diodes using platinum complexes. Advanced Materials. 2012;**24**:5099-5103. DOI: 10.1002/adma.201202167

[48] Li G, Ecton J, O'Brien B, Li J. Efficient and stable organic light emitting devices from a tetradentate cyclometalated platinum complex. Organic Electronics. 2014;**15**:1862-1867. DOI: 10.1002/adma.201305507

[49] Fleetham T, Li G, Li J. Efficient red-emitting platinum complex with long operational stability. ACS Applied Materials & Interfaces. 2015;**7**:16240-16246. DOI: 10.1021/acsami.5b01596

[50] Zhu Z-Q, Klimes K, Holloway S, Li J. Efficient cyclometalated platinum(II) complexes with superior operational stability. Advanced Materials. 2017;**29**:1605002. DOI: 10.1002/adma.201605002

[51] Lin Y-Y, Chan S-C, Chan MCW, Hou Y-J, Zhu N, Che C-M, Liu Y, Wang Y. Structural, photophysical, and electrophosphorescent properties of platinum(II) complexes supported by tetradentate N_2O_2 chelates. Chemistry–A European Journal. 2003;**9**:1264-1272. DOI: 10.1002/chem.200390143

[52] Cheng G, Chow P-K, Kui SCF, Kwok C-C, Che C-M. High-efficiency polymer light-emitting devices with robust phosphorescent platinum(II) emitters containing tetradentate dianionic O^N^C^N ligands. Advanced Materials. 2013;**25**:6765-6770. DOI: 10.1002/adma.201302408

[53] Cheng G, Kui SCF, Ang W-H, Ko M-Y, Chow P-K, Kwong C-L, Kwok C-C, Ma C, Guan X, Low K-H, Su S-J. Che C-M. Structurally robust phosphorescent [Pt(O^N^C^N)] emitters for high performance organic light-emitting devices with power efficiency up to 126 lm W1 and external quantum efficiency over 20%. Chemical Science. 2014;**5**:4819-4830. DOI: 10.1039/C4SC01105H

[54] Lai S-L, Tong W-Y, Kui SCF, Chan M-Y, Kwok C-C, Che C-M. High efficiency white organic light-emitting devices incorporating yellow phosphorescent platinum(II) complex and composite blue host. Advanced Functional Materials. 2013;**23**:5168-5176. DOI: 10.1002/adfm.201300281

[55] Zhao X, She Y, Fang K, Li G. CuCl-catalyzed Ullmann-type C-N cross-coupling reaction of carbazoles and 2-bromopyridine derivatives. The Journal of Organic Chemistry. 2017;**82**:1024-1033. DOI: 10.1021/acs.joc.6b02595

[56] Li G, Zhao X, Fang K, Li J, She Y. CuCl-catalyzed hydroxylation of N-heteroarylcarbazole bromide: Approach for the preparation of N-heteroarylcarbazolyl phenols and its application in the synthesis of phosphorescent emitters. The Journal of Organic Chemistry. 2017;**82**:8634-8644. DOI: 10.1021/acs.joc.7b01568

[57] Kui SCF, Chow PK, Cheng G, Kwok C-C, Kwong CL, Low K-H, Che C-M. Robust phosphorescent platinum(II) complexes with tetradentate O^N^C^N ligands: High efficiency OLEDs with excellent efficiency stability. Chemical Communications. 2013;**49**:1497-1499. DOI: 10.1039/C2CC37862K

[58] Liao K-Y, Hsu C-W, Chi Y, Hsu M-K, Wu S-W, Chang C-H, Liu S-H, Lee G-H, Chou P-T, Hu Y, Robertson N. Pt(II) metal complexes tailored with a newly designed spiro-arranged tetradentate ligand: Harnessing of charge-transfer phosphorescence and fabrication of sky blue and white OLEDs. Inorganic Chemistry. 2015;**54**:4029-4038. DOI: 10.1021/acs.inorgchem.5b00281

[59] Li J, Liang F, Yue Z, Liu X-Y, Fan J, Liao L-S. Highly phosphorescent cyclometalated platinum(II) complexes based on 2-phenylbenzimidazole-containing ligands. Journal of Materials Chemistry C. 2017;**5**:6202-6209. DOI: 10.1039/c7tc01369h

[60] Fukagawa H, Oono T, Iwasaki Y, Hatakeyama T, Zhimizu T. High-efficiency ultrapure green organic light-emitting diodes. Materials Chemistry Frontiers. 2018;**2**:704-709. DOI: 10.1039/c7qm00588a

[61] Fleetham TB. Organic optoelectronic devices employing small molecules [thesis]. Arizona: Arizona State University; 2014

[62] Fleetham T, Ecton J, Li G, Li J. Improved out-coupling efficiency from a green microcavity OLED with a narrow band emission source. Organic Electronics. 2016;**37**:141-147. DOI: 10.1016/j.orgel.2016.05.041

[63] Fukagawa H, Shimizu T, Iwasaki Y, Yamamoto T. Operational lifetimes of organic light-emitting diodes dominated by Förster resonance energy transfer. Scientific Reports. 2017;**7**:1735. DOI: 10.1038/s41598-017-02033-3

Chapter 6

New Generation of High Efficient OLED Using Thermally Activated Delayed Fluorescent Materials

Manish Kumar, Miguel Ribeiro and Luiz Pereira

Additional information is available at the end of the chapter

http://dx.doi.org/10.5772/intechopen.76048

Abstract

The search for efficient materials for organic light emitting diodes is one of the most imperative research area. The focus is to obtain a bright large area emitter, limited by the low internal quantum efficiency of conventional organic emitters. Recently, a new generation of the organic materials (TADF) with a theoretical internal quantum efficiency up to 100%, opened new frameworks. However, significant challenges persist to achieve full understanding of the TADF mechanism and to improve the OLEDs stability. Starting from the photo-physical analysis, we show the relationship with the molecular electrical carrier dynamics and internal quantum efficiencies. The OLED structure, fabrication, and characterization are also discussed. Several examples for the full color emitters are given. Special emphasis on experimental results is made, showing the major milestones already achieved in this field.

Keywords: organic light emitting diodes, thermally activated delayed fluorescence, photoluminescence, electroluminescence, triplet harvesting

1. Introduction

Since the first invention of the organic light emitting diodes (LEDs) in 1987 by Tang and Van Slyke [1] that represented an advancement in display and lightening technologies, Organic light-emitting diodes (OLEDs) have emerged as an extensive active field in the both scientific as well technological aspects. Organic light-emitting diodes (OLEDs) are cheap, flexible, and cheap like a movie projector screen. They have attracted considerable attention due to their promising applications in cheap, energy-saving, eco-friendly and solid-state lighting [2–4].

The current research in OLEDs is emerging technology which is also a growing market and expected to cross 20 billion by 2030 [5]. OLEDs are used in several flat and roll displays, also in white EDs for the lightning. OLEDs give freedom of taking advantage of emission in different colors, color modulation (color coordinates, temperature and color rendering—white lighting), diffused light—(light from flat panels (large area) and high viewing angle), Freedom design (thin, lightweight, flexible transparent—easy incorporation into 3D surfaces), etc. Along with these characteristics, there is some difficulty in getting a large homogeneous emitter area, where the organic materials rapidly degrade in the presence of oxygen and/or humidity. Although solved with rigid OLEDs, flexible ones have low lifetime (no efficient encapsulation system has been developed). The main principle behind OLED technology is electroluminescence and such devices offer brighter, thinner, high contrast, and flexibility.

In the conventional OLEDs, the materials used are π-electron-rich molecules, which helps in the fast charge transfer at the interface. But in these OLEDs, the internal quantum efficiency (IQE) is lower which results to the lower external quantum efficiency (EQE) of 5% and limits the OLEDs development because of the nonradiative triplet exciton non-harnessing. Usually, materials used for OLEDs are phosphorescent emitters such as iridium [6–8] or platinum complexes [9, 10] that are used to achieve the electroluminescence efficiency. In such systems, both 25% singlet excitons and 75% triplet excitons can be used for harnessing the electroluminescence. In phosphorescent OLEDs, the internal quantum efficiency was reported close to 100% [11–16], but the disadvantage in such phosphorescent material is their high cost and poor stability. Along with phosphorescent material harnessing phosphorescence [7, 17], triplet-triplet annihilation [18] were also used. Therefore, to achieve 100% low-cost IQE, the development of an alternative to harvest the 75% triplet exciton is important for the future of OLEDs. In this context, response to this need, the development of the thermally activated delayed fluorescence (TADF) materials with the most promising exciton harvesting mechanism used in OLED devices, which was firstly reported by Adachi et al. in [19] received tremendous attention, and in recent years, considerable efforts have been devoted towards the fabrication of OLEDs based on TADF materials where the IQE can be easily achieved up to 100% [20, 21].

In this chapter, we summarize the fundamentals of thermally activated delayed fluorescence process, their optoelectronic behavior linking with the device performance and recent experimental studies of the introduction of TADF emitters used as the doping/guest material for OLED fabrication. Along with, a summary of the best TADF emitters used for fabrication of orange-red, blue and green-yellow OLEDs is provided. In addition, a correlation is provided between the structure and doping percentage of TADF emitters and their optoelectronic properties.

2. Theory and concepts of thermally activated delayed fluorescence

The starting point to understand the TADF principle in organic luminescent materials is to consider the fundamental *sp.* orbitals hybridization. The carbon–carbon (C-C) conjugation, employing two *2 s*-orbital electrons and two *2p*-orbitals electrons, leads to the *s* and *p* orbitals mix, giving place to three *sp.* orbitals and one non-hybridized p orbital. The C-C

covalent bond is made using two *sp.* orbitals, from each carbon atom, giving rise to a usually called π bond; the third makes a covalent bond around the inter-nuclear axis and is usually called as σ bond. This simplified framework can explain the major electro-optical behavior of organic compounds. Effectively, whereas the π bonds located above and below (respectively, π* - anti-bonding and π bond), originating an overlapping of the *sp.* orbitals in each side, the σ bond is a pure bond between two adjacent atoms. Besides the orbitals geometry, the electrical carriers are allowed to hopping among the ππ* cloud, in contrary to σ carriers that are confined. The ππ* cloud is the basic formation of the occupied and unoccupied energy levels and the further definition of HOMO (highest occupied molecular orbital) and LUMO (lowest unoccupied molecular orbital) levels. The σ energy region is typically a forbidden gap. From this simple configuration, organic molecule energy levels are typically singlet (S) and triplet (T) with the ground state a singlet S_0 [22]. The excited levels comprise, therefore, several S_n and T_n energy states, although in a simple model we may consider the first S_1 and T_1 excited levels. Under excitation (electrical and/or optical), the electrons are promoted to these excited levels, one in S_1 and three in T_1. This is the main drawback of pure organic compounds: the de-excitation towards the S_0 ground state can be evaluated by the transition probability that is given by $\langle \psi_1 | r | \psi_0 \rangle$ where Ψ_1, Ψ_0 an r are the wave-functions of the excited level and of the fundamental one, and *r* the electrical dipole quantum operator. By spin multiplicity rules, the $T_1 \rightarrow S_0$ transition is strictly forbidden and 75% of excited electrons can only relax by the nonradiative process, remaining only 25% of excited carriers available for the radiative (luminescent) transition $S_1 \rightarrow S_0$ (spin allowed). This means that the maximum internal efficiency of a pure organic luminescent material is only 25%. Overcoming this constraint is an absolute priority for achieving highly efficient organic electroluminescent devices. Besides the well-known transition metals organic–inorganic complexes [22] that promote a strong spin-orbit coupling (SOC) with further enhanced phosphorescence, several other paths have been considered. The most promising, and subject of this chapter, is the TADF materials.

The analysis of this process can be based on the exciton formation (electron-hole pair) in a conjugated organic material. An electronic charge can be transferred between both entities in a two molecules system (or also in different parts of the same molecule). This process is called of charge-transfer (donor-acceptor complex) leading origin to the CT energy levels. The primary effect of these levels is to provide an electrostatic attraction, stabilizing the molecule. But, interestingly, this CT state is spin selective and is supposed to be able to change the triplet / singlet balance, allowing a conversion of triplet excitons to singlet ones. Although being still an unclear mechanism, was the fundamental starting point to the TADF materials. The **Figure 1** shows, in a simple scheme, the fundamental process involved in the excitation / de-excitation of an organic molecule.

An efficient TADF emission needs to enhance the transition probability k_{rISC} ($T_1 \rightarrow S_1$) relatively to the K_{nrp} transition $T_1 \rightarrow S_0$. Moreover, the TADF efficiency is directly related with the *rISC* transition probability, that, in turns, depends on the energy difference between the S_1 and T_1 states, ΔE_{ST} according to the following simple equation [23]:

$$k_{rISC} = A exp\left(-\frac{\Delta E_{ST}}{k_B T}\right) \quad (1)$$

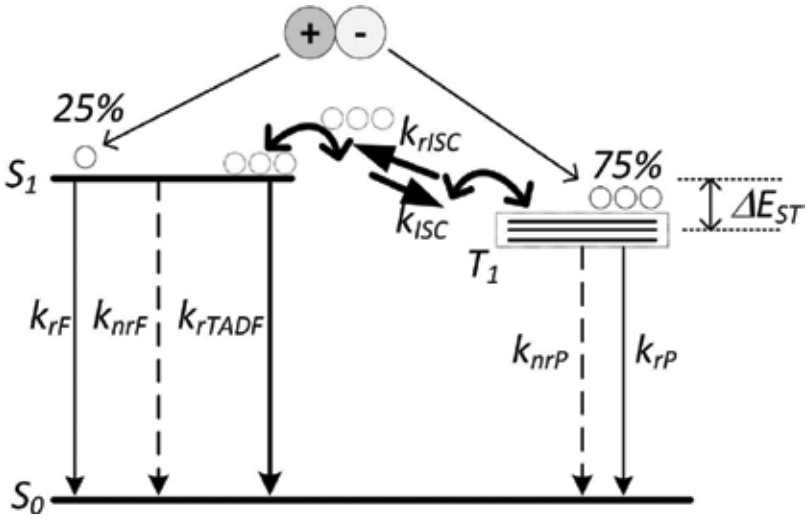

Figure 1. A simple scheme of the electroluminescence process involving an organic light emitter material. The transition probabilities (the inverse gives the transition lifetime) are k_{rF}, k_{rP}, k_{nrF}, k_{nrP}, k_{ISC} and k_{rISC} (radiative fluorescence, radiative phosphorescence, nonradiative, inter-system crossing and reverse inter-system crossing). TADF emission is related to k_{rTADF} and strictly depends on k_{rISC}.

where k_B is the Boltzmann constant, T the temperature and A the pre-exponential factor. The value of ΔE_{ST}, naturally depends on the typical energy arising from the electrostatic interactions among the molecular orbitals. Particularly important, we need to consider the one-electron orbital energy in excited state (E) (supposing a fixed nuclear model), the typical electron repulsion energy (K) and the exchange energy (J) resulting from electron–electron repulsion based on the Pauli exclusion principle, affecting two excited unpaired electrons (one in LUMO and another one in HOMO levels) [24]. As the singlet and triplet excited states have a different spin ordering, the J value is usually higher in S_1 state and lower (in the same amount) in T_1 state [20]. With such consideration, the energy associated with the S_1 and T_1 states (respectively E_{S1} and E_{T1}) and therefore the ΔE_{ST}, can be easily established, by the following relationships:

$$\begin{aligned} E_{S_1} &= E + K - J \\ E_{T_1} &= E + K - J \\ \Delta E_{ST} = E_{S_1} - E_{T_1} &\Longrightarrow \Delta E_{ST} = 2J \end{aligned} \tag{2}$$

The immediate conclusion is that the minimization of ΔE_{ST} implies a lowest possible exchange energy. Remembering that the two unpaired electrons should be considered as distributed in the frontier orbitals of the LUMO and HOMO levels (T_1 or S_1, excited states) resulting in pure LUMO-HOMO transitions, J can be given by [20]:

$$J = \iint \psi_L(r_1)\,\psi_H(r_2)\left(\frac{q^2}{r_1 - r_2}\right)\psi_L(r_2)\,\psi_H(r_1) d\,r_1\,d\,r_2 \tag{3}$$

where ψ_H, ψ_L, r_1, r_2, and q are the HOMO and LUMO wave functions, the coordinate positions and electronic charge, respectively. From this equation, is very easy to verify that a minimization of J requires a negligible wave functions overlapping and therefore, a very low (or absence) of spatial overlapping between HOMO and LUMO levels (a spatial separation between HOMO and LUMO frontier orbitals). In a single molecule, this basic rule can be obtained if the molecule has independent structural moieties, one containing electron-donor (D) and another with electron-acceptor (A) which promotes the D-A charge transfer in the excited state. Therefore, the basic rule for an efficient *rISC* process in a single molecule is to guarantee if such molecule has at least, two unities (D and A, with non-overlapped orbitals) spatially separated. This can be achieved by increasing the spatial distance between such unities using a π-conjugated link or forcing a large dihedral angle between the planes of the donor and the acceptor, i.e. roughly speaking, forces a twist between D and A unities around the common axis [25]. In any case, we expect a strong CT character in the excited states.

The physical model to explain the *rISC* process is so far little understood. The first successful application [26] precisely focuses on the twisted D-A unities. In the first explanations, the CT states are used as a key to promoting the *rISC* process (singlet and triplet character, ^{1}CT and ^{3}CT). Following the known rules, the *ISC* (and therefore the *rISC*) process will be efficient under an occurrence of symmetry change of the excited states. This means in triplet/singlet systems, if a high value for k_{ISC} and k_{rISC} exist, T_1 and S_1 can be found in LE (local excited) and CT states respectively. However, we know that efficient TADF can occur even if such rule is not observed. Moreover, the excited states involved in TADF organic material, are typically a mixture of CT-LE states and not pure CT or LE states. Furthermore, extensive studies involving photoluminescence data reveal some discrepancies and new hypothesis involving also the LE states begin to be considered. In a general organic molecule (system), the excited states can be described in terms of their binding energy: the CT (low binding energies) and LE (strong binding energies). This LE has a very high radiative probability (with a strong emission) due to the high orbitals overlapping (the dipole electrical operator in the wave functions gives a high resulting probability). The *rISC* process model with only CT states starts to pose some problems with the discovery of SOC between such intramolecular states are zero [27]. Several hypotheses have been discussed and it was found that it is possible to tune independently two excited states involved in the *rISC* process [28] (for instance with different characters like ^{1}CT and ^{3}LE); or a more sophisticated model involving a mixture of ^{3}LE and ^{3}CT states [29] giving rise to an hypothesis where the *rISC* process depends on the SOC (^{3}LE → ^{1}CT) and also on a hyperfine coupling induced *ISC* process (^{3}CT → ^{1}CT). However, and in spite of an allowed SOC between these states, the calculations of the *rISC* probabilities (relatively low) cannot explain the experimental data that gives much higher values. Recently [30] a more complex model involving two steps was proposed. In such model, the first equilibrium between ^{3}LE and ^{3}CT states is promoted by vibronic coupling between them (also called as *rIC* – reserve intersystem crossing, helping the thermally assisted internal conversation); next, a coupling between the ^{3}CT and ^{1}CT states via ^{3}LE state (very efficient) promotes the *rISC* finalization process. In this model, both SOC and vibronic coupling are involved. All these models are, in general, well supported by several experimental data but at this moment, and depending on the specific organic emitter studied, different pathways need to be considered, leading to several open questions. In any case, this topic remains heavily investigated.

Besides the usual D-A molecule separated structure, some new molecules based on D-A-D (so-called "butterfly-shaped" structure) also exhibits TADF emission. Surprisingly, in several of such molecules, the energy gap between the lowest ^{1}CT state and the lowest ^{3}LE state (with $\pi \rightarrow \pi^*$ transition) are much higher than those found between ^{1}CT and ^{3}CT energy states in the conventional D-A molecules. The explanation was the two-step model above referred. This model appears to be the most interesting and well supported by experimental results.

Particularly important in this model, is the ability to modulate the energy of the excited ^{1}CT state via the environment polarity [31]. In solution, the photophysics analysis can help in revealing the main process involved, in turn, dependent on the solvent polarity. On film (solid state), this possibility opens a wide range of choice for the organic host material in order to significantly improve the efficiency of an OLED based on a TADF material. In a simple scheme, we can, therefore, represent the excited state of the TADF molecule as shown in **Figure 2**.

It must be noted that, according to this model, and following several experimental data (see [30] and references therein) the energy transfer SOC-ISC is more efficient in a D-A perpendicular geometry, in a transition $n\pi^*$-like. This is a consequence of the maximum change in the orbital angular momentum as the SOC depends on the spin magnetic quantum number of the electrons and simultaneously on its spatial angular momentum quantum number (the SOC operator is proportional to $\hat{s} \cdot \hat{l}/\hbar^2$). Following this two steps model, the probabilities of k_{rIC} and k_{rISC} can be written in terms of both physical process involved [31]:

$$\begin{aligned} k_{rIC} &= \frac{2\pi}{\hbar Z}\left|\left\langle \psi_{3CT} \mid \hat{H}_{SOC} \mid \psi_{3LE} \right\rangle\right|^2 \times \Delta\left(E_{3LE} - E_{3CT}\right) \\ k_{rISC} &= \frac{2\pi}{\hbar Z}\left|\frac{\left\langle \psi_{1CT} \mid \hat{H}_{SOC} \mid \psi_{3LE} \right\rangle\left\langle \psi_{3LE} \mid \hat{H}_{VIB} \mid \psi_{3CT} \right\rangle}{\Delta\left(E_{3LE} - E_{3CT}\right)}\right|^2 \times \Delta\left(E_{3CT} - E_{1CT}\right) \end{aligned} \tag{4}$$

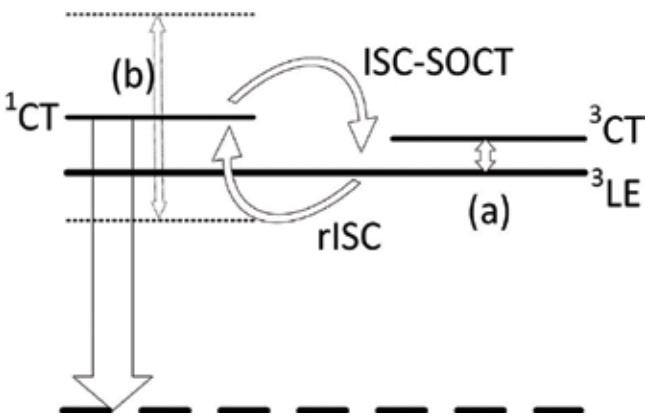

Figure 2. A simple representation of a TADF emitter in excited state, following the model proposed in [30]. In (a) the SOC-ISC transition is enhanced by vibronic coupling between the ^{3}CT and ^{3}LE states whereas in (b) the ^{1}CT state can be modulated by the environment polarity.

with Z being the canonical partition function for vibrational motion in the initial electronic state. These terms are therefore the starting point for a more detailed description of the TADF process. Knowing these probabilities, that we can estimate, several possibilities to further tuning the TADF process is possible. Despite several well-founded hypothesis, the fully understand of TADF process in organic emitters, still remains under major studies.

3. Fundamental photophysics of an organic TADF emitter

The starting point for developing an efficient OLED using TADF emitter is based on the luminescence properties of the emitter itself. As an earlier point, the physical process involved are not really straightforward, but leaving aside the pure photophysics process studies, the important figures of merit regarding efficiency can be easily obtained.

From **Figure 1**, we can formally consider two different kinds of radiative emissions arising in S_1 state: from its own electrons population (25% of excited ones) and from the population via r_{ISC} process (the remaining 75% of excited electrons). In the first case, with a very high transition probability k_F, we have a prompt fluorescence (PF) whereas in the second situation, depending on a lower k_{rISC} probability, we have a delayed fluorescence (DF). A strong TADF emission is usually observed in molecules where the yield of triplet levels formation (by intersystem crossing), as well the singlet level formation (by reverse intersystem crossing) are high (particularly the last one as expected). In this condition, we must assume that the r_{ISC} yield that is given by $\phi_{rICS} = \frac{k_{rISC}}{k_{rISC} + k_{nRP} + k_{rP}}$ is approximately equal to 1. This appears when (and usually found in TADF materials) $k_{rISC} \gg k_{nRP} + k_{rP}$, meaning that all relaxation process from triplet excited state are much less probable that the r_{ISC} (as expected). The emission from a TADF material is naturally the sum of the observed from the PF and DF and therefore its quantum yield is given by:

$$\phi_{TADF} = \phi_{PF} + \phi_{DF} = \phi_{PF} \frac{1}{1 - \phi_{rISC}\,\phi_{ISC}} \tag{5}$$

According [32], if the ratio ϕ_{DF}/ϕ_{PF} is near (or above) four, the yield of the *rISC* process will be near 100%. In practice, most TADF materials where the value of ΔE_{ST} is less than near 150 mV, such yield is obtained. In this situation, the triplet yield is relatively easy to obtain with precision, and is given by:

$$\phi_{ISC} = \frac{\phi_{DF}}{\phi_{DF} + \phi_{PF}} \tag{6}$$

This relationship can be useful to determine the ratio of ϕ_{DF}/ϕ_{PF} that is a fundamental key for the material characterization. In simple but practical ways, two different approaches can be used for such determination. Both are related to the fact that almost know TADF materials exhibit very poor or none DF in the presence of oxygen. Thus, measuring the luminescence emission parameters under a normal or degassed environment, we can achieve either PF or PF + DF. Under steady state photo physics, the direct measurement of the luminescence spectra in both environment conditions

will give only (with great certainty) the PF (normal environment) and PF + DF (degassed environment). The direct ratio of the integrated spectra (intensity) further gives a very precise value for ϕ_{DF}/ϕ_{PF}. Naturally this simple calculation is possible (quantum yield ratio from integrated intensity) because the intensity is proportional to the quantum yield and, in the case of TADF materials, the values of the proportionality constants for both emissions (DF and PF) are the same due to the fact that both arise from the same excited energy level [33]. The exact calculation is the performed considering the simple relationship is given by $\frac{I_{DF+PF}}{I_{PF}} = \frac{\phi_{DF}+\phi_{PF}}{\phi_{PF}} = 1+\frac{\phi_{DF}}{\phi_{PF}}$. **Figure 3** shows a simple example of this behavior.

By another hand, the higher transition probability associated with PF compared to the DF probability (that in a crude way depends on the *rISC* process probability) allows an experimental emission separation under the time-resolved photoluminescence (TRP). In a typical TADF material, the PF lifetime is in the order of dozens of *ns* whereas the DF lifetime falls into *μs*. Therefore, measuring both lifetimes, an estimative of the ϕ_{DF}/ϕ_{PF} can be done because the transition probabilities are related to the inverse of the lifetime. If we consider (and is a very good approach) that the emission follows a single exponential decay for both PF and DF, therefore the measured photoluminescence intensity under time can be simply given by the sum of the two single exponential decay expressions as follow:

$$I(t) = I_0^{PF} exp\left(-\frac{t}{\tau_{PF}}\right) + I_0^{DF} exp\left(-\frac{t}{\tau_{DF}}\right) \tag{7}$$

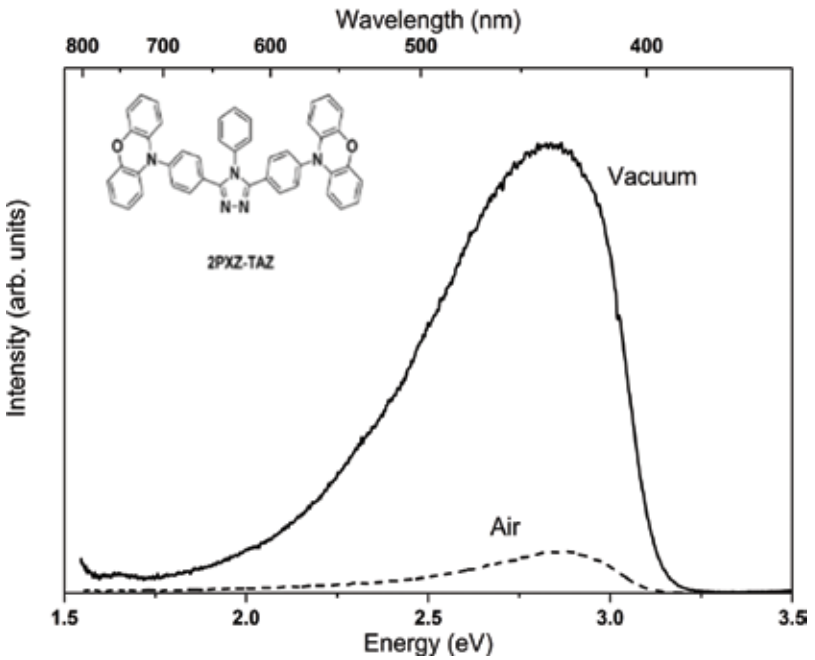

Figure 3. Steady state photoluminescence spectra of 2PX-TAZ under normal (air) and degassed (vacuum) environments. The ratio of integrated spectrum in both situations allows a simple calculation of the DF/PF quantum yield. In this case, the ratio ϕ_{DF}/ϕ_{PF} is near 9.

http://dx.doi.org/10.5772/intechopen.76048

being τ_{PF}, I_0^{PF}, τ_{DF} and I_0^{DF} the lifetime and pre-exponential intensity factor for the PF and DF. Once again, calculating the intensity (integral) for both time-resolved emissions, the ϕ_{DF}/ϕ_{PF} can be obtained and is given simply by:

$$\frac{\phi_{DF}}{\phi_{PF}} = \frac{I_0^{DF} \times \tau_{DF}}{I_0^{PF} \times \tau_{PF}} \tag{8}$$

Finally, and by TRP is possible to estimate the transition probability of the *rISC* process. Knowing the values for quantum yields and lifetime, an estimation for k_{rISC} can be given by (and considering $\phi_{rISC} \approx 1$)

$$k_{rISC} = \frac{1}{\tau_{DF}}\left(\frac{\phi_{PF} + \phi_{DF}}{\phi_{PF}}\right) \tag{9}$$

Due to several different kinds of triplet harvesting in an organic molecule, sometimes is not simple to attribute an enhanced luminescence to a TADF process. For instance, triplet-triplet annihilation (TTA) is also a wide investigated process for emission efficiency improvement. Distinguish both process is important. Due to the competition between the triplet quenching and decay of triplet states, usually the DF from TTA is non-linear on excitation energy; on the contrary, and because TADF process is purely intramolecular, its DF must follow a linear relationship with excitation energy. **Figure 4** shows an example of the 2PX-TAZ emitter.

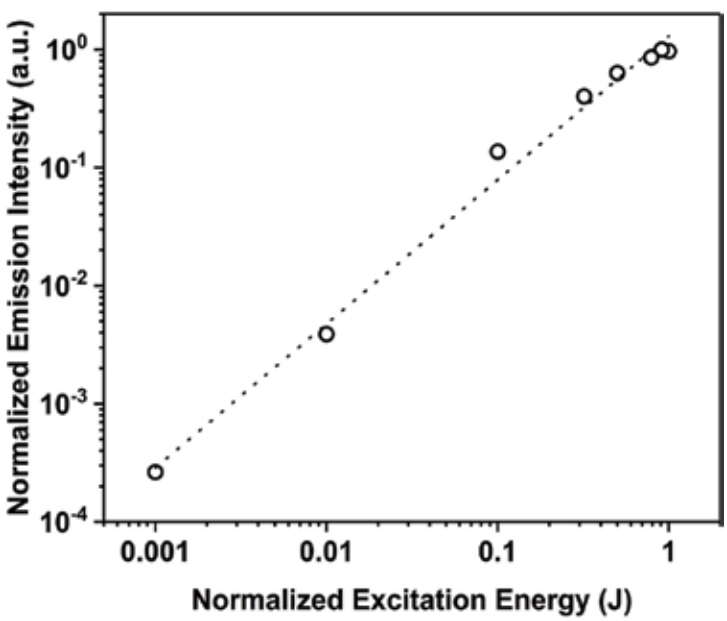

Figure 4. Emission intensity of 2PX-TAZ emitter as a function of excitation energy. The perfect linear fit is the expected result for a TADF material.

Besides the excitation energy dependence, the TADF emission is also strongly dependent on temperature. As the DF is thermally activated, we expect that its intensity decreases strongly with temperature and eventually vanishes at very low temperature. On the contrary, PF must be unaffected by thermal variations. This means that under TRP we must observe a decrease of the high lifetime emission as temperature decreases until remaining only the fast component.

The full understanding of the photo physics properties of the TADF emitter is naturally of extreme importance for further OLED development.

4. OLEDs based on TADF emitters

In the contest of finding best organic emitters for the lightening industry, in 2011 Adachi et al. [34] reported the very first purely organic TADF emitter **PIC-TRZ** (**Figure 5**) which showed promising calculated PLQY in a host matrix of mCP and was 39% and the device showed 5.3% EQE. Since then, in the past 5 years, over 200 new compounds have been reported. Among various emitters, many of them showed EQE of more than 20% composed in a device and this can be reached up to 30% using stipulated device structure with an optimized concentration of TADF emitters and fabrication process [35]. There have been several reviews published focusing on photo physics, device characteristics of TADF and chemistry of TADF emitters [20, 23, 35]. Apart from the use of TADF molecules for OLEDs, there are some challenges must be taken

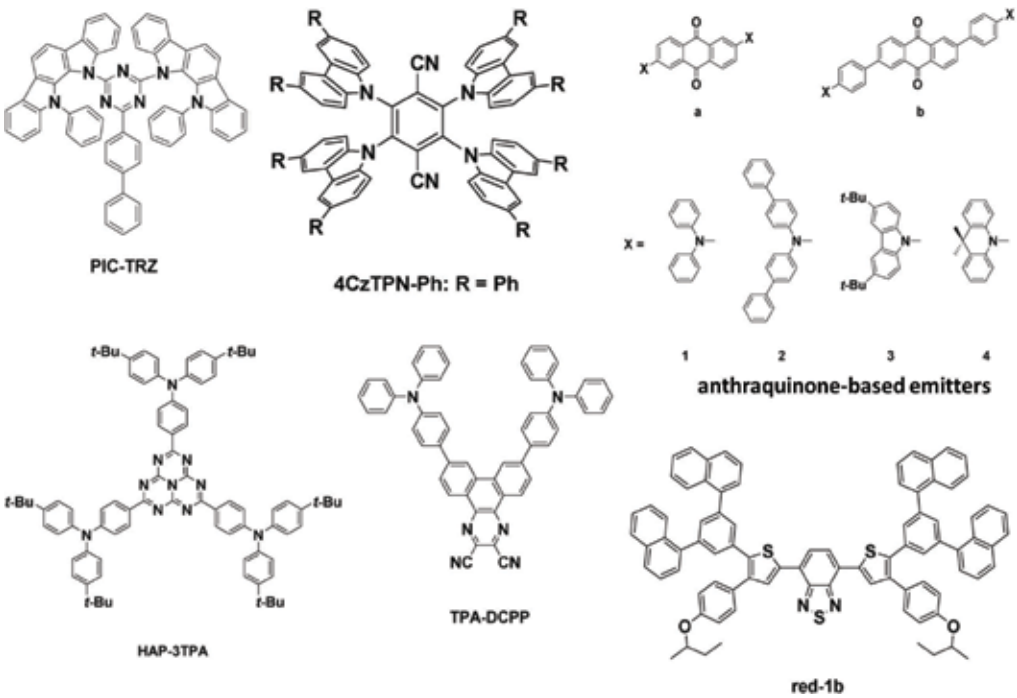

Figure 5. Chemical structures of red-orange TADF emitters.

http://dx.doi.org/10.5772/intechopen.76048

for the development of TADF emitters such as these emitters are very limited and only few can be used for highly EQE and stable OLEDs, another is the lower maximum brightness and roll-offs at high brightness related triplet annihilation [20, 36]. These can be solved by understanding the structure-property relationship in emitters. In this chapter, we focused more on the photo physical relation of TADF emitter with device performance. In this section, we will describe different TADF emitters and their photo physics-device performance characteristics.

The application of TADF emitters is generally focused on OLEDs applications. As we have discussed in photo physics behavior of TADFs, it requires a solid host to disperse TADF emitters and this host material has a strong influence on the photo physical properties of these emitters [37]. To encounter this, the design and optimization of TADF emitter is a key factor for the fabrication of OLEDs, and this requires the photo physical characterization of TADF in the host molecule which used in the device. Some of the most used hosts are DPEPO, CBP, mCP, mCBP, TPBi, TCTA and TAPC. The OLEDs are usually fabricated by thermally vacuum deposition, but several reports have been focused on fabrication via spin coating solution processed methods which is more suitable for large area OLEDs.

Many groups reported various green TADF based on different donor and acceptor molecules, due to less space it is difficult to discuss all of them. Herein, we will discuss some of the TADF red, green and blue emitters based on their donor and acceptor groups, photo-physical characteristics, and device performance.

4.1. Red-orange TADFs

Herein, we present red-orange TADF emitters which exhibit an electroluminescence peak at wavelength (EL_{max}) > 580 nm. The first reported red TADF emitter, **4CzTPN-Ph** (**Figure 5**) with green emission by Adachi et al. [38] Figure which exhibits calculated PLQY of 26% in toluene and, τ_d 1.1 μs. The device showed remarkable EQE of 11.2%, the fabricated device structure was ITO/NPD/5 wt% **4CzTPN-Ph**:CBP/TPBi/LiF/Al. In another report [39], they demonstrated the effect of a higher transition dipole moment which is induced by increasing the distance between D-A units. They compared orange-red anthraquinone based TADFs based on D-A-D (**a1-a4**) and D-Ph-A-Ph-D (**b1-b4**) molecular scaffold showing higher PLQY. The fabricated device was ITO/HAT-CN/Tris-PCz/10wt%***TADF emitter***:CBP/T2T/Bpy-TP2/LiF/Al) (Tris-PCz = 9,9′-diphenyl-6-(9-phenyl-9H-carbazol-3-yl)-9H,9′H-3,39′H-bicarbazole; T2T =2, 4,6-tris(biphenyl-3-yl)-1,3,5-triazine; Bpy- TP2 = 2,7-di(2,2′-bipyridin-5-yl)triphenylene) using **b1** emitter. The compound showed 80% PLQY and τ_d 416 μs in a host CBP matrix. The calculated ΔE_{ST} from experimental value was 0.24 eV. The device exhibit 12.5% EQE and the CIE coordinates were (0.61, 0.39).

In 2013, Li et al. [40] synthesized orange-red emitter, **HAP-3TPA** (**Figure 5**), based on heptaazaphenalene acceptor with a small ΔE_{ST} of 0.17 e ΔEST of 0.17 eV. The molecules show absorbance at 610 nm. The calculated PLQY of 6 wt% TADF in a host matrix 26mCPy was 91%, and the τ_d of 100 μs. The molecule showed very weak TADF behavior, and the ϕ_{DF}/ϕ_{PF} was 0.07 compared to ϕ_{DF}/ϕ_{PF} of 1.58 in the fabricated device i.e. ITO/NPD/6 wt% **HAP-3TPA**:26mCPy/Bphen/Mg:Ag/Ag with a high EQE value of 17.5% and the CIE was (0.60, 0.40).

In another study, Wang et al. [41] demonstrated the effect of the twist angle during the designing strategy of TADF emitters. This twist angle can be reduced by increasing the D-A distance which gives an orbital overlap to increase k_t. They synthesized the first near-infrared (NIR) TADF emitter **TPA-DCPP** (**Figure 5**) based on dicyanodiazatriphenylene acceptor moiety. The experimental calculated ΔE_{ST} was 0.13 eV. The calculated PLQY of 10 wt% **TPA-DCPP** in TPBi host matrix was 50%, and the τ_d of 86.2 μs. The fabricated device ITO/NPB/TCTA/20 wt% **TPA-DCPP**:TPBi/TPBi/LiF/Al exhibit EQE value of 9.8% with the CIE at (0.68, 0.32). Similarly, Chen et al. [42] also reported a novel solution processed red TADF using **red-1b** molecule which can undergo both TADF and TTA process, depends on current density. The calculated ΔE_{ST} was 0.40 eV. The photo-physical characteristics of the molecule are λ_{max} of 622 nm and the solid state calculated PLQY of 28%, while the EQE was very low 1.75% in fabricated device. Very recently in another report, Data et al. [43] reported dibenzeno-phenanzine acceptors based TADF emitters which showed a formation of exciplex when doped in m-MTDATA host and a strong NIR emission at 741 nm was observed with EQE of 5%, but no concluded evidence was provided in the work to support the TADF mechanism of this exciplex system.

4.2. Blue TADF emitters

In 2012, Adachi et al. reported the very first class of blue TADF emitter based on diphenylsulfone (**DPS**) as an acceptor [27] (see **Figure 6**).

To synthesize efficient blue TADF emitter and their use in the device, it is important to take account of the π-conjugation length and the redox potential of the donor and acceptor moieties and in DPS derivatives the advantage is that the oxygens of the sulfonyl group have significant electronegativity, which gives the sulfonyl group electron-withdrawing properties and sulfonyl group exhibit tetrahedral geometry which limit the conjugation [35]. The device fabricated with 10 wt% emitter showed good results, the device ITO/α-NPD/TCTA/CzSi/10 wt% *TADF emitter*:DPEPO/ DPEPO/TPBI/LiF/Al and the EQE was 9.9%, the emitter incorporated in the device was **DTS-DPS** [44]. The photo-physical characteristics of the molecules are λ_{max} of 423 nm. The calculated PLQY in DPEPO host was 80% and τ_d was to be 540 μs. The ΔE_{ST} was 0.32 eV. They suggested that for small ΔE_{ST}, the energy gap between ^{3}LE and ^{3}CT must be small, and the *rIC* occurs from ^{3}LE to ^{3}CT which was followed by *rISC* to ^{1}CT and similar results were seen in other derivatives. In a similar approach, Dias et al. proposed a mechanism to understand the mechanism of *rISC* in such type of molecules [45]. The results suggested that *rISC* mechanism is still possible if the ΔE_{ST} is greater than 0.3 eV. They studied a molecule DTC-DBT (**Figure 6**), where the ΔE_{ST} is 0.35 eV, but in the molecule, it is possible to harvest 100% triplet excitons. According to the authors, the presence of heteroatom loan pairs form "hidden" 3n-π* state sandwiched between higher ^{3}CT and lower ^{3}LE states and the up-conversion follow the pattern: ^{3}LE → -3n-π* → ^{3}CT → ^{1}CT. In similar study, Chen et al. [46] demonstrated the importance of" non-adiabatic effects in butterfly donor-acceptor-donor molecules" **DTC-DBT**, and suggested that upon the rotation of D-A groups, a conical intersection (C_1) between long-lying excited states and at C_1 "the non-adiabatic coupling matrix element between two excited stated becomes infinite, which is proportional to the RISC rate." This was further supported by Etherigton et al. [47].

http://dx.doi.org/10.5772/intechopen.76048

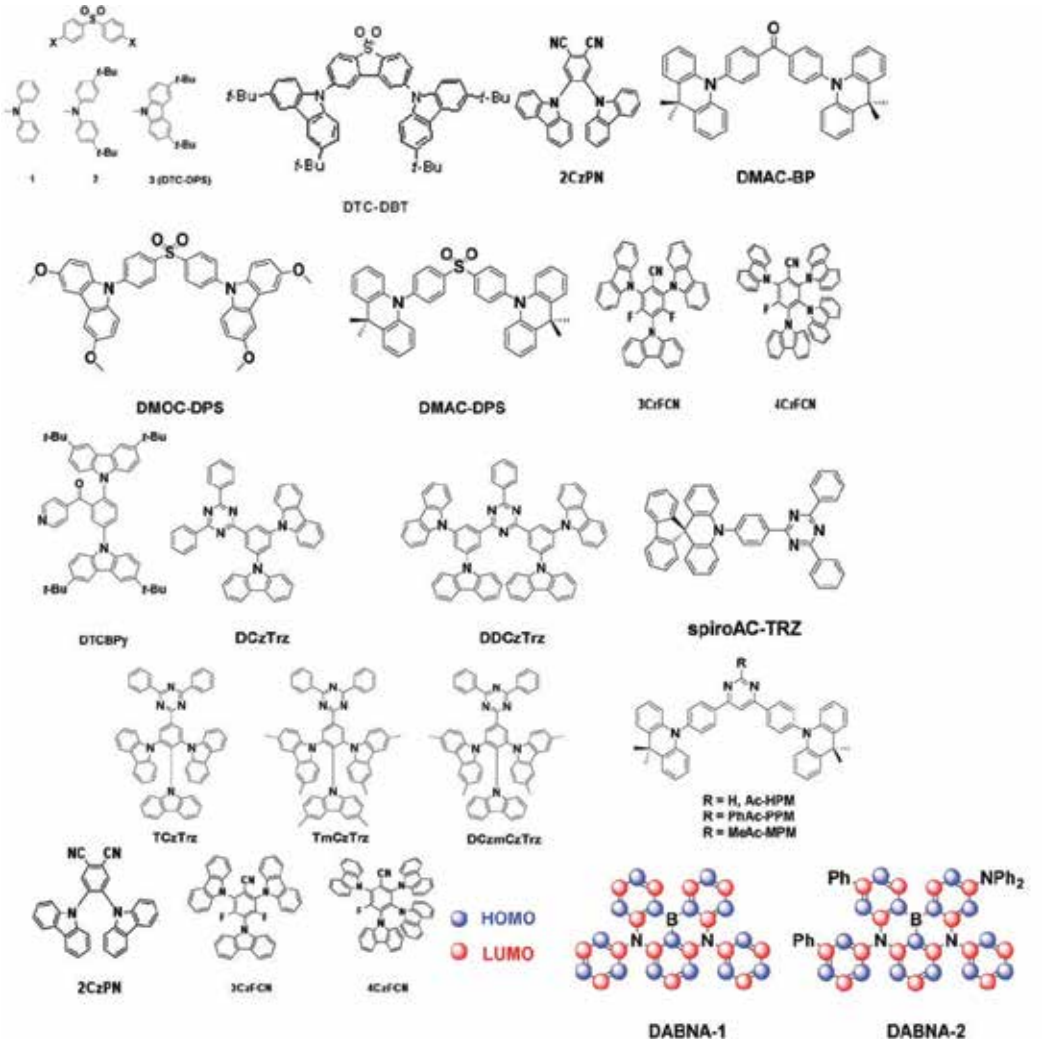

Figure 6. Chemical structures of blue TADF emitters.

Adachi et al. [48] reported deep blue emitters **DMOC-DPS** (**Figure 6**) with the ΔE_{ST} of 0.21 eV. The calculated PLQY in DPEPO host at 10 wt% was 80% along with measured τ_d of 114 μs and the device ITO/a-NPD (30 nm)/TCTA (20 nm)/CzSi (10 nm)/ **DMOC-DPS:**DPEPO (20 nm)/ DPEPO (10 nm)/TPBI (30 nm)/LiF (0.5 nm)/Al showed an EQE of 14.5%. They further reported another blue TADF **DMAC-DPS** with the absorbance of 464 nm. The PLQY in mCP host was 80%, and τ_d was 3.1 μs. For this **DMAC-DPS,** the experimentally calculated ΔE_S was very low and was 0.08 eV. The fabricated device performed at an excellent EQE of 19.5% [44], where the reduced ΔE_{ST} is a result of higher ^{3}LE state than ^{3}CT state, caused by inducement of dimethylacridan donor. Another molecule **DMAC-BP** which ΔE_{ST} is 0.07 eV with calculated PLQY of 85%, and τ_d of 2.7 μs showed EQE of 18.9%.

It is very important to design the geometry of TADF molecule to induce TADF process, to counter this, Rajmalli et al. [49] reported novel blue TADF emitters based on benzoylpyridine acceptor **DCBPy** and **DTCBPy**, in **DTCBPy** (**Figure 6**) a tert-butyl group is present. Upon photo-physical characterization, the second molecule **DTCBPy** showed a small redshift in emission by 4 nm. The ΔE_{ST} was smaller in both emitters, and was 0.07 and 0.08 eV in **DCBPy** and **DTCBPy**, respectively. The calculated PLQY in host matrix was 88 for DCBPy and 91% for DTCBPy. The PLQY in the solid state was 91% compared to lower 14–36% in solution. The device exhibit sky-blue and green emission. The EQEs was 24.0% CIE (0.17, 0.36) and 27.2% CIE (0.30, 0.64) for **DCBPy** and **DTCBPy**, respectively. The efficiency roll-off was low at practical brightness level.

In 2015, Kim et al. [50] synthesized two new blue TADF emitters **DCzTrz** and **DDCzTrz** (**Figure 6**), where "two additional carbazole moieties attached to phenyl ring in a meta fashion" in **DDCzTrz** and as "meta linkage" both emitters have similar emission as well as ΔE_{ST}. The photo-physical characteristics of both molecules are absorbance maximum of 420 and 430 nm. The calculated PLQY for both emitters was 43 and 66%, respectively. The smaller ΔE_{ST} 0.25 eV for **DCzTrz** and 0.27 eV for **DDCzTrz.** The OLED using **DDCzTrz** showed an excellent EQE of 18.9% but in the device, the LT80 (time required to drop 80% luminescence) was 52 h, three-time longer than conventional blue phosphorescent Iridium complex. It is due to first stabilization through carbazole moiety, secondly, stable positive carbazole and negative triazine excited state pair, and thirdly excellent glass transition temperature for both 160 for **DCzTrz** and 218°C for **DDCzTrz** give the stability to the device. But the device composed of **DCzTrz** was stable only for 5 h and this caused due to the high emission of the molecule. Upon modification of **DCTrz** through the addition of more carbazole donors, they synthesized another three molecules **TCzTrz, TmCzTrz**, and **DCzmCzTrz** (**Figure 6**). Where calculated PLQY was 100% in DPEPO host, and the ΔE_{ST} was 0.16, 0.07, and 0.20 eV, respectively [51]. It was found that in **TCzTrz** the ΔE_{ST} is lower by 0.09 eV compare to **DCzTrz**. The device composed of **TCzTrz** showed an excellent EQE of 25.5%, while **TmCzTrz** and **DCzmCzTrz** showed EQE of 25.3 and 21.3%, respectively.

In another study, Lin et al. demonstrated [52] a novel triazine-based blue TADF emitter named **spiroAC-TRZ** (**Figure 6**) which showed photo-physical characteristics of calculated PLQY of 100% in 12 wt% mCPCN host, τ_d of 2.1 μs. The experimentally calculated ΔE_{ST} was very small and to be 0.07 eV. The device ITO/ MoO3/TAPC/mCP/12 wt% **spiroAC-TRZ**:mCPCN/3TPYMB/ LiF/Al an EQE of 37%, which is highest among the reported blue TADF. In a similar approach, Komatsu et al. [53] reported three novel deep blue TADF (**Figure 6**). **Ac-RPMs**, on the modification of triazine acceptor to pyrimidine. All the compounds exhibited similar photo-physical properties i.e. PLQY of 80%, τ_d of 26.2 μs in a host matrix at 10 wt% in DPEPO and the calculated ΔE_{ST} was 0.19 eV for **Ac-MPM**, and the OLEDs showed an EQE of 24.5% and CIE coordinates of (0.19, 0.37), interestingly the turn-on voltage vas very low and was 2.80 V, such device can be used for highly efficient light devices.

Among various D-A and D-A-D structured TADF molecules, the main chemical moiety plays an important role for the exhibition of the TADF behavior, and as we have discussed various acceptors have been used for the synthesis of TADF materials, among them Cyano-based

acceptors are used as most usual building blocks for the synthesis of deep-blue TADFs. The first Cyano based blue TADF **2CzPN** (**Figure 6**) was firstly reported by Adachi et al. [36] PLQY of 47% in solution state and the EQE was 13.6% in device. Sun et al. [54] reported a blue TADF emitter showing an excellent EQE of 21.8% in composed OLED structure of ITO/4 wt% ReO3:mCP/5 wt% **TADF emitter**:mCP:PO15/4 wt% Rb2CO3:PO-15/Al) (PO-15 = poly[N,N′-bis(4-butylphenyl)-N,N′-bisphenylbenzidine]) by using a mixed co-host system (mCP:PO15 = 1:1).

Solution-processed TADF materials was reported by Cho et al. [55], they synthesized two blue TADF emitters named **3CzFCN** and **4CzFCN** (**Figure 6**), showing photo-physical characteristics of calculated PLQY in 10 wt% diphenyldi(4-(9-carbazolyl)phenyl)silane (SiCz) host at 10 wt%, and was 74% for **3CzFCN** and 100% for **4CzFCN**, while the experimentally calculated small ΔE_{ST} of 0.06 eV for both emitters. The λ_{max} was 440 and 460 nm, respectively. The fabricated device with **4CzFCN** emitter showed an excellent EQE of 20% with CIE coordinates of (0.16, 0.26), the device structure was ITO/PEDOT:PSS/PVK/15 wt%**4CzFCN**:SiCz/TPBI/LiF/Al.

In another study, very recently, Hatakeyama et al. [56] demonstrated synthesis of boron-based acceptor TADFs. They synthesized TADF emitters **DABNA-1** and **DABNA-2** (**Figure 6**) showing ΔE_{ST} of 0.18 and 0.14 eV, respectively. The λ_{max} was 460 and 469 nm, while calculated PLQY in mCBP host at 1 wt% was 88 and 90%. The device fabricated with **DABNA-2** emitter showed an excellent EQE of 20.2%. In such boron based TADFs, the ΔE_{ST} is very low, this is due to the presence of strong LUMO localization called as "multiple resonance effect", induced by boron atom. The PLQY in solid state is 87–100%, which makes boron based TADF emitter a potential candidate for blue TADFs.

4.3. Green-yellow TADFs

Among various TADF emitters, plenty of them are the green-yellow emitter and most those green to yellow emitters are based on cyano-based acceptors. The molecular design of these cyano-based emitters is based "on the presence of a twisted conformation of donor carbazoles with respect to phthalonitrile plane" to confer the HOMO-LUMO separation and result to lower ΔE_{ST}. These cyano-based green TADF emitters are classified in three categories: (a) monomeric series with orthosteric hindrance, (b) homoconjugation series, and (3) dimeric emitters. In monomeric emitters, ΔE_{ST} is very small and high PLQY yield. In homoconjugation series, the HOMO and LUMO separation is easily achievable but lower PLQY yield and in dimeric series the ΔE_{ST} is very higher i.e. 0.11–0.21 eV. The first green emitter was reported by Adachi et al. [38] in 2012, **4CzIPN** (**Figure 7**), exhibiting ΔE_{ST} of 0.08 eV. The calculated PLQY in CBP host was 82% and τ_d of 3370 μs and the device showed excellent 19.3% EQE.

In the similar contest, Taneda and co-workers [57] synthesized a highly efficient green TADF emitter **3DPA3CN** (**Figure 7**) and it showed PLQY of 100% in solid state and 100% triplet harvesting via *rISC* mechanism. The molecule showed photo-physical characteristics of absorbance of 533 nm. The calculated PLQY of 6 wt% thin film in DPEPO host matrix was 100% while the τ_d was 550. The ΔE_{ST} was to be small 0.10 eV and is due to the strongly localized molecular geometry the HOMO and LUMO, which gives the small separation between

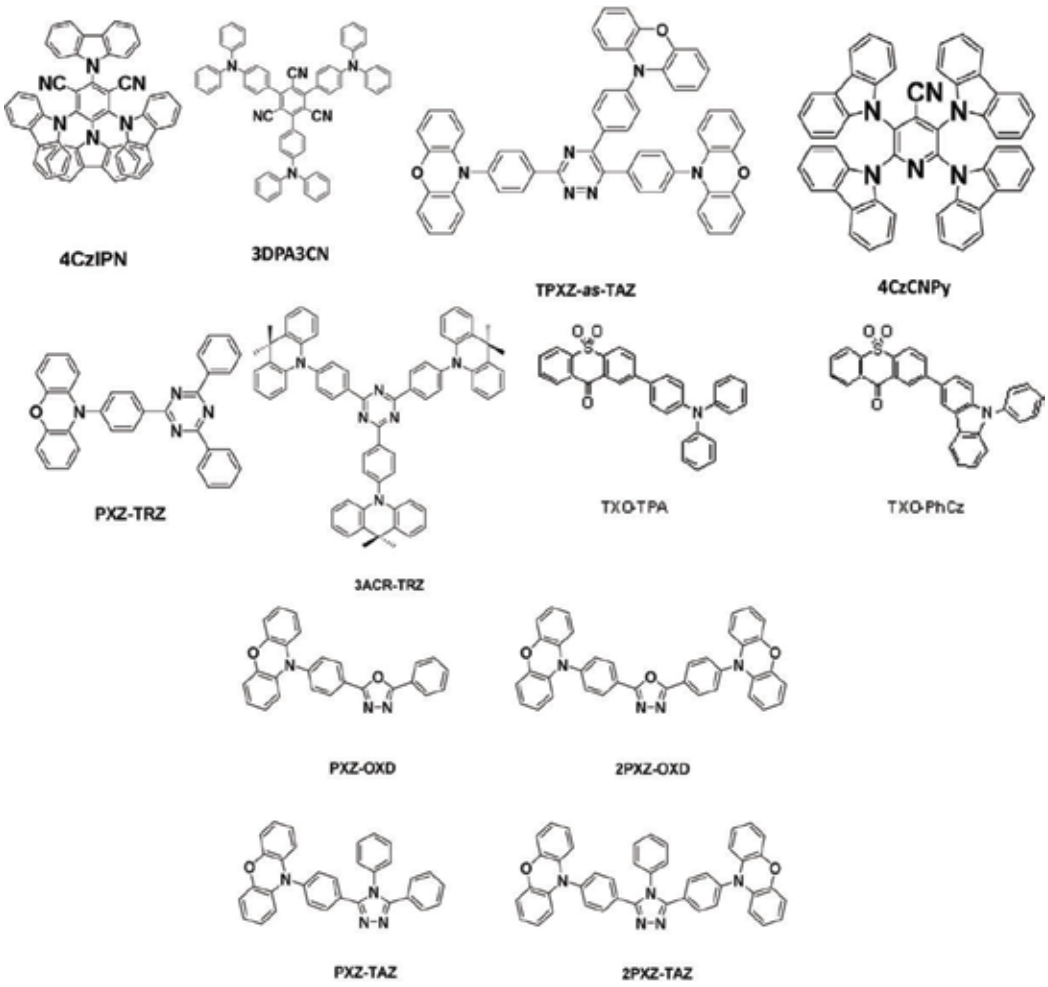

Figure 7. Chemical structures of green-yellow TADF emitters.

HOMO and LUMO. The fabricated device ITO/α-NPD/mCBP/6 wt% ***TADF emitter***:DPEPO/TPBI/LiF/Al) shows an excellent EQE of 21.4% with EL_{max} at ≈540 nm. In another study, Xiang et al. [58] reported a triazine based acceptor along with phenoxazine as donor and synthesized a yellow TADF emitter **TPXZ-as-TAZ** (**Figure 7**) with very low ΔE_{ST} of 0.03 eV. The molecule showed excellent EQE of 13%. The calculated PLQY in 1.5 wt% thin film in host CBP was 53% while the calculated τ_d was to be 1.10 μs. The λ_{max} for emitter was 555 nm.

Tang et al. revealed the strategy to synthesized solution processed green TADF emitters [59]. They synthesized emitter **4CzCNPy** (**Figure 7**) which has small ΔE_{ST} of 0.07 eV. The λ_{max} for emitter was 560 nm. The calculated PLQY was quite low in toluene with a value of 55% and τ_d calculated of 8.4 μs. The fabricated device ITO/PEDOT:PSS/8 wt% ***TADF emitter***:mCP/TmPyPB/LiF/Al showed EQE of 11.3% and CIE coordinate was (0.34, 0.59). They suggested that without cyano group the TADF emission could not be observed in the molecule along

with enhancement to the PLQY. In this molecule, the emission is dominated by ^{1}CT state to reduce the n-π^* quenching of the 4CzPy group.

Apart from Cyano-based green TADF emitters, many researchers reported TADF emitters based on 1,2,5-triazine acceptor (**TRZ**). Tanaka and co-workers [60] reported in 2012 a TADF emitter **PXZ-TRZ** (**Figure 7**) with a small ΔE_{ST} exhibiting λ_{max}: near 540 nm. The calculated PLQY of the thin film in 6 wt% CBP was 66%, while τ_d was 0.68 μs. The twisted structure of the phenoxazine can easily be achieved and induces the charge transfer, results to a small ΔE_{ST} of 0.07 eV. In such molecule, the dihedral angle between donor and acceptor is 74.9, which helps to localize the HOMO and LUMO for efficient TADF exhibition. The device was fabricated using the emitter ITO/α-NPD/6 wt% ***TADF emitter***:CBP/TPBi/LiF/Al showed EQE of 12.5%. Adachi et al. [61] also reported anther green emitter based on TRZ acceptor, **3ACR-TRZ** (**Figure 7**), with a small ΔE_{ST} of 0.02 eV which can be solution processed. It exhibits the Photo-physical characteristics of λ_{max} of 504 nm. The calculated PLQY in 16 wt% CBP was near a unit value of 98% and τ_d of 6.7 μs in Host matrix, while in device ITO/PEDOT:PSS/16 wt% ***TADF emitter***:CBP/BmPyPhB/Liq/Al, the EQE was 18.6% along with EL_{max} at 520 nm.

In 2014, Wang et al. reported [62] sulfone-based acceptor green TADF emitters. They synthesized two green TADF emitter named **TXO-PhCz** and **TXO-TPA** (**Figure 7**). The photo-physical characteristic of these molecules is λ_{max} of 520 nm, calculated PLQY of thin film was 90% in 5 wt% mCP, and a small ΔE_{ST} value of 0.07 eV for TXO-PhCz and λ_{max} of 580 nm, the PLQY of thin film was 83% and even smaller ΔE_{ST} of 0.05 eV were demonstrated. The fabricated device structure was ITO/PEDOT (30 nm)/ TAPC (20 nm)/***TADF emitter*** 5 wt%: mCP (35 nm)/TmPyPB (55 nm)/ LiF(0.9 nm)/Al and the device showed an EQEs of 21.5% for **TXO-TPA** emitter and 18.5% for **TXP-PhCz** emitter, respectively with the turn-on voltage of 4.7–5.2 V which is low for such devices.

1,3,4-Oxadiazole was used to synthesized green TADF emitter and these emitters are most commonly used for the applications. Three new green TADF emitters were synthesized by Lee et al. [63]. The three emitters were **PXZ-OXD, PXZ-TAZ, 2PXZ-OXD,** and **2PXZ-TAZ** (**Figure 7**). In emitters, the D-A moieties, where the donor was phenoxazine group while the acceptor was 1,3,4-oxadiazole and 1,2,4-triazole. In molecules, the PLQY was calculated in a host material and the PLQY was high in donor-acceptor-donor **2PXZ-OXD** and **2PXZ-TAZ** with high *rISC* compare to donor-acceptor **PXZ-OXD** and **PXZ-TAZ** molecules. The best device showed an EQE of 14.9% with emitter as **2PXZ-OXD**. The emitter exhibit photo-physical characteristics of λ_{max} of 517 nm, PLQY yield was 87%, τ_d of 520 μs in 6 wt% DPEPO and the ΔE_{ST} of 0.15 eV and the fabricated device structure was ITO/NPD (30 nm)/mCP (10 nm)/6 wt% ***TADF emitter***: DPEPO (15 nm)/DPEPO (10 nm)/TPBi (40 nm)/ LiF (0.8 nm)/Al (90 nm).

Many groups reported various green TADF based on different donor and acceptor molecules. The more significant are focused here.

5. Conclusions and outlook

Past few years have witnessed tremendous development in the field of organic electronics and especially in synthesis of organic light emitting materials which helped to boost the cost

reduction of OLEDs and performance enhancement. The potential inexpensive synthesis methods, OLEDs fabrication process, flexibility and lightweight make them one of the promising materials for energy devices. A large number of phosphorescent and fluorescent organic materials have been already synthesized for their use in OLEDs. Recently, TADF materials have been introduced in OLEDs fabrication to achieve 100% IQE and high EQE, which can be achieved near 50%.

The actual development of organic TADF emitters achieves a status that surpasses a simple curiosity. The new OLED framework based on highly efficient TADF materials opens a new field of applications for display and lightening. These materials, based on separated donor-acceptor moieties in one molecule, leads to a unique luminescent process of a triplet harvesting in the excited state with a further huge increase of internal efficiency up to the 100% limit. This simple way to tailored pure organic emitters is really one of the most recent advances in chemistry and OLEDs filed. Achieving very high external efficiencies without using an expensive and rare transition metals, puts the organic emitters towards new possibilities. Particularly important is the application in lighting from large area emitters, a field that is until now, a technological problem. The possibility to have a full range color emitters with high efficiency (as shown, and particularly in blue) is also an outstanding achievement towards a new device design and application, particularly in white emission. Nevertheless, improving the efficiency towards the theoretical efficiency limit, can only be achieved with a deep understand of the TADF process in these organic molecules. This is due to the fact that the interactions between energy levels of TADF emitter and the host can condition the emission due to the TADF process itself as referred before. Thus, the next steps must be focused on the physical models for this *rISC* pathway and the relationship with the molecular structure. In the OLEDs point of view, the design of reliable host materials that fulfills the requirements needs to allow an efficient luminesce emission form the TADFs. A new era is opened.

TADFs have been studied and used for OLEDs so far, and this field is relatively young but it has developed significantly during the past 5 years. By the incorporation of TADFs 40–50% EQE can be achieved. However, at the present stage despite of numerous characterization techniques to understand the TADF behavior, more rigorous efforts are required for their understanding and use for commercially production. The fabrication cost of the OLEDs based on TADF emitter should be less to make them major candidate in both display and lightening industry and the cost is critical. To reduce the cost, it is necessary to develop solution processed OLED fabrication methods and synthesis of polymeric or dendrimeric TADF emitters. These TADFs have already been found a significant role in next-generation displays and lightning materials and their use can only be realized as their synthesis characterization and device fabrication progresses.

Acknowledgements

The authors would like to acknowledge the i3N support from UID/CTM/50025/2013 and the EXCILIGHT Project from the European Union's Horizon 2020 research and innovation program under the Marie Sklodowska-Curie grant agreement No 674990.

Author details

Manish Kumar[1,2], Miguel Ribeiro[1] and Luiz Pereira[2]*

*Address all correspondence to: luiz@ua.pt

1 CeNTI – Centre for Nanotechnologies and Smart Materials, R. Fernando Mesquita, Portugal

2 Department of Physics and i3N – Institute for Nanostructures, Nanomodulation and Nanofabrication, University of Aveiro, Portugal

References

[1] Tang CW, Van Slyke SA. Organic electroluminescent diodes. Applied Physics Letters. 1987;**51**(12):913-915. DOI: 0.1063/1.98799

[2] Yersin H. Highly Efficient OLEDs with Phosphorescent Materials. 1st ed. Verlag GmbH & Co. KGraA: Wiley-VCH; 2008

[3] Franky S, editor. Organic Electronics Materials, Processing, Devices and Applications. 1st ed. Boca Raton: CRC Press; 2010

[4] Gaspar DJ, Polikarpov E, editors. OLED Fundamentals: Materials, Devices, and Processing of Organic Light-Emitting Diodes. 1st ed. Boca Raton: CRC Press; 2015

[5] Sasabe H, Kido J. Recent progress in phosphorescent organic light-emitting devices. European Journal of Organic Chemistry. 2013;**2013**(14):7653-7663. DOI: 10.1002/ejoc.201300544

[6] Baldo M, Lamansky S, Burrows P, Thompson M, Forrest S. Very high-efficiency green organic light-emitting devices based on electrophosphorescence. Applied Physics Letters. 1999;**75**(1):4-6. DOI: 10.1063/1.124258

[7] Adachi C, Baldo MA, Thompson ME, Forrest SR. Nearly 100% internal phosphorescence efficiency in an organic light-emitting device. Journal of Applied Physics. 2001;**90**(10):5048-5051. DOI: 10.1063/1.1409582

[8] Tsuzuki T, Nakayama Y, Nakamura J, Iwata T, Tokito S. Efficient organic light-emitting devices using an iridium complex as a phosphorescent host and a platinum complex as a red phosphorescent guest. Applied Physics Letters. 2006;**88**(24):243511. DOI: 10.1063/1.2213017

[9] Kwong RC, Sibley S, Dubovoy T, Baldo M, Forrest SR, Thompson ME. Efficient, saturated red organic light emitting devices based on phosphorescent platinum(II) porphyrins. Chemistry of Materials. 1999;**11**(12):3709-3713. DOI: 10.1021/cm9906248

[10] Kalinowski J, Fattori V, Cocchi M, Williams JG. Light-emitting devices based on organometallic platinum complexes as emitters. Coordination Chemistry Reviews. 2011;**255**(21):2401-2425. DOI: 10.1016/j.ccr.2011.01.049

[11] Sun Y, Giebink NC, Kanno H, Ma B, Thompson ME, Forrest SR. Management of singlet and triplet excitons for efficient white organic light-emitting devices. Nature. 2006; **440**(7086):908-912. DOI: 10.1038/nature04645

[12] Tanaka D, Sasabe H, Li YJ, Su SJ, Takeda T, Kido J. Ultra high efficiency green organic light-emitting devices. Japanese Journal of Applied Physics. 2006;**46**(1L):L10. DOI: 10.1143/JJAP.46.L10

[13] Reineke S, Lindner F, Schwartz G, Seidler N, Walzer K, Lüssem B, Leo K. White organic light-emitting diodes with fluorescent tube efficiency. Nature. 2009;**459**(7244):234-238. DOI: 10.1038/nature08003

[14] Helander MG, Wang ZB, Qiu J, Greiner MT, Puzzo DP, Liu ZW, Lu ZH. Chlorinated indium tin oxide electrodes with high work function for organic device compatibility. Science. 2011;**332**(6032):944-947. DOI: 10.1126/science.1202992

[15] Tao Y, Wang Q, Yang C, Zhong C, Qin J, Ma D. Multifunctional triphenylamine/oxadiazole hybrid as host and exciton-blocking material: High efficiency green phosphorescent OLEDs using easily available and common materials. Advanced Functional Materials. 2010;**20**(17):2923-2929. DOI: 10.1002/adfm.201000669

[16] Lee CW, Lee JY. Above 30% external quantum efficiency in blue phosphorescent organic light-emitting diodes using Pyrido [2, 3-b] indole derivatives as host materials. Advanced Materials. 2013;**25**(38):5450-5454. DOI: 10.1002/adma.201301091

[17] Baldo MA, O'brien DF, You Y, Shoustikov A, Sibley S, Thompson ME, Forrest SR. Highly efficient phosphorescent emission from organic electroluminescent devices. Nature. 1998;**395**(6698):151-154. DOI: 10.1038/25954

[18] Kondakov DY, Pawlik TD, Hatwar TK, Spindler JP. Triplet annihilation exceeding spin statistical limit in highly efficient fluorescent organic light-emitting diodes. Journal of Applied Physics. 2009;**106**(12):124510. DOI: 10.1063/1.3273407

[19] Endo A, Sato K, Yoshimura K, Kai T, Kawada A, Miyazaki H, Adachi C. Efficient up-conversion of triplet excitons into a singlet state and its application for organic light emitting diodes. Applied Physics Letters. 2011;**98**(8):42. DOI: 10.1063/1.3558906

[20] Tao Y, Yuan K, Chen T, Xu P, Li H, Chen R, Zheng C, Zhang L, Huang W. Thermally activated delayed fluorescence materials towards the breakthrough of organoelectronics. Advanced Materials. 2014;**26**(47):7931-7958. DOI: 10.1002/adma.201402532

[21] Adachi C. Third-generation organic electroluminescence materials. Japanese Journal of Applied Physics. 2014;**53**(6):060101. DOI: 10.7567/jjap.53.060101

[22] Pereira L. Organic Light Emitting Diodes - The Use of Rare Earth and Transition Metals. Singapore: Pan Stanford Publishing; 2012. 348p. ISBN: 978-9814267298

[23] Dias Fernando B, Penfold Thomas J, Monkman AP. Photophysics of thermally activated delayed fluorescence molecules. Methods and Applications in Fluorescence. 2017;**5**:012001. DOI: 10.1088/2050-6120/aa537e

[24] Turro NJ, Scaiano JC, Ramamurty V. Principles of Molecular Photochemistry: An Introduction. 1st ed. Mill Valleri, CA, USA: University Science Books; 2010

[25] Wong Michael Y, Eli Z-C. Purely organic thermally activated delayed fluorescence materials for organic light-emitting diodes. Advanced Materials. 2017;**29**:1605444. DOI: 10.1002/adma.201605444

[26] Milián-Medina B, Gierschner J. Computational design of low singlet–triplet gap all-organic molecules for OLED application. Organic Electronics. 2012;**13**(6):985-991. DOI: 10.1016/j.orgel.2012.02.010

[27] Zhang Q, Li J, Shizu K, Huang S, Hirata S, Miyazaki H, Adachi C. Design of efficient thermally activated delayed fluorescence materials for pure blue organic light emitting diodes. Journal of the American Chemical Society. 2012;**134**(36):14706-14709. DOI: 10.1021/ja306538w

[28] Lim BT, Okajima S, Chandra AK, Lim EC. Radiationless transitions in electron donor-acceptor complexes: Selection rules for S1 → T intersystem crossing and efficiency of S1 → S0 internal conversion. Chemical Physics Letters. 1981;**79**(1):22-27. DOI: 10.1016/0009-2614(81)85280-3

[29] Nobuyasu RS, Ren Z, Griffiths GC, Batsanov AS, Data P, Yan S, Monkman AP, Bryce MR, Dias FB. Rational design of TADF polymers using a donor–acceptor monomer with enhanced TADF efficiency induced by the energy alignment of charge transfer and local triplet excited states. Advanced Optical Materials. 2016;**4**(4):597-607. DOI: 10.1002/adom.201500689

[30] Ogiwara T, Wakikawa Y, Ikoma T. Mechanism of intersystem crossing of thermally activated delayed fluorescence molecules. The Journal of Physical Chemistry. A. 2015;**119**(14):3415-3418. DOI: 10.1021/acs.jpca.5b02253

[31] Gibson J, Monkman AP, Penfold TJ. The importance of vibronic coupling for efficient reverse intersystem crossing in thermally activated delayed fluorescence molecules. ChemPhysChem. 2016;**17**(19):2956-2961. DOI: 10.1002/cphc.201600662

[32] Meches G, Goushi K, Potscavage WJ, Adachi C. Influence of host matrix on thermally-activated delayed fluorescence: Effects on emission lifetime, photoluminescence quantum yield, and device performance. Organic Electronics. 2014;**15**(9):2027-2037. DOI: 10.1016/j.orgel.2014.05.027

[33] Dias FB, Santos J, Graves DR, Data P, Nobuyasu RS, Fox MA, Batsanov AS, Palmeira T, Berberan-Santos MN, Bryce MR, Monkman AP. The role of local triplet excited states and D-A relative orientation in thermally activated delayed fluorescence: Photophysics and devices. Advancement of Science. 2016;**3**(12):1600080. DOI: 10.1002/advs.201600080

[34] Kaji H, Suzuki H, Fukushima T, Shizu K, Suzuki K, Kubo S, Komino T, Oiwa H, Suzuki F, Wakamiya A, Murata Y. Purely organic electroluminescent material realizing 100% conversion from electricity to light. Nature Communications. 2015;**19**(6):8476. DOI: 10.1038/ncomms9476

[35] Yang Z, Mao Z, Xie Z, Zhang Y, Liu S, Zhao J, Xu J, Chi Z, Aldred MP. Recent advances in organic thermally activated delayed fluorescence materials. Chemical Society Reviews. 2017;**46**(3):915-1016. DOI: 10.1039/C6CS00368K

[36] Masui K, Nakanotani H, Adachi C. Analysis of exciton annihilation in high-efficiency sky-blue organic light-emitting diodes with thermally activated delayed fluorescence. Organic Electronics. 2013;**14**(11):2721-2726. DOI: 10.1016/j.orgel.2013.07.010

[37] Komino T, Nomura H, Koyanagi T, Adachi C. Suppression of efficiency roll-off characteristics in thermally activated delayed fluorescence based organic light-emitting diodes using randomly oriented host molecules. Chemistry of Materials. 2013;**25**(15):3038-3047. DOI: 10.1021/cm4011597

[38] Uoyama H, Goushi K, Shizu K, Nomura H, Adachi C. Highly efficient organic light-emitting diodes from delayed fluorescence. Nature. 2012;**492**(7428):234-238. DOI: 10.1038/nature11687

[39] Zhang Q, Kuwabara H, Potscavage WJ Jr, Huang S, Hatae Y, Shibata T, Adachi C. Anthraquinone-based intramolecular charge-transfer compounds: Computational molecular design, thermally activated delayed fluorescence, and highly efficient red electroluminescence. Journal of the American Chemical Society. 2014;**136**(52):18070-18081. DOI: 10.1021/ja510144h

[40] Li J, Nakagawa T, Macdonald J, Zhang Q, Nomura H, Miyazaki H, Adachi C. Highly efficient organic light-emitting diode based on a hidden thermally activated delayed fluorescence channel in a heptazine derivative. Advanced Materials. 2013;**25**(24):3319-3323. DOI: 10.1002/adma.201300575

[41] Wang S, Yan X, Cheng Z, Zhang H, Liu Y, Wang Y. Highly efficient near-infrared delayed fluorescence organic light emitting diodes using a phenanthrene-based charge-transfer compound. Angewandte Chemie, International Edition. 2015;**54**(44):13068-13072. DOI: 10.1002/anie.201506687

[42] Chen P, Wang LP, Tan WY, Peng QM, Zhang ST, Zhu XH, Li F. Delayed fluorescence in a solution-processable pure red molecular organic emitter based on dithienylbenzothiadiazole: A joint optical, electroluminescence, and magnetoelectroluminescence study. ACS Applied Materials & Interfaces. 2015;**7**(4):2972-2978. DOI: 10.1021/am508574m

[43] Data P, Pander P, Okazaki M, Takeda Y, Minakata S, Monkman AP. Dibenzo [a, j] phenazine-cored donor–acceptor–donor compounds as green-to-red/NIR thermally activated delayed fluorescence organic light emitters. Angewandte Chemie, International Edition. 2016;**55**(19):5739-5744. DOI: 10.1002/anie.201600113

[44] Zhang Q, Li B, Huang S, Nomura H, Tanaka H, Adachi C. Efficient blue organic light-emitting diodes employing thermally activated delayed fluorescence. Nature Photonics. 2014;**8**(4):326-332. DOI: 10.1038/nphoton.2014.12

[45] Dias FB, Bourdakos KN, Jankus V, Moss KC, Kamtekar KT, Bhalla V, Santos J, Bryce MR, Monkman AP. Triplet harvesting with 100% efficiency by way of thermally activated

delayed fluorescence in charge transfer OLED emitters. Advanced Materials. 2013; **25**(27):3707-3714. DOI: 10.1002/adma.201300753

[46] Chen XK, Zhang SF, Fan JX, Ren AM. Nature of highly efficient thermally activated delayed fluorescence in organic light-emitting diode emitters: Nonadiabatic effect between excited states. The Journal of Physical Chemistry C. 2015;**119**(18):9728-9733. DOI: 10.1021/acs.jpcc.5b00276

[47] Etherington MK, Gibson J, Higginbotham HF, Penfold TJ, Monkman AP. Revealing the spin–vibronic coupling mechanism of thermally activated delayed fluorescence. Nature Communications. 2016;**7**. DOI: 10.1038/ncomms13680

[48] Wu S, Aonuma M, Zhang Q, Huang S, Nakagawa T, Kuwabara K, Adachi C. High-efficiency deep-blue organic light-emitting diodes based on a thermally activated delayed fluorescence emitter. Journal of Materials Chemistry C. 2014;**2**(3):421-424. DOI: 10.1039/C3TC31936A

[49] Rajamalli P, Senthilkumar N, Gandeepan P, Huang PY, Huang MJ, Ren-Wu CZ, Yang CY, Chiu MJ, Chu LK, Lin HW, Cheng CH. A new molecular design based on thermally activated delayed fluorescence for highly efficient organic light emitting diodes. Journal of the American Chemical Society. 2016;**138**(2):628-634. DOI: 10.1021/jacs.5b10950

[50] Kim M, Jeon SK, Hwang SH, Lee JY. Stable blue thermally activated delayed fluorescent organic light-emitting diodes with three times longer lifetime than phosphorescent organic light-emitting diodes. Advanced Materials. 2015;**27**(15):2515-2520. DOI: 10.1002/adma.201500267

[51] Lee DR, Kim M, Jeon SK, Hwang SH, Lee CW, Lee JY. Design strategy for 25% external quantum efficiency in green and blue thermally activated delayed fluorescent devices. Advanced Materials. 2015;**27**(39):5861-5867. DOI: 10.1002/adma.201502053

[52] Lin TA, Chatterjee T, Tsai WL, Lee WK, Wu MJ, Jiao M, Pan KC, Yi CL, Chung CL, Wong KT, Wu CC. Sky-blue organic light emitting diode with 37% external quantum efficiency using thermally activated delayed fluorescence from spiroacridine-triazine hybrid. Advanced Materials. 2016;**28**(32):6976-6983. DOI: 10.1002/adma.201601675

[53] Komatsu R, Sasabe H, Seino Y, Nakao K, Kido J. Light-blue thermally activated delayed fluorescent emitters realizing a high external quantum efficiency of 25% and unprecedented low drive voltages in OLEDs. Journal of Materials Chemistry C. 2016;**4**(12):2274-2278. DOI: 10.1039/C5TC04057D

[54] Sun JW, Kim KH, Moon CK, Lee JH, Kim JJ. Highly efficient sky-blue fluorescent organic light emitting diode based on mixed cohost system for thermally activated delayed fluorescence emitter (2CzPN). ACS Applied Materials & Interfaces. 2016;**8**(15):9806-9810. DOI: 10.1021/acsami.6b00286

[55] Cho YJ, Chin BD, Jeon SK, Lee JY. 20% external quantum efficiency in solution-processed blue thermally activated delayed fluorescent devices. Advanced Functional Materials. 2015;**25**(43):6786-6792. DOI: 10.1002/adfm.201502995

[56] Hatakeyama T, Shiren K, Nakajima K, Nomura S, Nakatsuka S, Kinoshita K, Ni J, Ono Y, Ikuta T. Ultrapure blue thermally activated delayed fluorescence molecules: Efficient HOMO–LUMO separation by the multiple resonance effect. Advanced Materials. 2016;**28**(14):2777-2781. DOI: 10.1002/adma.201505491

[57] Taneda M, Shizu K, Tanaka H, Adachi C. High efficiency thermally activated delayed fluorescence based on 1, 3, 5-tris (4-(diphenylamino) phenyl)-2, 4, 6-tricyanobenzene. Chemical Communications. 2015;**51**(24):5028-5031. DOI: 10.1039/C5CC00511F

[58] Xiang Y, Gong S, Zhao Y, Yin X, Luo J, Wu K, Lu ZH, Yang C. Asymmetric-triazine-cored triads as thermally activated delayed fluorescence emitters for high-efficiency yellow OLEDs with slow efficiency roll-off. Journal of Materials Chemistry C. 2016;**4**(42):9998-10004. DOI: 10.1039/C6TC02702D

[59] Tang C, Yang T, Cao X, Tao Y, Wang F, Zhong C, Qian Y, Zhang X, Huang W. Tuning a weak emissive blue host to highly efficient green dopant by a CN in tetracarbazolepyridines for solution-processed thermally activated delayed fluorescence devices. Advanced Optical Materials. 2015;**3**(6):786-790. DOI: 10.1002/adom.201500016

[60] Tanaka H, Shizu K, Miyazaki H, Adachi C. Efficient green thermally activated delayed fluorescence (TADF) from a phenoxazine–triphenyltriazine (PXZ–TRZ) derivative. Chemical Communications. 2012;**48**(93):11392-11394. DOI: 10.1039/C2CC36237F

[61] Wada Y, Shizu K, Kubo S, Suzuki K, Tanaka H, Adachi C, Kaji H. Highly efficient electroluminescence from a solution-processable thermally activated delayed fluorescence emitter. Applied Physics Letters. 2015;**107**(18):105_1. DOI: 10.1063/1.4935237

[62] Wang H, Xie L, Peng Q, Meng L, Wang Y, Yi Y, Wang P. Novel thermally activated delayed fluorescence materials–thioxanthone derivatives and their applications for highly efficient OLEDs. Advanced Materials. 2014;**26**(30):5198-5204. DOI: 10.1002/adma.201401393

[63] Lee J, Shizu K, Tanaka H, Nomura H, Yasuda T, Adachi C. Oxadiazole-and triazole-based highly-efficient thermally activated delayed fluorescence emitters for organic light-emitting diodes. Journal of Materials Chemistry C. 2013;**1**(30):4599-4604. DOI: 10.1039/C3TC30699B

Chapter 7

Recent Progress in AlGaN Deep-UV LEDs

Hideki Hirayama

Additional information is available at the end of the chapter

http://dx.doi.org/10.5772/intechopen.79936

Abstract

AlGaN deep ultraviolet light-emitting diodes (DUV LEDs) have a wide variety of potential applications, including uses for sterilization, water purification, and UV curing and in the medical and biochemistry fields. However, the wall-plug efficiency (WPE) of AlGaN DUV LEDs remains below values. We have developed crystal growth techniques for wide-bandgap AlN and AlGaN and, using these techniques, fabricated DUV LEDs in the 220–350 nm-band. Considerable increases in the internal quantum efficiency (IQE) of AlGaN quantum wells (QW) were achieved by developing low-threading dislocation density (TDD) AlN grown on sapphire substrates. The electron injection efficiency (EIE) was substantially increased by introducing a multi-quantum barrier (MQB) as an electron-blocking layer (EBL). The light-extraction efficiency (LEE) was also improved by using a transparent p-AlGaN contact layer, a highly reflective (HR) p-type electrode, and an AlN template fabricated on a patterned sapphire substrate (PSS). Further improvements were made by implementing a reflective photonic crystal (PhC) p-contact layer. We demonstrated a record external quantum efficiency (EQE) of 20.3% for an AlGaN UVC-LED.

Keywords: deep-UV LEDs, AlN, AlGaN, MOCVD, threading-dislocation density, internal quantum efficiency, light-extraction efficiency

1. Introduction

Growth techniques for AlN/AlGaN semiconductors and recent advances in AlGaN-based deep-ultraviolet (DUV) light-emitting diodes (LEDs) are demonstrated. DUV LEDs operating in the 220–350-nm band were realized by developing new crystal growth techniques for the wide-bandgap semiconductors, AlN and AlGaN. The efficiency of an AlGaN DUV LED was significantly increased through past 10 years developments, by increasing in internal quantum efficiency (IQE), which was achieved by developing low threading dislocation density (TDD)

AlN crystals on sapphire substrates, as well as, by improving electron injection efficiency (EIE) and light extraction efficiency (LEE).

In Section 2, the background to this research, including device applications, history and the current status of DUV LEDs, is described. In Section 3, we describe the development of the crystal growth techniques undertaken in order to obtain high-quality AlN and AlGaN crystals. The realization of devices with high IQE and fabrication of the LEDs are dealt with in Sections 4 and 5, respectively. We discuss ways in which EIE and LEE can be improved, and the future prospects for DUV LEDs, in Sections 6, 7 and 8, respectively.

2. Research background of UV LEDs

The development of semiconductor light sources operating in the DUV region, such as DUV LEDs and laser diodes (LDs), is an important subject because these devices are required for a wide variety of applications. **Figure 1** gives an overview of these applications, divided into three wavebands. Potential applications for UVC and UVB lights are in sterilization, water purification, medicine and biochemistry, agriculture, and as light sources for high-density optical memory. UVA together with UVB and UVC lights also have potential for curing, adhesives, printing and coating [1, 2].

Figure 2 shows the wavelength range of UV light from UVA to UVC, and possible wavelength range of DUV LEDs developed by AlGaN. As well known, UVA light causes sunburn and UVB light is dangerous light, which causes skin cancer or cataracts. Indicated curve in **Figure 2** with peak wavelength at 265 nm in UVC waveband is known as sterilization effects curve, which well matches to the absorption spectrum of DNA (deoxyribonucleic acid). The wavelength between 260 and 280 nm is effective for sterilization, water purification and surface

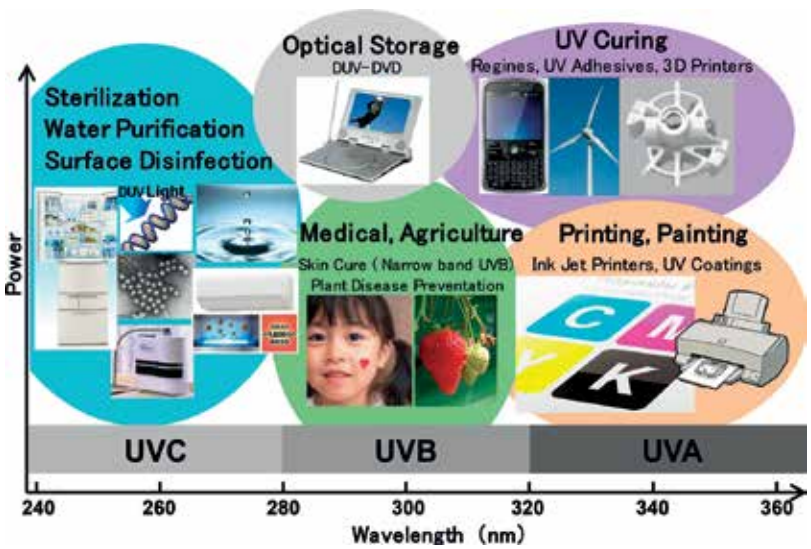

Figure 1. Potential applications of DUV LEDs and LDs.

http://dx.doi.org/10.5772/intechopen.79936

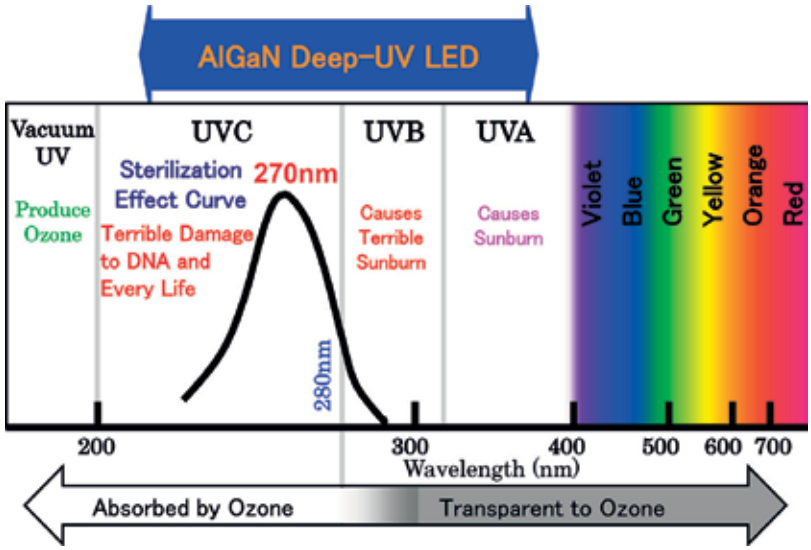

Figure 2. Classification of UV light and the wavelength range achieved by AlGaN DUV LEDs.

disinfection. As shown in **Figure 2**, the wavelength range covered by AlGaN LEDs is from UVA to UVC.

The direct transition energy range of AlGaN covers the region from 6.2 eV (AlN) to 3.4 eV [2]. **Figure 3** shows the bandgap of the wurtzite (WZ) AlInGaN material system, as well as, the lasing wavelengths of several kinds of gas lasers. AlGaN is a direct transition semiconductor having an emission wavelength range from 200 to 360 nm. Both p- and n-type conductivities are obtained in DUV wavelength range. AlGaN is physically hard and suitable for long lifetime devices. Also, the material is free from harmful elements, i.e., As, Hg and Pb. Therefore, AlGaN is considered to be the most appropriate semiconductor to develop a DUV LED [2].

Several research groups have started the research on AlGaN-based UV LEDs with wavelength below 360 nm, between 1996 and 1999 [3–5]. In the US, the effort, directed at DUV light sources, was driven by DARPA's Semiconductor Ultraviolet Optical Sources (SUVOS) program. The sub-300 nm DUV LEDs were achieved by a group at the University of South Carolina between 2002 and 2006 [6–8]. The shortest wavelength (210 nm) LED using an AlN emitting layer was reported by a group at NTT in 2006 [9]. We started research into AlGaN-based DUV LEDs in 1997, and reported the first efficient DUV (230 nm) photoluminescence (PL) from AlGaN/AlN QWs [10], and a 330 nm-band AlGaN-QW UV LED on SiC in 1999 [4]. We have also developed highly efficient UV LEDs by incorporating In into AlGaN [1, 11, 12]. We demonstrated cw operation with powers of several mWs for 340–350 nm InAlGaN-QW UV LEDs on both GaN single-crystal substrates [13] and sapphire substrates [14].

The development of 260–280 nm AlGaN DUV LEDs performed in 2005–2010 was an important step in the progress toward sterilization applications. High IQEs in AlGaN and quaternary InAlGaN QWs were achieved in 2007 [15–17], by developing a low-threading dislocation density (TDD) AlN buffer layers on sapphire substrates utilizing a pulse-flow growth method. EIE was significantly increased by introducing a multi-quantum barrier (MQB) [18]. Wide

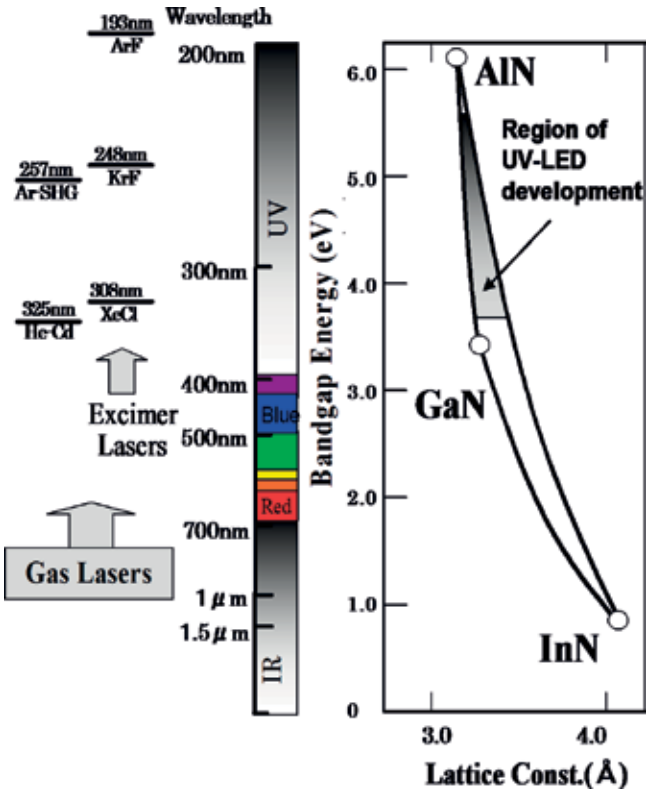

Figure 3. Relationship between the direct transition bandgap energy and the lattice constant of the wurtzite (WZ) InAlGaN material system and the lasing wavelengths of various gas lasers.

range emissions from 222 to 351 nm were demonstrated in AlGaN and InAlGaN LEDs [17–21]. We began to improve LEE of UVC LEDs by introducing a transparent p-AlGaN contact layer and a reflective p-type electrode [22–24]. We also developed commercially available DUV LED modules to be used for sterilization in 2014 [25, 26].

Sensor Electronic Technology (SET) developed the first commercially available LEDs with wavelengths ranging between 240 and 360 nm [27–28]. They reported a maximum EQE of 11% for a 278 nm LED in 2012 [28]. They also did detailed investigations into the properties of AlGaN epilayers and UVC LED devices [29–31].

Since 2010, many companies have started developing UVC LEDs aiming at sterilization applications. Nikkiso has developed highly efficient UVC LEDs [32–34] and reported EQEs of over 10% [32]. They improved the LED properties by introducing an encapsulating resin that does not deteriorate under UVC radiation [34]. Crystal IS developed efficient 265 nm LEDs on bulk AlN substrates fabricated by a sublimation method [35, 36], and Tokuyama developed UVC LEDs on a thick transparent AlN layer grown, also on bulk AlN substrates, by hydride vapor phase epitaxy (HVPE) [37–40]. Nichia has developed high wall-plug efficiency (WPE) UVC LEDs [41, 42] using a lens bonding technique [42]. Also, M. Kneissl's group in the Technical

University of Berlin recently carried out a series of studies on the properties of AlGaN epilayers and AlGaN and InAlGaN UV LEDs [2, 43–45]. The reported EQEs for AlGaN and InAlGaN UVA-UVC LEDs up to 2015 are summarized in Figure 1.1 of Ref. [2].

In spite of continuous efforts to develop an AlGaN DUV LED, its wall plug efficiency (WPE) is still as low as 3%, which is much lower than that of InGaN blue LEDs. The limited efficiency of DUV LED is mainly due to the following three factors:

1. The IQE of AlGaN is sensitive to TDD and still much lower than that of InGaN.
2. Hole concentration of p-AlGaN is low and the carrier injection efficiency (IE) is low.
3. By the light absorption by p-GaN contact layer, the LEE is quite low.

For InGaN QWs, high IQE more than 80% was already demonstrated. On the other hand, IQE at around 50% is standard value after developing the low-TDD (5×10^8 cm^{-2}) AlN templates on sapphire. We need to develop further reduction of TDD of AlN, i.e. TDD of below 1×10^8 cm^{-2}, in order to achieve more than 80% IQE. AlN single crystal wafers have advantages for high IQE, although they are expensive for commercially available DUV LEDs. The hole concentration of p-AlGaN used in UVC LEDs is as low as 1×10^{14} cm^{-3} owing to its deep acceptor levels, i.e., 240 (GaN)–590 meV (AlN). Electron overflow to the p-side layers results in the reduction of EIE for UVC LEDs. Since the hole density of p-type AlGaN is not very high, we use p-GaN for the contact layer. This results in a significant reduction in LEE, typically to below 8%, owing to the strong absorption of DUV light.

The usual value of EQE for 270 nm UVC LEDs obtained by our group is approximately 7%, which is determined by the IQE, EIE, and LEE of approximately 60, 80, and 15%, respectively. The technical issues to increase IQE, EIE and LEE are described in the following sections.

3. Growth of high-quality AlN on sapphire substrates

In order to obtain low-TDD, crack-free AlN buffer layer with atomically flat surface on sapphire, we introduced an 'ammonia (NH_3) pulsed-flow multilayer (ML) growth method [15]. **Figure 4** shows a schematic view of the growth control method and a typical gas flow sequence using pulsed and continuous gas flows.

The samples were grown on sapphire (0001) substrates at 76 Torr by metal-organic chemical vapor deposition (MOCVD). First, an AlN nucleation layer and a 'buried' AlN layer were deposited, both by NH_3 pulsed-flow growth. The pulsed-flow mode is effective for initial high-quality AlN growth on sapphire because of the increased migration of the precursor. After the growth of the first layers, we introduced a continuous-flow mode AlN growth to reduce the surface roughness. By repeating the pulsed- and continuous-flow modes, we can obtain crack-free, thick AlN layers with atomically flat surfaces. By maintaining Al-rich growth conditions, we can obtain stable Al (+c) polarity, which is necessary for suppressing polarity inversion from Al to N. The detailed growth conditions are described in Ref. [15, 19]. The advantages in comparison with former approaches [46, 47] are that the method is in-situ

process, and low TDD AlN can be obtained without the need for AlGaN layers, yielding a device structure with minimal DUV absorption.

Figure 5 shows the full-width at half maximum (FWHM) of X-ray diffraction (10–12) ω-scan rocking curves (XRC) for various stages in the ML-AlN growth. This was reduced from 2160 to 550 arcsec by executing the pulsed-flow mode twice. **Figure 6** shows atomic-force microscope

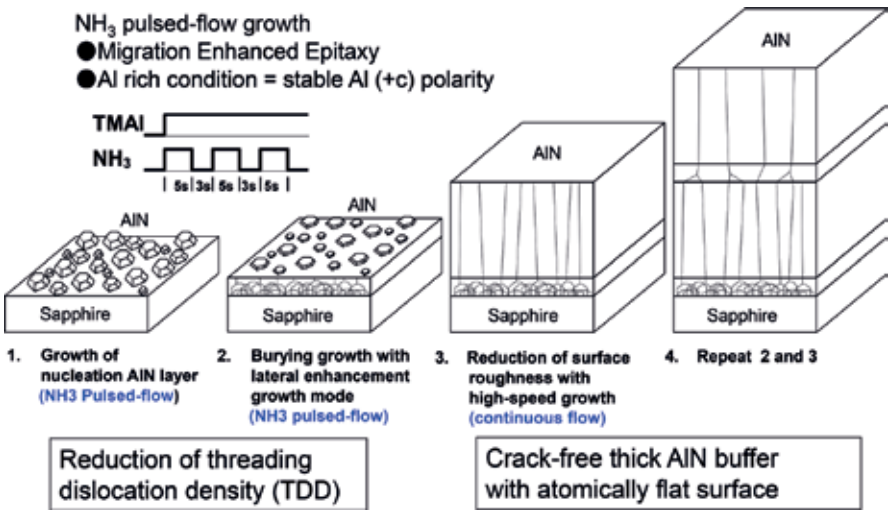

Figure 4. Gas flow sequence and schematic view of the growth control method used for the NH_3 pulsed-flow multilayer (ML)-AlN growth technique.

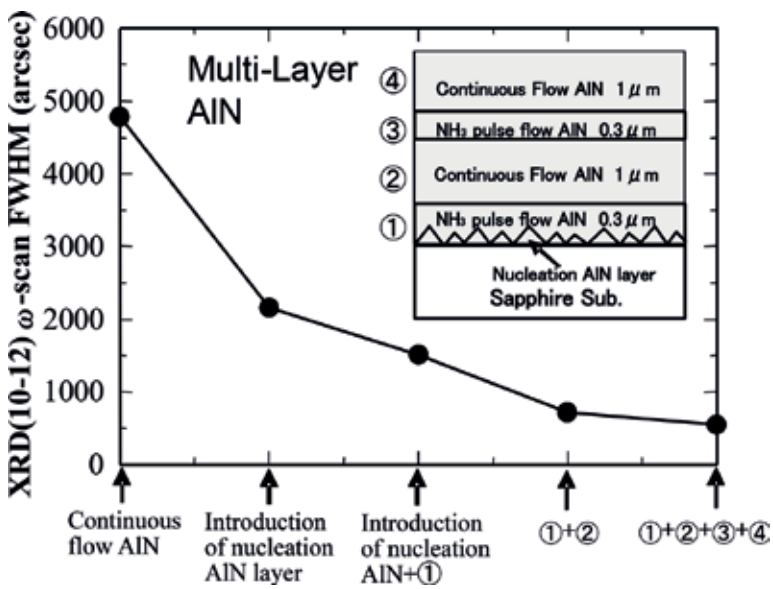

Figure 5. FWHM of the X-ray diffraction (10–12) ω-scan rocking curve (XRC) at various stages in the growth of the ML-AlN layer.

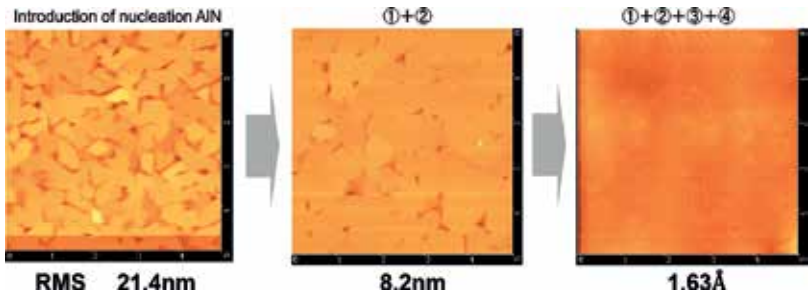

Figure 6. AFM images of the surface of the ML-AlN layer with an area of 5 × 5 μm^2 at various stages in the growth.

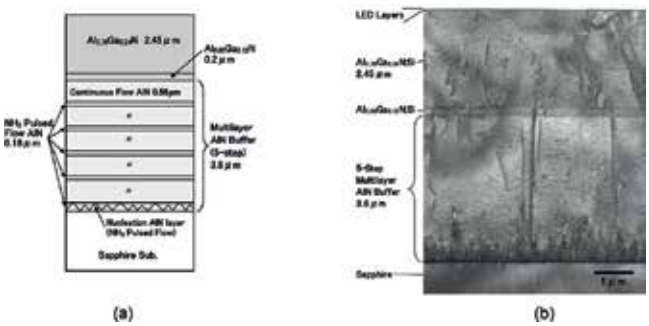

Figure 7. (a) Schematic diagram and (b) cross-sectional TEM image of an AlGaN/AlN template including a 5-step ML-AlN buffer layer grown on a sapphire substrate.

(AFM) images of the surface of ML-AlN on sapphire at various stages of growth. We can see that the surface improves as more layers are grown, ending with an atomically flat surface. The typical root-mean-square (RMS) of the surface roughness was 0.16 nm, as seen in **Figure 6**.

Figure 7 shows (a) a schematic illustration of the structure and (b) a cross-sectional transmission electron microscope (TEM) image of an AlGaN/AlN template including ML-AlN buffer layer grown on a sapphire substrate. The typical FWHMs of the (10–12) and (0002) XRCs of the ML-AlN were approximately 330 and 180 arcsec, respectively. This was grown in a 3 × 2 inch MOCVD reactor [25]. The minimum corresponding FWHMs obtained using a 1 × 2 inch MOCVD reactor were approximately 290 and 180 arcsec, respectively. The minimum edge- and screw-type dislocation densities were below 5 × 10^8 and 4 × 10^7 cm^{-2}, respectively, as observed in the TEM image. To further reduction of TDD, we introduced an AlN epitaxial lateral overgrowth (ELO) technique on a patterned sapphire substrate (PSS) and obtained TDDs of the order of 10^7 cm^{-2}.

4. Increasing the internal quantum efficiency (IQE)

Figure 8 shows a cross-sectional TEM image of an AlGaN multi-quantum well (MQW) of a 227 nm DUV LED fabricated on a ML-AlN buffer. In order to suppress the spontaneous

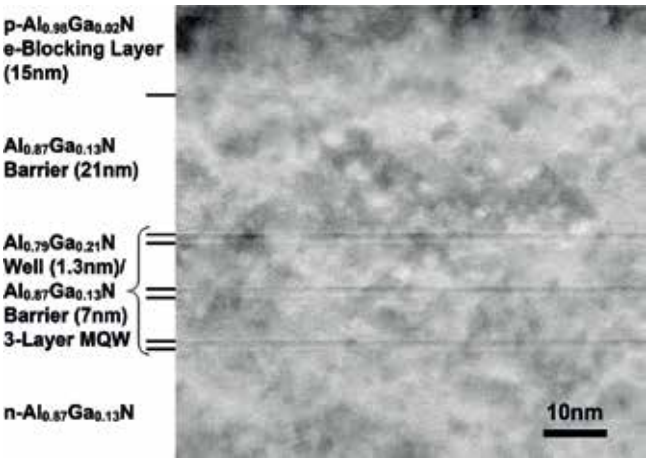

Figure 8. Cross-sectional TEM image of the quantum well region of an AlGaN MQW DUV-LED.

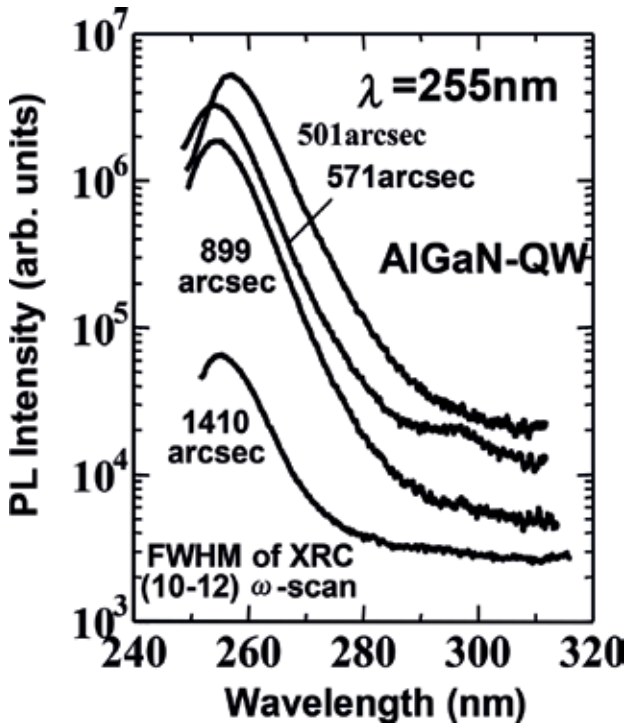

Figure 9. Photoluminescence (PL) spectra of AlGaN QWs on ML-AlN templates with various FWHMs of the XRC (10–12) measured at room temperature.

polarization effects induced in the wells, very thin quantum well was used. It is important to obtain atomically smooth hetero-interfaces to achieve high IQE from such thin QWs. As shown in the cross-sectional TEM image in **Figure 8**, the three 1.3 nm-thick QWs have atomically-flat hetero-interfaces.

http://dx.doi.org/10.5772/intechopen.79936

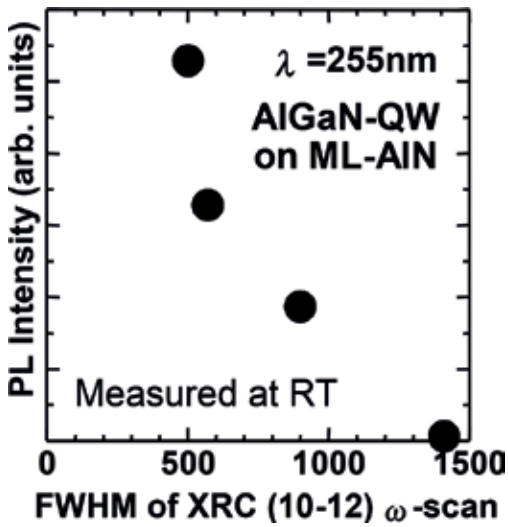

Figure 10. PL intensity of AlGaN-QWs as a function of the FWHM of the XRC (10–12) of AlGaN buffers measured at room temperature.

We observed a considerable increase in the DUV emission from AlGaN-QWs by fabricating them on low TDD AlN templates [16, 17]. **Figure 9** shows the photoluminescence (PL) spectra of AlGaN QWs with emission peaks at around 255 nm fabricated on ML-AlN measured at room temperature (RT). We used a 244 nm Ar-ion second-harmonics generation (SHG) laser for the excitation of the sample. The excitation power density was approximately 200 W/cm^2. The PL intensity significantly increases with narrower FWHM. We can see from **Figure 9** that the efficiency depends strongly on the edge-type TDDs.

Figure 10 shows the intensity of the PL peak at 255-nm measured at RT as a function of the FWHM of the XRC (10–12). Reducing the FWHM from 1400 to 500 arcsec increases the PL intensity by a factor of about 80. Between 500 and 800 arcsec the PL intensity increases rapidly. This rapid increase can be explained by a reduction in the non-radiative recombination rate as the distance between the TDs becomes greater compared with the carrier diffusion length in the QW. We obtained similar degrees of improvement for QWs operating at other wavelengths. The relationship between IQE and TDD in DUV AlGaN-QWs was also investigated in Ref. [27, 48].

The quaternary alloy InAlGaN is also a strong candidate as a material for realizing DUV LEDs, since the inclusion of In leads to efficient UV emission as well as higher hole concentration. Just a few percent of In in AlGaN is needed to obtain high IQE, where the increases in efficiency are due to the In segregation effect, an effect previously investigated for the ternary alloy, InGaN. We have described the advantages of the use of InAlGaN in Ref. [1, 11, 12, 14, 17].

We took up the challenge of developing the crystal growth technology needed to obtain high quality InAlGaN alloys operating at the 'sterilization' wavelength (280 nm) [17]. Growing crystals of InAlGaN with a high Al content is relatively difficult, because incorporating In becomes more challenging as the growth temperature is increased, which is necessary in order

to maintain the crystal quality. We obtained high-quality InAlGaN with a high amount of Al (>45%) by using epitaxy at a relatively low growth rate, i.e., 0.03 μm/h. The intensity of the light at 280 nm emitted by an InAlGaN QW at RT was increased by a factor of 5 by reducing the growth rate from 0.05 to 0.03 μm/h.

5. AlGaN- and InAlGaN-based UVA-UVC LEDs

We fabricated AlGaN and InAlGaN MQW DUV LEDs on low-TDD AlN templates [15–26]. **Figure 11** shows a schematic diagram of the structure of an AlGaN-based DUV LED fabricated on a sapphire substrate. **Table 1** shows typical design values for the fraction of Al (x) in the $Al_xGa_{1-x}N$ wells, in the buffer and barrier layers, and in the electron-blocking layers (EBLs) used for 222–273 nm AlGaN-MQW LEDs. Large compositions of Al in AlGaN were used to obtain DUV LEDs operating at short wavelengths, as shown in **Table 1**. The detail layer structures and device geometries of the LEDs are described in Ref. [15, 17]. The output power was measured using a Si photodetector located behind the LED sample. The photodetector was calibrated by measuring the luminous flux from a flip-chip LED. The forward voltages

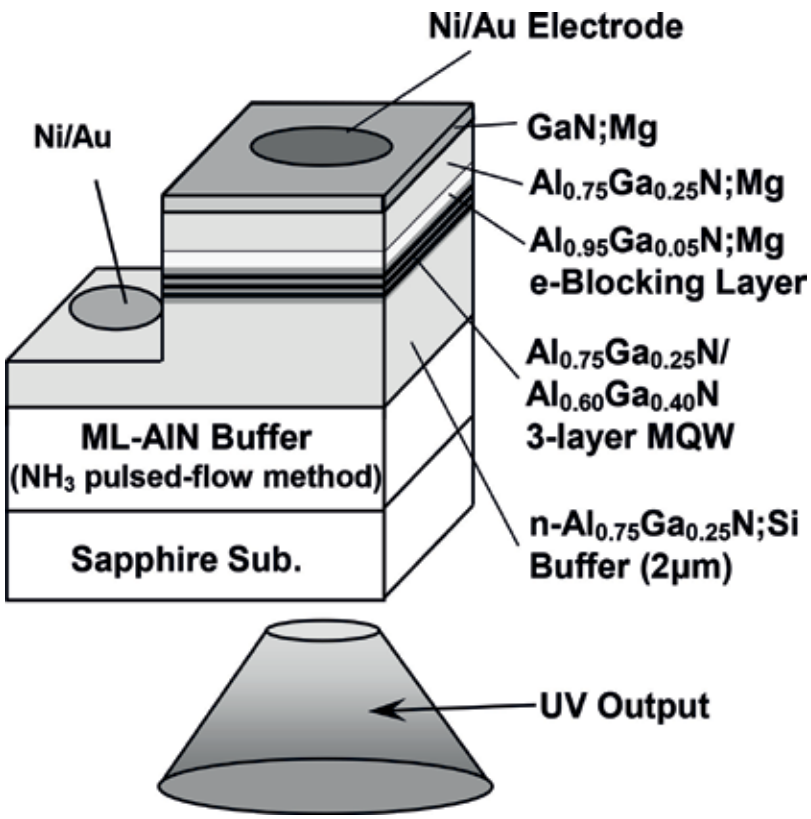

Figure 11. Schematic structure of a typical AlGaN-based DUV LED fabricated on a sapphire substrate.

Wavelength	Well	Barrier & Buffer	Electron Blocking Layer
222 nm	0.83	0.89	0.98
227 nm	0.79	0.87	0.98
234 nm	0.74	0.84	0.97
248 nm	0.64	0.78	0.96
255 nm	0.60	0.75	0.95
261 nm	0.55	0.72	0.94
273 nm	0.47	0.67	0.93

Table 1. Typical design values of the fraction of Al (x) in the $Al_xGa_{1-x}N$ wells, the buffer and barrier layers, and the electron-blocking layers (EBLs) used for 222–273 nm AlGaN-MQW LEDs.

(Vf) of the bare wafer and the flip-chip samples were approximately 15 and 8 V, respectively, with an injection current of 20 mA.

Figure 12 shows the electroluminescence (EL) spectra of the AlGaN and InAlGaN MQW LEDs measured at RT. We obtained single-peak operations for LED samples with emission wavelength from 222 to 351 nm. **Figure 13** shows the EL spectra of a 227 nm AlGaN LED on a log scale [19]. The deep-level emissions with wavelengths at around 255 and 330–450 nm are more

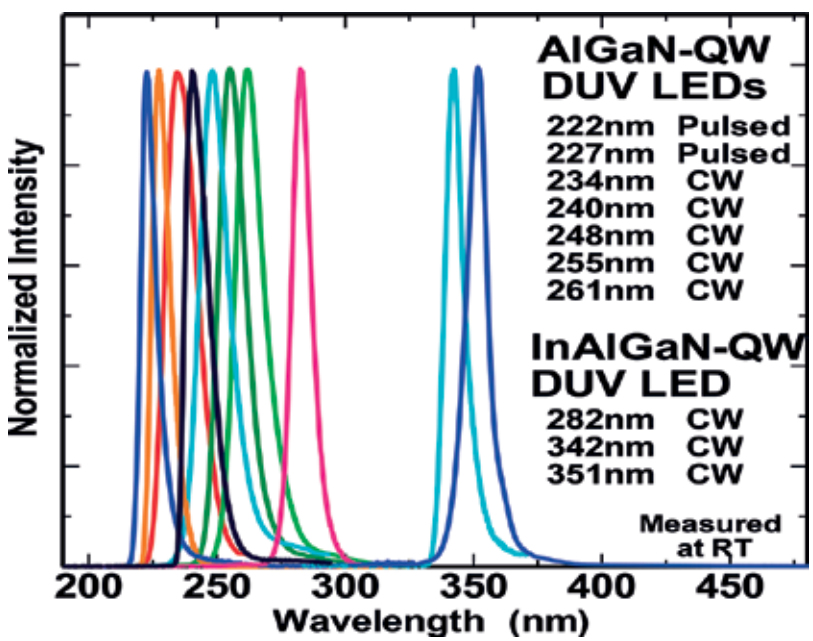

Figure 12. Electroluminescence (EL) spectra of fabricated AlGaN and InAlGaN MQW LEDs with emission wavelengths between 222 and 351 nm, all measured at room temperature (RT) with injection currents of around 50 mA.

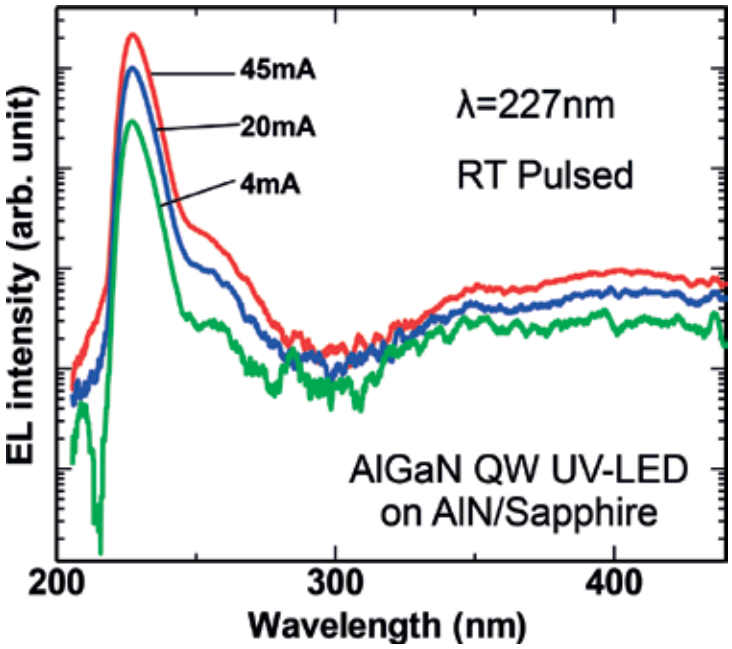

Figure 13. EL spectra on a log scale of a 227 nm AlGaN DUV LED for various injection currents.

than two orders of magnitude smaller than the main peaks. The output power of the 227 nm LED was 0.15 mW at an injection current of 30 mA, and the maximum EQE was 0.2% under pulsed operation at RT. **Figure 14** shows (a) the EL spectra for various injection currents and (b) the current-output power (I-L) and current-EQE (η_{ext}) (I-EQE) characteristics for a 222 nm AlGaN-MQW LED measured under pulsed operation at RT [20]. Single-peak operation at

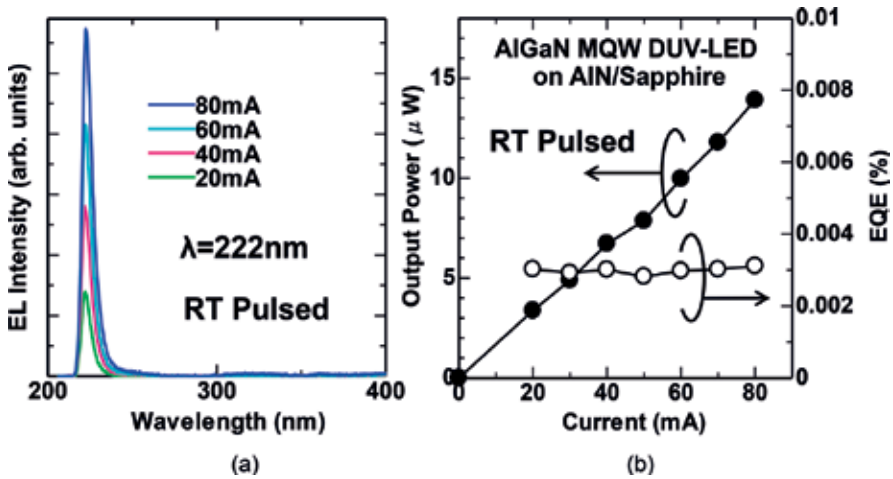

Figure 14. (a) EL spectra for various injection currents and (b) the output power and EQE (η_{ext}) *vs* current characteristics for a 222 nm AlGaN-MQW LED measured under pulsed operation at RT.

222 nm, which is the shortest wavelength ever reported for a QW LED, was achieved. The output power was 0.14 μW at an injection current of 80 mA, and the maximum EQE was 0.003%.

It has been reported that 'normal' c-axis (vertical) emission is difficult to obtain from an AlN (0001). This is because the optical transition between the conduction band and the top of the valence band is mainly only allowed for light that has its electric field parallel to the c-axis (E//c) [9]. The lateral propagation of the transvers-magnetic (TM) mode emission results in a significant reduction of LEE. Therefore, short wavelength AlGaN UVC LED shows a very low LEE. Several groups have reported on this [49, 50]. Banal et al. reported that the critical Al composition for 'polarization switching' could be expanded to approximately 0.82 by using very thin (<1.5 nm) AlGaN quantum wells on an AlN/sapphire template [49]. We investigated the variation in the spectrum of a 222 nm AlGaN QW LED with the angle of emission, and demonstrated that normal vertical emission can be obtained, even at short-wavelengths, for LEDs with as much as 83% Al [20].

6. Increasing the electron injection efficiency (EIE) by introducing an MQB

EIE into the QW is reduced due to the electron leakage caused by the low hole concentrations in the p-type AlGaN layers. The EIE reduction is particularly severe for LEDs with wavelength shorter than 260 nm, because an electron barrier height of an EBL becomes smaller [17]. We introduced a MQB [51, 52] to serve as an EBL, and consequently achieved a marked increase in EIE [18].

Figure 15 shows schematic illustrations of the electron flow for an AlGaN DUV LED with (a) a MQB EBL and (b) a conventional single barrier EBL. In usual case, we are using single barrier EBL for 250–280 nm UVC LEDs. However, the electron barrier height of the single barrier EBL is determined by the bandgap of the barrier material, and it is not sufficiently high for UVC LED with wavelength shorter than 260 nm. On the other hand, we can increase the 'effective' barrier height of the EBL by introducing MQB. Even electrons having higher energy above the MQB band-edge can be reflected by the multi-reflection effects of the MQB, and injected into the QWs, resulting in higher EIE.

Figure 16 shows the electron transmittance through an AlGaN MQB and a conventional single barrier EBL for a 250 nm AlGaN LED calculated by a transfer-matrix method. It was shown, using barriers with thickness modulation, that the 'effective' barrier height of an AlGaN/AlGaN MQB is up to twice that of a conventional single-barrier EBL.

Figure 17 shows a schematic diagram of the structure of a 250 nm AlGaN QW DUV LED with an MQB EBL and a cross-sectional TEM image of a fabricated device. We carried out experiments to find an appropriate MQB structure, and found that the insertion of an initial thick-barrier is important for reflecting low energy electrons. We also found that thin barriers contribute to the reflection of higher-energy electrons. The optimum MQB comprised five layers of $Al_{0.95}Ga_{0.05}N/Al_{0.77}Ga_{0.23}N$ with thicknesses of **7**/4/**5.5**/4/**4**/2.5/**4**/2.5/**4** nm, in which

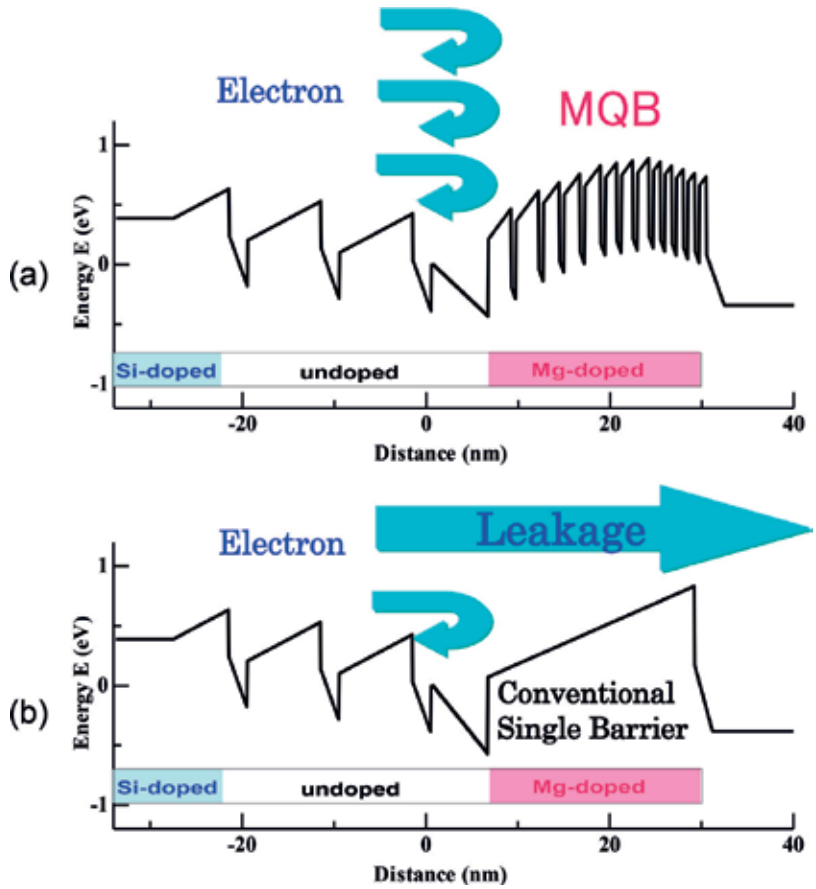

Figure 15. Schematic images of the electron flow in AlGaN DUV LEDs with (a) a MQB EBL and (b) a conventional single barrier EBL.

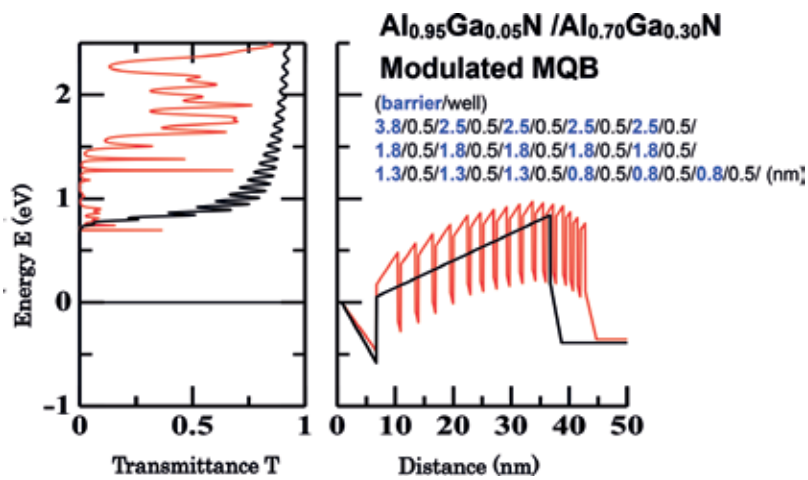

Figure 16. Electron transmittance through AlGaN/AlGaN MQB (red-line) and conventional single barrier EBL (black-line) calculated for a 250 nm-band AlGaN-QW LED.

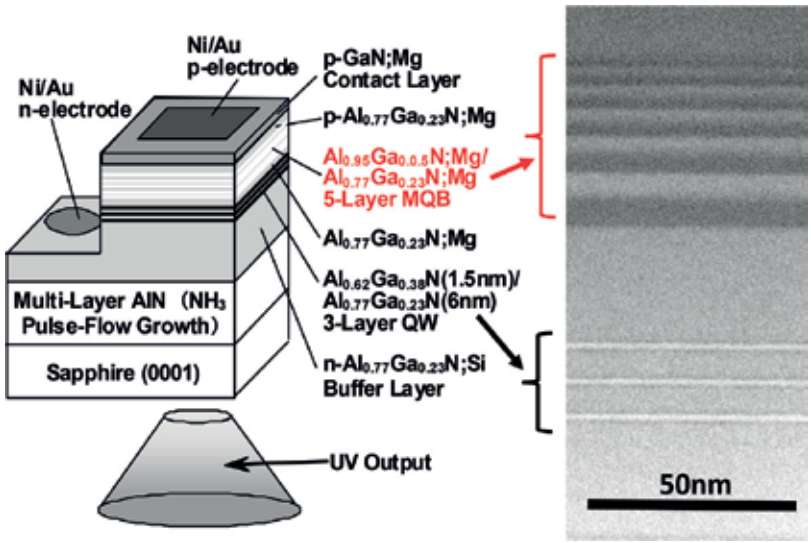

Figure 17. Schematic structure and cross-sectional TEM image of a 250 nm AlGaN QW DUV LED with an MQB.

the barriers are in bold type and the valleys are normal type. The coherence length for obtaining the multi-reflection effect of the MQB means the total thickness of the MQB should be less than 40 nm.

Figure 18 shows (a) the I-L and (b) I-EQE characteristics for 250 nm AlGaN MQW LEDs with an MQB and with a single-barrier EBL, both measured under cw operation at RT. These show significant increases in output power and EQE when the single-EBL is replaced by the MQB. The maximum output powers of LEDs with the MQB and with the single-barrier EBL are 15 mW and 2.2 mW, respectively, and the introduction of the MQB has increased the EQE by a

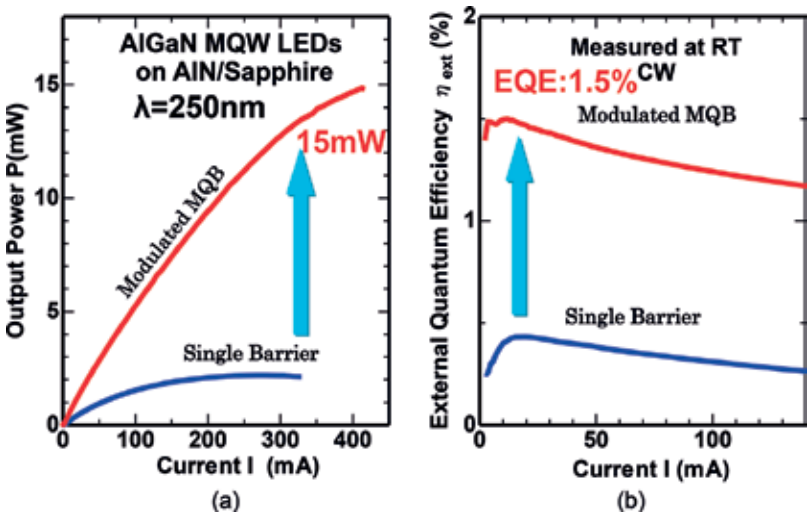

Figure 18. (a) Current-output power (I-L) and (b) current-EQE (η_{ext}) characteristics for 250 nm AlGaN-MQW LEDs with an MQB and with a single-EBL.

factor of approximately 4. From **Figure 18**, we estimate that the EIE would have been improved from approximately 25% to more than 80% by introducing the MQB.

Figure 19 shows the I-L characteristics for a 237 nm AlGaN MQW LED with an MQB and a 234 nm LED with a single-barrier EBL, both measured under cw operation at RT. The increase in EIE when using the MQW was found to be extremely high. The output power has been increased by a factor of 12 by replacing the single-barrier EBL with a MQB.

Figure 20 shows the wavelength dependence of the EQE for AlGaN DUV LEDs with MQBs and single-barrier EBLs. Introducing the MQB has increased the EQE by 10, 4 and 3 times for 235, 250 and 270 nm AlGaN LEDs, respectively. We obtained a cw output power of 33 mW from a 270 nm AlGaN-MQW LED with an MQB on a bare chip, but expect to get higher output power by using flip-chip geometry and heat dissipation. The value of EQE was 3.8% in the absence of any means to increase LEE [21].

RIKEN and Panasonic have developed commercially available UVC LED modules for use in sterilization in 2014 [25, 26]. To develop commercially available devices with constant high EQEs and long device lifetimes, the reproducibility and uniformity of the AlN template and the AlGaN LED layer structure need to be maintained. Reproducibility is particularly difficult because the growth conditions are very sensitive to the vapor-reaction between NH_3 and TMAl induced by high growth temperatures (1250–1400°C). We achieved highly uniform ML-AlN templates on sapphire in a 3 × 2 inch MOCVD reactor using pulsed NH_3 flow. The

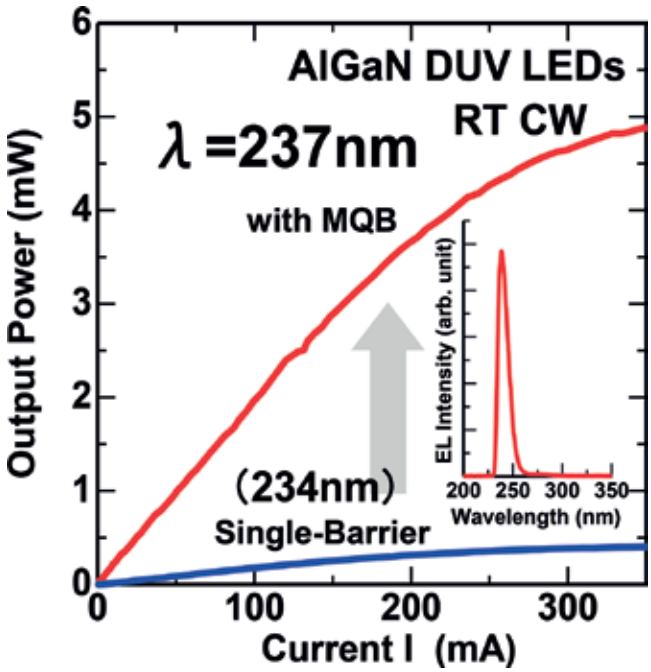

Figure 19. Current-output power (I-L) characteristics for a 237 nm AlGaN-MQW LED with an MQB and a 234 nm AlGaN-MQW LED with a single-EBL.

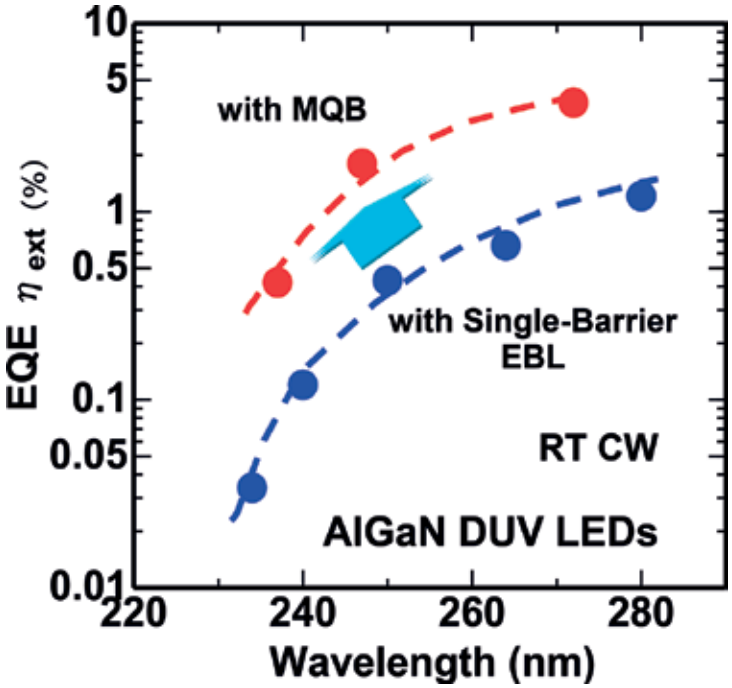

Figure 20. Wavelength dependence of the EQE of AlGaN DUV-LEDs with MQBs and single-EBLs.

fluctuation in FWHM for these was within 4%. We consistently obtained FWHMs of the XRC (10–12) of 340 arcsec for these templates. These highly uniform and low TDD templates are suitable for producing commercial DUV LEDs. **Figure 21** shows (a) a photograph of a 270 nm 10 mW DUV LED module containing 6 chips and (b) the operating properties of this module for applications to sterilization. Lifetimes longer than 10,000 h have already been achieved for devices with EQEs of 2–3% [25, 26].

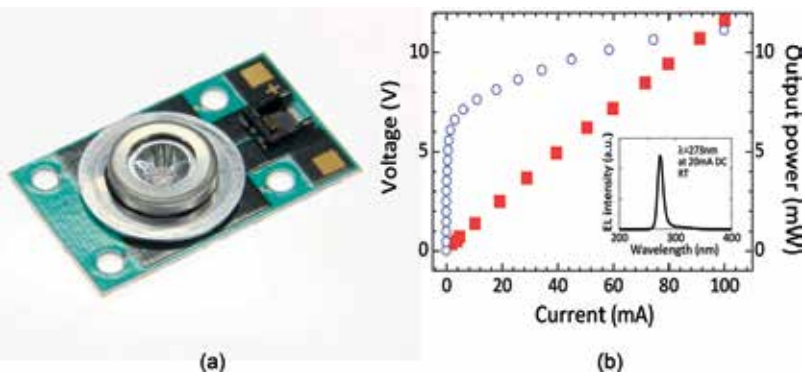

Figure 21. (a) Photograph of a commercially available 270 nm 10 mW DUV LED module developed by RIKEN and Panasonic for applications to sterilization and (b) the operating properties of this module.

7. Increasing the light-extraction efficiency (LEE)

Improving the LEE is particularly important for the development of AlGaN DUV LEDs, because LEE is currently quite low in comparison with that of InGaN-based blue LEDs. However, increasing LEE is not so easy because of the scarcity of suitable transparent, conducting p-type contact layers and transparent p-type electrodes, and also the lack of highly reflective p-type electrodes applicable to UVB-UVC range.

Figure 22 shows schematic diagrams of several structures designed to improve LEE, and the approximate values of LEE calculated for them [24]. In a conventional DUV LED, the light going upward from the QWs is completely absorbed by the p-GaN contact layer. The light going downward is reflected at the sapphire/air interface by total internal reflection. As a result, the LEE is less than 8%. Although we have used photonic nanostructures on the surface of the sapphire substrate or an encapsulating technique, the improvement in LEE is not sufficiently high (a maximum of approximately 15% is expected). To improve LEE, we must introduce a transparent contact layer and a highly reflective p-type electrode. If we use a transparent p-AlGaN contact layer and an electrode with a reflectivity of 80%, LEEs more than 20% can be obtained. Further improvements can be made from light scattering effects obtained by having an AlN buffer layer grown on a patterned sapphire substrate (PSS). LEEs of approximately 35% are expected by combining a transparent contact layer with a reflective electrode and a PSS. Yet more improvements can be made by having a vertical LED with a back-surface photonic structure, which can be realized by removing the sapphire substrate. LEEs of >70% are expected for such LEDs, as analyzed in Ref. [53]. We also proposed using a highly reflective (HR) PhC for the p-contact layer, as we discuss later, which has almost perfect reflectivity for UV light. Using a structure with a transparent p-AlGaN contact layer, a HR-PhC on p-AlGaN, and vertical geometry with a backside photonic patterned structure for light extraction, EQEs of more than 40% are expected for UVC LEDs.

We demonstrated a DUV LED with a transparent p-AlGaN contact layer and a reflective p-type electrode [24]. We replaced the conventional Ni (20 nm)/Au (100 nm) p-type electrode with a highly reflective Ni (1 nm)/Al (200 nm) electrode [54]. **Figure 23** shows the relative reflectivities of Ni/Al (200 nm) electrodes for various thicknesses of Ni (0.5–4 nm), and also that

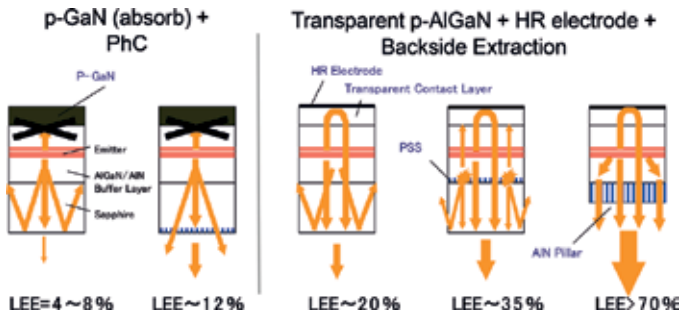

Figure 22. Schematic illustrations of structures designed to improve the LEE of a DUV LED and rough estimates of the values of LEE for each structure.

http://dx.doi.org/10.5772/intechopen.79936

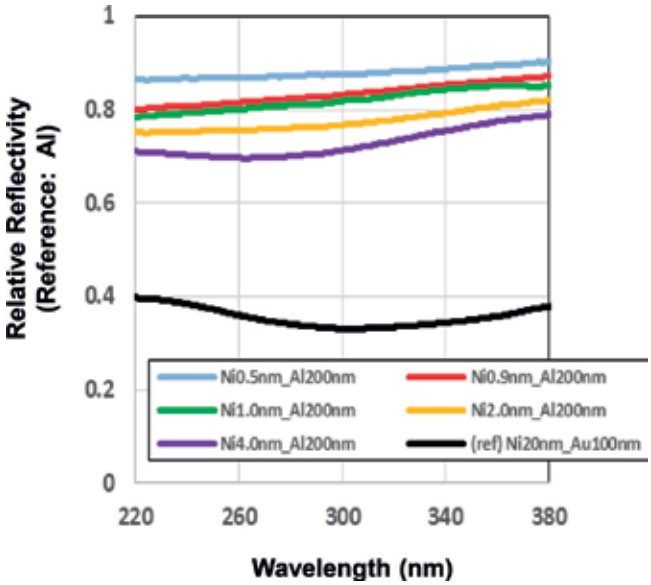

Figure 23. Wavelength dependence of the reflectivity for various types of p-type electrode for AlGaN DUV LEDs.

for Ni (20 nm)/Au (100 nm), normalized to the reflectivity of Al (92%). Although the reflectivity of Al metal is high (92%) in the DUV range, ohmic contact to p-AlGaN cannot be obtained. The insertion of a thin layer of Ni to improve this causes a significant reduction in reflectivity. Therefore, we did a thorough examination of the reflectivities of Ni/Al electrodes with very thin Ni layers. We confirmed normal operation of a UVC LED with a Ni (1 nm)/Al (200 nm) p-type electrode. The reflectivities of Ni (1 nm)/Al (200 nm) and Ni (20 nm)/Au (100 nm) electrodes are approximately 76 and 31%, respectively, as shown in **Figure 23**.

Figure 24 compares the effect of the different p-type electrodes on (a) the I-L and (b) the I-EQE characteristics of 279 nm AlGaN DUV LEDs with transparent p-AlGaN contact layers [54]. Using the highly reflective Ni(1 nm)/Al(200 nm) in place of the conventional Ni(20 nm)/Au(100 nm) electrode increases the EQE from 5 to 9% owing to the increase in LEE [54]. We also confirmed that Ni(1 nm)/Mg and rhodium (Rh) p-electrodes are effective to increase the LEE of UVC LED [55].

Increases in LEE were demonstrated for a 275 nm UVC flip-chip (FC) LED by using a transparent p-type AlGaN contact layer, an Rh mirror electrode, an AlN buffer layer grown on PSS, and an encapsulating resin. The effects of each of these were systematically investigated [56]. Conventional and LEE enhanced type LED structures were fabricated to investigate the effects of the aforementioned features on LEE. Schematics of these are shown in **Figure 25(a)** and **(b)**, respectively. The structures were grown by MOCVD for a conventional LED on a 4 μm thick AlN/sapphire template, and for a LEE enhanced type on an AlN/PSS. The detail layer and devise structures were described in Ref. [56].

Figure 26 shows a photograph of the FC LED sample. An Al-coated Si submount was used for the FC LED. The chip was encapsulated in hemispherical lens-like by silicon resin. We

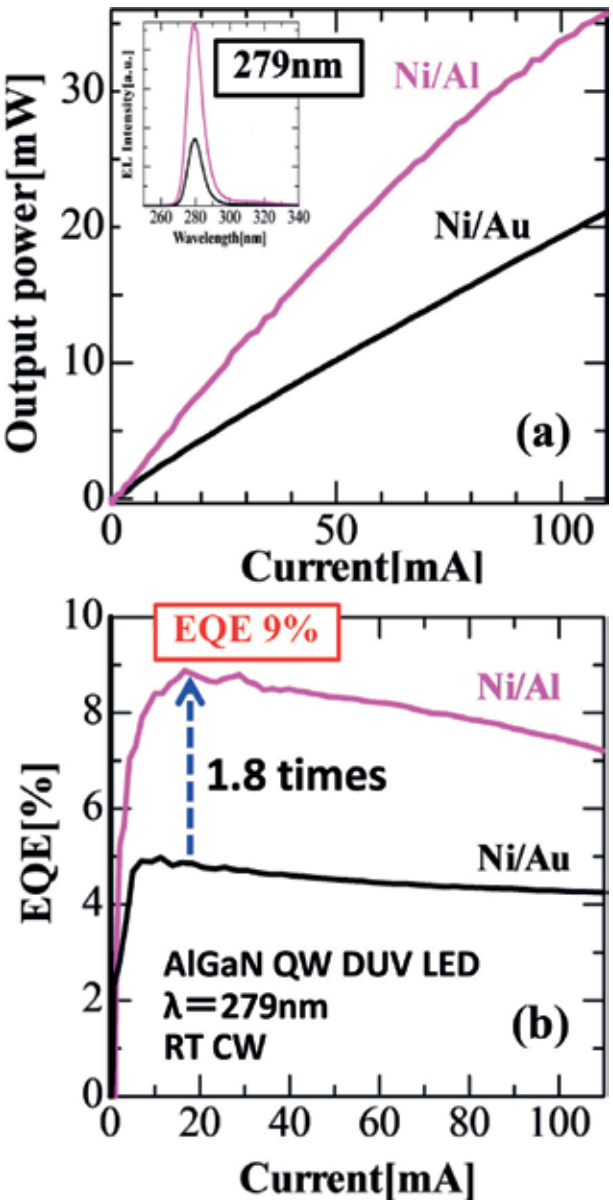

Figure 24. (a) Current-output power (I-L) and (b) current-EQE (η_{ext}) characteristics for 279 nm AlGaN-MQW DUV LEDs measured under cw operation at RT. comparison is made between LEDs with different p-type electrodes (conventional Ni/Au and highly reflective Ni/Al p-electrodes).

evaluated the transmittance of p-$Al_{0.65}Ga_{0.35}N$ prior to introducing it as a p-type contact layer. We confirmed almost perfect transparency for the p-AlGaN contact layer, and even the Mg doping concentration was as high as 8×10^{19} cm^{-3} as measured by secondary ion mass spectrometry (SIMS).

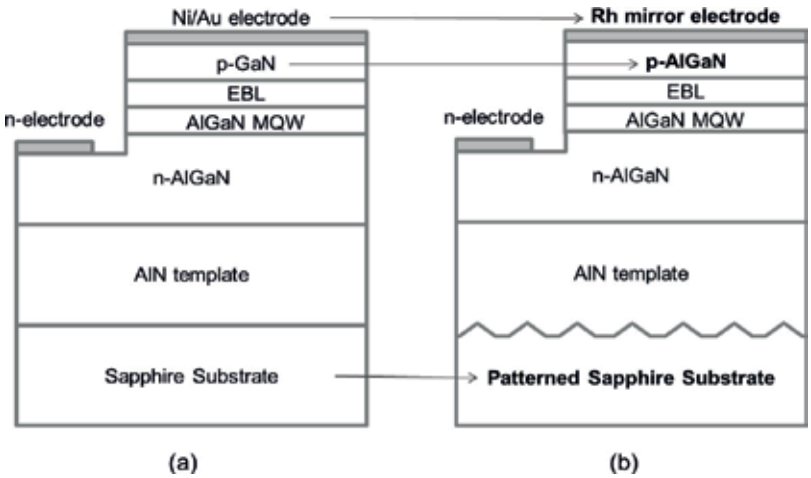

Figure 25. Schematics of (a) conventional and (b) LEE enhanced UV-LED structures. In the LEE enhanced UV-LED structure, we introduced a transparent p-type AlGaN:Mg contact layer, a Rh mirror electrode, a PSS, and an encapsulating resin.

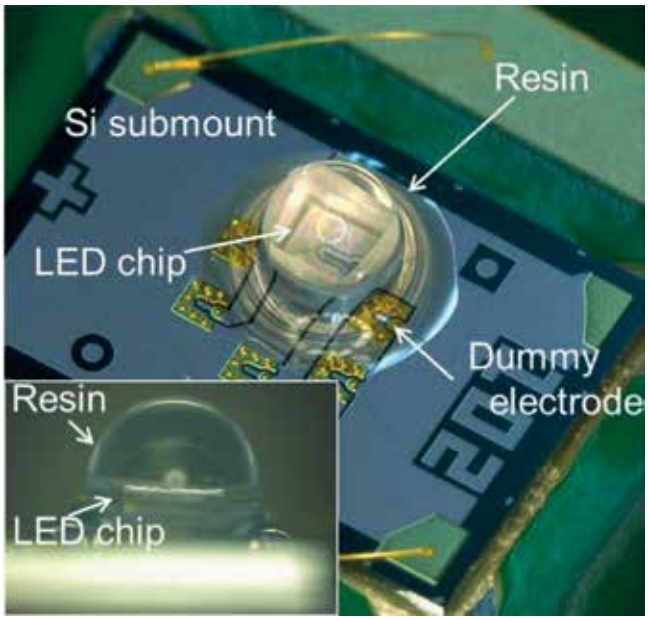

Figure 26. Photograph of the flip-chip (FC) LED mounted on a Si submount with an Al coating. The chip size is 0.5×0.5 mm^2 and it is encapsulated in resin with a hemispherical shape. The Si submount is in contact with the Al baseplate. The inset shows a side view of the encapsulating resin.

Figure 27(a) and **(b)** show the I-L and I-EQE characteristics for the conventional and LEE enhanced type UVC LEDs under RT cw operation. The inset in **Figure 27(a)** shows the EL spectra at 20 mA. Each spectrum has the same peak at 275 nm. The output power for both

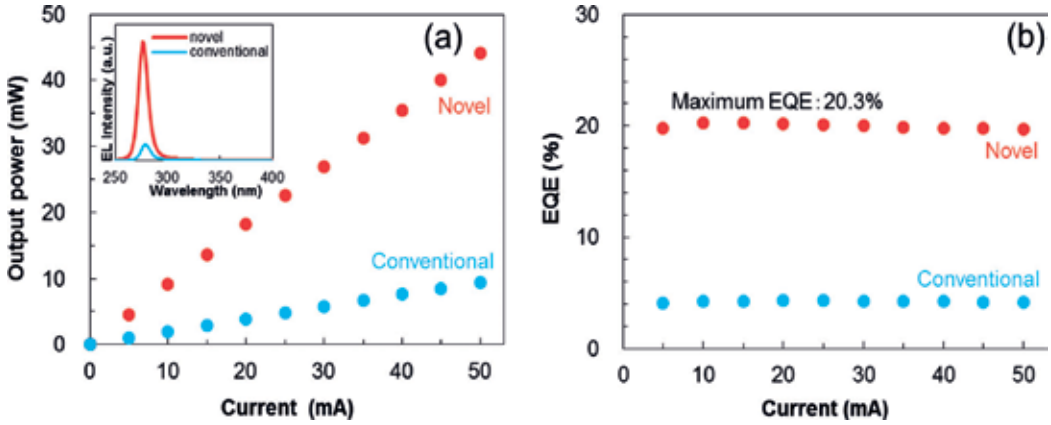

Figure 27. (a) Current-output power (I-L) and (b) current-EQE (η_{ext}) characteristics for the conventional and LEE enhanced UVC-LED. The inset in (a) shows the EL spectra of the LEDs at a direct current of 20 mA.

samples has good linearity, and the EQEs are almost constant up to 50 mA. The output power was increased from 3.9 to 18.3 mW at 20 mA and from 9.3 to 44.2 mW at 50 mA, both by a factor of five, by introducing LEE enhanced structure. These values correspond to EQEs of 4.3 and 20.3%, respectively. Thus, the EQE was substantially improved by including a transparent p-AlGaN contact layer, an Rh mirror electrode, a PSS, and the lens-like encapsulating.

To clarify the individual effects on the EQE, each structure for LEE enhancement was introduced step-by-step. **Table 2** summarizes the device structures and the LED characteristics. From **Table 2**, we found that the enhancement factors for introducing a transparent p-AlGaN contact layer and Rh electrode, PSS, and lens-like encapsulation were approximately 3, 1.5, and 1.5, respectively.

The driving voltage of the LED was increased from 9 to 16 V at 20 mA by introducing p-AlGaN contact layer. The main reason for the increase in driving voltage is the increase of contact resistant by introducing p-AlGaN contact layer. The WPE of the LEE enhanced type LEE

sample No.	Device structures				LED characteristics	
	substrate	p-type contact layer	p electrode	geometry	output power @20mA (mW)	maximum EQE(%)
1	flat	GaN:Mg	NiAu	FC only	3.9	4.3
2	flat	AlGaN:Mg	Rh	FC only	11.6	12.7
3	PSS	AlGaN:Mg	Rh	FC only	14.5	16.1
4	PSS	AlGaN:Mg	Rh	FC + resin coating	18.3	20.3

Table 2. Summary of the device structures and their LED characteristics. Samples no. 1 and 4 correspond to the conventional and novel UV-LED structures, respectively. Samples no. 2 and 3 demonstrate the effects of including the AlGaN:Mg/Rh layers and the PSS, respectively.

remained 5.7%. Improving the conductivity of the p-AlGaN contact layer is important issue in future for obtaining high WPE.

In summary of this section, LEE of the 275 nm AlGaN UVC LED was increased by approximately five times by introducing a transparent p-AlGaN contact layer, an Rh reflective electrode, a PSS, and a lens-like encapsulating. A maximum EQE of 20.3% at 275 nm was obtained by combining all of the aforementioned light extraction features.

8. Highly reflective (HR) PhC for increasing LEE

To improve the LEE of UVB and UVC LEDs, the introduction of a transparent contact layer and a highly reflective electrode is important as indicated in the previous section. A p-AlGaN layer with high Al composition (50–70%) is used for the transparent p-contact layer for UVC LEDs, however, the low hole concentration of this layer leads an increase in the contact resistance, resulting in a higher operating voltage.

In order to realize both high LEE and low voltage operation in DUV LEDs, we proposed using a highly-reflective photonic crystal (HR-PhC) [57–60]. It is possible to reflect UV light efficiently by using a 2-dimensional (2D) PhC on the surface of the p-GaN top contact layer. We can obtain low contact resistance because the top p-GaN layer has a high hole concentration. Therefore, a HR-PhC fabricated on p-GaN contact layer makes it possible to achieve not only high LEE but also high WPE in DUV LEDs.

It is possible to increase LEE by lens bonding or lens-shaped encapsulation [34, 56], or by fabrication of a PhC on the backside of the device for suppressing the total reflection [40]. However, LEE still remains low if we are unable to eradicate the strong absorption in the p-GaN layer.

We fabricated DUV LEDs with a HR-PhC on the p-AlGaN contact layer. The fabrication of a uniform PhC with low damage made it possible to obtain high EQE [57]. **Figure 28** shows a schematic structure of DUV LED with and without a HR-PhC region fabricated on the p-AlGaN contact layer. We used two-types of p-type electrodes, i.e., low-reflective (30%) Ni electrode and highly-reflective Ni(1 nm)/Mg (80%) [55] electrode.

We performed a finite-difference time-domain (FDTD) analysis for obtaining an appropriate HR-PhC design using the following Bragg equation [57]:

$$m\lambda/n_{eff} = 2a \tag{1}$$

where m is an integer, λ is the wavelength of the light, n_{eff} is the effective refractive index of the PhC, and a is the lattice period of the PhC. Electromagnetic field analysis by the FDTD method is suitable for analyzing structures with sub-wavelength size geometry, and is usually used for the analysis of optical PhC devices. An air hole-type 2D PhC with hexagonal configuration was assumed. We observe that a larger photonic bandgap is obtained with larger R/a, i.e., with R/a = 0.4, where R is the radius of the holes in the PhC. The values used in this work were λ = 280 nm, n_{eff} = 2.3, m = 4 and a = 250 nm [57–60].

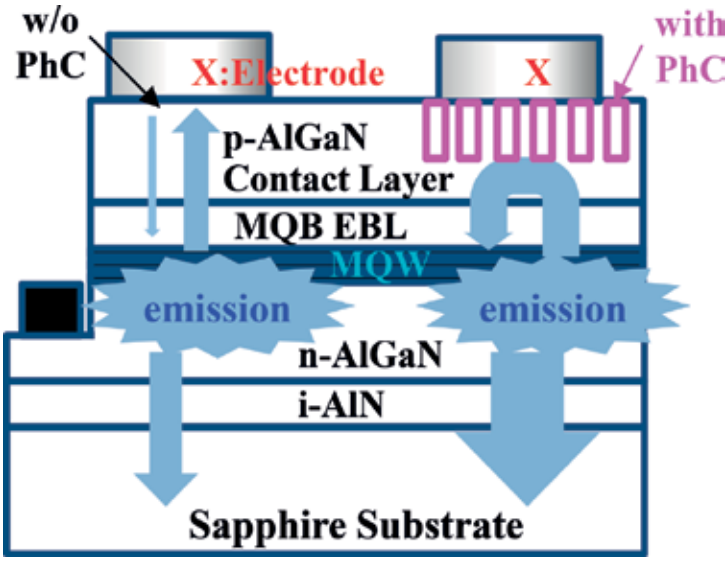

Figure 28. Schematic diagram of the structure of DUV LEDs with and without a reflective PhC on the p-AlGaN contact layer.

Figure 29 shows the schematic cross-sectional structures and electronic-field (E-field) mappings calculated by using FDTD method for 280 nm UVC LEDs (a) with and (b) without reflective HR-PhC, which is fabricated in the p-AlGaN/p-GaN contact layer. To obtain high reflectivity of UV radiation from the QW emitting region, we set the distance between the bottom of PhC air-rod and the QW to be 60 nm [57]. As can be seen in **Figure 29(b)**, the UV light from the QWs propagates equally in all directions for a usual Led case. On the other hand, if we introduce the HR-PhC, radiation from the QWs does not penetrate into the PhC, as shown in **Figure 29(a)**, resulting in realizing a highly-reflection of radiated light. From the FDTD analysis, we found that the LEE is increased by factors of approximately 2.8 and 1.8 at maximum by introducing the HR-PhC into the p-GaN and p-AlGaN contact layers, respectively. We also found that the LEE enhancement factor significantly depends on the value of R/a and that the appropriate R/a value is around 0.4 [57].

Based on these design, we fabricated DUV LEDs with HR-PhCs on the p-AlGaN contact layer. We used nano-imprinting and inductively-coupled plasma (ICP) dry-etching to fabricate a low-damage PhC. **Figure 30** shows (a) a cross-sectional scanning electron microscopy (SEM) image and (b) a high-resolution (HR) TEM image of the hexagonally configured PhC, as well as (c) surface and (d) cross-sectional SEM images of the Ni-electrode.

The period, diameter and depth of the air-holes were 252, 100 and 64 nm, respectively, confirmed by HR-TEM. Also, three-layer MQW and the 2-layer MQB-EBL located just below the air-holes of the PhC were observed in the HR-TEM. Finally, Ni and Ni/Mg electrodes were deposited via a tilted-evaporation method. We confirmed that the air-holes remained clear, with partial evaporation of Ni at the edges.

Figure 31 shows (a) the *I-L* and (b) the *I*-EQE characteristics of 283 nm AlGaN DUV LEDs with high-reflectivity Ni/Mg electrodes (reflectivity of >80%) with and without a PhC on the

http://dx.doi.org/10.5772/intechopen.79936

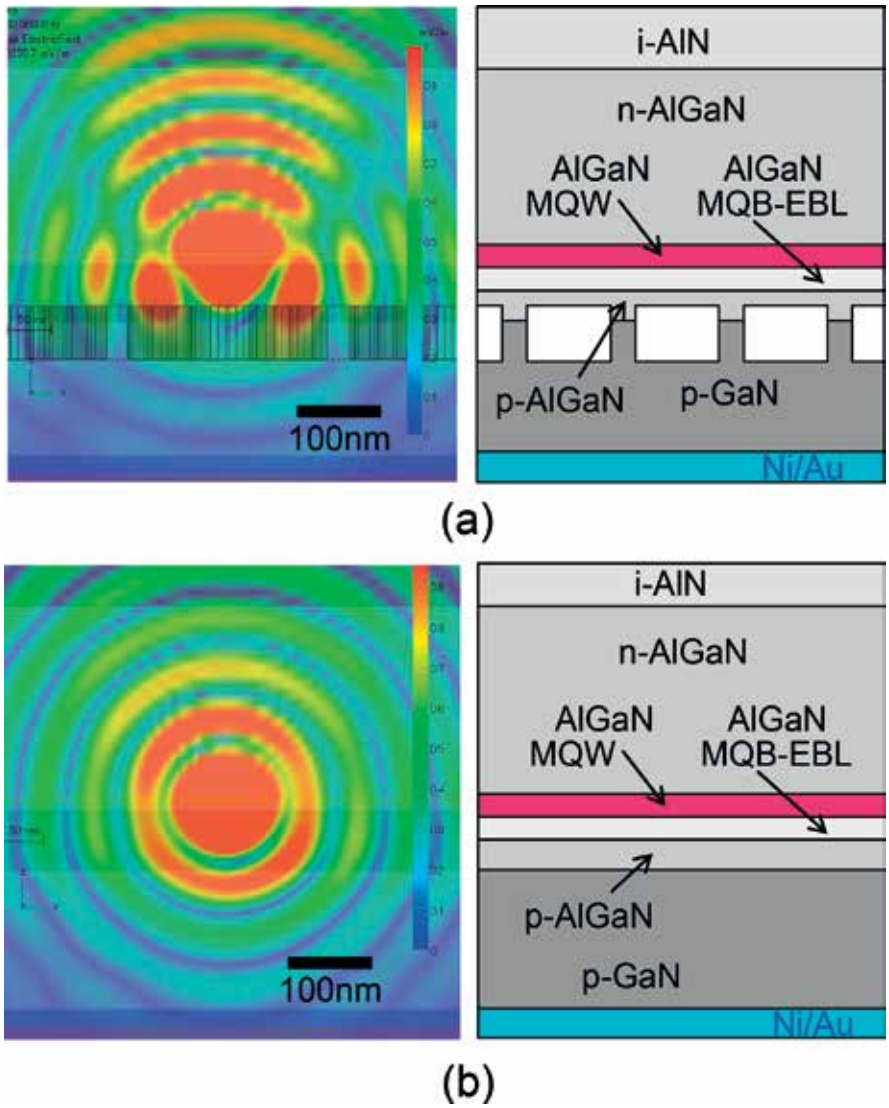

Figure 29. Cross-sectional structures and electronic-field mappings calculated by using FDTD method for 280 nm DUV LEDs (a) with and (b) without reflective PhC.

transparent p-AlGaN contact layer. The LEDs were measured under continuous wave operation on the bare wafers at room temperature. The maximum EQEs of the LEDs with and without the HR-PhC were 10 and 7.9%, respectively. The introduction of the PhC increased the EQE by a factor of 1.23, which is almost the same as obtained by FDTD simulation [57]. We also performed the same experiments using low-reflective Ni p-electrode, and obtained the maximum EQEs with and without the HR-PhC of 6 and 4.8%, respectively. The relatively low EQE of 4.8% is attributed to the low reflectivity of Ni. According to a simple estimate of the relationships between the EQEs of 4.8% (Ni; 30%), and 7.9% (Ni/Mg; 80%) for the LEDs without the PhC, the reflectance for the HR-PhC p-AlGaN with the Ni/Mg electrode is

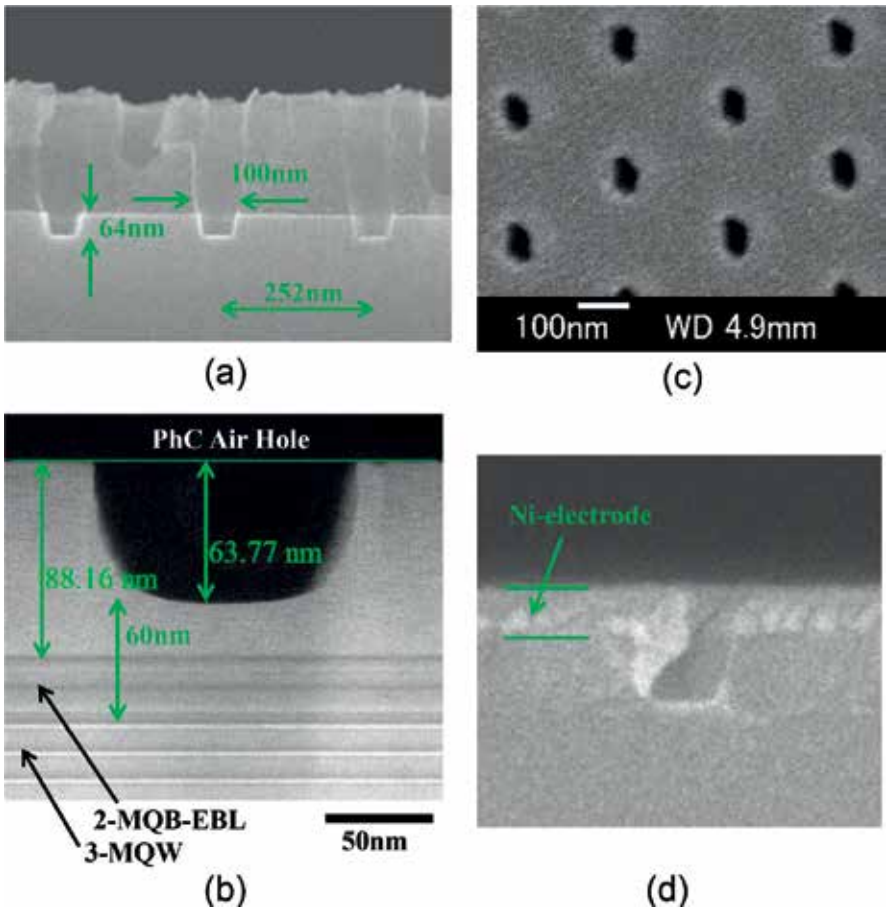

Figure 30. (a) Cross-sectional SEM and (b) HR-TEM images of the PhC fabricated on the p-AlGaN contact layer, along with (c) surface and (d) cross-sectional SEM images of a Ni electrode deposited on the PhC p-AlGaN layer by the tilted-evaporation method.

estimated to exceed 90%. These results indicate that the surface damage caused to the PhC during fabrication was negligible.

The value of *R*/*a* used in the experiments (*R*/*a* = 0.2) were not optimized value. If we had used a larger value of *R*/*a*, i.e., *R*/*a* = 0.4, we would have expected to obtain a significantly higher LEE. The LEE can be further increased by adopting FC technology and encapsulation. By introducing a PhC into the contact layer and reducing the operating voltage, it is expected that LEDs with higher WPE can be obtained.

9. Summary

We have demonstrated on the technologies to develop high-efficiency AlGaN-based DUV LEDs from the view point of increasing IQE, EIE and LEE. Significant increases in IQE of

http://dx.doi.org/10.5772/intechopen.79936

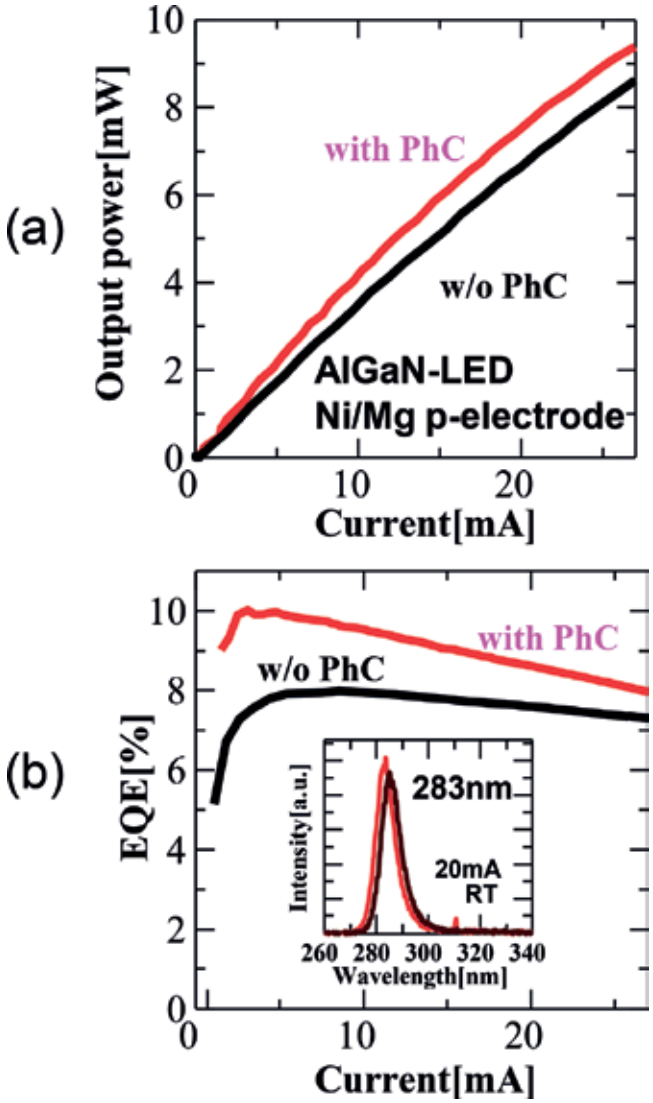

Figure 31. Comparison between the (a) I-L and (b) I-EQE characteristics of 283 nm AlGaN DUV LEDs with high-reflectivity Ni/Mg electrodes (reflectance of >80%) with and without a PhC on the transparent p-AlGaN contact layer.

DUV emission have been achieved for AlGaN-QWs by developing a low-TDD AlN layer grown on sapphire substrate. 222–351 nm DUV LEDs were made using this technology. The EIE of the LEDs was increased significantly by controlling the electron flow using an MQB. We also demonstrated improvements in LEE by using a transparent p-AlGaN contact layer, a highly reflective p-electrode, an AlN buffer layer on a PSS, and an encapsulating resin. The maximum EQE obtained was 20.3% for a 275 nm UVC LED, which is the highest EQE reported so far. We also demonstrated that an HR-PhC fabricated on the p-contact layer significantly increases the efficiency.

Author details

Hideki Hirayama

Address all correspondence to: hirayama@riken.jp

RIKEN, Wako, Saitama, Japan

References

[1] Hirayama H. Quaternary InAlGaN-based high-efficiency ultraviolet light-emitting diodes. Journal of Applied Physics. 2005;**97**:091101

[2] Kneissl M. III-nitride ultraviolet emitters. In: Springer Series in Material Science 227. Woodhead Publishing, ISSN 0933-033X; 2016

[3] Han J, Crawford MH, Shul RJ, Figiel JJ, Banas M, Zhang L, Song YK, Zhou H, Nurmikko AV. AlGaN/GaN quantum well ultraviolet light emitting diodes. Applied Physics Letters. 1998;**73**:1688

[4] Kinoshita A, Hirayama H, Ainoya M, Hirata A, Aoyagi Y. Room-temperature operation at 333 nm of Al0.03Ga0.97N/Al0.25Ga0.75N quantum-well light-emitting diodes with mg-doped superlattice layers. Applied Physics Letters. 2000;**77**:175

[5] Nishida T, Saito H, Kobayashi N. Efficient and high-power AlGaN-based ultraviolet light-emitting diode grown on bulk GaN. Applied Physics Letters. 2001;**79**:711

[6] Sun WH, Adivarahan V, Shatalov M, Lee Y, Wu S, Yang JW, Zhang JP, Khan MA. Continuous wave milliwatt power AlGaN light emitting diodes at 280 nm. Japanese Journal of Applied Physics. 2004;**43**:L1419

[7] Adivarahan V, Wu S, Zhang JP, Chitnis A, Shatalov M, Madavilli V, Gaska R, Khan MA. High-efficiency 269 nm emission deep ultraviolet light-emitting diodes. Applied Physics Letters. 2004;**84**:4762

[8] Adivarahan V, Sun WH, Chitnis A, Shatalov M, Wu S, Maruska HP, Asif Khan M. 250 nm AlGaN light-emitting diodes. Applied Physics Letters. 2004;**85**:2175

[9] Taniyasu Y, Kasu M, Makimoto T. An aluminium nitride light-emitting diode with a wavelength of 210 nanometres. Nature. 2006;**444**:325

[10] Hirayama H, Enomoto Y, Kinoshita A, Hirata A, Aoyagi Y. Efficient 230–280 nm emission from high-Al-content AlGaN-based multiquantum wells. Applied Physics Letters. 2002;**80**:37

[11] Hirayama H, Kinoshita A, Yamabi T, Enomoto Y, Hirata A, Araki T, Nanishi Y, Aoyagi Y. Marked enhancement of 320-360 nm ultraviolet emission in quaternary $In_xAl_yGa_{1-x-y}N$ with in-segregation effect. Applied Physics Letters. 2002;**80**:207

[12] Hirayama H, Enomoto Y, Kinoshita A, Hirata A, Aoyagi Y. Room-temperature intense 320 nm band ultraviolet emission from quaternary InAlGaN-based multiple-quantum wells. Applied Physics Letters. 2002;**80**:1589

[13] Hirayama H, Akita K, Kyono T, Nakamura T, Ishibashi K. High-efficiency 352 nm quaternary InAlGaN-based ultraviolet light-emitting diodes grown on GaN substrates. Japanese Journal of Applied Physics. 2004;**43**:L1241

[14] Fujikawa S, Takano T, Kondo Y, Hirayama H. Realization of 340-nm-band high-output-power (>7 mW) InAlGaN quantum well ultraviolet light-emitting diode with p-type InAlGaN. Japanese Journal of Applied Physics. 2008;**47**:2941

[15] Hirayama H, Yatabe T, Noguchi N, Ohashi T, Kamata N. 231–261 nm AlGaN deep-ultraviolet light-emitting diodes fabricated on AlN multilayer buffers grown by ammonia pulse-flow method on sapphire. Applied Physics Letters. 2007;**91**:071901

[16] Hirayama H, Yatabe T, Ohashi T, Kamata N. Remarkable enhancement of 254-280 nm deep ultraviolet emission from AlGaN quantum wells by using high-quality AlN buffer on sapphire. Physica Status Solidi C. 2008;**5**:2283

[17] Hirayama H, Noguchi N, Fujikawa S, Norimatsu J, Takano T, Tsubaki K, Kamata N. 222–282 nm AlGaN and InAlGaN-based deep-UV LEDs fabricated on high-quality AlN on sapphire. Physica Status Solidi A. 2009;**206**:1176

[18] Hirayama H, Tsukada Y, Maeda T, Kamata N. Marked enhancement in the efficiency of deep-ultraviolet AlGaN light-emitting diodes by using a multiquantum-barrier Electron blocking layer. Applied Physics Express. 2010;**3**:031002

[19] Hirayama H, Noguchi N, Yatabe T, Kamata N. 227 nm AlGaN light-emitting diode with 0.15 mW output power realized using a thin quantum well and AlN buffer with reduced threading dislocation density. Applied Physics Express. 2008;**1**:051101

[20] Hirayama H, Noguchi N, Kamata N. 222 nm deep-ultraviolet AlGaN quantum well light-emitting diode with vertical emission properties. Applied Physics Express. 2010;**3**: 032102

[21] Fujikawa S, Hirayama H, Maeda N. High-efficiency AlGaN deep-UV LEDs fabricated on a- and m-axis oriented c-plane sapphire substrates. Physica Status Solidi C. 2012;**9**(3–4):790-793

[22] Maeda N, Hirayama N. Realization of high-efficiency deep-UV LEDs using transparent p-AlGaN contact layer. Physica Status Solidi C. 2014;**10**:1521

[23] Hirayama H, Maeda N, Fujikawa S, Toyoda S, Kamata N. Development of AlGaN deep-UV LEDs with high light-extraction efficiency by introducing transparent layer structure. Optronics. 2014;**33**:58

[24] Hirayama H, Maeda N, Fujikawa S, Toyota S, Kamata N. Recent progress and future prospects of AlGaN based high-efficiency deep-ultraviolet light-emitting diodes. Japanese Journal of Applied Physics (Selected Topic). 2014;**53**:100209

[25] Mino T, Hirayama H, Takano T, Noguchi N, Tsubaki T. Highly-uniform 260 nm-band AlGaN-based deep-ultraviolet light-emitting diodes developed by 2-inch×3 MOVPE system. Physica Status Solidi C. 2012;**9**:749

[26] Mino T, Hirayama H, Takano T, Tsubaki K, Sugiyama M. Development of 260 nm band deep-ultraviolet light emitting diodes on Si substrate. Proceedings of SPIE. 2013;**8625**:59

[27] Shatalov M, Sun M, Bilenko Y, Sattu A, Hu X, Deng J, Yang J, Shur M, Moe C, Wraback M, Gaska R. Large chip high power deep ultraviolet light-emitting diodes. Applied Physics Express. 2010;**3**:062101

[28] Shatalov M, Sun W, Lunev A, Hu X, Dobrinsky A, Bilenko Y, Yang J. AlGaN deep-ultraviolet light-emitting diodes with external quantum efficiency above 10%. Applied Physics Express. 2012;**5**(8):082101

[29] Mickevičius J, Tamulaitis G, Shur M, Shatalov M, Yang J, Gaska R. Internal quantum efficiency in AlGaN with strong carrier localization. Applied Physics Letters. 2012; **101**(21):211902

[30] Moe CG, Garrett GA, Rotella P, Shen H, Wraback M, Shatalov M, Sun W, Deng J, Hu X, Bilenko Y, Yang J, Gaska R. Impact of temperature-dependent hole injection on low-temperature electroluminescence collapse in ultraviolet light-emitting diodes. Applied Physics Letters. 2012;**101**(25):253512

[31] Mickevičius J, Tamulaitis G, Shur M, Shatalov M, Yang J, Gaska R. Correlation between carrier localization and efficiency droop in AlGaN epilayers. Applied Physics Letters. 2013;**103**(1):011906

[32] Pernot C, Kim M, Fukahori S, Inazu T, Fujita T, Nagasawa Y, Hirano A, Ippommatsu M, Iwaya M, Kamiyama S, Akasaki I, Amano H. Improved efficiency of 255–280 nm AlGaN-based light-emitting diodes. Applied Physics Express. 2010;**3**(6):061004

[33] Inazu T, Fukahori S, Pernot C, Kim MH, Fujita T, Nagasawa Y, Hirano A, Ippommatsu M, Iwaya M, Takeuchi T, Kamiyama S, Yamaguchi M, Honda Y, Amano H, Akasaki I. Improvement of light extraction efficiency for AlGaN-based deep ultraviolet light-emitting diodes. Japanese Journal of Applied Physics. 2011;**50**(12R):122101

[34] Yamada K, Furusawa Y, Nagai S, Hirano A, Ippommatsu M, Aosaki K, Morishima N, Amano H, Akasaki I. Development of underfilling and encapsulation for deep-ultraviolet LEDs. Applied Physics Express. 2015;**8**(1):012101

[35] Grandusky JR, Gibb SR, Mendrick MC, Moe C, Wraback M, Schowalter LJ. High output power from 260 nm Pseudomorphic ultraviolet light-emitting diodes with improved thermal performance. Applied Physics Express. 2011;**4**:082101

[36] Grandusky JR, Chen J, Gibb SR, Mendrick MC, Moe C, Rodak L, Garrett GA, Wraback M, Schowalter LJ. 270 nm Pseudomorphic ultraviolet light-emitting diodes with over 60 mW continuous wave output power. Applied Physics Express. 2013;**6**:032101

[37] Kinoshita T, Hironaka K, Obata T, Nagashima T, Dalmau R, Schlesser R, Moody B, Xie J, Inoue S, Kumagai Y, Koukitu A, Sitar Z. Deep-ultraviolet light-emitting diodes fabricated

on AlN substrates prepared by hydride vapor phase epitaxy. Applied Physics Express. 2012; **5**:122101

[38] Kinoshita T, Obata T, Nagashima T, Yanagi H, Moody B, Mita S, Inoue S, Kumagai Y, Koukitu A, Sitar Z. Performance and reliability of deep-ultraviolet light-emitting diodes fabricated on AlN substrates prepared by hydride vapor phase epitaxy. Applied Physics Express. 2013;**6**:092103

[39] Kinoshita T, Obata T, Yanagi H, Inoue S. High p-type conduction in high-Al content mg-doped AlGaN. Applied Physics Letters. 2013;**102**:012105

[40] Inoue S, Tamari N, Taniguchi M. 150 mW deep-ultraviolet light-emitting diodes with large-area AlN nano-photonic light extraction structure emitting at 265 nm. Applied Physics Letters. 2017;**110**:141106

[41] Fujioka A, Misaki T, Murayama T, Narukawa Y, Mukai T. Improvement in output power of 280-nm deep ultraviolet light-emitting diode by using AlGaN multi quantum wells. Applied Physics Express. 2010;**3**:041001

[42] Ichikawa M, Fujioka A, Kosugi T, Endo S, Sagawa H, Tamaki H, Mukai T, Uomoto M, Shimatsu T. High-output-power deep ultraviolet light-emitting diode assembly using direct bonding. Applied Physics Express. 2016;**9**:072101

[43] Li XH, Detchprohm T, Kao TT, Satter MM, Shen SC, Yoder PD, Dupuis RD, Wang S, Wei YO, Xie H, Fischer AM, Ponce FA, Wernicke T, Reich C, Martens M, Kneissl M. Low-threshold stimulated emission at 249 nm and 256 nm from AlGaN-based multiple-quantum-well lasers grown on sapphire substrates. Applied Physics Letters. 2014;**105**(14):141106

[44] Mehnke F, Kuhn C, Stellmach J, Kolbe T, Ploch NL, Rass J, Rothe MA, Reich C, Ledenstov N, Pristovsek M, Wernicke T, Kneissl M. Effect of heterostructure design on carrier injection and emission characteristics of 295 nm light emitting diodes. Journal of Applied Physics. 2015;**117**(19):195704

[45] Susilo N, Hagedorn S, Jaeger D, Miyake H, Zeimer U, Reich C, Neuschulz B, Sulmoni L, Guttmann M, Mehnke F, Kuhn C, Wernicke T, Weyers M, Kneissl M. AlGaN-based deep UV LEDs grown on sputtered and high temperature annealed AlN/sapphire. Applied Physics Letters. 2018;**112**(4):041110

[46] Iida K, Kawashima T, Miyazaki A, Kasugai H, Mishima A, Honshio A, Miyake Y, Iwaya M, Kamiyama S, Amano H, Akasaki I. 350.9 nm UV laser diode grown on low-dislocation-density AlGaN. Japanese Journal of Applied Physics. 2004;**43**:L499

[47] Takano T, Narita Y, Horiuchi A, Kawanishi H. Room-temperature deep-ultraviolet lasing at 241.5 nm of AlGaN multiple-quantum-well laser. Applied Physics Letters. 2004;**84**:3567

[48] Ban K, Yamamoto J, Takeda K, Ide K, Iwaya M, Takeuchi T, Kamiyama S, Akasaki I, Amano H. Internal quantum efficiency of whole-composition-range AlGaN multiquantum wells. Applied Physics Express. 2011;**4**:052101

[49] Banal RG, Funato M, Kawakami Y. Optical anisotropy in [0001]-oriented $Al_xGa_{1-x}N$/AlN quantum wells (x>0.69). Physical Review B. 2009;**79**(R):121308

[50] Kawanishi H, Senuma M, Yamamoto M, Niikura E, Nukui T. Extremely weak surface emission from (0001) ***c***-plane AlGaN multiple quantum well structure in deep-ultraviolet spectral region. Applied Physics Letters. 2006;**89**:081121

[51] Iga K, Uenohara H, Koyama F. Electron reflectance of multiquantum barrier (MQB). Electronics Letters. 1986;**22**:1008

[52] Kishino K, Kikuchi A, Kaneko Y, Nomura I. Enhanced carrier confinement effect by the multiquantum barrier in 660 nm GaInP/AlInP visible lasers. Applied Physics Letters. 1991; **58**:1822

[53] Yun J, Hirayama H. Investigation of the light-extraction efficiency in 280 nm AlGaN-based light-emitting diodes having a highly transparent p-AlGaN layer. Journal of Applied Physics. 2017;**121**:013105

[54] Maeda N, Jo M, Hirayama H. Efficiency improvement of AlGaN deep UV-LEDs using highly-reflective Ni/Al p-type electrode. Physica Status Solidi A, in press. 2018

[55] Maeda N, Yun J, Jo M, Hirayama H. Enhancing the light-extraction efficiency of AlGaN deep-ultraviolet light-emitting diodes using highly reflective Ni/Mg and Rh as p-type electrodes. Japanese Journal of Applied Physics. 2018;**57**:04H08-1-04H08-4

[56] Takano T, Mino T, Sakai J, Noguchi N, Tsubaki K, Hirayama H. Deep-ultraviolet light-emitting diodes with external quantum efficiency higher than 20% at 275 nm achieved by improving light-extraction efficiency. Applied Physics Express. 2017;**10**:031002

[57] Kashima Y, Maeda N, Matsuura E, Jo M, Iwai T, Morita T, Kokubo M, Tashiro T, Kamimura R, Osada Y, Takagi H, Hirayama H. High external quantum efficiency (10%) AlGaN based deep-ultraviolet light-emitting diodes achieved by using highly reflective photonic crystal on p-AlGaN contact layer. Applied Physics Express. 2018;**11**:012101

[58] Kashima Y, Matsuura E, Kokubo M, Tashiro T, Ohkawa T, Hirayama H, Kamimura R, Osada Y, Shimatani S, Deep-UV LED device and its fabrication method, Japan Patent 5757512; 2015

[59] Kashima Y, Matsuura E, Kokubo M, Tashiro T, Ohkawa T, Hirayama H, Maeda N, Jo M, Kamimura R, Osada Y, Shimatani S, Deep-UV LED device and its fabrication method, Japan Patent 5999800; 2016

[60] Kashima Y, Matsuura E, Kokubo M, Tashiro T, Hirayama H, Kamimura R, Osada Y, Morita T, Deep-UV LED device and its fabrication method, Japan Patent 6156898; 2017

Edited by Jagannathan Thirumalai

The broad vision of this book is to offer book lovers a comprehensive appraisal of topics in the global advancements of experimental facts, instrumentation, and practical applications of LED and OLED materials and their applications. The prime feature of this book is connected with LED and OLED materials approaches of fabrication, optimization limits, and their extensive technical applications. This book is comprised of seven chapters encompassing the importance of LEDs and OLEDs, the history of LEDs and OLEDs with necessary examples, the phototoxic-cum-bactericidal effect due to the usage of blue LED irradiation, DC network indoor and outdoor LED lighting, WLEDs with thermally activated delayed fluorescence emitters, tetradentate cyclometalated platinum (II) complex-based efficient organic LEDs, the impact of the use of large LED lighting loads in low-voltage networks, highly efficient OLEDs using thermally activated delayed fluorescent materials, and AlGaN deep ultraviolet LEDs. Individual chapters provide a base for the wide range of common bibliophiles in diversified fields, students, and researchers, who may conduct research pertinent to this book and will find simply explained basics as well as advanced principles of designated subjects related to these phenomena. The book was created from seven contributions from experts in the diversified fields of LED and OLED fabrication and technology from over 15 research institutes across the globe.

Published in London, UK

IntechOpen

ISBN 978-1-83881-496-0